

University of Alberta

**Optical Single Sideband for Broadband
And Subcarrier Systems**

by

Robert James Davies ©

A thesis submitted to the faculty of Graduate Studies and Research in partial fulfillment
of the requirements for the degree of **Doctor of Philosophy**

Department of Electrical And Computer Engineering

Edmonton, Alberta

Spring 1999



National Library
of Canada

Acquisitions and
Bibliographic Services

395 Wellington Street
Ottawa ON K1A 0N4
Canada

Bibliothèque nationale
du Canada

Acquisitions et
services bibliographiques

395, rue Wellington
Ottawa ON K1A 0N4
Canada

Your file Votre référence

Our file Notre référence

The author has granted a non-exclusive licence allowing the National Library of Canada to reproduce, loan, distribute or sell copies of this thesis in microform, paper or electronic formats.

The author retains ownership of the copyright in this thesis. Neither the thesis nor substantial extracts from it may be printed or otherwise reproduced without the author's permission.

L'auteur a accordé une licence non exclusive permettant à la Bibliothèque nationale du Canada de reproduire, prêter, distribuer ou vendre des copies de cette thèse sous la forme de microfiche/film, de reproduction sur papier ou sur format électronique.

L'auteur conserve la propriété du droit d'auteur qui protège cette thèse. Ni la thèse ni des extraits substantiels de celle-ci ne doivent être imprimés ou autrement reproduits sans son autorisation.

0-612-39520-0

Canada

To Kathie

Abstract

Radio systems are being deployed for broadband residential telecommunication services such as broadcast, wideband Internet and video on demand.

Justification for radio delivery centers on mitigation of problems inherent in subscriber loop upgrades such as Fiber to the Home (FTTH) and Hybrid Fiber Coax (HFC). While radio will alleviate some of these subscriber loop upgrade problems there are still problems to be solved, the most pressing of which is the propagation difficulties encountered by high frequency wideband radio signals in multipath environments. Deployment of the radio structure on optical fiber has been suggested as a mitigation for these path problems by allowing the reduction the propagation distance between the optical/RF interface point and the consumer premises. While the radio propagation problem may be alleviated by fiber deployment, a new problem arises due to the interaction of fiber chromatic dispersion and the spectral characteristics of the optical signal. A dispersion penalty in the form of reduced power from the optical link results when radio signals are transmitted on fiber in conventional Double Sideband (DSB) Mode.

It will be shown that Optical Single Sideband Modulation (OSSB) is an effective tool for combatting dispersion effects on fiber. A new and general theory is presented that addresses OSSB from the optical broadband perspective. The theory is adapted from the studies of Compatible Single Sideband radio modulation for AM radio in the 1960's. The core of the theory involves the behavior of time domain signals that have similar amplitude and phase relationships to the 'Minimum Phase' class of signal. It will be shown that immediate dispersion benefits for optical modulation are attained by using these

signals and that further benefits are available for post-detection compensation. The theory will then be modified to accommodate optical subcarrier modulation with the end result being a new class of optical link that has general application in fiber optic communications. Predistortion schemes for modulated subcarriers will be developed to efficiently utilize the OSSB theory on optical links that also function as harmonic upconverters. Finally, experimental results will be presented to verify the theoretical claims.

Acknowledgments

I gratefully acknowledge the guidance and facilities provided to me by Dr. Jan Conradi, my supervisor. His, David Dodds, and Mike Seiben's pioneering work on Optical Single Sideband for broadband optical structures was the foundation stone for this work. I'm particularly grateful to have been a part of the Optical Single Sideband 'team' in which a unique mix of talents coalesced to produce a number of new and exciting perspectives for optical transmission. I thank Dr. Filanovsky for supervising my thesis when Dr. Conradi returned to industry.

I would also thank my examining committee: Dr. J. Conradi, Dr. I. Filanovsky, Dr. W. Krzymien, Dr. J. McMullin, Dr. I. Fair, Dr. F. Hegmann and Dr. J. Cartledge for their suggestions and for reviewing this document.

I would like to thank TELUS corporation, particularly Roger Pederson and Craig Dobson who supported me by allowing me to work on this project as part of my duties as TELUS/TRLabs Industry Representative.

I would like to thank TRLabs, particularly George Squires, for their financial and technical support, allowing me to work on this thesis as part of my duties as TRLabs Staff. I also thank Dr. Spence Nichols for the stimulating discussions on CSSB systems, Sheldon Walklin, Mike Seiben and Sean Hum for advice and assistance in the optical test bed development.

This work was supported in part by the Natural Sciences and Engineering Research Council of Canada, Nortel, TRLabs and The University of Alberta through the NSERC/NORTEL/TRLabs Industrial Research Chair in Fiber Optic Communications at the University of Alberta.

Table of Contents

1.	Introduction	1
1.1	Wireless Access	3
1.2	Radio Channel Impacts	4
1.3	The Premise: Radio on Fiber	7
1.4	Subcarrier Optical Systems Background	8
	1.4.1. Early Studies	9
	1.4.2. Systems Research	10
	1.4.4. The Basic Optical Link	14
	1.4.5. Chromatic Dispersion	14
1.5	Research Objectives and Scope	17
1.6	Thesis Structure	17
	1.6.1. Chapter 2. Optical Single Sideband Modulation	18
	1.6.2. Chapter 3. Post Detection Equalization for Broadband Signals	18
	1.6.3. Chapter 4. Subcarrier Optical Single Sideband: Transmission Characteristics	19

1.6.4.	Chapter 5. Transmission of Modulated Harmonically Upconverted OSSB Subcarriers	19
1.6.5.	Chapter 6. Proof-Of-Concept Experiments	20
1.6.6.	Chapter 7. Conclusions	20
2.	Optical Single Sideband Modulation	21
2.1	Introduction	21
2.2.	Theory	22
2.2.1.	Complex Envelope Representation of Bandpass Signals	22
2.2.2.	Single Sideband Modulation	28
2.2.3.	Analytic Signals	31
2.3.	AM Compatibility	36
2.4.	Compatible Optical Single Sideband	37
2.5.	Implementation: The Ideal Minimum Phase Modulator	39
2.5.1.	Computer Simulation	41
2.5.2.	Dispersion Effects And Ideal CSSB Optical Modulation	48
2.5.2.1.	Sinusoidal Modulation	48
2.5.2.2.	Broadband Dispersion Effects	50
2.6.	OSSB Optical Modulator Structures	57
2.6.1.	Laser Intensity/Phase Modulator	57

2.6.1.1. Laser Diode Model	57
2.6.1.2. External Phase Modulator	60
2.6.1.3. Laser/Phase COSSB Simulation	60
2.6.1.4. More On Laser Chirp	65
2.6.1.5. Laser Chirp and The Subcarrier Process	66
2.6.2. Laser FM Modulator Coupled to External Amplitude Modulator	66
2.6.3. External Mach-Zehnder Amplitude Modulator and Cascaded External Phase Modulator	70
2.6.4. Other Structures	75
2.7. Conclusions	75
3. Post Detection Equalization for Broadband Signals	76
3.1. Introduction	76
3.2. Dispersion Compensation	76
3.2.1. Antidispersive Filtering with Self-HomoDyne Detection	76
3.3. Minimum Phase Dispersion Compensator	80
3.4. Simulation Results	81
3.5. Theoretical Development	85
3.6. Forced Minimum Phase Condition	89

3.7.	Conclusions	94
4.	Subcarrier Optical Single Sideband: Transmission Characteristics	95
4.1.	Introduction	95
4.2.	Chromatic Dispersion and CW Subcarrier Signals	95
	4.2.1. Non-Ideal OSSB	97
4.3.	Finite Bandwidth Subcarrier Signals	98
	4.3.1. Double Sideband Modulation	98
	4.3.2. Single Sideband Modulation	100
4.4.	Subcarrier Hilbert Transforms	101
4.5.	Linear Subcarrier OSSB Hybrid Modulators	102
	4.5.1. Laser intensity Modulator with Cascaded External Phase Modulator	102
	4.5.2. Laser FM Cascaded with MZM External Amplitude Modulator.	108
	4.5.3. MZM Amplitude Modulator with Cascaded External Phase Modulator	109
4.6.	Harmonic Generation With Optical SSB	112
	4.6.1. Laser/Phase Non-Linear Upconverter	113
	4.6.2. Laser FM Cascaded with MZM External Amplitude Modulator.	116

- 4.6.3. Hartley MZM and MZM/Phase Modulator Cascade 117
 - 4.7. Fiber Dispersion and Harmonic Subcarriers 121
 - 4.7.1. Mathematical Model 121
 - 4.7.2. OSSB Harmonic Modulation 129
 - 4.8. Conclusions 130
- 5. Transmission of Modulated Harmonically Upconverted OSSB Subcarriers 132
 - 5.1. Introduction 132
 - 5.2. Linear Subcarrier Modulation 132
 - 5.3. General Harmonic Upconversion 133
 - 5.3.1. Optical Harmonic Upconverter 138
 - 5.4. Dispersion Performance 142
 - 5.4.1. Amplitude/Phase Predistortion 146
 - 5.4.2. Amplitude/Phase Predistortion and Fiber Dispersion 155
 - 5.5. Conclusions 156
- 6. Proof-Of-Concept Experiments 157
 - 6.1. Introduction 157
 - 6.2. Studies 157

6.2.1. Verification of Transmission Characteristics of CW OSSB Linear Subcarrier Modulation	158
6.2.1.1. Linear Modulation	159
6.2.1.2. Harmonic Subcarrier Modulation	166
6.3. Modulated Subcarriers	171
6.3.1. Linear BPSK Modulation	172
6.3.2. Linear QPSK Modulation	176
6.3.3. Linear Link Characteristics	178
6.4. Harmonic Modulated Subcarriers	178
6.4.1. Biphase Modulation	179
6.4.2. Quadrature Modulation	180
6.4.2.1. QPSK On Dispersive Fiber	184
6.5. Conclusions	187
7. Conclusions	189
7.1. Thesis Review	189
7.2. Further Research	192
References	196
Appendix A: The IRIS System	208

A.1.	Introduction	208
A.2.	System Description	209
A.2.1.	Transmitter	209
A.2.2.	Receiver	211
A.2.3.	Design Philosophy	212
A.3.	Applications	213
A.3.1.	Channel/Device Characterization	213
A.3.2.	Pseudo Noise Channel/Device Probes	213
A.3.3.	Modulation Testing	216
A.3.4.	Component Studies	216
A.3.5.	Instrumentation and Control	216
A.3.6.	Access	217
	Appendix B: Fiber Dispersion.....	218
B.1.	Wave Packets and Group Velocity	218

List of Tables

Table 2.1. Ideal COSSB simulation parameters.	41
Table 2.2. Parameters for ideal COSSB simulation on dispersive fiber.	51
Table 2.3. Parameters for laser/phase simulation on dispersive fiber	62
Table 2.4. Parameters for MZM/Phase simulation on dispersive fiber.	72
Table 3.1. Ideal COSSB simulation parameters.	82
Table 4.1. Harmonic components for laser/phase electric field.	106

List of Figures

Figure 1.1. Typical impulse response of a short radio channel at 18 GHz.....	6
Figure 1.2. Conventional fixed cellular broadband delivery system	7
Figure 1.3. Distributed radio on fiber broadband delivery system.....	8
Figure 1.4. Direct modulation optical link	11
Figure 1.5. Externally modulated optical/RF link	12
Figure 1.6. Detected power as a function of fiber length for $f = 18$ GHz, $\lambda_0 = 1550$ nm, $D = 18$ ps/(nm•km).	15
Figure 1.7. Detected power as a function of subcarrier frequency for fiber length - 60 km., $\lambda_0 = 1550$ nm, $D = 18$ ps/(nm•km).....	16
Figure 2.1. Narrowband bandpass signal	23
Figure 2.2. Quadrature modulator.....	25
Figure 2.3. Quadrature SSB modulator.....	29
Figure 2.4. USSB and LSSB bandpass spectra.....	30

Figure 2.5. Coherent detector.	30
Figure 2.6. Complex z plane and infinite half circle 'Q'.	34
Figure 2.7. Ideal minimum phase modulator.	40
Figure 2.8. PRBS sequence	42
Figure 2.9. Bandlimited and scaled PRBS sequence.	42
Figure 2.10. Spectrum of double sideband PRBS modulated carrier.	43
Figure 2.11. Spectrum of minimum phase single sideband PRBS modulated carrier.	43
Figure 2.12. Recovered PRBS sequence	44
Figure 2.13. Hilbert transforms of the \ln of $p(t)$ (solid line) and of $p(t)$ (both on linear scale).	45
Figure 2.14. Approximate minimum phase modulator.	45
Figure 2.15. Spectral plot of hybrid signal with scaled Hilbert transform phase function.	46
Figure 2.16. Recovered PRBS sequence.	47
Figure 2.17. Plot of $p(t)$ (solid) and $\ln(p(t))$ (both on linear scale).	47

Figure 2.18. Double sideband optical electric field spectrum, $B = 10$ GB/s.	52
Figure 2.19. Detected power spectrum without dispersion.	52
Figure 2.20. Detected power spectrum after 200 km dispersive fiber, $B = 10$ GB/s, $D = 18$ ps/(nm•km).	53
Figure 2.21. Eye pattern from detected signal after 200 km dispersive fiber $B = 10$ GB/s, $D = 18$ ps/(nm•km).	54
Figure 2.22. Detected power spectrum after 500 km dispersive fiber $B = 10$ GB/s, $D = 18$ ps/(nm•km).	54
Figure 2.23. COSSB detected power spectrum after 200 km dispersive fiber. ...	55
Figure 2.24 Eye diagram from COSSB detected signal after 200 km dispersive fiber.	55
Figure 2.25. Eye diagram from COSSB detected signal on zero length fiber.	56
Figure 2.26. Laser intensity/phase COSSB modulator.	57
Figure 2.27. Laser diode transfer characteristic.	58
Figure 2.28. Circuit model for laser/phase simulation.	61
Figure 2.29. Information signal eye pattern.	62

Figure 2.30. Square law detected signal for a zero length or nondispersive fiber link.	63
Figure 2.31. OSSB frequency plot for the laser/phase device.	63
Figure 2.32. Detected signal from a DSB modulated optical signal over 200 km dispersive fiber.	64
Figure 2.33. Detected signal from a COSSB modulated optical signal over 200 km dispersive fiber.	64
Figure 2.34. Laser FM/external COSSB modulator.	67
Figure 2.35. MZM/phase modulator.	70
Figure 2.36. MZM/phase modulator modified for MZM non-linear distortion.	72
Figure 2.37. SSB electric field spectrum from MZM/phase modulator.	73
Figure 2.38. Eye pattern of envelope of SSB MZM/phase modulator at modulator output.	73
Figure 2.39. Eye pattern of envelope of DSB MZM modulator at output of square-law detector after 200 km dispersive fiber.	74
Figure 2.40. Eye pattern of envelope of SSB MZM/phase modulator at output of square-law detector after 200 km dispersive fiber.	74
Figure 3.1. Optical electric field frequency plot for COSSB modulator.	77

Figure 3.2. Self homodyne detector and anti-dispersive filter block diagram.	79
Figure 3.3. Minimum phase dispersion compensator.	80
Figure 3.4. Eye Pattern For Original Data Before Transmission.....	82
Figure 3.5. Eye Pattern for 10 GB/s 300 km dispersive Fiber COSSB signal - no compensation.....	83
Figure 3.6. Eye pattern for 300 km dispersive fiber COSSB signal enhanced with AFHD.	83
Figure 3.7. Eye pattern for 300 km COSSB signal - minimum phase compensation.....	84
Figure 3.8. Eye pattern for 800 km dispersive fiber COSSB signal enhanced with AFHD.	84
Figure 3.9. Eye pattern for 800 km dispersive fiber COSSB signal with minimum phase compensation.	85
Figure 3.10. Trajectory of 10 GB/s complex minimum phase signal (parametric in 't').	87
Figure 3.11. Trajectory of 10 GB/s complex minimum phase signal after transmission on 800 km dispersive fiber: $D = 18 \text{ ps}/(\text{nm}\cdot\text{km})$	87
Figure 3.12. Trajectory of 10 GB/s complex minimum .phase signal after transmission on 600 km dispersive fiber: $D = 18 \text{ ps}/(\text{nm}\cdot\text{km})$	88

Figure 3.13. Trajectory of minimum phase signal with large modulation index...	92
Figure 4.1. Simulated detected power as a function of dispersive fiber length, $f_c = 18$ GHz, $D = 18$ ps/(nm•km), $\lambda_0 = 1550$ nm.	96
Figure 4.2. Normalized detected power as a function of fiber length for DSB ($r = 1$ - solid) And $r = 0.2$ (dotted).	98
Figure 4.3. OSSB E-field spectrum for subcarrier modulated laser/phase modulator with simple sinusoid phase function with $m = 0.2$, $m_p \sim 0.1$	104
Figure 4.4. Detected power for dispersive fiber using ideal laser phase modulator with $m = 0.2$, $m_p \sim 0.1$, $D = 18$ ps/(nm•km), $f_c = 18$ GHz, and $\lambda_0 = 1550$ nm. ...	104
Figure 4.5. OSSB E-field spectrum for subcarrier modulated laser/phase modulator With $m = 0.8$, $m_p \sim 0.4$	107
Figure 4.6. Detected power for dispersive fiber using ideal laser phase modulator with $m = 0.8$, $m_p \sim 0.4$, $D = 18$ ps/(nm•km), $f_c = 18$ GHz, and $\lambda_0 = 1550$ nm. .	108
Figure 4.7. MZM/Phase COSSB modulator.	109
Figure 4.8. Detected power vs. fiber length for dispersive fiber using MZM/phase modulator for $m = 0.2$, $D = 18$ ps/(nm•km) and $\lambda_0 = 1550$ nm.	111
Figure 4.9. Laser transfer characteristic.....	114
Figure 4.10. Clipped laser E-field spectrum, $m = 1.5$	114

Figure 4.11. Clipped laser detector output spectrum $m = 1.5$	115
Figure 4.12. Ratio of detected harmonic amplitude to detected dc term versus modulation index from laser diode IMDD harmonic upconverter, H_x refers to harmonic order x	116
Figure 4.13. Electric field spectrum from Hartley MZM driven with sinusoids at $m = 0.7$	118
Figure 4.14. Detected photocurrent spectrum from Hartley MZM driven with sinusoids at $m = 0.7$	119
Figure 4.15. Ratio of detected harmonic amplitude to detected DC term versus modulation index from MZM/phase IMDD harmonic upconverter.	120
Figure 4.16. Power in H5 from nonlinear phase modulator as a function of fiber length, $f_c = 18/5$ GHz, $m = 0.7$ $D = 18$ ps/(nm•km) and $\lambda_0 = 1550$ nm.	126
Figure 4.17. Power in H5 as a function of fiber length for a 'chirpless' MZM $D = 18$ ps/(nm•km), $\lambda_0 = 1550$ nm, $f_c = 18/5$ GHz and $m = 0.7$	128
Figure 4.18. Power in H5 from Hartley OSSB harmonic upconverter as a function of fiber length $D = 18$ ps/(nm•km), $\lambda_0 = 1550$ nm, $f_c = 18/5$ GHz and $m = 0.7$. .	130
Figure 5.1. Compressed input constellation.	134
Figure 5.2. Circuit model for general non-linear upconverter and demodulator simulation.	135

Figure 5.3. Eye diagram of recovered output from fifth harmonic for general non-linear upconverter.	136
Figure 5.4. Cross-correlation function of recovered output with original information signal from fifth harmonic for general non-linear upconverter.	137
Figure 5.5. Recovered output from fifth harmonic without phase predistortion.	138
Figure 5.6. Circuit model for optical MZM/phase COSSB upconverter and demodulator simulation.	140
Figure 5.7. Eye diagram recovered output from fifth harmonic for MZM/phase OSSB modulator, $m_z = 0.7$, $m_p = 0.7$, $f_c = 18$ GHz, $D = 18$ ps/(nm•km) $\lambda_0 = 1550$ nm and $L = 0$	141
Figure 5.8. Cross-correlation function of recovered output with original information signal from fifth harmonic for optical mzm/phase non-linear upconverter.	142
Figure 5.9. Recovered QPSK constellation from harmonically upconverted modulated subcarrier on zero length link (with phase recovery), $H_5 = 18$ GHz, $D = 18$ ps/nm•km, $\lambda_0 = 1550$, $B = 30\%$	143
Figure 5.10. Recovered QPSK constellation from dispersive link harmonically upconverted modulated subcarrier, $H_5 = 18$ GHz, $D = 18$ ps/nm•km, $\lambda_0 = 1550$, $B = 30\%$	144
Figure 5.11. Eye diagram from recovered output from fifth harmonic for mzm/phase OSSB modulator, $m_z = 0.7$, $m_p = 0.7$, $f_c = 18$ GHz, $D = 18$ ps/(nm•km) $\lambda_0 = 1550$ nm and $L = 40$ km.	145

Figure 5.12. Eye diagram from recovered output from fifth harmonic for mzm/phase OSSB modulator, $m_z = 0.7$, $m_p = 0.7$, $f_c = 18$ GHz, $D = 18$ ps/(nm•km) $\lambda_0 = 1550$ nm and $L = 80$ Km.	146
Figure 5.13. 16 QAM constellation.	147
Figure 5.14. Fifth order Bessel function.	148
Figure 5.15. Fifth order Bessel function.	148
Figure 5.16. AM/PM harmonic upconverter block diagram.	149
Figure 5.17. Comparison of 'Q' recovered data with original information signal from 16QAM signal predistorted for harmonic upconversion.	150
Figure 5.18. Comparison of 'I' recovered data with original information signal from 16QAM signal predistorted for harmonic upconversion.	151
Figure 5.19. COSSB harmonic upconverter simulation block diagram, $f_c = 18$ GHz.	152
Figure 5.20. Comparison of 'Q' recovered data with original information signal from 16qam signal predistorted for harmonic upconversion.	153
Figure 5.21. Comparison of 'Q' recovered data with original information signal from 16qam signal without phase pre-distortion.	153
Figure 5.22. 16QAM signal without phase pre-distortion.	154

Figure 5.23. 16QAM signal without amplitude pre-distortion.	154
Figure 5.24. Phase and amplitude of 5th harmonic mzm/phase over 60 km dispersive fiber modulation index. $D = 18 \text{ ps}/(\text{nm}\cdot\text{km})$, $f_c = 18 \text{ GHz}$	155
Figure 6.1. Experimental test bed for transmission experiments.	158
Figure 6.2. Chirpless DSB Mach-Zehnder modulator.	160
Figure 6.3. Cascaded MZM/Phase OSSB modulator.	160
Figure 6.4. Hartley Mach-Zehnder modulator.	161
Figure 6.5. DSB experimental optical spectrum.	162
Figure 6.6. Experimental OSSB optical spectrum from cascade MZM/phase modulator.	162
Figure 6.7. Experimental OSSB optical spectrum from Hartley configured MZM.	163
Figure 6.8. Detected power as a function of fiber length for DSB and OSSB modulation on dispersive Fiber, $D \sim 16.5 \text{ ps}/(\text{nm}\cdot\text{km})$, $f_c = 17.16 \text{ GHz}$, $\lambda_0 = 1550 \text{ nm}$, $m = 0.2$	163
Figure 6.9. Theoretical and experimental linear OSSB electric field spectrum from Hartley MZM, $f_c = 17.35 \text{ GHz}$, $m = 0.1$	164

Figure 6.10. Detected power vs fiber length for OSSB and DSB over dispersive fiber, $m = 0.1$, $f_c = 17.16$ GHz, $\lambda_0 = 1550$ nm, $D \sim 16.5$ ps/(nm•km).....	165
Figure 6.11. Experimental harmonic DSB optical spectrum for $m \sim 0.7$, $f_c = 3.47$ GHz, $\lambda_0 = 1550$ nm.	166
Figure 6.12. Simulated harmonic DSB optical spectrum, $m \sim 0.7$, $f_c = 3.47$ GHz, $\lambda_0 = 1550$ nm.	167
Figure 6.13. Experimental OSSB harmonic spectrum from OSSB Hartley MZM, $m \sim 0.7$, $f_c = 3.47$ GHz, $\lambda_0 = 1550$ nm.....	167
Figure 6.14. Experimental OSSB harmonic spectrum from OSSB MZM/phase hybrid modulator, $m = 0.7$, $f_c = 3.47$ GHz.	168
Figure 6.15. Simulated OSSB harmonic spectrum from OSSB MZM/Phase hybrid modulator $m \sim 0.7$, $f_c = 3.47$ GHz, $\lambda_0 = 1550$ nm.....	168
Figure 6.16. Experimental transmission characteristics of 5th harmonic modulation of CW subcarrier signals on dispersive fiber, $m \sim 0.7$, $f_c = 3.47$ GHz.	169
Figure 6.17. Power in H5 as a function of fiber length for a 'chirpless' MZM and an OSSB Hartley modulator, $m = 0.7$, $D = 16.5$ ps/(nm•km), $f_c = 3.47$ GHz.	170
Figure 6.18. Linear modulation test bed.....	172
Figure 6.19. Eye diagram of test bed in back to back mode on 17.35 GHz radio carrier At B = 200 Mb/s.	173

Figure 6.20. Eye diagram for 200 MB/s BPSK signal on DSB linear 17.35 GHz radio carrier and zero length fiber, $m = 0.1$	174
Figure 6.21. Eye diagram for 200 MB/s BPSK Signal on DSB linear 17.35 GHz radio carrier 10 km fiber (at null), $m = 0.1$	174
Figure 6.22. Eye diagram For 200 MB/s BPSK signal on DSB linear 17.35 GHz radio carrier at 20 Km fiber, $m = 0.1$	175
Figure 6.23. Eye diagram For 200 MB/s BPSK signal on OSSB linear 17.35 GHz radio carrier at 10 km fiber, $m = 0.1$	175
Figure 6.24. Constellation For 100 MS/s QPSK signal on back-to-back 17.35 GHz radio carrier.....	176
Figure 6.25. Constellation For 100 MS/s QPSK signal on OSSB linear 17.35 GHz radio carrier at 10 km fiber	177
Figure 6.26. Eye diagram For 100 MS/s QPSK signal I process on OSSB linear 17.35 GHz radio carrier at 10 km fiber, $m = 0.1$	177
Figure 6.27. Eye diagram for H5 Hartley MZM upconverter with 100 MB/s BPSK modulation, $L = 60$ km.....	179
Figure 6.28. PN correlation function from BPSK data on H5 Hartley MZM harmonic upconverter.	180
Figure 6.29. Compressed input constellation.....	181

Figure 6.30. Recovered QPSK constellation From 5th order harmonic upconverter at data rate 5 MS/s, $m = 0.1$, $\lambda_0 = 1550$ nm, $D \sim 16.5$ ps/(nm•km)	182
Figure 6.31. Eye diagram from recovered QPSK constellation from zero length fiber 5th order harmonic upconverter at data rate 5 MS/s.....	183
Figure 6.32. Correlation function for recovered data from QPSK phase compressed signal in Figure 6.29.	183
Figure 6.33. Constellation for QPSK phase compressed signal at 50 MS/s, $f = 17.35$ GHz, $L = 60$ Km.....	184
Figure 6.34. Eye diagram for I process for QPSK phase compressed signal at 50 MS/s, $f = 17.35$ GHz, $L = 60$ Km.	185
Figure 6.35. Correlation function for recovered data from p/4 50 MS/s OSSB QPSK phase compressed signal over 60 km of dispersive fiber $f = 17.35$ GHz.	185
Figure 6.36. Eye diagram for the Q process from a harmonically upconverted 5 MS/s QPSK signal on a zero length fiber, $f = 17.35$ GHz, radio channel path length 3 m.	186
Figure 6.37. Eye diagram for the Q process from a harmonically upconverted 5 MS/s QPSK signal on a 60 km dispersive fiber, $f = 17.35$ GHz radio channel path length 3 m.	187
Figure A.1. IRIS Transmitter	209
Figure A.2. IRIS Receiver	211

List Of Abbreviations

AM	Amplitude Modulation
BER	Bit Error Rate
BPSK	Biphase Shift keying
CATV	Cable Television
COSSB	Compatible Optical Single Sideband
CSSB	Compatible Single Sideband
CW	Continuous Wave
dB	Decibel
DC	Direct Current
DSB	Double Sideband
E-Field	Electric Field
EDFA	Erbium Doped Fiber Amplifier
EHF	Extra High Frequency
EO	Electro-Optic
FET	Field Effect Transistor
FFP	Fiber Fabry-Perot Device
FM	Frequency Modulation
FTTH	Fiber to the home
GB	Giga-Byte
GHz	Giga-Hertz

HFC	Hybrid Fiber Coax
IM	Intensity Modulation
IMDD	Intensity Modulation Direct Detection
ISI	Inter-Symbol Interference
kHz	Kilo-Hertz
km	Kilometer
LHP	Lower Half Plane
LMCS	Local Multipoint Communication System
ln	Natural Log
LO	Local Oscillator
LSSB	Lower Single Sideband
MB	Mega-Byte
MCS	Multipoint Communication System
MHz	Mega-Hertz
μm	micro-Meter
MP	Minimum Phase
MPC	Minimum Phase Compensation
MZ	Mach-Zehnder
MZM	Mach-Zehnder Modulator
nm	nano-meter
ns	nano-second
OE	Opto-Electronic
ORF	Optical/Radio Frequency

OSSB	Optical Single Sideband
PCS	Personal Communication Service
PN	Pseudo-Noise
PRBS	Pseudo-Random Binary Sequence
QAM	Quadrature Amplitude Modulation
QPSK	Quadrature Phase Shift Keying
RF	Radio Frequency
RHP	Right Half Plane
SBS	Stimulated Brillouin Scattering
SHC	Self Homo-Dyne Compensation
SNR	Signal To Noise Ratio
SSB	Single Side Band
TDMP	Time Domain Minimum Phase
THz	Tera-Hertz
TRLabs	Telecommunications Research Laboratories
UHF	Ultra High Frequency
UHP	Upper Half Plane
US	United States
USSB	Upper Single Sideband

1. Introduction

Broadband telecommunication services, consisting of broadcast and interactive telecommunication services are invading the residential market. Residential Internet and interactive multimedia capability is becoming commonplace and this has placed bandwidth demands on the residential subscriber loop that will eventually require a complete replacement of existing subscriber loop infrastructure. Bandwidth capabilities that only a few years ago would have accommodated large businesses are now being planned for private residential connections. Simultaneously, tight government regulation on residential telecommunication services is relaxing, allowing new service providers to participate who are exploiting new technologies to assist them in the development of new markets. As barriers are broken with regard to bandwidth delivery capacity, a positive feedback phenomenon results in which the requirement for even larger bandwidths in the associated consumer end user equipment increases in-turn.

A number of subscriber access approaches are being developed to meet the demands of these new broadband telecommunication services to be offered for residential markets. These may be sectioned into four main groups, each of whom are planning infrastructure upgrades to capture their particular market. These are:

1. The large established telecommunication service provider (Telco) such as TELUS, SaskTel, BCTel, Bell etc. The access philosophy involves a gradual evolution to Fiber to the Home (FTTH) in which every subscriber accesses the network through a wideband fiber optic cable. This group appears to be the best prepared to deal with the infrastructure revolution with its established right-of-way, large reserves of development capital, and experience.

2. The CATV supplier, Shaw Cable for example, already established with broadband CATV distribution equipment but poorly outfitted to offer the total range of broadband services due to the absence of switching capability. However the cable companies are pressing on with current market offerings for wideband Internet, digital music and broadcast and pay-per-view.
3. Satellite suppliers such as ExpressView, who are also well established in broadcast services and others such as Iridium, and Teledesic, who are in the process of building infrastructure for global bi-directional voice and Internet service. Additionally, large Telcos such as Bell Canada have recently aligned with the satellite service suppliers to add broadcast to its service offering.
4. Local Multipoint Communication Service (LMCS) providers who offer the same basic services but on a new infrastructure based on a wireless subscriber loop. The first Canadian licenses were awarded in 1996 to three service providers who claim that they will be on-line in the first quarter, 1999.

The large telecommunication service providers have adopted the philosophy that the best approach to the marketing of these new services is bundling, so that the consumer can choose from many services from the same provider. To support the large infrastructure required for this offering, it is also perceived by the Telcos that an evolution toward the infrastructure of fiber to the home (FTTH) is the most practical delivery vehicle for the residential interactive multimedia market. This is apparent in the fact that large FTTH based field trials are being conducted to characterize the market and recommend specific delivery technologies.

The existing CATV providers on the other hand are offering high speed Internet as part of a more gradual service ramp-up. This represents a different marketing strategy to the bundling approach in that the infrastructure upgrade is more gradual than a complete overhaul as outlined above. This is likely a function of the limited development resources of CATV providers to support the bundled service approach. It is apparent however, that this approach is acceptable to the consumer and many users are ordering Internet service from cable companies. Concurrently, to strengthen the traditional cable broadcast suite of services, cable companies are adding large blocks of additional content to their current offerings as well as digital music services and pay-per-view.

All of the above plus the fact that the evolution of the telecommunications industry will involve an inextricable linkage with the computer industry means that the telecommunication network and the subscriber loop technology will undergo major changes. On the subscriber loop side, the problems are somewhat alleviated in new neighborhoods where coax or fiber is standard prewiring practice by telecommunication service providers and cable companies. Established neighborhoods present a different problem however since upgrading the subscriber loop requires some level of inconvenience to the resident. This will create opportunities for new technologies that were beyond consideration only a few years ago.

The fourth entity in the service provider suite, wideband radio subscriber loop replacement or wireless access, is one such technology being proposed by communication system developers as a replacement for conventional cabled residential local loops.

1.1 Wireless Access

Interest in wireless access comes about as a result of the fact that recabling in older residential environments to accommodate broadband services is costly and it is unlikely that homeowners will allow excavation on their property when presented with the more convenient installation alternative that wireless offers.

Consequently there now are a number of companies in Canada and the US that are deploying wireless broadband delivery systems including:

WIC Connexus (Cellular Vision Canada Inc.) (C)
Maxlink Communications Inc.
RegionalVision Inc.
CellularVision Inc. (US)
Hewlett-Packard
Lucent Technologies

This wireless platform is additionally supported by government regulators who wish to see more variability and choice for consumers, not only for content, but also for service platform alternatives.

The above more or less summarizes the market profile in North America. The third world presents an entirely different deployment scenario. Due to the fact that throughout most of the third world, no telecommunications infrastructure exists, complete wireless solutions for toll and residential telephone as well as Internet and broadcast services may be the most economical solution. Thus wireless access is gaining credibility worldwide; not only for infrastructure upgrades in established communities but also as a first choice local loop alternative in new communities.

1.2 Radio Channel Impacts

For a broadband wireless delivery schemes to carry the required information, large frequency allocations have been granted. WIC Connexus in collaboration with CellularVision, the originator of the LMCS concept, has been licensed to provide residential television broadcast on a 29 GHz frequency allocation across Canada. Cellular Vision's original field trial in Brighton Beach, New York required 1 GHz of bandwidth to deliver 50 television channels using a wideband FM modulation scheme. Conversations between the author and WIC officials indicate that the technology being deployed in Canada is more bandwidth efficient but the bandwidth allocations are still on the order of 1 GHz. This size of allocation is

only available under current Canadian and US regulatory structures at frequencies in the range of 20 - 30 GHz.

The major impediments to successful transmission of radio signals are received power loss over propagation distance and distortion of the received signal due to multipath propagation[1]. Received power is generally characterized as an average quantity that follows a distance power law given by

$$P_r(d) = P_t - L(d) \quad (1-1)$$

where P_t and P_r are the transmitted and received power and L is a loss term in dB given by

$$L(d) = L(d_0, \lambda) + 10 \cdot n \cdot \log_{10} \left[\frac{d}{d_0} \right]. \quad (1-2)$$

$L(d_0, \lambda)$ is a loss term in dB at a reference distance from the transmitter as a function of both distance and radio carrier wavelength that incorporates the effect of wavelength antenna type and other factors. The factor n is a path loss exponent (2-6 typ.) that is dependent on the type of radio channel, for cluttered channels n may be as high as 6 and as low as 1 in open tunnels and hallways., The factor d is the separation between transmitter and receiver in suitable units. When the reference distance is small (< 500 m) $L(d_0, \lambda)$ is modeled as a free space loss characteristic and has a direct relationship with the carrier wavelength squared and so received power is expected to fall with increasing carrier frequency. As a result the carrier frequencies of interest in this document (20 - 30 GHz) would attenuate significantly (~ 30 dB) over those of, say, cellular frequencies (1 - 2 GHz). Consequently, for the system architectures proposed for LMCS service delivery, with cell radii on the order of 5 - 10 km, high power transmitters are required. Any architecture that inherently reduces the transmitter/receiver separation will mitigate the power roll-off characteristics and reduce power requirements at the transmitter.

The power equation in (1-1) gives the received power in an average sense but tells very little about the statistical power fluctuation that is inherent in complex time varying multipath channels. What is also required in this situation is the transient channel behavior that is available from a wideband probe of the channel[1]. In this type of test the channel is treated as a test device in a standard system identification effort[1]. A wideband Pseudo-Noise (PN) signal is injected into the channel at the carrier frequency of interest and the received signal is processed so as to recover the bandpass impulse response of the radio channel(see Appendix A, subsection A.1.3.2). A typical impulse response of a short residential radio channel at 18 GHz is plotted in Figure 1.1.

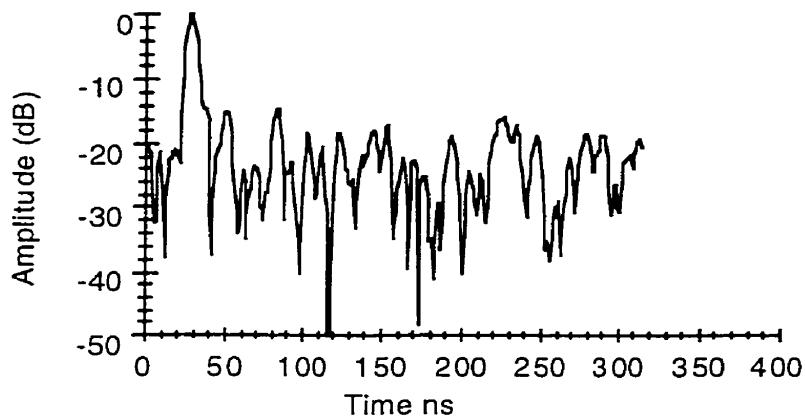


Figure 1.1. Typical impulse response of a short radio channel at 18 GHz

The ideal impulse response would be a solitary spike similar to that observed at approximately 30 ns with none of the other smaller spikes observed at 50 and 80 ns. The extra spikes represent reflections of the transmitted signal from objects in the propagation path of the radio signal and this causes the channel to become dispersive which in turn causes intersymbol interference in received digital data. The impulse response shown in Figure 1.1 is indicative of the radio channel proposed for the present application and it can be concluded that the channel impulse response will only become more dispersed with increasing complexity of the multipath channel and transmitter/receiver separation. This reinforces the argument for engineering close proximity of the transmitter and receiver.

1.3 The Premise: Radio on Fiber

It has been proposed that a step toward the solution to the subscriber loop upgrade problem for broadband services is replacement of the existing platform with broadband wireless access[2-7]. This mitigates the problems associated with right-of-way and hard-wired loop upgrade issues. It is further proposed that the radio subscriber loop platform be supported on a fiber distribution system similar to that proposed for the FTTH schemes outlined previously. This allows the signal to be transported over fiber to a point within close proximity (1-2 km) of the consumer thus reducing the overall length of the radio subscriber loop. This increases the chance that the propagation difficulties inherent to the LMCS range of frequencies can be addressed with directional antennas and other measures. Shorter distances will mean a greater chance of achieving line-of-sight propagation thus additionally reducing the requirement for large transmission towers. Not only are the effects of the propagation distance alleviated by this arrangement but the environmental factors such as rain attenuation, which is exacerbated by propagation distance, are also reduced[1]. The coverage areas are populated with a less noticeable distributed transmission infrastructure that is more cosmetically acceptable. This concept is illustrated in Figures 1.2 and 1.3. Figure 1.2 represents a conventional LMCS system similar to the original CellularVision proposal whereas Figure 1.3 represents a fiber distributed system.

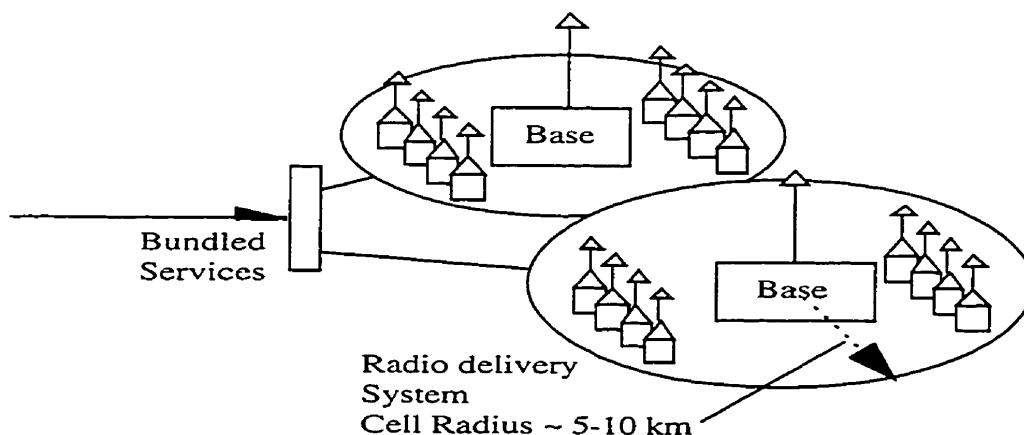


Figure 1.2. Conventional fixed cellular broadband delivery system

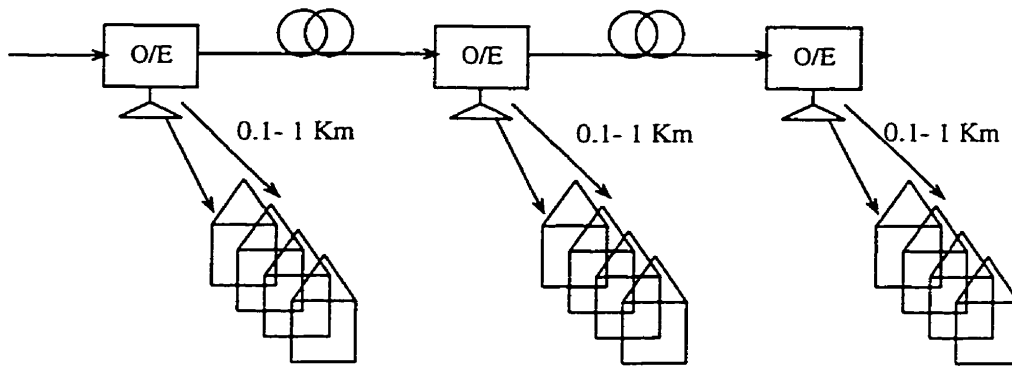


Figure 1.3. Distributed radio on fiber broadband delivery system

In Figure 1.3 the spacing of the Opto-Electronic interfaces devices (OE) is approximately 2-3 km whereas the maximum spacing of the base stations in Figure 1.2 may be as large as 20 km. The small spacing in the fiber deployed structure restricts the radio path to a maximum of 1-2 km. The advantage of the shorter link from a path loss perspective becomes clear when one calculates the path loss value at 10 km from equation (1-2) to be 50 dB higher than that at 1 km for a path loss exponent of $n = 5$ [1].

1.4 Subcarrier Optical Systems Background

Two fundamental modulation methods are applied in optical communication systems: baseband modulation (for broadband optical systems) in which the information signal is modulated onto the optical carrier directly and subcarrier modulation where the information signal is first modulated onto a electronic carrier signal which is then modulated onto the optical carrier. At the optical receiver, the subcarrier signal is demodulated and reverts back to a radio or electronic carrier signal. Subcarrier systems are generally multiplexed so that many subcarrier signals may be transported by the optical carrier. The classical example of this type of optical modulation is Cable Television (CATV) in which a large number of relatively narrowband subcarrier signals are transported over fiber[8]. This is done so that the signal format is compatible with regular television reception at the consumer premises.

The role of fiber technology in subcarrier systems has steadily expanded over the years. Fiber is used extensively as a distribution medium in Cable Television CATV[8] and is finding more use in Cellular Telephone, Personal Communication Services (PCS) and multipoint communication systems (MCS)[9,10]. New research is also focusing on the use of fiber devices and cable as functional components (i.e. modulators, frequency multipliers) in hybrid Optical/Radio Frequency (ORF) systems. It is clear that many advantages are attainable by incorporating fiber into radio systems that typically use cable or wave guide for transmission. Fiber is much lighter and easier to install. It has electromagnetic immunity along with large bandwidth capability and fiber will likely be deployed to meet the demand of the all of the service providers identified in the introduction. This means that fiber will be available to the radio service providers as a trunking element. If a significant portion of the subscriber loop problem can be solved with radio, then a fiber distribution system will be the most sensible deployment tool.

1.4.1. Early Studies

Early studies of subcarrier optical systems for CATV transmission were conducted during the 70's[11]. These studies addressed the problems associated with second and third order distortion inherent in multiplexed systems that occupy octave bandwidths on the fiber. This represents a problem in CATV systems since the ideal is to have the link perform as a perfectly linear element that does not impose harmonic distortion on the subcarrier multiplexed signal.

While linearity is required in most cases, the non-linear characteristics of optical devices have been also been exploited to achieve frequency translation without the requirement for local oscillators and mixing operations. Daryoush[12] investigated indirect optical injection locking of X band FET oscillators by exploiting the nonlinear characteristics (and resulting harmonic generating potential) of the laser diode and FET amplifiers. Numerous advantages were noted in this study relating to the efficacy of fiber cable in military strategic applications due to its electromagnetic immunity, wide bandwidth and ease of

installation. The notable characteristics that were exploited in this study concerned the non-linearities in the laser diodes that were used to generate the optical signal. It was found that by operating the laser diode in a non-linear region sinusoidal signals could be upconverted to higher frequencies through the optical link by simply isolating harmonics of the injected subcarrier signal at the optical link output. This topic will be addressed later.

Researchers then began to investigate the general applicability of optical devices in radio communications systems. In linear systems the nonidealities of the laser diode were detrimental to system performance. In other systems the non-ideal effects in the form of nonlinearities could be exploited to produce high frequency components via harmonic generation that would serve the purpose of eliminating the need for separate RF oscillators while providing modulation capability[13].

1.4.2. Systems Research

More central to the objectives in this study is the state of optical subcarrier system research. Many devices and configurations allow the conversion from RF to optical and vice versa. The pressing issues involve reducing the component count and price of the Optical/Radio system while dealing with the added fiber specific degradations to service such as chromatic dispersion and limited dynamic range.

In this thesis only intensity modulated-direct detection (IMDD) optical links are investigated[8]. This involves modulation of the amplitude of the optical carrier in manner that allows the signal to be recovered through square-law detection at the optical receiver. Two basic methods are examined for modulating the information signal onto the optical carrier. These are direct modulation and external modulation. Square law detection through a photo-diode is assumed in all cases.

In direct modulation systems, the optical signal source is modulated with the electronic signal[8], usually via the bias line on a laser diode as shown in Figure

1.4 . The term 'intensity' modulation , rather than 'amplitude' is used due to the fact that the laser output power is modulated with input current.

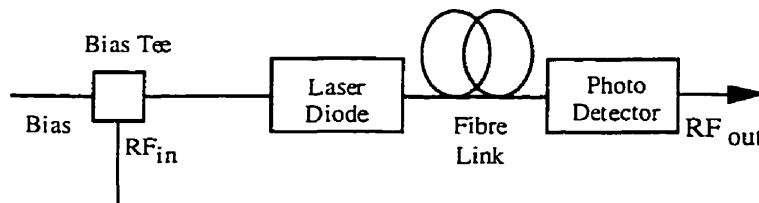


Figure 1.4. Direct modulation optical link

Direct modulation links are used for the transmission of baseband or lowpass signals as well as for radio carrier bandpass signals. Intensity modulation generally relies on a certain amount of linearity in the relationship between the optical output power and the driving signal current or voltage in the optical modulating device. This ensures that the information signal is detectable after the subcarrier signal is extracted from the fiber and converted back to a radio signal. In subcarrier applications, this type of link is most often used for CATV and Cellular Telephone applications where the optical information signal bandwidth is relatively narrow and unwanted residual FM modulation from the laser (referred to as laser 'chirp') is manageable. These systems usually involve extensive signal multiplexing and as such have complicated design procedures to deal with dynamic range issues such as laser clipping[8].

A study by Shibutani et al[14] investigated the use of direct modulation optical feeders to improve the operation of microcellular base stations. This scheme involved the linking of a central base station via fiber link with a "micro base station" which was fundamentally an antenna port that allowed inclusion of a small group of remote users on the base station. Advantages listed in the study were, among others, low cost and the ability of centralizing base station function over large areas. Several variations on this theme were reported in [9]. Most of the studies focused on cellular systems that linked mini base stations with larger central base stations and proposed direct subcarrier modulation.

External modulation refers to the case where the modulation is applied through a device external to the optical source as shown in Figure 1.5.

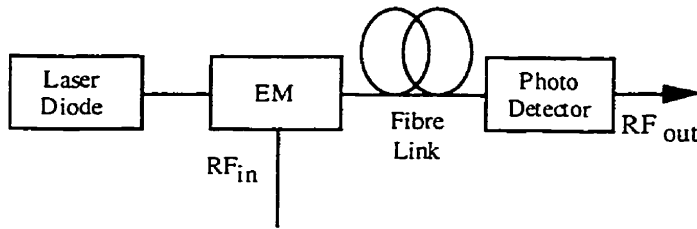


Figure 1.5. Externally modulated optical/RF link

The information signal may once again be baseband or subcarrier. The external amplitude modulator is usually a Mach Zehnder Modulator (MZM) [8]. The MZM, which will be discussed in detail, is used in subcarrier multiplexed and broadband applications due to the fact that more control of the modulating device behavior (e.g. chirp) is afforded.

A study by Ogawa[15] demonstrated an ORF link that used both direct subcarrier and external modulation to transmit a 70 MHz carrier with a 6 MHz bandwidth QPSK signal and a 25 GHz carrier FM signal (frequency deviation and information bandwidth were not specified) on the same fiber. The QPSK signal was directly modulated onto the fiber via a laser diode which also supplied optical power for a Mach-Zehnder Modulator. The 25 GHz FM signal was externally modulated onto the composite signal from the laser diode through the MZM. The 6 MHz QPSK signal BER deviated from theory by 3 to 4 dB which Ogawa claimed was at least equal in performance to that of coax cable. The FM signal maintained an SNR of 55 to 60 dB over an FM modulation index of 0.2 to 0.8. Both modulation types were constant envelope and as such resistant to nonlinear distortion in the optical link.

The highly nonlinear characteristic and high bandwidth capability of the Mach-Zehnder modulator along with the inherent square law behavior of optical detection of light have been exploited to produce harmonically upconverted subcarrier signals thus eliminating the need for RF upconversion at the detector

output [3-6,13,16]. O'Reilly[13] proposed a complete optical forward and reverse link for The R2005 Microwave Optical Duplex Antenna Link (MODAL) project. It was shown that by correctly biasing the MZM, suppression of the optical carrier was possible allowing a simple and efficient form of frequency multiplexing. O'Reilly later verified by experiment [16] that optical generation of narrow linewidth electric signals at EHF (30 -300 GHz) frequencies was possible.

Wake [7] and others investigated the laser diode operating in non-linear mode to produce harmonics of an FM signal that would produce a 40 GHz subcarrier signal at the optical link output. The laser diode was driven at a high modulation index with an FM modulated carrier at 4 GHz. Through the combination of laser diode non-linearity, fiber dispersion and photodiode square law behavior, a 40 GHz FM carrier was produced at the optical link output.

In another study involving the author, the non-linear characteristic of the detector was exploited to allow upconversion of the radio signal during the direct detection process [17]. This allowed a lower frequency subcarrier to be transmitted on the fiber reducing bandwidth requirements of the optical modulator. A local oscillator signal was added to the bias line to the detector (which was biased in a non-linear region of the responsivity curve) which produced a mixing effect between the optical subcarrier signal and the applied LO signal. The resulting output was an upconverted radio signal.

In more recent studies [18,19] cascaded structures of direct and external or external/external optical modulators have been implemented to deal with fiber non-linearity such as Stimulated Brillouin Scattering (SBS), Harmonic Suppression in the detector output [20] and, as will be shown, Optical Single Sideband.

While the previous research has contributed to the development of Optical/Radio transmission schemes, much investigation is still required. Some of the most pressing topics are:

1. Effective deployment of radio on fiber links at frequencies that allow broadband service delivery.
2. Mitigation of chromatic dispersion distortion for optical subcarrier modulation.
3. Use of optical modulator non-linearities to achieve harmonic upconversion on optical/radio hybrid systems.
4. Radio modulation schemes that coexist with the technical issues in the previous points.

1.4.4. The Basic Optical Link

The most effective approach regarding the first point is to deploy fiber links that deliver the subcarrier signal at the operating frequency of the final radio link. This ensures that no additional radio frequency translation circuitry, consisting of a local oscillator source and mixer, is required after the detector. In short, once the radio signal is emitted from the detector it should be suitable for radio transmission to the destination. This method has an immediate two-fold advantage in that it is simpler and whatever complexity is involved in the design may be concentrated at some central location.

1.4.5. Chromatic Dispersion

The transfer function requirements for distortionless transmission of a signal through any two-port device are twofold. Firstly, a flat envelope or amplitude response over the input signal bandwidth is required so that the signal doesn't incur any amplitude distortion. Secondly, a flat group delay or linear phase response is required so that the signal incurs only pure delay through the network. As will be shown in Chapter 2 and Appendix B, chromatic dispersion on fiber is accurately modeled as a linear group delay which causes variation in propagation velocity of the upper and lower sidebands of the frequency domain

optical signal thus violating the phase requirement above. In the case of subcarrier signals where the signal that is modulated onto the fiber is narrowband in nature this variation in velocity between the signal sidebands causes fiber length dependent destructive interference of the detected radio signal at the fiber link output. This behavior is governed by a squared sinusoidal power fluctuation according to

$$W(l) \propto \cos^2\left(\frac{\pi L \lambda_0^2 D f_c^2}{c}\right) \quad (1-3)$$

where D is the dispersion parameter in ps/(nm•km), λ_0 is the optical wavelength, f_c is the subcarrier frequency, L is the fiber length in km and c is the speed of light in a vacuum. This effect will be discussed in detail in the following chapters however the effect is depicted graphically in Figure 1.7, which shows the detected power versus fiber length for an 18 GHz subcarrier on a 1550 nm wavelength optical carrier through fiber with standard dispersion properties ($D = 18$ ps/(nm•km))[21].

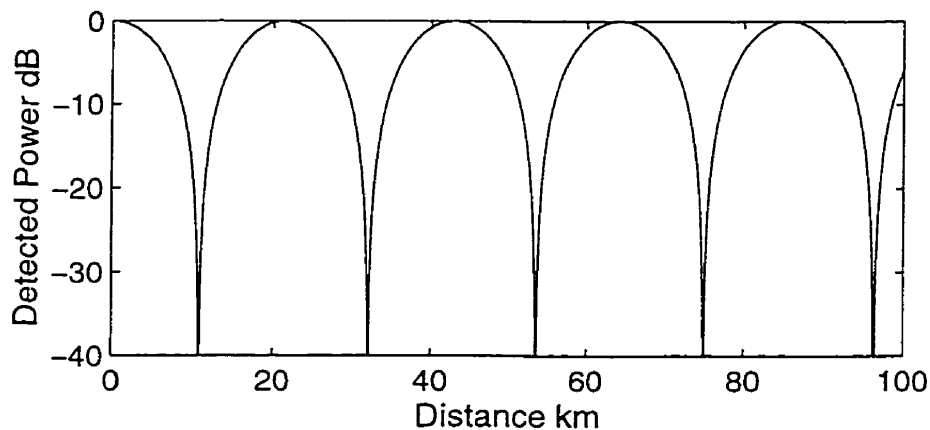


Figure 1.6. Detected power as a function of fiber length for $f = 18$ GHz, $\lambda_0 = 1550$ nm, $D = 18$ ps/(nm•km).

At approximately 11 km (and at multiples of approx. 22 km) the detected signal disappears, which would be unacceptable in a RF delivery system. Directly related to this is the (single sided) frequency response of the dispersive fiber link

where the frequency is varied rather than the fiber length as shown in Figure 1.7. [22-24]

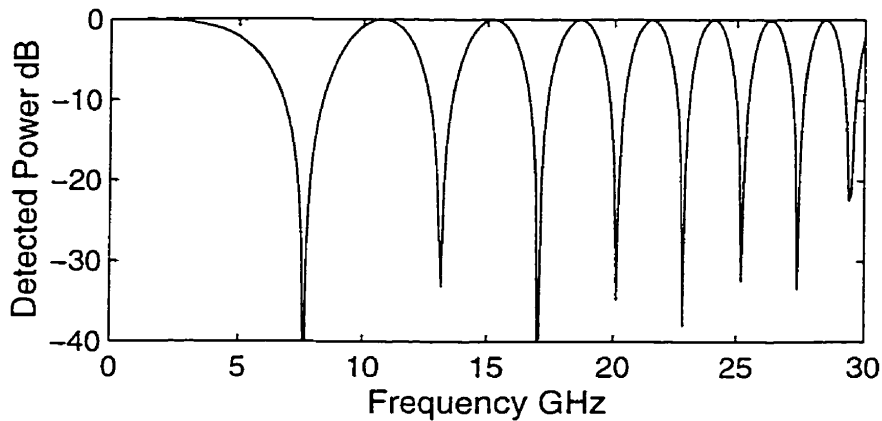


Figure 1.7. Detected power as a function of subcarrier frequency for fiber length - 60 km., $\lambda_0 = 1550$ nm, $D = 18$ ps/(nm•km).

Again there are undesirable nulls in the detected power. An obvious solution to this problem would be to set the optical wavelength to 1310 nm where the dispersion is at a minimum[8]. This however precludes the use of present day optical Erbium doped fiber amplifiers (EDFA) which operate in the 1550 nm region of the optical spectrum. Optical amplifiers would be required on fiber links exceeding a length of approximately 50 km to compensate for fiber loss. This topic will be addressed later in this thesis.

Suggestions for dealing with the power nulls due to dispersion have been to alter the fiber length so as to move the received signal away from the null point [25], and Single sideband (SSB) transmission by various means [18,19,26-28]. The latter seems to be the most practical method from a system standpoint for a number of reasons some of which are:

1. It is possible to completely mitigate the power cancellation effect of chromatic dispersion as will be shown.

2. Numerous optical modulator structures have been developed for the purpose.
3. Some structures work for baseband and subcarrier single sideband which promotes a common device for all applications.

The question that remains is how to best implement the OSSB structure. The bulk of suggestions to date focus specifically on producing single sideband structures for optical subcarrier processes[29-33]. This is useful but discards the question of potential improvement for optical baseband modulation as defined in section 1.4. The author proposes a method for generating OSSB signals, adapted from compatible single sideband structures developed in the late 50s and early 60's[34-36] that allows a variety of structures to be developed, is effective on baseband as well as subcarrier systems *and* may also be carried out with currently available optical modulators.

1.5 Research Objectives and Scope

The objective and scope of this study is the development of theory and methods for transporting radio signals on fiber. The focus will be on chromatic dispersion mitigations using OSSB, harmonic frequency translation over the optical link and associated subcarrier modulation methods. This study will include theoretical development, simulation and experimentation that will address the modulation method generally and then extend the practical aspects of the study to radio and subcarrier processes with experiments intended to prove concept only. Higher level system based studies such as signal multiplexing, simulations and experiments focusing on Bit Error Rate (BER) behavior, and systems deployment are not addressed.

1.6 Thesis Structure

The thesis will consist of 5 primary components covered in Chapters (2-6).

1.6.1. Chapter 2. Optical Single Sideband Modulation

Chapter 2 starts with mathematical preliminaries and the development of a modulation scheme for producing single sideband modulation on optical fiber. This phase will be treated generally and will include a review of theory for bandpass systems and complex envelope representation, and analytic functions. The theory will then be adapted for optical systems. The development will then address the particular characteristics of time domain minimum phase SSB systems that are exploited to enhance the received signal quality at the detector. To verify the theory, a few variations of modulator structures will be examined for their particular suitability. Three basic IMDD structures will be presented:

1. A laser intensity modulator in cascade with an external phase modulator.
2. A laser FM modulator in cascade with an external amplitude modulator.
3. An external amplitude modulator in cascade with an external phase modulator.

1.6.2. Chapter 3. Post Detection Equalization for Broadband Signals

This chapter will consist of a theoretical extension of the theory of Chapter 2 to show that improvements may be available for post-detection compensation using minimum phase (MP) properties of a received baseband optical signal that is badly distorted by chromatic dispersion. The method follows the assumption that if the time domain optical modulation signal with MP properties, (a term that will be described in detail later) and the spectral envelope of the signal is undistorted in shape, then the received signal, even after being badly distorted on the fiber will retain its MP properties. This being the case the phase of the optical signal may be recovered *after envelope detection* and the dispersion may be

compensated by filtering with an 'antidispersive filter' which reverses the effects of the dispersion induced quadratic phase distortion.

1.6.3. Chapter 4. Subcarrier Optical Single Sideband: Transmission Characteristics

Chapter 4 comprises a study of power transmission characteristics of unmodulated subcarriers on linear and harmonic optical links. This will consist of modification of the basic theory presented in Chapter 2 for linear and harmonic subcarrier modulation of optical signals. All of the modulator structures outlined in Chapter 2 will be re-addressed from the subcarrier modulation perspective. It will be shown that the modulation of OSSB waveforms with the associated signal conditioning is much easier for subcarrier systems than for baseband systems. Additionally it will be shown that different methods are required to build optical devices that are optimized for subcarrier operation as opposed to broadband operation. Finally a comprehensive mathematical tool is developed that simplifies the process of simulation of harmonic subcarrier systems.

1.6.4. Chapter 5. Transmission of Modulated Harmonically Upconverted OSSB Subcarriers

In this chapter, the focus is on transmission of modulated subcarriers over harmonic OSSB fiber links. Methods for predistorting subcarrier signals, to make them suitable for harmonic upconversion, are discussed, and it will be shown, in the case of phase modulated signals, that compression of the phase by a factor of n , where n is the desired frequency multiplier, prevents phase distortion of the subcarrier signal due to argument multiplication in the upconversion process. Additionally, an amplitude predistortion method is introduced that can be used in conjunction with the phase predistortion technique to allow harmonic upconversion of QAM type signals with improved distortion behavior on specific harmonic devices. Both methods are shown, by simulation example, to work on IMDD harmonic optical links.

1.6.5. Chapter 6. Proof-Of-Concept Experiments

This part will comprise a summary of the results of experiments that were conducted to prove the salient concepts outlined in Chapters 4 and 5. The fundamental similarity between the Mach-Zehnder Modulator configured as a Hartley single sideband modulator and the cascaded Mach-Zehnder amplitude/phase modulator will be confirmed. Included will be verification of the modulation theory developed in Chapter 5 for methods of signal predistortion that promote the use of phase and amplitude modulation on non-linear harmonic optical links.

1.6.6. Chapter 7. Conclusions

The outstanding issues will be addressed and recommendations for future work will be presented.

2. Optical Single Sideband Modulation

In this Chapter, the topic of optical SSB modulation is addressed. We start by reviewing the concepts of complex envelope representation of bandpass signals, single sideband modulation, and analytic functions. The theory of minimum phase signals will then be developed to show how an SSB signal may be made suitable for envelope detection. As a tutorial example, the theory will then be applied to the particular case of IMDD optical modulation over dispersive fiber using a sinusoidal information signal. The method will be shown in simulation to mitigate the effects of fiber dispersion for baseband optical signals. Once the theory is established, modifications and simplifications are developed for three primary optical modulator configurations. Simulations will then be conducted to verify the theory and observe the behavior of the particular modulator structure on dispersive fiber links.

2.1 Introduction

Amplitude modulation of a carrier with a real information signal results in a spectral symmetry around the carrier that renders either the upper or lower sideband redundant in terms of its absolute necessity for accurate demodulation [37]. This is due to the fact that the spectrum of a real signal has conjugate (or Hermitian) symmetry which causes the real part to be even over the origin and the imaginary part of the spectrum to be odd. These even and odd symmetry conditions apply also to the envelope and phase of the spectrum respectively. Either side of the spectrum may be discarded and the complete spectrum may always be reconstructed from either sideband. The obvious benefit from a system perspective is that the spectral occupancy of a single sideband signal is reduced by a factor of 2 from that of a double sideband signal.

The earliest implementation of SSB modulation was in radio broadcast systems as a mitigation for co-channel and adjacent channel interference [38,39]. While

SSB offered an advantage for spectral bandwidth reduction, a problem remained in that SSB was incompatible with AM detection type receivers. In order for the information to be extracted from an SSB waveform, either large carrier power was required for the case of envelope detection or coherent demodulation was necessary. The range of application of SSB was advanced by Voelker, Kahn and others with the development of SSB modulation with compatibility with AM systems[34-36]. This modulation scheme is referred to as Compatible Single Sideband (CSSB) and will be examined in detail.

Single sideband in optical systems (Optical SSB or OSSB) was first examined by Izutsu [40] as a means of simultaneously frequency translating a tonal component modulated onto an optical carrier to some other frequency offset and achieving efficient single sideband modulation in the process. Variations of the Izutsu structure were recorded by Smith et al [26] and Olshansky[29]. Other methods based on mode coupling[30,31], re-entrant traveling wave structures[32] and waveguides[33] have also been documented. While the Olshansky and Izutsu structure were aimed primarily at optical multiplexing tasks, Smith et al focused on the application of SSB to the problem of fiber chromatic dispersion on subcarrier signals. Shortly after the release of the Smith paper[26], Conradi, the author and others [18] disclosed an AM compatible cascaded hybrid optical SSB structure that was suitable for baseband as well as subcarrier optical processes and that allowed similar baseband postdetection dispersion compensation that had been observed for optically filtered OSSB systems[41]. Variations of the Conradi disclosure, referred to as Compatible Optical Single Sideband (COSSB), are covered in this study.

2.2. Theory

2.2.1. Complex Envelope Representation of Bandpass Signals

In this study, the complex envelope representation of narrowband bandpass signals will be used extensively[42]. The term narrowband is used to indicate

that the bandwidth of the optical signal is much smaller than the carrier frequency. This is easy to imagine when it is considered that the 'carrier frequency' of a bandpass optical signal in the 1550 nm range is approximately 200 THz. The term narrowband has further special implications when fiber dispersion is considered and this matter will be dealt with in later chapters. To review this concept we start by defining a real valued signal $s_b(t)$ with frequency content concentrated in a narrow range around a carrier frequency f_c , as shown in Figure 2.1.



Figure 2.1. Narrowband bandpass signal

To develop a model for this signal we first construct a signal that contains only the positive frequencies of $s_b(t)$ given by

$$A(f) = 2u(f)S_b(f) \quad (2-1)$$

where $S_b(f)$ is the Fourier transform of $s_b(t)$ and $u(f)$ is the frequency domain unit step function. The time domain expression for (2-1) is given by

$$a(t) = \frac{1}{\sqrt{2\pi}} \int_{-\infty}^{\infty} A(f)e^{j2\pi ft} df = \frac{2}{\sqrt{2\pi}} \int_{-\infty}^{\infty} S_b(f) \cdot u(f)e^{j2\pi ft} df. \quad (2-2)$$

Since multiplication in the frequency domain involves convolution in the time domain,

$$a(t) = F^{-1}[2u(f)] * F^{-1}[S_b(f)] \quad (2-3)$$

where F^{-1} denotes the inverse Fourier transform.

Noting that $s_b(t) = F^{-1}[S_b(f)]$ and

$$F^{-1}[2u(f)] = \delta(t) + \frac{j}{\pi t}, \quad (2-4)$$

$a(t)$ may be expressed as

$$a(t) = \frac{1}{\pi} s_b(t) * \left(\delta(t) + \frac{j}{\pi t} \right) = s_b(t) + \frac{j}{\pi} \int_{-\infty}^{\infty} \frac{s_b(\tau)}{t-\tau} d\tau. \quad (2-5)$$

The integral on the right side of (2-5) defined as

$$\hat{s}_b(t) = \frac{1}{\pi} \int_{-\infty}^{\infty} \frac{s_b(\tau)}{t-\tau} d\tau, \quad (2-6)$$

is called the Hilbert Transform of the signal $s_b(t)$ and the function $a(t)$ is called the *analytic signal* or *pre-envelope* associated with the real signal $s_b(t)$.

The signal $\hat{s}_b(t)$ may be represented as the response of the filter with impulse response:

$$h(t) = \frac{1}{\pi t}, \quad -\infty < t < \infty \quad (2-7)$$

to the input $s_b(t)$. This filter is called a Hilbert transformer and its frequency response is given by

$$H(f) = -j \operatorname{sgn}(f). \quad (2-8)$$

It is clear that the magnitude of $H(f)$ is unity with a $-\frac{\pi}{2}$ phase shift of all frequencies in the input signal.

The analytic signal acquired above is still bandpass in nature and a lowpass equivalent of $a(t)$ may be acquired by frequency translation of $A(f)$ given by

$$A_1(f) = A(f + f_c). \quad (2-9)$$

In the time domain this amounts to multiplication of $a(t)$ with a complex sinusoid as in:

$$a_1(t) = a(t) \exp(-j2\pi f_c t). \quad (2-10)$$

Conversely,

$$s_b(t) + j\hat{s}_b(t) = a_1(t) \exp(j2\pi f_c t). \quad (2-11)$$

The lowpass equivalent signal $a_1(t)$ (also called the complex envelope) is generally complex valued with real and imaginary parts expressed as

$$a_1(t) = x(t) + jy(t). \quad (2-12)$$

It can be shown that the following relations hold for $s_b(t)$ and $\hat{s}_b(t)$:

$$\begin{aligned} s_b(t) &= x(t) \cos(2\pi f_c t) - y(t) \sin(2\pi f_c t) \\ \hat{s}_b(t) &= x(t) \sin(2\pi f_c t) + y(t) \cos(2\pi f_c t), \end{aligned} \quad (2-13)$$

The first part of (2-12) is the desired form of the representation of bandpass signal and $x(t)$ and $y(t)$ are called the quadrature components of the bandpass signal $s_b(t)$. The quadrature modulator is shown in Figure 2.2.

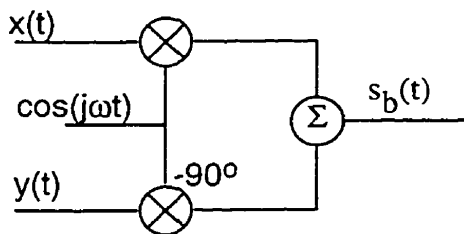


Figure 2.2. Quadrature modulator.

The signal $s_b(t)$ may also be extracted from the analytic signal

$$\begin{aligned} s_b(t) &= \Re\{[x(t) + jy(t)] \exp(j2\pi f_c t)\} \\ &= \Re\{[a_1(t)] \exp(j2\pi f_c t)\} \end{aligned} \quad (2-14)$$

where \Re denotes the real part. A final representation of $s_b(t)$ is given by expressing $a_1(t)$ in polar notation as

$$a_1(t) = m(t) \exp[j\phi(t)] \quad (2-15)$$

where $m(t)$ is the envelope of $s_b(t)$ given by

$$m(t) = \sqrt{x^2(t) + y^2(t)} \quad (2-16)$$

and

$$\phi(t) = \tan^{-1} \left[\frac{y(t)}{x(t)} \right]. \quad (2-17)$$

Thus

$$\begin{aligned} s_b(t) &= \Re\{a_1(t) \exp(j2\pi f_c t)\} \\ &= \Re\{m(t) \exp[j(2\pi f_c t + \phi(t))]\} \\ &= m(t) \cos[2\pi f_c t + \phi(t)]. \end{aligned} \quad (2-18)$$

The Fourier Transform of $s_b(t)$ may be given by

$$\begin{aligned} S_b(f) &= \int_{-\infty}^{\infty} \Re[a_1(t) \exp(j2\pi f_c t)] \exp(-j2\pi ft) dt \\ &= \frac{1}{2} \int_{-\infty}^{\infty} [a_1(t) \exp(j2\pi f_c t) + a_1^*(t) \exp(-j2\pi f_c t)] \exp(j2\pi ft) dt \quad (2-19) \\ &= \frac{1}{2} [A_1(f - f_c) + A_1^*(-f - f_c)], \end{aligned}$$

which shows the relationship between the spectrum of the bandpass signal $s_b(t)$ and its complex envelope $a_i(t)$. It can also be shown that for narrowband systems the energy in the bandpass signal may be acquired from the lowpass equivalent signal as in

$$\xi = \int_{-\infty}^{\infty} s_b^2(t) dt = \frac{1}{2} \int_{-\infty}^{\infty} |a_i(t)|^2 dt. \quad (2-20)$$

The principles applied to bandpass signals above may be extended to bandpass systems such as linear filters. This allows the acquisition of equivalent lowpass or complex envelope representations of linear systems. Defining the real impulse response of a bandpass system as $h(t)$ it can be shown that

$$\begin{aligned} h(t) &= h_i(t) \exp(j2\pi f_c t) + h_i^*(t) \exp(-j2\pi f_c t) \\ &= 2\Re[h_i(t) \exp(j2\pi f_c t)] \end{aligned} \quad (2-21)$$

where $h_i(t)$ is the complex envelope of the bandpass system. Additionally,

$$H(f) = H_i(f - f_c) + H_i^*(-f - f_c). \quad (2-22)$$

We can now show that the output of a bandpass system in response to a bandpass input may be acquired from the complex envelopes of the bandpass system and bandpass input. Consider a bandpass system $h(t)$ with bandpass input $s_b(t)$. The output of the system is given by

$$r(t) = \int_{-\infty}^{\infty} s_b(\tau) h(t - \tau) dt. \quad (2-23)$$

In the frequency domain

$$\begin{aligned} R(f) &= S_b(f) H(f) \\ &= \frac{1}{2} [A_i(f - f_c) + A_i^*(-f - f_c)] \cdot [H_i(f - f_c) + H_i^*(-f - f_c)] \end{aligned} \quad (2-24)$$

When $s_b(t)$ and $h(t)$ are narrowband, the terms $A_i(f - f_c)$ and $H_i(f - f_c)$ are zero valued for $f < 0$ so that the terms $[A_i(f - f_c) \cdot H_i^*(-f - f_c)]$ and $[A_i^*(-f - f_c) \cdot H_i(f - f_c)]$ vanish. Thus (2-24) simplifies to

$$\begin{aligned} R(f) &= \frac{1}{2} [A_i(f - f_c) \cdot H_i(f - f_c)] + [A_i^*(-f - f_c) \cdot H_i^*(-f - f_c)] \\ &= \frac{1}{2} [R_i(f - f_c) + R_i^*(-f - f_c)] \end{aligned} \quad (2-25)$$

Which implies that $r(t)$ the bandpass output may be given by

$$r(t) = \Re[r_i(t) \exp(j2\pi f_c t)]. \quad (2-26)$$

This relationship allows us to ignore the frequency translation aspect of bandpass systems and to treat the bandpass signal and its interactions with bandpass systems directly through the complex envelope. Thus the complex envelope is used throughout this document unless it is specifically stated otherwise. It is assumed throughout that the real bandpass signal may be acquired by taking the real part of the associated analytic bandpass signal.

2.2.2. Single Sideband Modulation

A single sideband signal is a bandpass signal with either the upper or lower half of its spectrum removed[43]. For example an upper single sideband USSB signal has a zero valued spectrum for $|f| < f_c$, and an LSSB signal has a zero valued spectrum for $|f| > f_c$. An SSB signal may be acquired by using the complex envelope given by

$$g(t) = s(t) \pm j\hat{s}(t) \quad (2-27)$$

where $s(t)$ is a real baseband information signal and $\hat{s}(t)$ is its Hilbert transform. In this case we briefly note that the analytic properties of the pairing of a real signal with its Hilbert Transform are being exploited to achieve single sideband

modulation on a bandpass signal. This subject will be addressed in more detail later. The real bandpass signal associated with (2-27) is given by

$$\begin{aligned} s_b(t) &= \Re[g(t) \exp(j2\pi f_c t)] \\ &= s(t) \cos(2\pi f_c t) - \hat{s}(t) \sin(2\pi f_c t), \end{aligned} \quad (2-28)$$

and will be USSB or LSSB depending on the sign of (2-27). The quadrature SSB modulator is shown in Figure 2.3.

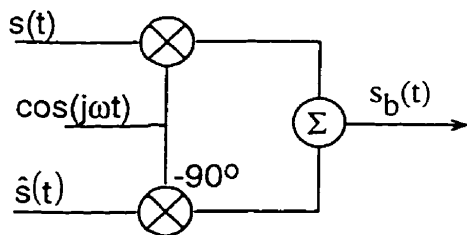


Figure 2.3. Quadrature SSB modulator.

The structure in Figure 2.2 is also called a Hartley modulator[37]. Thus the quadrature components of the bandpass SSB signal are the information signal and its Hilbert Transform. Considering that $g(t)$ contains only the positive or negative frequencies of $s(t)$ depending on the sign of (2-27), the single sided nature of $s_b(t)$ can be proven using (2-19):

$$\begin{aligned} S_b(f) &= \frac{1}{2} [A_1(f - f_c) + A_1^*(-f - f_c)] \\ &= \frac{1}{2} [G(f - f_c) + G^*(-f - f_c)]. \end{aligned} \quad (2-29)$$

Idealized bandpass spectra for (2-28) are shown in Figure 2.4.

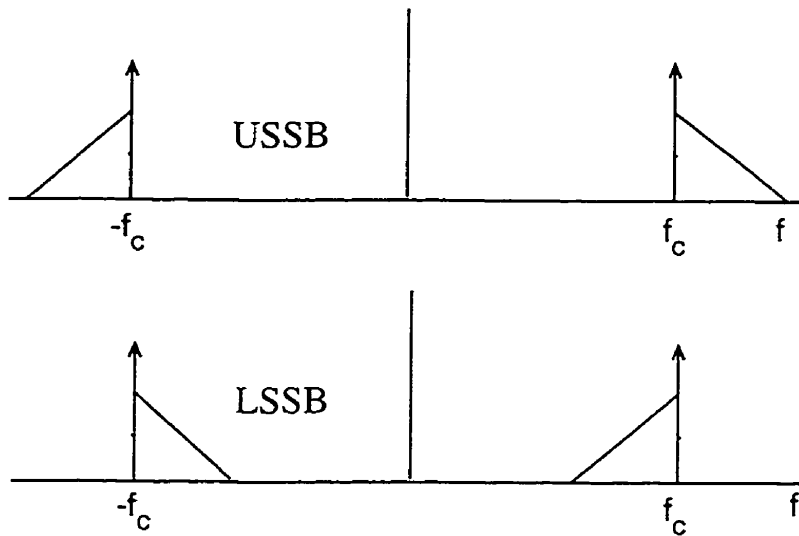


Figure 2.4. USSB and LSSB bandpass spectra.

Thus, it is shown that a bandpass signal will be SSB if the complex envelope of the signal is composed of Hilbert Transform pairs.

The information in the SSB signal is recovered through coherent product detection of the bandpass SSB signal as shown in Figure 2.5.

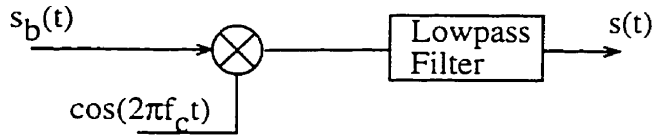


Figure 2.5. Coherent detector.

In Figure 2.5, $s_b(t)$ is mixed with the coherent local oscillator $\cos(2\pi f_c t)$ to produce the signal

$$\begin{aligned}
 s_{bm}(t) &= \cos(2\pi f_c t) [s(t) \cos(2\pi f_c t) - \hat{s}(t) \sin(2\pi f_c t)] \\
 &= \frac{s(t)}{2} [1 + \cos(4\pi f_c t)] + \frac{\hat{s}(t)}{2} \cos(4\pi f_c t)
 \end{aligned} \tag{2-30}$$

The double carrier frequency terms are filtered out leaving the baseband information signal, $s(t)/2$.

2.2.3. Analytic Signals

The signal $a(t)$ is called analytic because it satisfies the Cauchy Riemann conditions for analyticity [44]. If we consider the function $a(z)$, 'z' defining the complex z plane, which is single valued in the region \mathbf{R} , then the derivative of $a(z)$ is given by

$$a'(z) = \lim_{\Delta z \rightarrow 0} \frac{a(z + \Delta z) - a(z)}{\Delta z} \quad (2-31)$$

provided the limit exists independently of the manner in which $\Delta z \rightarrow 0$. If $a'(z)$ exist at all points in the region \mathbf{R} then $a(z)$ or 'a' is analytic in \mathbf{R} . Further, a is said to be analytic at a point z_0 if there is a neighborhood $|z - z_0| < \delta$ for which a' exists.

Now we consider the function $w = a(z) = u(x, y) + jv(x, y)$, in which u and v are mappings between Cartesian coordinates and the 'z' plane. For w to be analytic in the region \mathbf{R} then u, v must satisfy the Cauchy Riemann equations given by

$$\frac{\partial u}{\partial x} = \frac{\partial v}{\partial y}, \quad \frac{\partial u}{\partial y} = -\frac{\partial v}{\partial x}. \quad (2-32)$$

Additionally if the partial derivatives in (2-32) are continuous in \mathbf{R} , then the Cauchy-Riemann equations are sufficient to establish analyticity. We can show this by stating that for $a(z)$ to be analytic the limit

$$\begin{aligned} \lim_{\Delta z \rightarrow 0} \frac{a(z + \Delta z) - a(z)}{\Delta z} &= a'(z) = \\ \lim_{\substack{\Delta x \rightarrow 0 \\ \Delta y \rightarrow 0}} \frac{\{u(x + \Delta x, y + \Delta y) + jv(x + \Delta x, y + \Delta y)\} - \{u(x, y) + jv(x, y)\}}{\Delta x + j\Delta y} & \quad (2-33) \end{aligned}$$

must exist independently of the manner that Δz approaches 0. Two possibilities are

$$\Delta y = 0, \Delta x \rightarrow 0,$$

for which

$$\lim_{\Delta x \rightarrow 0} \left\{ \frac{u(x + \Delta x, y) - u(x, y)}{\Delta x} + \frac{jv(x + \Delta x, y) - v(x, y)}{\Delta x} \right\} = \frac{\partial u}{\partial x} + j \frac{\partial v}{\partial x} \quad (2-34)$$

and

$$\Delta y \rightarrow 0, \Delta x = 0,$$

for which

$$\lim_{\Delta y \rightarrow 0} \left\{ \frac{u(x, y + \Delta y) - u(x, y)}{j\Delta y} + \frac{v(x + \Delta x, y) - v(x, y)}{\Delta y} \right\} = -j \frac{\partial u}{\partial y} + \frac{\partial v}{\partial y}. \quad (2-35)$$

For $a'(z)$ to exist, the limits in (2-34) and (2-35) must be equal which proves the Cauchy Riemann equations in (2-32). The above shows the necessary condition for analyticity. To find the relationship between the real and imaginary parts of the analytic function, now interpreted as an analytic time domain signal ($x = t$ and $y = 0$), we can redefine the analytic function as

$$a(z = t) = u(t) + jv(t) \quad (2-36)$$

This relation is developed using the Cauchy Second Integral Theorem [44-47]. If $a(z)$ is analytic inside and on a closed contour C and z_0 is a point inside C then

$$a(z_0) = \frac{1}{2\pi j} \int_C \frac{a(z)}{z - z_0} dz. \quad (2-37)$$

This follows from the initial result that the integral of $a(z)$ over a closed contour vanishes. To calculate $a(z_0)$ we build a function $\frac{a(z)}{z-z_0}$ such that, in the vicinity of $z = z_0$, the Laurent expansion gives

$$\frac{a(z)}{z-z_0} = \frac{a(z_0)}{z-z_0} + \dots \quad (2-38)$$

Higher order terms do not contribute to the integral and are left out. Only the residue at $a(z_0)$ is important. Thus the integral part of (2-37) for the case of C which is a small circle around z_0 ,

$$z - z_0 = r \exp(j\theta), \text{ and } dz = r \exp(j\theta) j d\theta, \quad (2-39)$$

becomes

$$\begin{aligned} \int_C \frac{a(z_0)}{r \exp(j\theta)} r \exp(j\theta) j d\theta + \dots &= j a(z_0) \int_0^{2\pi} d\theta \\ &= 2\pi j a(z_0) \\ \Rightarrow \frac{1}{2\pi j} \int_C \frac{a(z)}{z-z_0} dz &= a(z_0), \end{aligned} \quad (2-40)$$

which proves (2-37).

When we use the analytic signal definition in (2-36) on the t axis, we must keep the condition of a closed contour intact. To achieve this, we define $z = t + jt$ and define the contour as an infinite half circle with radius Q which lies on the real axis ' t ', as shown in Figure 2.6.

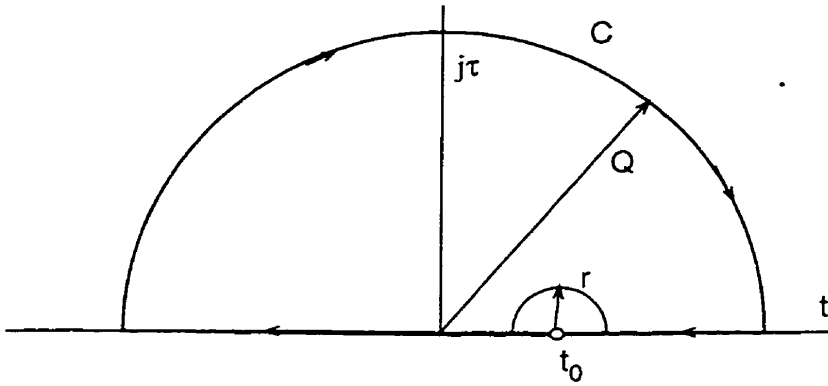


Figure 2.6. Complex z plane and infinite half circle 'Q'.

We need to acquire an analytic expression in t . To achieve this we first note that, since t_0 is excluded from the region enclosed by Q ,

$$\int_C \frac{a(z)}{z - t_0} dz = 0. \quad (2-41)$$

Next we estimate the contribution to the above result above from the different parts of the contour. The contribution from the small indentation at t_0 is $2\pi j$ times (one-half of the residue of the integrated at $t = t_0$) or $\pi j a(t_0)$. The contribution of the infinite circle Q is given by

$$\begin{aligned} \int_{C_1} \frac{a[Q \exp(j\theta)]}{Q \exp(j\theta) - t_0} j Q \exp(j\theta) d\theta &= a(\infty) j \int_{\pi}^0 d\theta \\ &= -j\pi a(\infty). \end{aligned} \quad (2-42)$$

Next the remainder of the contour on the t axis is evaluated as

$$\begin{aligned} \lim_{\substack{Q \rightarrow \infty \\ r \rightarrow 0}} \left[\int_{+\infty}^{t_0+r} \frac{a(x)}{t - t_0} (-dt) + \int_{t_0+r}^{-\infty} \frac{a(t)}{t - t_0} (-dt) \right] \\ = \int_{-\infty}^{\infty} \frac{a(t)}{t - t_0} dt. \end{aligned} \quad (2-43)$$

Finally combining the small indentation contribution with (2-42) and (2-43) and equating to (2-41) gives

$$\int_{-\infty}^{\infty} \frac{a(t)}{t-t_0} dt - j\pi a(\infty) + j\pi a(t_0) = 0, \quad (2-44)$$

and

$$a(t_0) = -\frac{1}{\pi j} \int_{-\infty}^{\infty} \frac{a(t)}{t-t_0} dt - j\pi a(\infty). \quad (2-45)$$

Note that the integration requires that $a(z)$ be analytic in the upper half plane. If $a(z)$ was analytic in the lower half plane then the contour would also be in the lower half plane. To capture the real and imaginary parts of $a(t)$ we assume that $a(\infty)$ is zero valued and note that

$$a(t) = -\frac{1}{\pi j} \int_{-\infty}^{\infty} \frac{a(\eta)}{\eta-t} d\eta = -\frac{1}{\pi j} \int_{-\infty}^{\infty} \frac{u(t) + jv(t)}{\eta-t} d\eta \quad (2-46)$$

which shows the relationship between the real and imaginary parts of the analytic signal as

$$\begin{aligned} \Re(a) = u(t) &= -\frac{1}{\pi} \int_{-\infty}^{\infty} \frac{v(t)}{\eta-t} d\eta \\ \Im(a) = v(t) &= \frac{1}{\pi} \int_{-\infty}^{\infty} \frac{u(t)}{\eta-t} d\eta. \end{aligned} \quad (2-47)$$

This shows generally that the analytic signal has real and imaginary parts that are related by the Hilbert Transform and thus has a single sided Fourier Transform. Note that we don't make a hard distinction between time and frequency as is commonly seen in communication theory textbooks. If a function or signal is analytic in one domain ('f' or 't') it is single sided in the transform domain due to symmetry properties in the Fourier Transform.

2.3. AM Compatibility

The optical links addressed in this study rely on square-law envelope detection for recovery of the signal at the optical receiver. The optical detector output current is directly proportional to the optical power or intensity. For direct detection systems the information is contained in the envelope of the bandpass carrier as in equation (2-18). There may be phase activity in the signal but this is discarded in the demodulation process. The envelope detection operator is given by

$$d(t) = |s_b(t)| \quad (2-48)$$

where it is more appropriate to express $s_b(t)$ as its analytic counterpart thus

$$\begin{aligned} d(t) &= |a(t)| = |a_i(t) \exp(j2\pi f_c t)| \\ &= |a_i(t) \exp(j2\pi f_c t)| \\ &= |x(t) + jy(t)| \\ &= \sqrt{x^2(t) + y^2(t)} \\ &= m(t). \end{aligned} \quad (2-49)$$

In the case of square law detection,

$$\begin{aligned} d(t) &= |x(t) + jy(t)|^2 \\ &= x^2(t) + y^2(t) \\ &= m^2(t). \end{aligned} \quad (2-50)$$

It can be stated that the envelope detector operates directly on the complex envelope of the analytic signal. Returning to the SSB complex envelope signal in (2-27) it is clear that envelope detection will not return the information signal $s(t)$ from the complex envelope. An approximation to the information signal may be recovered by envelope detection by adding a DC component [35].

Let

$$a(t) = c + s(t) + j\hat{s}(t). \quad (2-51)$$

The envelope of $a(t)$ is given by

$$|a| = \sqrt{c^2 + 2cs + s^2 + \hat{s}^2} \quad (2-52)$$

where 't' has been dropped.

Normalizing to 'c' we get

$$\frac{|a|}{c} = \sqrt{1 + \frac{2s}{c} + \frac{s^2}{c^2} + \frac{\hat{s}^2}{c^2}} \quad (2-53)$$

which for $c \gg s; \hat{s}$, approaches

$$\frac{|a|}{c} \approx 1 + \frac{s}{c}. \quad (2-54)$$

This type of approximation is problematic since the bulk of the signal power is contained in the carrier component and the signal to noise ratio (SNR) of the actual information is reduced. Additionally the remnant of the \hat{s} component is seen only as distortion. Fortunately, modifications may be made to overcome this difficulty.

2.4. Compatible Optical Single Sideband

So far we have shown that analytic signals are always composed of real and imaginary parts related by the Hilbert Transform and as such have the required complex envelope properties for SSB modulation. We have also shown that the analytic complex envelope signal attained by pairing a real information signal with its Hilbert transform is unsuitable for envelope detection. We now show

how a proper SSB complex envelope may be constructed so as to allow envelope detection without distortion. The fundamental problem may be characterized posing the question: How do we produce an SSB signal in which the envelope contains only the information part of the signal and the phase is used only to remove one of the sidebands of the signal? As regards the information we have little choice; the information part of the signal must be equal to or greater than zero. Thus $s(t) \geq 0$. If any part of the information signal is negative it will be distorted in envelope detection. Thus sufficient DC offset must be added to the information signal so as to cause it to always be positive. In this manner the signal may be recovered undistorted after envelope detection by removal of the DC artifact.

The phase function may be developed from the analytic signal definition[34-36]. It is stated without proof that the conditions for analyticity in the upper half plane (UHP) of Figure 2.6 are that there be no singularities in the UHP. Next we consider the logarithm (\ln) of the analytic signal. For the \ln of $a(t)$ to be analytic the same condition applies: no singularities in the UHP. Thus the signal $a(t)$ must not have zeros in the UHP because an UHP zero, upon taking the \ln becomes a singularity in the UHP. Being that the \ln is also analytic under this condition, the real and imaginary parts are given by

$$\ln[a(t)] = \ln[|a(t)|] + jH\{\ln[|a(t)|]\}. \quad (2-55)$$

Substituting the envelope of $a(t)$ with the positive information signal defined above, (2-55) becomes

$$\ln[a(t)] = \ln[s(t)] + jH_L[s(t)] \quad (2-56)$$

where $H_L(\cdot)$ denotes the Hilbert transform of the \ln . In this case the information signal must be greater than zero so as to prevent the formation of a singularity on the t axis by taking the \ln of $s(t)$. Taking the antilog of (2-56) gives

$$a(t) = s(t) \cdot \exp(jH_L[s(t)]) \quad (2-57)$$

which is also analytic. It is clear that the information signal is recoverable by envelope detection as in

$$\begin{aligned} s_r(t) &= |s(t) \exp\{jH_L[s(t)]\}| \\ &= |s(t)| \cdot |\exp\{jH_L[s(t)]\}| \\ &= s(t) \end{aligned} \quad (2-58)$$

Thus AM compatibility is achieved in theory. This type of signal is a time domain version of the 'minimum phase' signal studied in control theory[47] and digital signal processing[48]. Thus the practical implementation of this device is referred to as a minimum phase modulator. It is clear that there are practical difficulties in synthesizing this type of baseband signal. Firstly taking the \ln of the information signal is difficult, especially if the information signal has any appreciable bandwidth. Secondly, it is impossible to implement a perfect Hilbert Transformer for baseband analytic signals. This is due to the sharp transition at the frequency domain origin of the $-j\text{sgn}(f)$ operator. It will be shown, however, that for certain modulation instances (some of which are exactly the type commonly used in optical modulation) partial or vestigial sideband transmission is achievable without any log compression of the information signal simply by scaling the information signal and Hilbert Transform signal appropriately. These issues will be addressed in the following implementation example.

2.5. Implementation: The Ideal Minimum Phase Modulator

The first requirement in the composition of a signal that is suitable for our purposes is that the amplitude portion of the minimum phase signal must be positive. Defining a bipolar information signal $s(t)$, the amplitude portion of the CSSB signal is acquired as in

$$p(t) = \alpha + \beta \cdot s(t) \quad (2-59)$$

where α is a constant offset and β is a constant scaling factor set so that $p(t)$ is positive.

Now we take the Hilbert Transform of the \ln of $p(t)$,

$$H_L[p(t)] = H[\ln(p(t))]. \quad (2-60)$$

If at this point we combine the \ln of $p(t)$ and its Hilbert Transform as in

$$a'(t) = \ln[p(t)] + jH_L[p(t)], \quad (2-61)$$

and take the anti-log we get

$$a(t) = p(t)\exp[jH_L[p(t))]. \quad (2-62)$$

A block diagram of the modulation scheme is shown in Figure 2.7.[49]

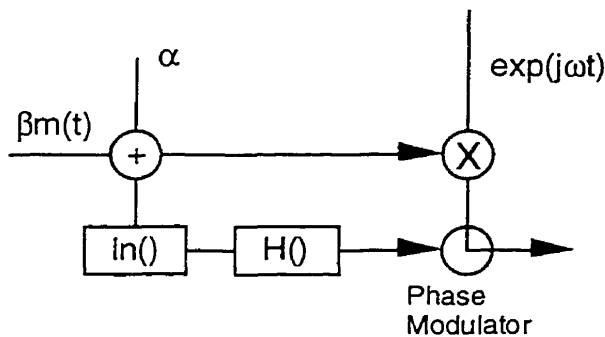


Figure 2.7. Ideal minimum phase modulator.

The important point derived from Figure 2.7 as regards optical devices is that the COSSB signal may be implemented in a variety of structures. The envelope (amplitude) modulation process may be carried out in a laser intensity modulator or a Mach-Zehnder Modulator (MZM) whereas the phase modulation may be carried out in an external waveguide modulator or as will be shown theoretically, a Laser Diode.

2.5.1. Computer Simulation

To verify the preceding theory, computer simulations were performed. To simplify the interpretation of the results, normalization of the frequency was undertaken. In all of the spectral plots that represent the spectrum of the modulated optical carrier, the complex envelope representation is assumed. The carrier in this case is shown at a normalized frequency of zero. The normalized frequency scale is graduated by unit increments where the fundamental frequency (in the case of optical subcarrier modulation) or the bitrate (in optical baseband modulation) is located at a normalized frequency of unity. For example, in a simulation of a 10 GB/s optical baseband signal a frequency offset of '1' represents a bandwidth of 10 GHz. For an optical subcarrier simulation, a frequency offset of '1' represents a bandwidth corresponding to the fundamental subcarrier frequency. In the time domain plots the abscissa is always a normalized time index. This simplifies the plots and removes the concerns for relative signal bandwidth and other system based issues.

We simulate (in MATLAB™) a system in which a maximal length pseudo random binary sequence (PRBS)[50] is modulated onto a optical carrier in minimum phase fashion[49] The pertinent parameters are shown in table 2.1:

Bitrate	10 GB/s
Input lowpass Filter	5th Order Butterworth LP, $f_{c0} = 5$ GHz
Receiver Filter	None
Optical Carrier Wavelength	1550 nm
Sampling Rate	5/bit
β	0.6
α	1
PRBS Length	2047
PRBS Polynomial Coefficients	{11,2,0}[50]

Table 2.1. Ideal COSSB simulation parameters.

The PRBS information sequence $s(t)$ was acquired from an 11th order prime polynomial[50]. A 500 point section of the sequence is shown in Figure 2.8.

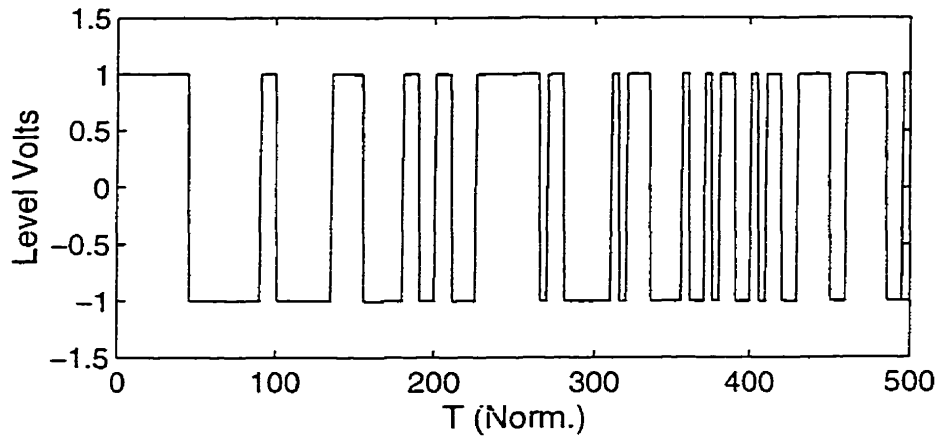


Figure 2.8. PRBS sequence

After bandlimiting and scaling the sequence looks like that in Figure 2.9.

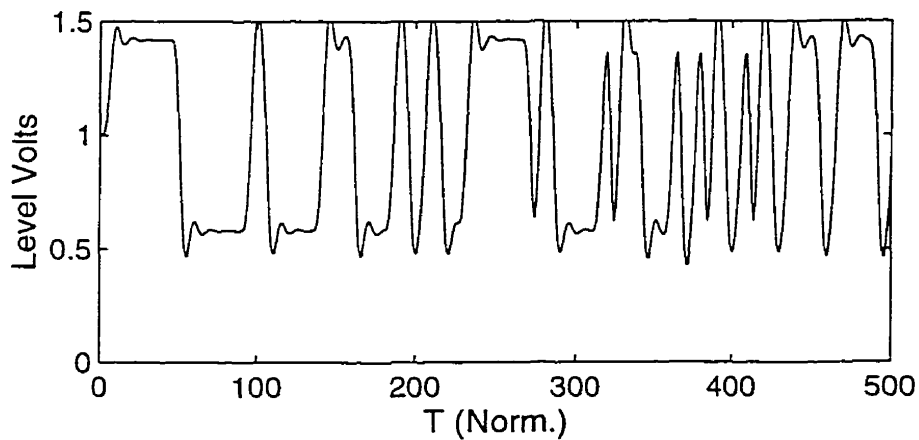


Figure 2.9. Bandlimited and scaled PRBS sequence.

A fifth order Butterworth filter with cutoff at one-half of the bitrate was used for bandlimiting. Referencing (2-59), the peak modulation index or β was approximately 0.6 and α , the DC level was set at unity.

The sequence in Figure 2.9. was modulated onto a complex carrier whose frequency characteristics are normalized as per the description at the beginning of this section. The spectral envelope of the DSB (envelope only) modulated signal is shown in Figure 2.10.

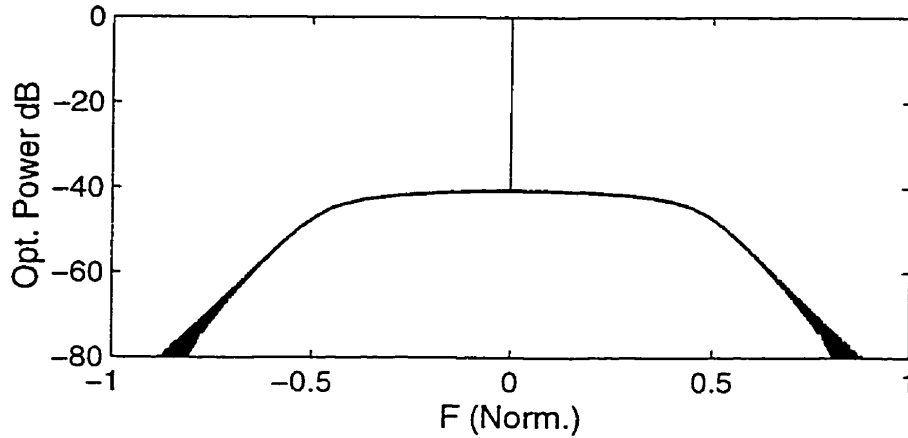


Figure 2.10. Spectrum of double sideband PRBS modulated carrier.

The Hilbert Transform of the In of the signal in Figure 2.9 is taken and the signal is combined as in (2-62) to produce a COSSB signal. The resultant analytic signal is modulated onto a complex carrier and the spectrum is shown in Figure 2.11.

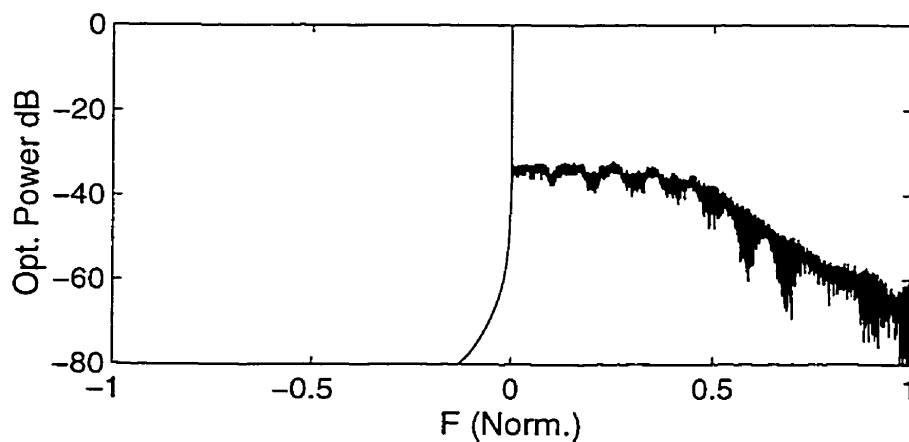


Figure 2.11. Spectrum of minimum phase single sideband PRBS modulated carrier.

Clearly, the signal is SSB in nature. The original signal is recovered after transmission by envelope detection to show that the phase modulation has had no effect on the information signal as shown in Figure 2.12.

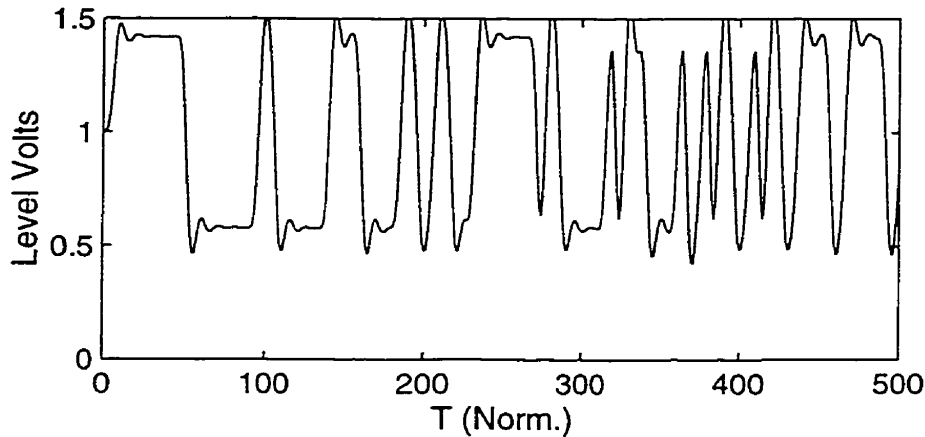


Figure 2.12. Recovered PRBS sequence

It is possible then to achieve distortionless SSB envelope modulation using the minimum phase modulation principle.

To achieve a more practical modulator structure, we observe some of the effects that taking the \ln of the signal has on the scaling and characteristics of the Hilbert transformed signal[51,52]. Figure 2.13 shows the relationship between the Hilbert transform of the \ln of the information signal (in Figure 2.9) and its Hilbert transform without logarithmic conversion. It is apparent that these signals are quite similar except for a constant scaling factor and an offset. There is some logarithmic distortion on the Log Hilbert Transform but it is clear that a scaling factor would cause the Hilbert Transform of the signal to become closer in character to the Hilbert Transform of the \ln of the signal.

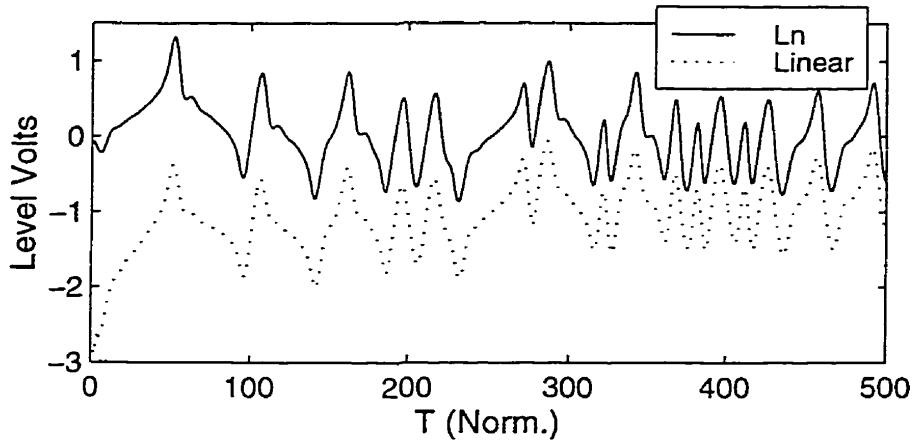


Figure 2.13. Hilbert transforms of the \ln of $p(t)$ (solid line) and of $p(t)$ (both on linear scale).

This means that we should be able to approximate the minimum phase modulator by simply scaling the Hilbert transform of the information signal rather than taking the \ln and Hilbert transform to acquire the phase portion of the analytic signal. This simpler modulator structure is shown in Figure 2.14 with a scaling function added for optimal scaling of the Hilbert Transform.

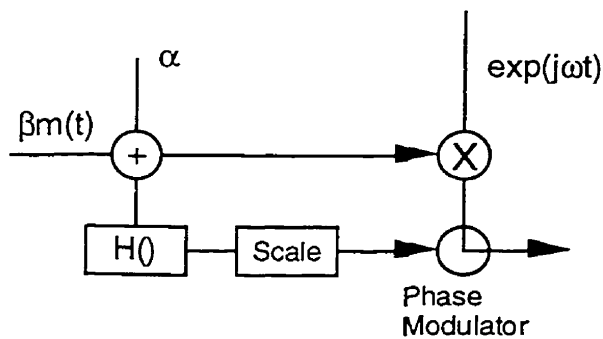


Figure 2.14. Approximate minimum phase modulator.

To illustrate the effectiveness of this simplification we show, in Figure 2.15, the spectral plot of the output signal from the approximate minimum phase modulator.

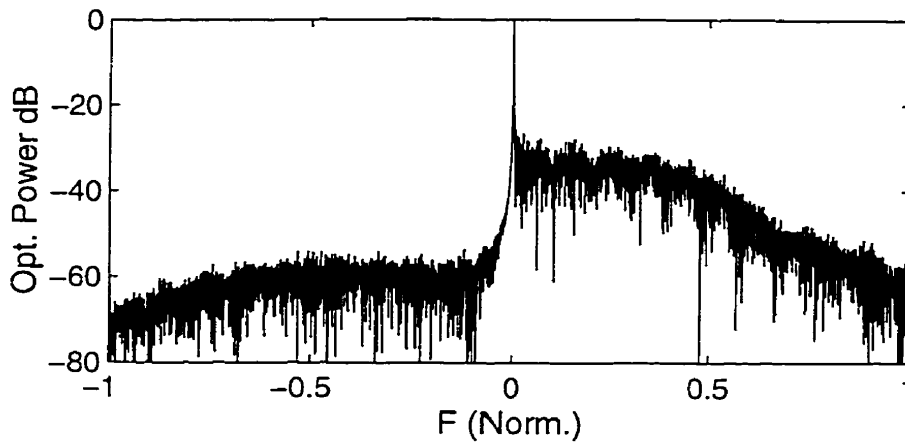


Figure 2.15. Spectral plot of hybrid signal with scaled Hilbert transform phase function.

We see in this case about 20 dB of sideband cancellation. This is interesting since it shows that if we do no preconditioning of the information signal at all we still achieve a significant amount of sideband cancellation. In the case of the above sequence no further improvements were achieved with offsetting or scaling the Hilbert Transform of the signal. It is also apparent that the noise standard deviation has increased over the case of DSB and perfect COSSB modulation as depicted in Figure 2.10 and 2.11. Since no noise was artificially added in the simulations this has to be due to an unknown numerical effect that comes about due to the imperfect phase and is likely only present in the simulations.

The envelope detected data for the reduced modulation scheme is shown in Figure 2.16. In the previous simulations we should qualify the results by stating that approximation of the Hilbert/ln is easier to achieve on a binary signal due to the similarity between the signal and its log as shown in Figure 2.17. This similarity will break down for more complicated multilevel signals or signals that are bandlimited such that the ln operation causes distortion.

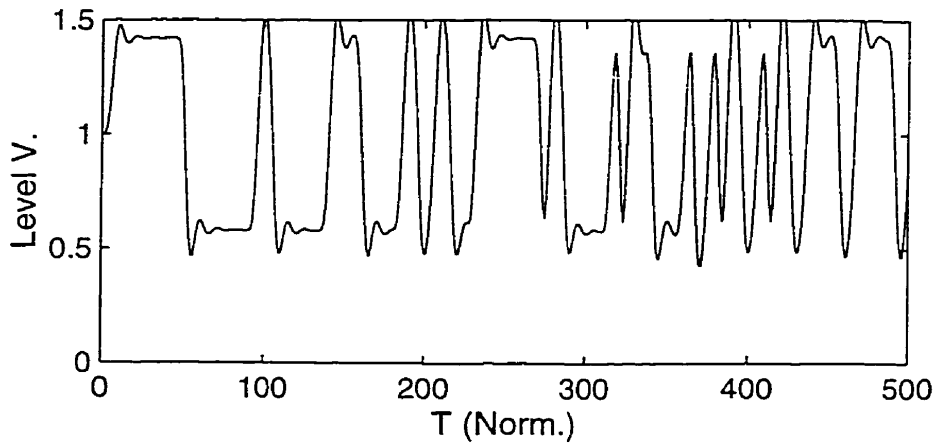


Figure 2.16. Recovered PRBS sequence.

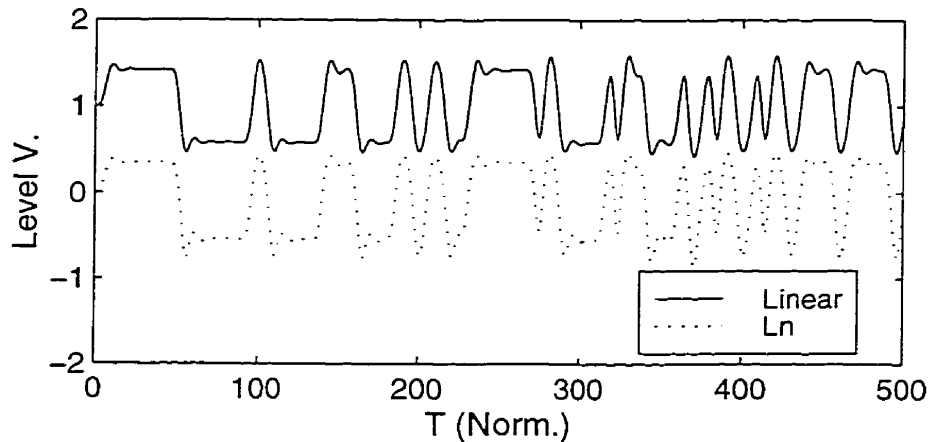


Figure 2.17. Plot of $p(t)$ (solid) and $\ln(p(t))$ (both on linear scale).

It has been shown that COSSB modulation has no distorting effect on the information signal. It remains to be shown that COSSB is useful for mitigation of dispersion effects on subcarrier and baseband modulation.

2.5.2. Dispersion Effects And Ideal CSSB Optical Modulation

2.5.2.1. Sinusoidal Modulation

We first deal with sinusoidal modulation since this case illustrates the fundamental mechanism of dispersion distortion.

Let a real subcarrier, given by

$$s(t) = \cos(2\pi f_c t) \quad (2-63)$$

be modulated onto an optical carrier in an ideal electric field envelope modulator whose analytic electric field output is given by

$$E_o(t) = [1 + ms(t)] \exp(j2\pi f_o t). \quad (2-64)$$

The Fourier transform of (2-64) is given by

$$F_E(f) = 2\pi\delta(f - f_o) + m\{\pi\delta[f - (f_o + f_c)] + \pi\delta[f - (f_o - f_c)]\}. \quad (2-65)$$

The frequency domain fiber dispersion transfer function at the optical carrier is given by

$$\Delta(f) = \exp\left(\frac{j\pi D \lambda_o^2 (f - f_o)^2 L}{c}\right) \quad (2-66)$$

where D is the dispersion parameter in ps/(nm•km), λ_o is the optical wavelength, f is the frequency offset from the optical carrier, L is the fiber length in km and c is the speed of light in a vacuum. A development of this formula is given in Appendix B. Introducing dispersion, (2-65) is modified to

$$F_E(f) = \left[2\pi\delta(f - f_o) + m\{\pi\delta[f - (f_o + f_c)] + \pi\delta[f - (f_o - f_c)]\} \right] \cdot$$

$$\exp\left(\frac{j\pi D\lambda_0^2(f-f_0)^2L}{c}\right) \quad (2-67)$$

which may be simplified to

$$F_E(f) = 2\pi\delta(f-f_0) + m\left\{\pi\delta[f-(f_0+f_c)] + \pi\delta[f-(f_0-f_c)]\right\} \cdot \exp\left(\frac{j\pi D\lambda_0^2 f_c^2 L}{c}\right). \quad (2-68)$$

The Fourier transform of the squared envelope operator in the time domain is the autocorrelation of the Fourier transform of the electric field function given by

$$F(|E_o(t)|^2) = \int_{-\infty}^{\infty} F_E(f)F_E^*(f+\xi)df = A_{FF}(\xi). \quad (2-69)$$

Considering only the fundamental term in A_{FF} at f_c we have

$$A_{FF}(f_c) = 2\pi\delta(f-f_c)m\left[\exp\left(\frac{j\pi D\lambda_0^2 f_c^2 L}{c}\right) + \exp\left(-\frac{j\pi D\lambda_0^2 f_c^2 L}{c}\right)\right]. \quad (2-70)$$

The inverse Fourier transform of (2-70) is given by

$$a_{FF}(t) = 2\pi \exp(j2\pi f_c t)m\left[\exp\left(\frac{j\pi D\lambda_0^2 f_c^2 L}{c}\right) + \exp\left(-\frac{j\pi D\lambda_0^2 f_c^2 L}{c}\right)\right], \quad (2-71)$$

and the real part of (2-71) which is proportional to the detector output current is given by

$$\begin{aligned} I_{DF1}(t) &\propto 2\pi^2 \left[\cos\left(2\pi f_c t + \frac{\pi D\lambda_0^2 f_c^2 L}{c}\right) + \cos\left(2\pi f_c t - \frac{\pi D\lambda_0^2 f_c^2 L}{c}\right) \right] \\ &\propto 2k \cos\left(\frac{\pi D\lambda_0^2 f_c^2 L}{c}\right) \cos(2\pi f_c t). \end{aligned} \quad (2-72)$$

The detected power at the fundamental frequency f_c for a given D and λ_0 as a function of fiber length varies as

$$W(l) \propto \cos^2\left(\frac{\pi L \lambda_0^2 D f_c^2}{c}\right). \quad (2-73)$$

It is clear from (2-72) and (2-73) that the detected power reduces to zero for fiber lengths corresponding to an argument of $\pm \pi/2$ as was shown in Figures 1.6 and 1.7 in Chapter 1. Further, the cancellation mechanism for an ideal optical amplitude modulator is actually an interference property governed by the dispersion parameter, frequency offset and other parameters. Real optical modulators such as laser intensity modulators and Mach-Zehnder interferometers may be configured to approximate the ideal amplitude modulator by controlling the modulation index. These cases will be dealt with in later sections. If the optical electric field is composed of a continuum of frequencies as in a broadband signal or a large set of discrete frequencies as in multicarrier modulation the situation becomes more complicated, however the qualitative distortion mechanism of interference still holds.

Observing (2-71) it can be shown that if one of the sidebands of the optical signal in (2-65) is removed as in single sideband modulation, the detector output current is given by

$$I_{DF1}(t) \propto 2\pi^2 \cos\left(2\pi f_c t + \frac{\pi D \lambda_0^2 f_c^2 L}{c}\right) \quad \text{or} \quad 2\pi^2 \cos\left(2\pi f_c t - \frac{\pi D \lambda_0^2 f_c^2 L}{c}\right) \quad (2-74)$$

depending on which sideband is removed. Both terms in (2-74) are constant in power as a function of fiber length. The cancellation mechanism is defeated and this process extends to the case of broadband modulation. Thus single sideband modulation theoretically overcomes dispersion cancellation in IMDD optical links.

2.5.2.2. Broadband Dispersion Effects

It was shown in the previous section that dispersion will create nulls in the detected power characteristic of a double sideband subcarrier signal for specific

lengths of dispersive fiber, subcarrier frequency and fiber dispersion parameters. We would expect that for a real double sideband (DSB) broadband signal on the optical carrier there would be a frequency selective nulling in the power spectrum of the detected broadband signal. The nulls would be located at points in the spectrum that would correspond to matchings between frequency, fiber length and dispersion severity on the fiber.

Consider once again the case of the ideal optical DSB modulator, whose complex output signal is given by (2-64). This modulator structure is simulated with the following parameters in Table 2.2 :

Bitrate	10 GB/s
Input lowpass Filter	5th Order Butterworth LP, $f_{c0} = 5$ GHz
Receiver Filter	None
Optical Carrier Wavelength	1550 nm
Fiber Dispersion parameter	18 ps/(nm•km)
Sampling Rate	5/bit
Receiver Demodulation	Square Law Envelope
β	0.6
α	1
PRBS Length	2047
PRBS Polynomial Coefficients	{11,2,0}[50]

Table 2.2. Parameters for ideal COSSB simulation on dispersive fiber.

The DSB output electric field complex envelope spectrum is shown in Figure 2.18. Since the simulations are simply to illustrate comparative effects, no filtering is applied at the output of the square law detector for the spectral plots or the following eye diagrams.

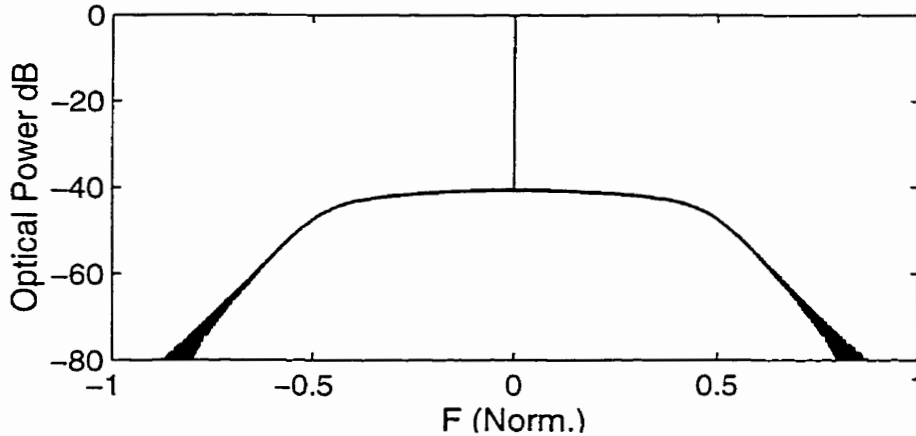


Figure 2.18. Double sideband optical electric field spectrum, $B = 10$ GB/s.

The spectrum of a dispersionless detected signal at the photodetector output is shown in Figure 2.19.

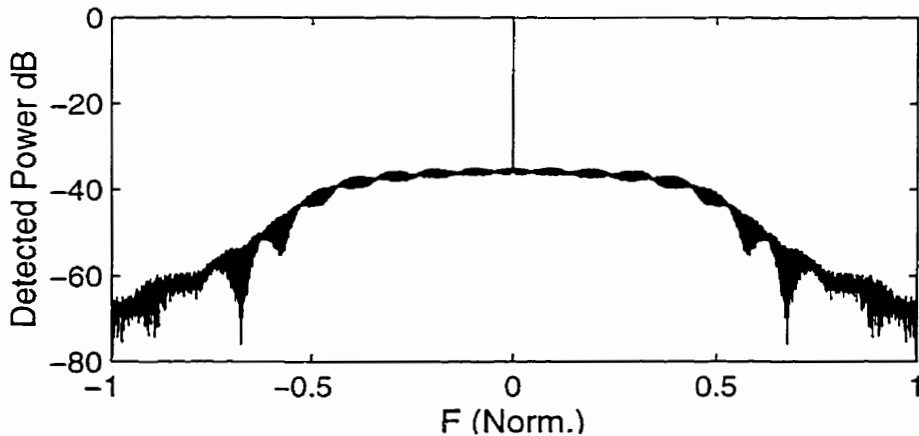


Figure 2.19. Detected power spectrum without dispersion.

The detected spectrum has undergone little distortion in the higher power ($|f| > 0.7$) sections of the spectrum. The distortion seen on the lower power section is

due to beating of the signal with itself in the square law detection process. The information is easily recovered as was shown earlier. When dispersion is introduced by propagation down a 200 km fiber link the effect of chromatic dispersion is shown in Figure 2.20.

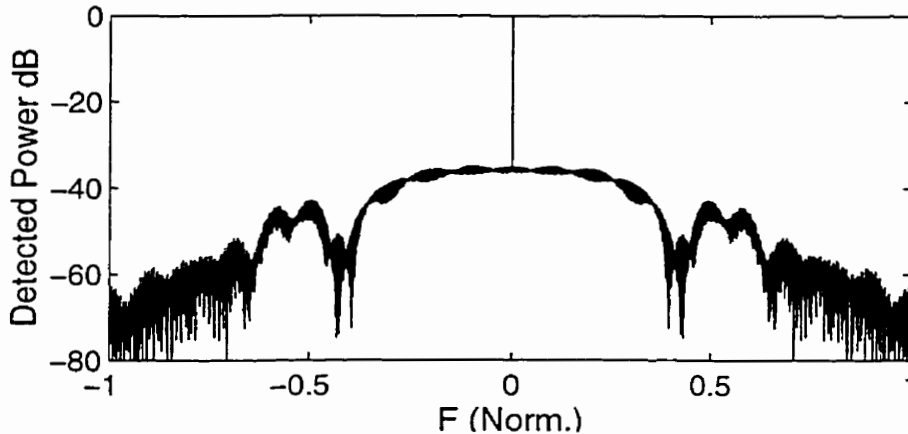


Figure 2.20. Detected power spectrum after 200 km dispersive fiber, $B = 10$ GB/s, $D = 18$ ps/(nm•km).

Frequency selective fading is obvious in Figure 2.20. The frequency nulls may be explained in terms of the dispersion mechanism outlined for the case of pure sinusoidal modulation examined in subsection 2.5.1. The detection process of the wideband information signal is identical to the sinusoidal process. The nulls in Figure 2.20 correspond to the Fourier components in the information signal that are at a frequency that interacts with the fiber dispersion to cause cancellation of the signal.

The resulting degraded condition of the eye diagram for the detected signal from the distorted spectrum is shown in Figure 2.21. The transient artifact at the beginning of the eye is due to the baseband filtering operation. This section has been left in the plots to observe settling effects through the various modulator structures.

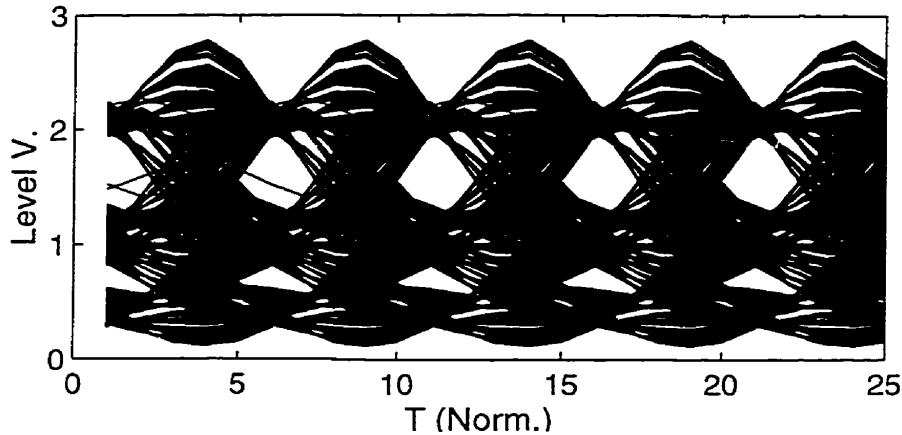


Figure 2.21. Eye pattern from detected signal after 200 km dispersive fiber $B = 10$ GB/s, $D = 18$ ps/(nm•km).

The frequency selective fading effect is intensified by increasing the fiber length to 500 km, as is shown in Figure 2.22.

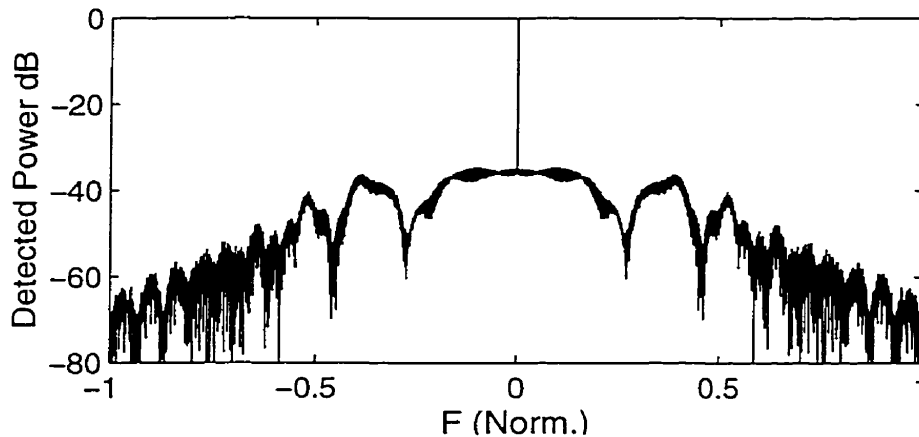


Figure 2.22. Detected power spectrum after 500 km dispersive fiber $B = 10$ GB/s, $D = 18$ ps/(nm•km).

The simulation results in Figures 2.18 to 2.22 show the effects of dispersion on broadband signals. To verify that COSSB is an effective tool for mitigation of dispersion distortion, we can quickly show that for fiber length 200 km with ideal COSSB modulation, the situation is drastically improved over the DSB case.

Figure 2.23 shows the COSSB detected spectrum for the same simulation parameters as above over a 200 km dispersive fiber.

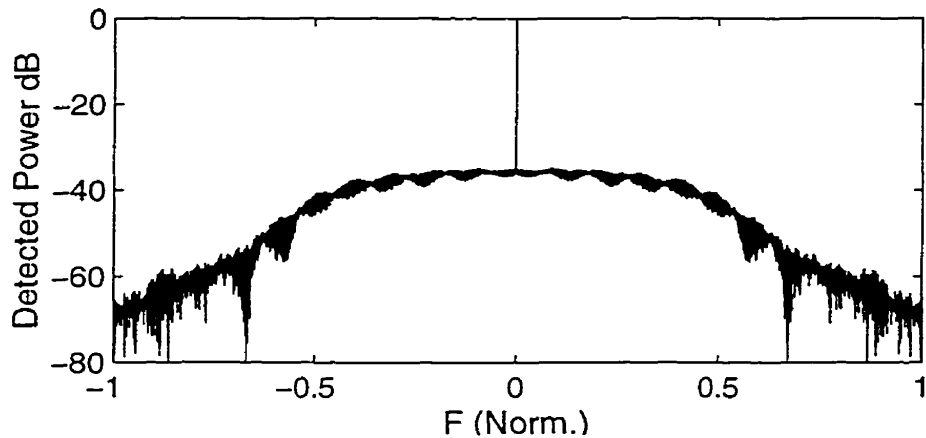


Figure 2.23. COSSB detected power spectrum after 200 km dispersive fiber.

The spectrum is now more even, without evidence of frequency selective fading. The resulting eye diagram, shown in Figure 2.24 has a larger opening.

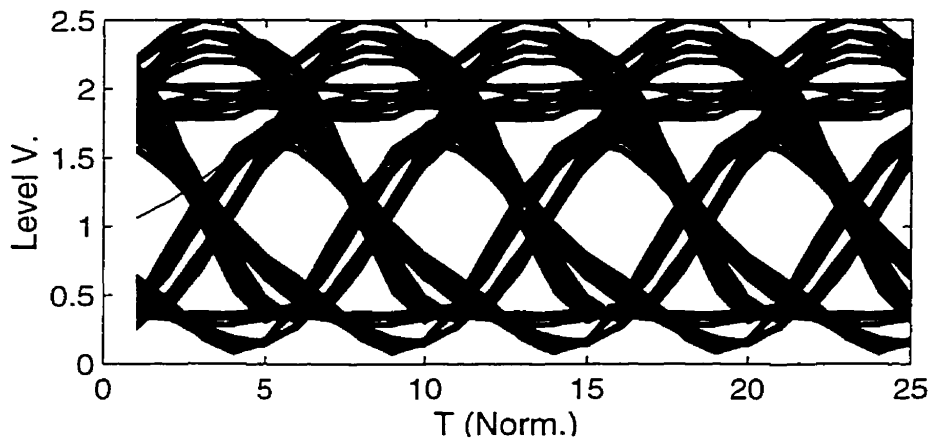


Figure 2.24 Eye diagram from COSSB detected signal after 200 km dispersive fiber.

Some distortion is present but the recovered data is much improved over the DSB case. The transmitted electric field spectrum from Figure 2.11 is reprinted for convenience for comparative purposes.

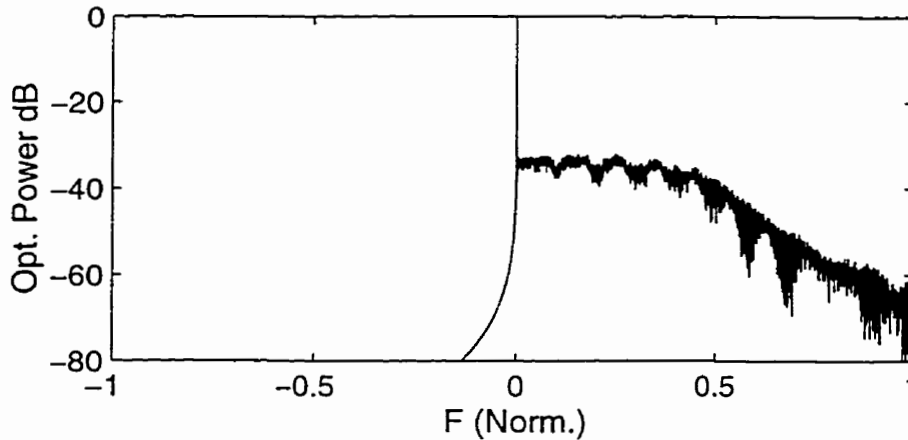


Figure 2.11. Spectrum of COSSB PRBS modulated carrier.

The improvement in the spectrum is due to the fact that, since the signal input to the detector is single sideband, there is no selective cancellation of signal Fourier components. The eye diagram from a non-dispersive or 'back-to-back' optical link is shown in Figure 2.25 and it is clear that the 200 km eye diagram from Figure 2.24 is very similar.

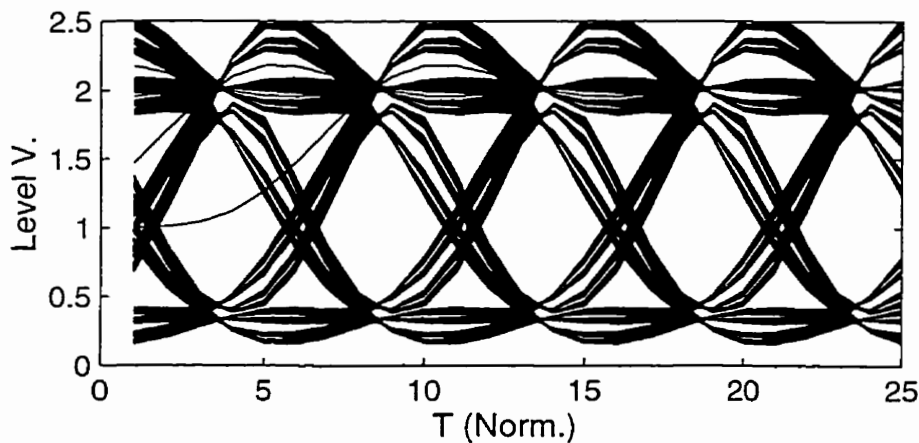


Figure 2.25. Eye diagram from COSSB detected signal on zero length fiber.

Thus it has been shown in simulation that OSSB modulation mitigates chromatic dispersion distortion for an ideal amplitude modulator. The focus will now move to optical modulator structures.

2.6. OSSB Optical Modulator Structures

To make use of the above theory for optical modulators certain modifications must be made to accommodate the specific characteristics of the modulator in question. For example, if the COSSB modulator consists of a laser diode source configured as an intensity modulator coupled to an external phase modulator, allowances must be made for the fact that the laser modulation process is an optical power modulation process while the phase modulator is one of electric field modulation. This study will address the three structures outlined in Chapter 1, namely the laser-intensity/phase modulator, the laser configured for FM modulation coupled to an external amplitude modulator and the MZM/phase cascade .

2.6.1. Laser Intensity/Phase Modulator

The Laser/phase modulator consists of a cascade of a laser diode intensity modulator coupled to an external phase modulator. The information signal is applied to the laser via a bias TEE connected to the bias of the laser. A schematic diagram of the Laser/Phase Modulator is shown in Figure 2.26.

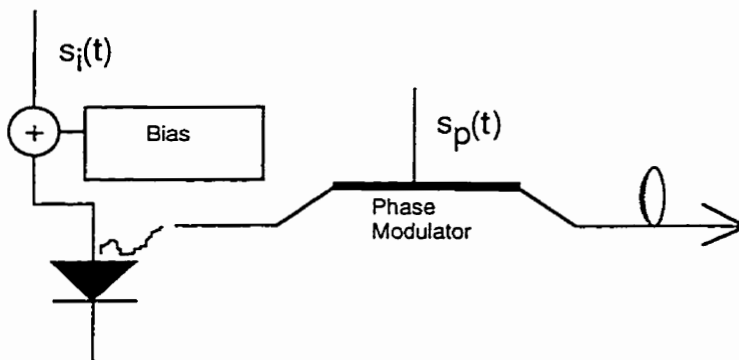


Figure 2.26. Laser intensity/phase COSSB modulator.

2.6.1.1. Laser Diode Model

A graphical representation of the ideal laser power transfer characteristic as a function of laser input current is shown in Figure 2.27.

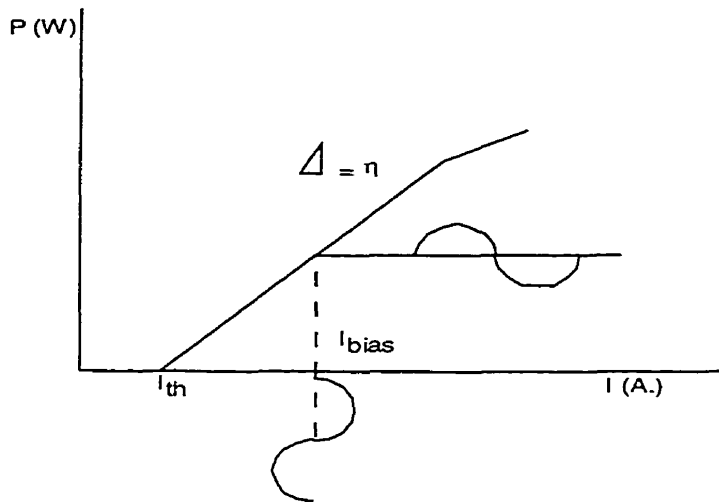


Figure 2.27. Laser diode transfer characteristic.

Since real lasers are prone to non-linear distortion by clipping, careful biasing and modulation index control must be carried out. If this is done correctly the device has good linearity between the output power and input current. For this reason the laser is typically used in IMDD links with good results.

The ideal laser instantaneous output power expression is approximated by

$$P_{out}(t) = \eta(I_{in}(t) - I_{th}) \quad (2-75)$$

where $P(t)$ is the output power, η is the laser modulation efficiency in Watts/Amp, I_{th} is the threshold current required to drive the device into lasing mode and I_{in} is the instantaneous input current which includes a DC bias current required to bring the device into a linear range. This expression ignores spontaneous emission for input currents less than the threshold. The input current is given by

$$I_{in}(t) = I_{bias} + m_{LD}i(t) \quad (2-76)$$

where $i(t)$ is the current modulation signal and m_{LD} is the laser modulation index. The bias current is usually set so that the laser operating point is in the middle of the linear operating range of the device which is determined by the laser clipping point below the bias current and the saturation point above the

bias point. The modulation index is the ratio of the peak value of the modulation current to the current required to clip the laser at the bias point.

Even though this investigation focuses on the ideal laser, the subject of laser chirp needs mention. The term 'chirp' generally refers to an undesired FM modulation process that accompanies a desired intensity or amplitude modulation signal at the laser output. This effect is quite deleterious when the output signal from the modulator is transmitted down a dispersive fiber. Detailed investigation of this phenomenon is beyond the scope of this study. However, it can be shown that for subcarrier modulation, laser chirp can actually enhance the SSB effect as will be shown later[53].

To analyze the laser diode modulator in the context of COSSB modulation, with a minimum of confusion, a number of simplifications to the ideal laser model are applied. The laser threshold current is set to zero and the modulation efficiency is set to unity thus (2-75) becomes

$$P_{out}(t) = I_{bias} + m_{LD}i(t). \quad (2-77)$$

The bias current is normalized to unity and since $i(t)$, the modulation current, is proportional to $s(t)$, the information signal, the normalized laser output power is given by

$$P_{out}(t) = 1 + ms(t) \quad (2-78)$$

where $s(t)$ is the information signal and m is a normalized modulation index relative to the unity laser bias. For the modulation index to correctly characterize the modulation conditions the peak signal level is assumed to be unity. To illustrate the characteristics of the laser we assume an ideal (no chirp) laser. The laser output electric field is then given by

$$E_i(t) = \sqrt{1 + ms(t)}. \quad (2-79)$$

The square root is due to the fact that the electric field output from the laser scales with the square root of the laser power.

2.6.1.2. External Phase Modulator

The external optical phase modulator transfer characteristic is given by

$$E_{\text{out}}(t) = E_{\text{in}}(t) \exp\left[j \frac{\pi v(t)}{V_{\pi}}\right] \quad (2-80)$$

where $E_{\text{in}}(t)$ is the input optical electric field, $v(t)$ is the voltage applied to the modulation input, V_{π} is the voltage required to produce a phase shift in the optical output $E_{\text{out}}(t)$ of ' π ' radians relative to phase of the input signal. This device is usually implemented in an external waveguide device in which the refractive index of the waveguide may be modulated with application of an electric field across the guide substrate. As with the ideal laser expression, the phase modulator is normalized so that the argument shows the net phase shift required to achieve the particular objective. This requires that $V_{\pi} = 1$ in (2-80) so that the normalized modulator expression is given by

$$E_{\text{out}}(t) = E_{\text{in}}(t) \exp[jm_p s(t)] \quad (2-81)$$

where $s(t)$ is the phase modulation signal and m_p is a phase modulation index that incorporates the factor of π in (2-80).

2.6.1.3. Laser/Phase COSSB Simulation

To achieve COSSB modulation in the laser/phase cascade, the required amplitude and phase signals are combined as in

$$E_i(t) = \sqrt{(1+ms(t))} \exp\{jm_p H_L[(1+ms(t))]\}. \quad (2-82)$$

The production of the required phase signal is very similar to that of the idealized envelope modulator in section 2.5. The fact that there is a \ln operation in the H_L operator dictates that to implement the strict COSSB theory, m_p must be set to 1/2. Thus (2-82) is re-written as:

$$E_i(t) = \sqrt{1+ms(t)} \exp\left\{j \frac{H_L[(1+ms(t))]}{2}\right\}. \quad (2-83)$$

To verify the theory some simulations were performed for a laser modulated with a binary random code in a similar manner to the ideal amplitude modulator. The circuit model used for the simulations was a laser/phase modulator connected via a length of fiber to a detector diode modeled as a square-law detector as shown in Figure 2.28.

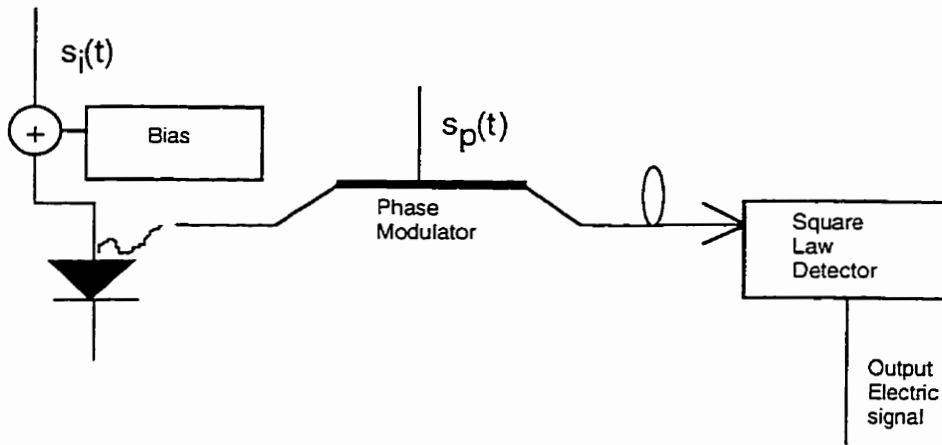


Figure 2.28. Circuit model for laser/phase simulation.

The output current for the detector is given by

$$I_{out} = \sigma |E_i(t)|^2. \quad (2-84)$$

where E_i is the input optical electric field and σ represents the detector responsivity. The first simulated case for the Laser/Phase modulator is with a non-dispersive line. This was done to show the effects, if any, of the modulation scheme on the information signal. Once again the bias current is normalized to unity and the modulation index m is relative to the required clipping current. The intensity modulation signal is given by $s_i(t)$ and the phase signal is given by $s_p(t)$; thus the laser/phase modulator complex electric field output is given by

$$E_i(t) = \sqrt{1+ms_i(t)} \exp\left[j \frac{s_p(t)}{2}\right] \quad (2-85)$$

and $s_p(t)$ is given by

$$s_p(t) = H_L[1 + m s_i(t)]. \quad (2-86)$$

The simulation conditions were as shown in Table 2.3:

Bitrate	10 GB/s
Input lowpass Filter	5th Ord. Butterworth LP, $f_{c0} = 5$ GHz
Receiver Filter	None
Optical Carrier Wavelength	1550 nm
Fiber Dispersion parameter	18 ps/(nm•km)
Sampling Rate	5/bit
Receiver Demodulation	Square Law Envelope
PRBS Length	2047
PRBS Polynomial Coefficients	{11,2,0}[50]
m	0.8

Table 2.3. Parameters for laser/phase simulation on dispersive fiber

An eye diagram of the information signal before modulation on the laser is shown in Figure 2.29.

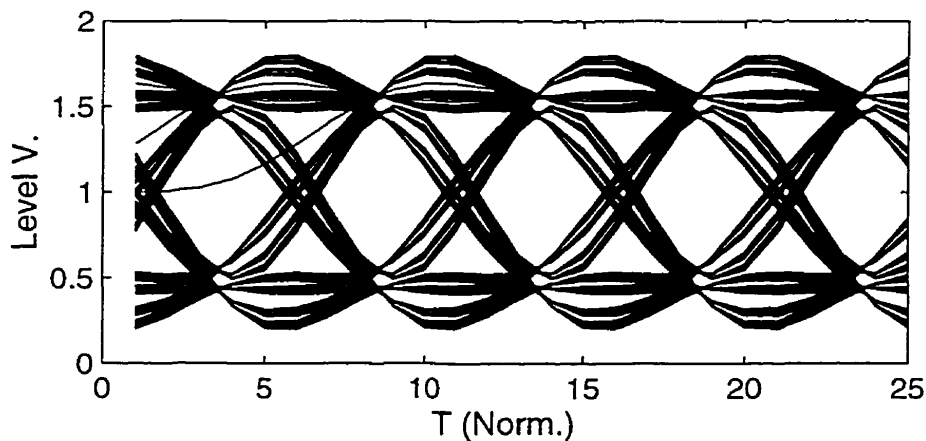


Figure 2.29. Information signal eye pattern.

Figure 2.30 shows the detected signal for a COSSB signal for a zero length or nondispersive fiber link.

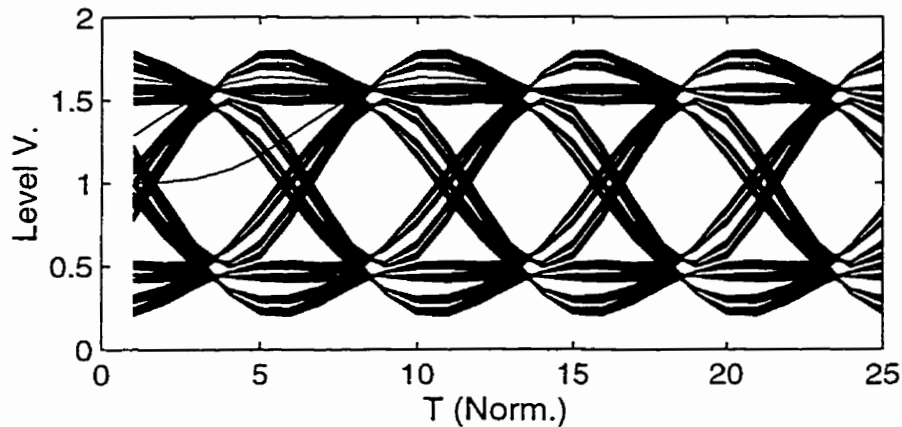


Figure 2.30. Square law detected signal for a zero length or nondispersive fiber link.

The double sideband case with laser modulator only was identical. Figure 2.31 shows the single sideband spectrum of the COSSB laser/phase output electric field.

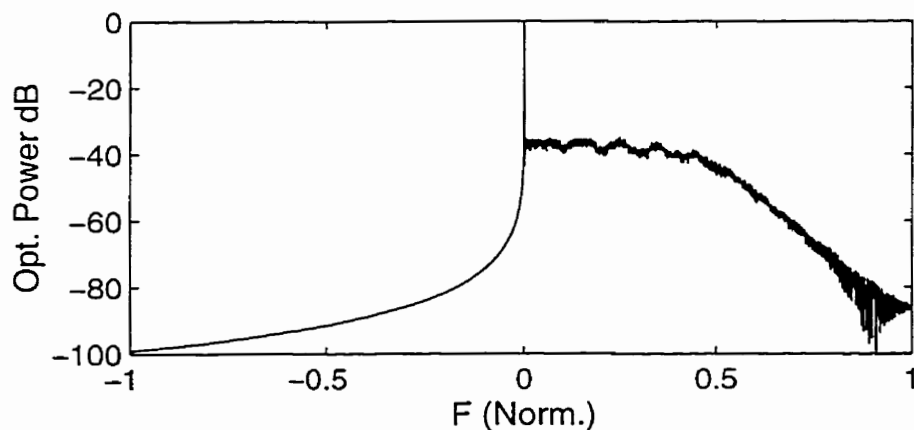


Figure 2.31. OSSB frequency plot for the laser/phase device.

To illustrate the effect of dispersion, the above transmission example is carried out over a dispersive line. The same signal used in the previous simulation was transmitted over a dispersive 200 km fiber link. Figure 2.32 shows the eye pattern of the detected signal from a DSB modulated optical signal.

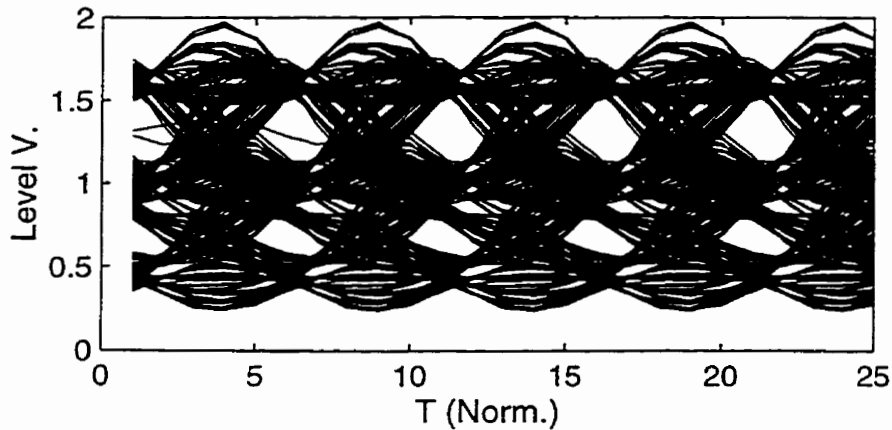


Figure 2.32. Detected signal from a DSB modulated optical signal over 200 km dispersive fiber.

The eye pattern is quite distorted with no clear openings as in the information signal eye pattern in Figure 2.29. Figure 2.33 shows the COSSB signal under the same transmission parameters. While the eye shows the effects of nonlinear distortion from the fiber dispersion, it is greatly improved over the DSB case.

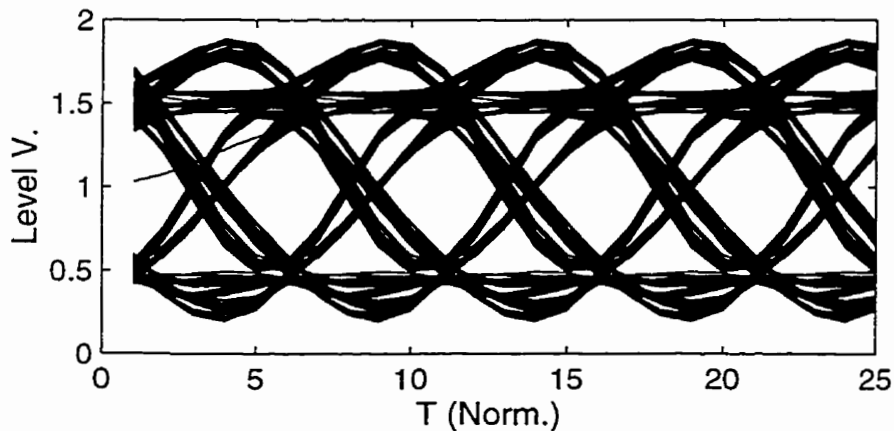


Figure 2.33. Detected signal from a COSSB modulated optical signal over 200 km dispersive fiber.

Clearly Laser/Phase COSSB modulation offers a direct improvement for dispersion distortion of optical signals as is observed in the larger eye openings of Figure 2.33.

2.6.1.4. More On Laser Chirp

Laser chirp may be modeled as a linear FM process that accompanies the intensity modulation process in a laser diode modulator. Chirp occurs due to the fact that changes in the carrier concentration (adiabatic chirp) and temperature (thermal chirp) in the laser diode active region cause changes in the refractive index [22-24,53-56]. The effect of laser chirp on the CSSB modulation process may be characterized assuming that the process is linear with modulation current. In the case that the laser is configured strictly as an intensity modulator, the associated FM modulation process is seen as undesired interference. Conversely, if the laser is used as an FM modulator the intensity modulation process is seen as interference as will be shown in the next section.

If chirp is present, the expression for the laser electric field complex envelope may be given by

$$E_i(t) = \sqrt{1 + m s_i(t)} \exp\left[j \cdot k \int m s_i(t) dt\right] \quad (2-87)$$

where m and s_i are the modulation index and information signal and k is the FM proportionality constant. It is assumed that the total chirp from all processes is represented by equation (2-87). The complex E-Field expression for the output of the COSSB laser/phase modulator with chirp is given by

$$E_i(t) = \sqrt{1 + m s_i(t)} \cdot \exp\left[j \cdot k \int m s_i(t) dt\right] \cdot \exp\left[j \frac{s_p(t)}{2}\right]. \quad (2-88)$$

We state without proof that the FM component of the signal in (2-88) will degrade the SSB characteristics and inevitably reduce the effectiveness of the modulation scheme. It is also clear that an additional phase signal may be added to the phase component $s_p(t)$ to compensate the FM distortion.

Investigation of the broadband COSSB process is left for further study. However some discussion of the subcarrier process in laser chirp is merited.

2.6.1.5. Laser Chirp and The Subcarrier Process

Consider the laser expression in (2-87) in the case of small modulation index, using a Taylor expansion we get

$$E_i(t) \approx \left[1 + \frac{ms_i(t)}{2} \right] \cdot \exp\left[j \cdot k \int ms_i(t) dt \right]. \quad (2-89)$$

In the case of cosinusoidal modulation we have

$$\begin{aligned} E_i(t) &\approx \left[1 + \frac{m \cos(2\pi f_c t)}{2} \right] \cdot \exp\left[j \cdot k \int m \cos(2\pi f_c t) dt \right] \\ &= \left[1 + \frac{m \cos(2\pi f_c t)}{2} \right] \cdot \exp\left[-j \cdot k m \sin(2\pi f_c t) \right]. \end{aligned} \quad (2-90)$$

Since a sine function is the Hilbert Transform of a cosine function, the structure of (2-90) is reminiscent of the approximate COSSB process outlined in the introductory section of this chapter. In that case the H_L operation was replaced with a Hilbert Transform with reasonable results for sideband cancellation. The conclusion to be drawn is that, for subcarrier processes in which the information bandwidth is small and with careful parameterization of the laser, it may be possible to produce subcarrier OSSB with a single laser[53].

This concludes the investigation of the broadband characteristics of laser/phase COSSB modulator. The previous simulations serve as motivation that the COSSB theory is worth pursuing in further study.

2.6.2. Laser FM Modulator Coupled to External Amplitude Modulator

A block diagram of the Laser FM/External Modulator is shown in Figure 2.34.

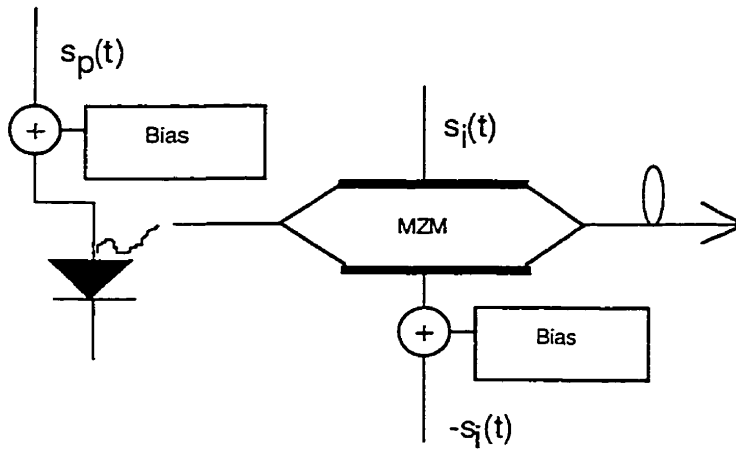


Figure 2.34. Laser FM/external COSSB modulator.

This device exploits the fact that laser diodes have an associated frequency modulation when the bias current is varied to produce intensity modulation[53-56]. It is important to note however that in addition to FM modulation there is an associated intensity modulation that in this case is seen as distortion. In the laser FM / AM modulator structure the laser takes the place of the phase modulator in the minimum phase modulator structure. Since amplitude modulation is still required to produce the required AM signal, an external amplitude modulator is connected in cascade with the phase modulator. The interchange of modulation operations has no effect on the desired results since the combined amplitude and phase modulation has commutative properties.

To accommodate the strict COSSB theory, the laser must be modulated with some form of the Hilbert/ln of the signal so as to remove one side of the AM DSB signal spectrum. Again normalizing the laser bias and threshold current, and assuming the chirp process is linear with bias current, the complex E-field from the output of an FM laser modulator with intensity distortion is given by

$$E_{FM}(t) = \left[\sqrt{1 + m_D s_p(t)} \right] \exp \left(j \left[m_{FM} \int_{-\infty}^t s_p(t) dt \right] \right) \quad (2-91)$$

where m_D is the intensity distortion index (ideally small), s_p is the desired phase signal constructed so as to produce the required phase modulation, m_{FM} is the FM modulation index.

The MZM shown in Figure 2.34 above is composed of an optical splitter which splits the optical signal into 2 equal components which are then passed through waveguide phase modulators similar to the external phase modulator described in the previous section. Each modulator has a drive terminal to which a signal may be applied. After the phase modulated optical signals emerge from the waveguides they are combined into a single optical signal in an optical combiner. The general input/output relation for the MZM is given by

$$\begin{aligned} E_{mzm}(t) &= E_{in} \left\{ \exp\left(\frac{j m_{mzm} \pi v_1(t)}{V_\pi}\right) + \exp\left(j \left[\frac{\pi m_{mzm} (v_2(t) + V_{bias})}{V_\pi} \right] \right) \right\} \\ &= E_{in} \cos\left[\frac{m_{mzm} \pi [v_1(t) - v_2(t)] - V_{bias}}{2V_\pi}\right] \exp\left(j \left[\frac{m_{mzm} \pi [v_1(t) - v_2(t)] - V_{bias}}{2V_\pi} \right] \right) \end{aligned} \quad (2-92)$$

where m_{MZM} is the MZM modulation index, $v_1(t)$ and $v_2(t)$ are the normalized voltages applied to the phase modulating arms of the MZM, V_{bias} is the constant bias voltage applied to either arm of the MZM so as to cause a constant phase bias between the arms and V_π is the extinction voltage. The extinction voltage is the bias voltage required to cause a phase shift of π radians between the modulator arm so as to produce a zero output for a CW optical input.

Note that we are attempting to exploit the laser chirp process, which is a frequency modulation process, to achieve phase modulation. Realizing that the phase of a signal is the integral of the frequency of the signal, the input modulating signal to the laser s_p in (2-91) should be of the form

$$s_p(t) = \frac{d}{dt} [H_L (1 + m_{FM} s(t))] \quad (2-93)$$

where $s(t)$ is the basic information signal. This realizes the strict COSSB phase signal. The input signal to the MZM is given by

$$v_1(t) = s_i(t); \quad v_2(t) = -s_i(t) \quad (2-94)$$

where $s_i(t)$ is a conditioned version of the basic information signal $s(t)$. The MZM transfer characteristic for this drive condition is given by

$$E_{\text{out}} = E_{\text{in}} \cos \left[\frac{2m_{\text{mzm}}\pi(s_i(t) - V_{\text{bias}})}{2V_{\pi}} \right]. \quad (2-95)$$

So the overall modulator complex envelope is given by

$$E_{\text{LDFM}}(t) = \left[\sqrt{1 + m_D s_p(t)} \right] \exp \left(j \left[m_{\text{FM}} \int_{-\infty}^t s_p(t) dt \right] \right) \cos \left[\frac{2m_{\text{mzm}}\pi s_i(t) - V_{\text{bias}}}{2V_{\pi}} \right]. \quad (2-96)$$

In order to compensate for the intensity distortion on the laser an additional term may be added to the MZM input. Assuming this compensation to be exact, the Laser FM/ MZM Amplitude modulator expression is now given by

$$\begin{aligned} E_{\text{LDFM}}(t) &= \exp \left(j \left[m_{\text{FM}} \int_{-\infty}^t s_p(t) dt \right] \right) \cos \left[\frac{2m_{\text{mzm}}\pi s_i(t) - V_{\text{bias}}}{2V_{\pi}} \right] \\ &= \exp \left(j m_{\text{FM}} [H_L (1 + m_{\text{FM}} s(t))] \right) \cdot \cos \left[\frac{m_{\text{mzm}}\pi 2s_i(t) - V_{\text{bias}}}{2V_{\pi}} \right]. \quad (2-97) \end{aligned}$$

The expression in (2-97) will yield single sideband with proper modulation indices applied to the Laser FM modulator and MZM. Assuming that the modulation is done correctly and the laser intensity modulation is compensated, it can be shown that the expression in (2-97) is equivalent to a cascade of a Mach Zehnder amplitude modulator and an external phase modulator which

will be addressed in the next section. Thus the discussion of the Laser Phase/MZM device is concluded.

2.6.3. External Mach-Zehnder Amplitude Modulator and Cascaded External Phase Modulator

The MZM/Phase cascade is the structure that will be covered most completely in this study. The modulator (shown in Figure 2.35) so named is composed of a Mach-Zehnder Modulator (MZM) coupled to an external phase modulator[18,52].

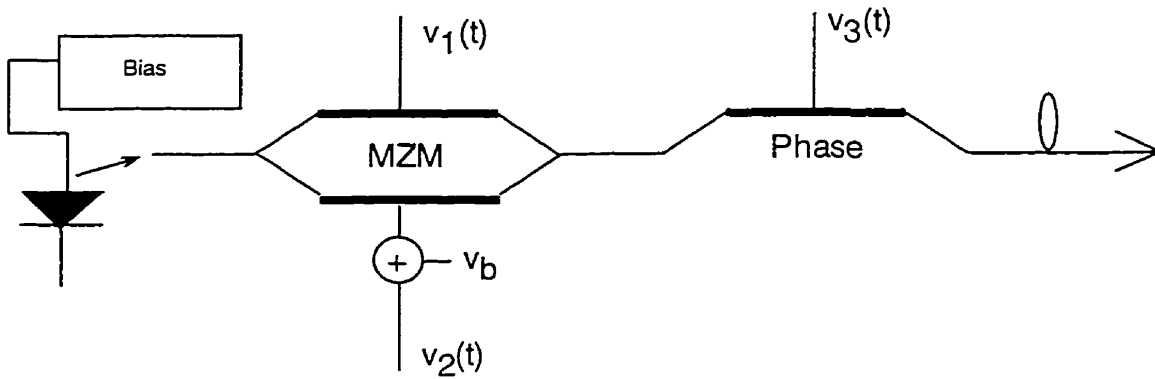


Figure 2.35. MZM/phase modulator.

As with the previous device, the MZM serves as an external amplitude modulator. The amplitude signal from the MZM is then fed into a external phase modulator, which consists of a single waveguide with identical properties to the waveguides in the MZM .

For baseband COSSB modulation, the MZM is driven in the same manner as the laser FM / MZM device outlined in the previous section, that is $v_1 = s_i(t)$ and $v_2 = -s_i(t)$. The output expression from the MZM/Phase device is given by

$$E_{\text{out}} = \cos \left[\frac{2m_{\text{mzm}} \pi s_i(t) - V_{\text{bias}}}{2V_{\pi}} \right] \exp(jm_p s_p(t)) . \quad (2-98)$$

Clearly the output from the MZM device is non-linear in nature. This means that the phase signal requires special conditioning to be optimal for COSSB modulation. In the case of small MZM modulations indices, the phase function may be calculated directly from the MZM input signal with suitable DC offset. Setting $\frac{2m_{mzm}\pi s_i(t)}{2V_\pi} = ms(t)$; $\frac{V_{bias}}{2V_\pi} = \frac{\pi}{4}$, , using a bias of $\pi/2$ and a Taylor expansion, the MZM output is given by

$$\begin{aligned}
 E_{mzm} &= \cos[ms(t)]\cos\left(\frac{\pi}{4}\right) - \sin[ms(t)]\sin\left(\frac{\pi}{4}\right) \\
 &= \frac{1}{\sqrt{2}} \left\{ 1 - ms - \frac{m^2s^2}{2!} + \frac{m^3s^3}{3!} + \dots \right\} \\
 E_{mzm} &= \frac{1}{\sqrt{2}}(1 - ms), \quad m \text{ small.} \tag{2-99}
 \end{aligned}$$

In this case the required phase signal is simply

$$s_p(t) = H_L \left[\frac{1}{\sqrt{2}}(1 - ms) \right]. \tag{2-100}$$

When an information signal of any significant modulation index is applied to the MZM the output will be distorted due to the non-linear transfer characteristic of the MZM. This creates concerns relating to the method used to acquire the Hilbert/ln of the envelope signal for the phase modulator. A novel method that will be briefly discussed involves detecting the MZM signal at the modulator output via a square law detector, taking the Hilbert/ln function and dividing by 2 to remove the squaring effect. The resulting signal is then optimally scaled to any modulation index applied to the MZM. The modified modulator structure is shown in Figure 2.36.

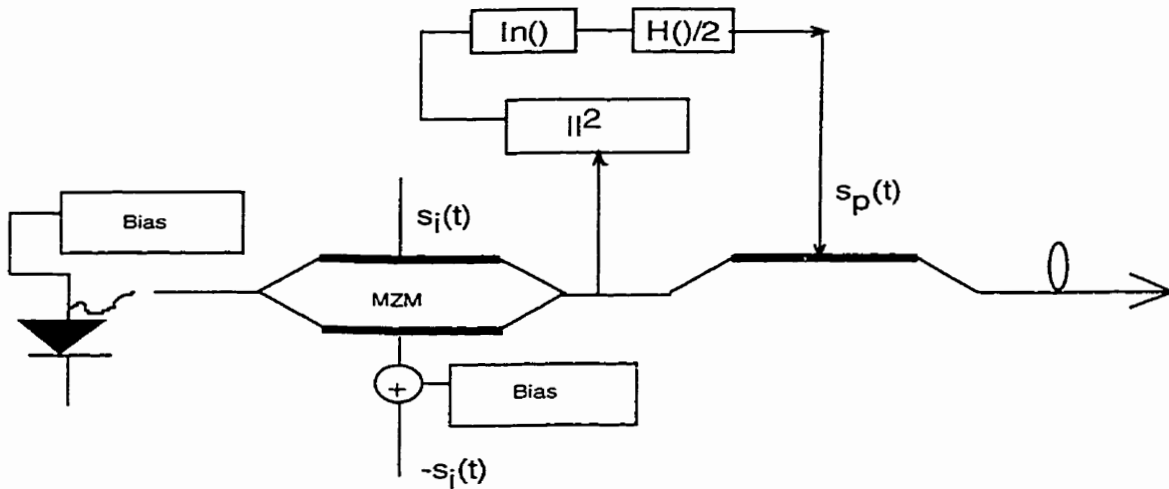


Figure 2.36. MZM/phase modulator modified for MZM non-linear distortion.

Obviously this method has a dependency on the modulator order. It could not be applied in the laser FM/MZM device above. For the purpose of simulation only, the circuit in Figure 2.31 is used. In all practical cases in the following chapters, different circuits are used and will be outlined as required. The simulation parameters for the MZM/Phase case are shown in Table 2.4:

Bitrate	10 GB/s
Input lowpass Filter	5th Butterworth LP, $f_{c0} = 5$ GHz
Receiver Filter	None
Optical Carrier Wavelength	1550 nm
Fiber Dispersion parameter	18 ps/(nm•km)
Sampling Rate	5/bit
Receiver Demodulation	Square Law Envelope
m_{mzm} relative to V_{π}	0.1
m_p relative to V_{π}	0.1
PRBS Length	2047
PRBS Polynomial coefficients	{11,2,0}[50]
MZM phase bias	$\pi/2$

Table 2.4. Parameters for MZM/Phase simulation on dispersive fiber.

As stated previously the simulation results for the laser FM/External Amplitude modulator and the present device may be combined if it is assumed that the laser FM/phase device intensity distortion and MZM non-linear distortion are compensated. The simulated single sideband spectrum is shown in Figure 2.37.

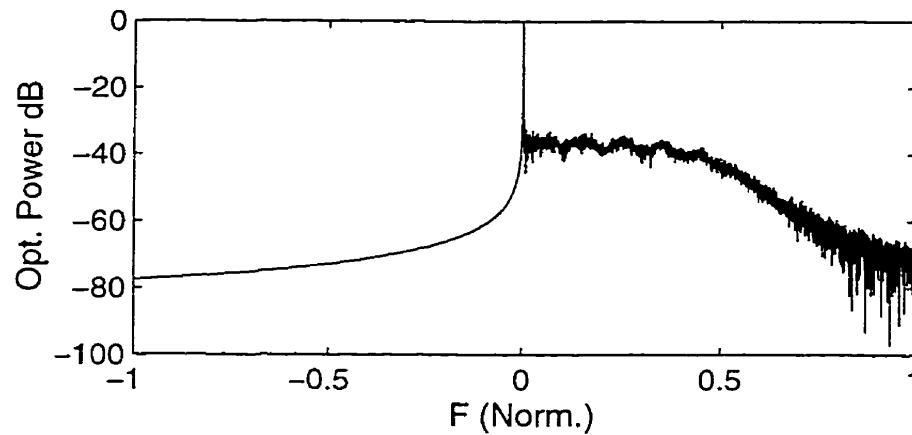


Figure 2.37. SSB electric field spectrum from MZM/phase modulator.

The post detection eye pattern at the output of the COSSB modulator for a non-dispersive line is shown in Figure 2.38.

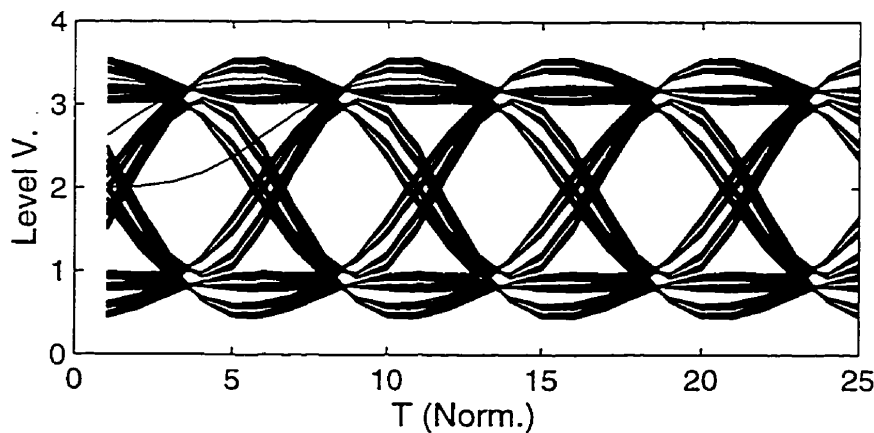


Figure 2.38. Eye pattern of envelope of SSB MZM/phase modulator at modulator output.

The post detection eye pattern for a double sideband MZM modulator after 200 km of dispersive fiber is shown in Figure 2.39.

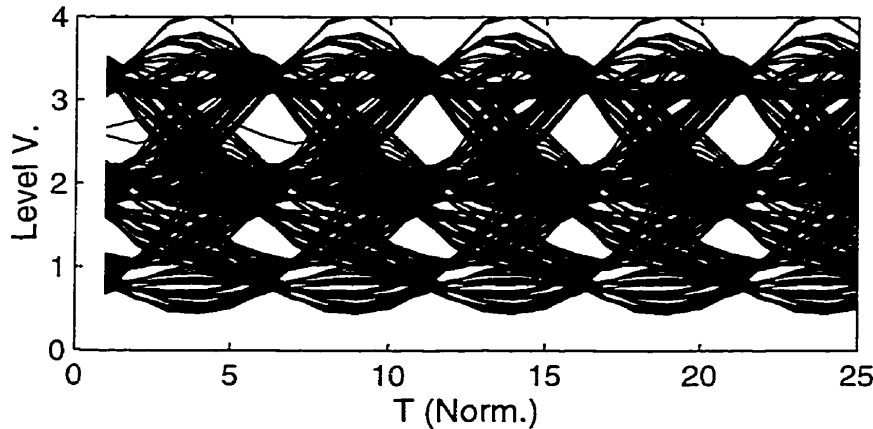


Figure 2.39. Eye pattern of envelope of DSB MZM modulator at output of square-law detector after 200 km dispersive fiber.

Finally the post detection eye pattern for the COSSB signal after 200 km of dispersive fiber is shown in Figure 2.40.

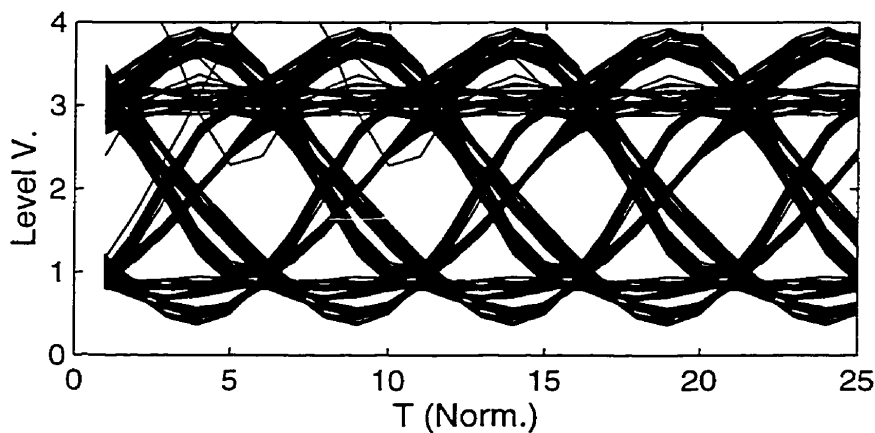


Figure 2.40. Eye pattern of envelope of SSB MZM/phase modulator at output of square-law detector after 200 km dispersive fiber.

There is a more pronounced transient artifact that settles out after a number of sweeps. This could be due to the non-linear behavior of the MZM in conjunction with the In operation. However the steady state behavior shows that the eye

diagram is greatly improved with OSSB modulation, similar to the linear modulation case with the laser/phase modulator structure and the ideal amplitude modulator.

2.6.4. Other Structures

There are likely many more variations of the basic structures outlined in this chapter depending on the type of modulator available. Phase modulation may be carried out in a dual-drive MZM by driving both arms with the same signal. Additionally the MZM may serve as a combined amplitude and phase modulator if the proper combinations of input signal are applied[52]. The above structures are addressed as a sampling of the various structures that might be available. Since this document focuses more explicitly on subcarrier optical systems no further discussion of baseband structures is undertaken.

2.7. Conclusions

It has been shown that COSSB modulation with AM compatibility is a potential tool in mitigating the effects of fiber chromatic dispersion on broadband fiber optic links. Three basic optical modulator structures have been addressed for the purpose of illustrating variations of the theory of Compatible Optical Single Sideband and indicating their usefulness to the stated purpose. Additionally addressed was the fundamental mechanism of dispersion from the perspective of a single tone modulated onto the optical carrier. This process was then logically extended to the broadband case via simulation. It was also shown as a theoretical peculiarity that subcarrier OSSB may be achieved in a single laser diode if the chirp parameter can be controlled.

3. Post Detection Equalization for Broadband Signals

3.1. Introduction

In chapter 2 it was shown that for a DSB-IMDD optical signal, the effect of dispersion distortion was a frequency selective nulling characteristic that resulted in distortion of the eye pattern of the optical link output signal. It was further shown that SSB modulation had an immediate mitigating effect on the signal due to the fact that there was no spectral cancellation effect in the detected signal. In this chapter it will be shown that further benefits available through SSB modulation are found in the fact that improved post detection equalization is possible if the signal is transmitted in COSSB format. It will be shown that dispersion compensation using identical methods at the receiver to those used to synthesize the signal at the transmitter result in improved signal quality over regular self-homodyne demodulation with subsequent equalization of the dispersion induced phase distortion. While this chapter is not meant to be an exhaustive examination of fiber chromatic dispersion compensation, it is included in the thesis since the novel method outlined is believed to be of theoretical importance to the general topic of COSSB modulation. The intent is to introduce the concept as a foundation for future work.

3.2. Dispersion Compensation

We will first analyze antidispersive filtering with self homodyne detection (AFHD) and then introduce a novel theory for post detection equalization based on minimum phase modulation[49].

3.2.1. Antidispersive Filtering with Self-Homodyne Detection

We start by observing the spectrum from a perfect linear minimum phase modulator whose complex electric field output is given by

$$E_o(t) = [1 + ms(t)] \exp\{j \cdot H_L[1 + ms(t)]\} \quad (3-1)$$

where s is the information signal, m is the modulation index and H_L is the Hilbert /ln operator as defined in Chapter 2.

An example ideal COSSB spectral plot where $s(t)$ is again a binary PRBS with modulation index of 0.7 is shown in Figure 3.1.

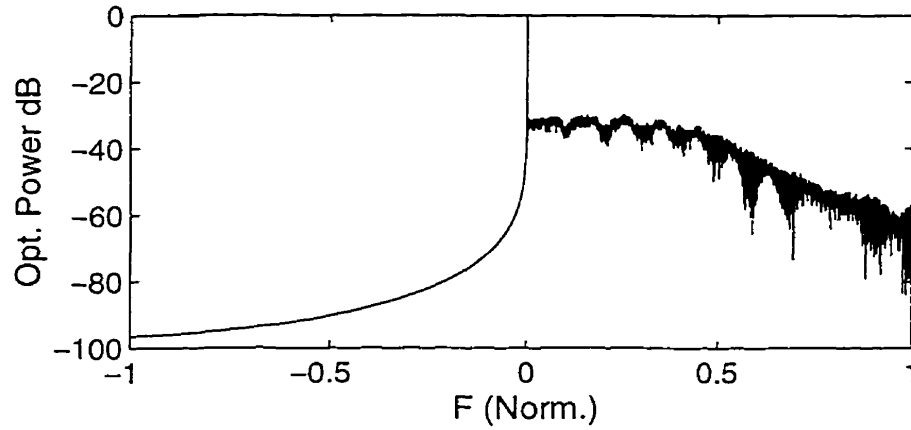


Figure 3.1. Optical electric field frequency plot for COSSB modulator.

In Figure 3.1 we see that the optical carrier component is considerably higher in amplitude than any of the following signal spectral components. Considering that the Fourier transform of the output of a square-law detector is an autocorrelation of the complex optical electric field, we can see that, for large carrier power, the detector output may be approximated by a cross correlation of an unmodulated raw optical carrier with the input signal electric field. This is equivalent to downconversion with a coherent carrier wave. This concept may be illustrated also in the time domain. Let the input to the detector be given by

$$E_i(t) = \exp(j2\pi f_0 t)(1 + ms(t)). \quad (3-2)$$

The detector output is given by

$$i(t) = (1 + ms(t))^2 \quad (3-3)$$

$$= 1 + 2ms(t) + m^2s(t)^2 \quad (3-4)$$

and if $|m^2s(t)|^2 \ll 1$ ie. m small

$$i(t) \cong 1 + 2ms(t) \quad (3-5)$$

This type of demodulation is referred to as self-homodyning [8] and it is clear that if sufficient carrier power is maintained in the received optical signal then accurate demodulation is achievable as long as no other distortion mechanisms such as chromatic dispersion are present. However, if the relative carrier power is reduced, by increasing the modulation index, the crossterm distortion in the autocorrelation distorts the signal.

In the case of COSSB modulation the self-homodyne detected signal is essentially composed of the optical single sideband spectrum translated to the origin(DC), and added to another single sideband signal with conjugate symmetry and frequency inversion from the original signal. The result is a double sideband Fourier spectrum with conjugate symmetry that produces a real signal in the time domain. The phase characteristics of the chromatic dispersion distortion is preserved in the baseband spectrum from the detector. Since the detected signal is at baseband, the dispersion distortion may be removed by filtering. This involves transmitting the detected signal through a two-port device with a similar but inverted phase response to that of the optical fiber at the optical carrier frequency. The baseband filter transfer function is given by

$$C(f) = \begin{cases} \exp\left(-\frac{j\pi D\lambda^2 f^2 L}{c}\right); & f \geq 0 \\ \exp\left(\frac{j\pi D\lambda^2 f^2 L}{c}\right); & f < 0. \end{cases} \quad (3-6)$$

The positive frequency phase response is negative to the baseband equivalent fiber transfer function to compensate the fiber induced phase distortion. The negative frequency response is inverted from the positive response since the detected signal is real with conjugate symmetry over the origin in the frequency domain. A block diagram of a self homodyne detector with antidispersive filter is shown in Figure 3.2.

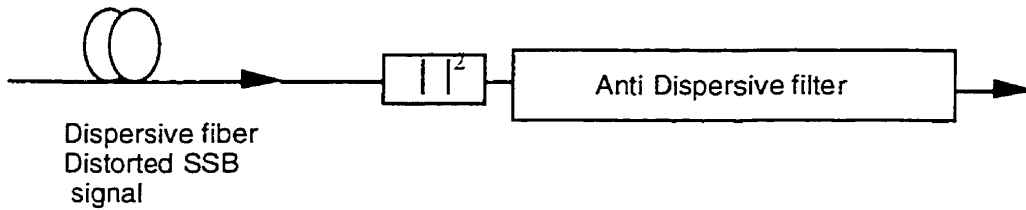


Figure 3.2. Self homodyne detector and anti-dispersive filter block diagram.

The disadvantage of this method is that a large carrier power versus signal power ratio is required for the method to work accurately. If the signal power is increased the distortion cross terms become more significant in the square-law detection process and this, coupled with dispersion distortion, renders the signal unrecoverable. The large carrier power required for self-homodyne demodulation necessitates that the signal to carrier power be small at the optical modulator. This reduces the effective signal to noise ratio at the modulator and necessarily, also at the detector.

A theoretical approach to this problem may be found in the modulated signal minimum phase characteristic. Recall that when the signal was modulated onto the optical carrier it was done so with a fixed relationship between the envelope and phase of the modulating signal. This was done to ensure envelope

detectability in the time domain and single sidedness in the transfer function of the signal. As the single sided signal propagates along the fiber, it encounters dispersion distortion that affects the time dispersion properties of the information signal and the frequency domain phase properties. Since the fiber transfer function is 'all-pass', the spectral envelope of the signal will be unchanged. This begs the question of whether or not the signal has maintained its minimum phase properties after it has undergone chromatic distortion and if so can this phenomenon be exploited to achieve more effective post-detection dispersion compensation.

For the present, we will present a comparison between AFHD and a novel compensation method based on the signal minimum phase characteristic in a computer simulation. We will once again use the linear modulator from section 2.5 in Chapter 2 and simulate, for various fiber lengths, the improvement of the received signal quality with the AFHD method and the minimum phase method.

3.3. Minimum Phase Dispersion Compensator

A block diagram of the minimum phase dispersion compensator is shown in Figure 3.3.

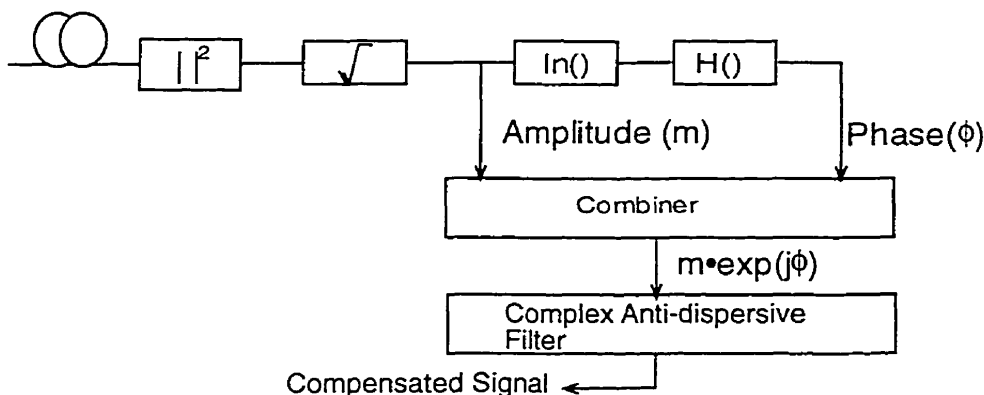


Figure 3.3. Minimum phase dispersion compensator.

The minimum phase compensator (MPC) structure could be thought of as a 'mirror' of the minimum phase modulator in which the optical electric field linear envelope (m) is recovered and preserved as the envelope portion of the detected signal. Under the minimum phase assumption the phase of the optical

electric field is recovered by the successive operation of the natural log and Hilbert Transform of the linear envelope (ϕ)[57]. The phase and amplitude signal are then combined in a polar representation of the complex *predetection* electric field, given by

$$a(t) = m(t) \cdot \exp[j\phi(t)]. \quad (3-7)$$

The complex signal is then passed through a complex antidispersive filter to remove the fiber induced distortion. The resulting signal which, is still complex, will be the corrected signal in which the original information is contained in the envelope. Since the recovered signal in this case is single sideband, the antidispersive filter transfer function is simply the inversion of the fiber transfer function:

$$C_{mp}(f) = \exp\left(-\frac{j\pi D\lambda^2 f^2 L}{c}\right); \quad f \geq 0. \quad (3-8)$$

3.4. Simulation Results

The AFHD compensation method was compared to the minimum phase compensation method in a simulation with the parameters in Table 3.1 (over). As with the simulations in Chapter 2, the input signal is a Pseudo-random binary sequence of length 2047. The sequence is again scaled and a DC offset is added to produce a positive signal. Then a phase function is added to produce the minimum phase complex envelope SSB signal. The same signal was used for the MPC and AFHD method and the simulation is meant to explore the fundamental operation of each device.

Bitrate	10 GB/s
Input lowpass Filter	5th Order Butterworth LP, $f_{c0} = 5$ GHz
Receiver Filter	None
Optical Carrier Wavelength	1550 nm
Fiber Dispersion parameter	18 ps/nm•km
Sampling Rate	5/bit
β	0.7
PRBS Length	2047
PRBS Polynomial coefficient	{11,2,0}[50]
α	1

Table 3.1. Ideal COSSB simulation parameters.

Figure 3.4 shows the eye pattern of the original signal before fiber transmission.

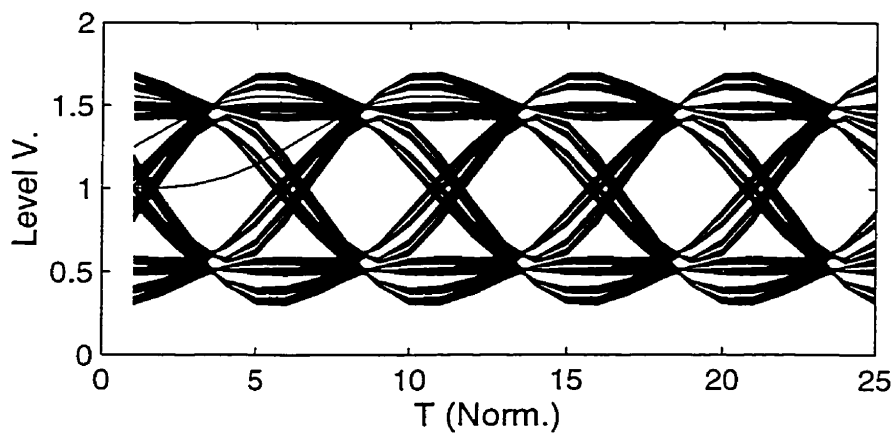


Figure 3.4. Eye Pattern For Original Data Before Transmission.

Figure 3.5 shows the eye pattern of the detected signal at 300 Km with no compensation directly at the output of an optical detector modeled as a square law device. Clearly, even though the signal is OSSB, the eye diagram is badly distorted.

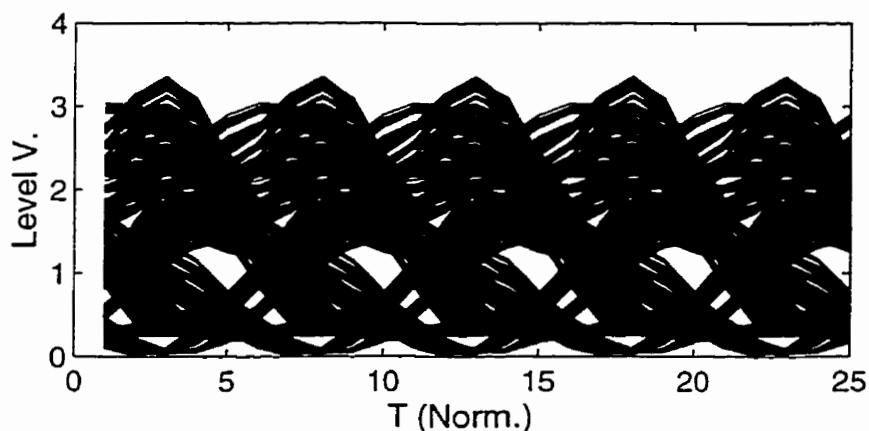


Figure 3.5. Eye Pattern for 10 GB/s 300 km dispersive Fiber COSSB signal - no compensation.

Figure 3.6 shows the eye pattern of an SSB signal at 300 Km where the detected signal is enhanced via the AFHD Method.

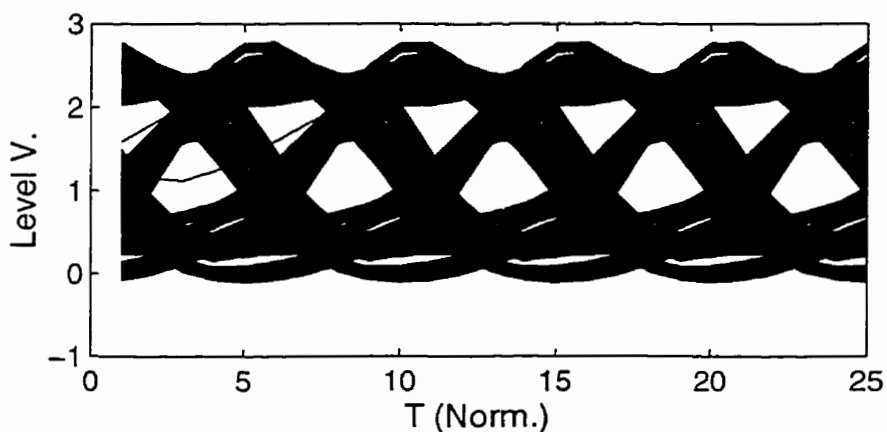


Figure 3.6. Eye pattern for 300 km dispersive fiber COSSB signal enhanced with AFHD.

Clearly the situation is improved as is shown in the larger eye openings. Figure 3.7 shows the eye pattern of an COSSB signal at 300 Km with minimum phase compensation.

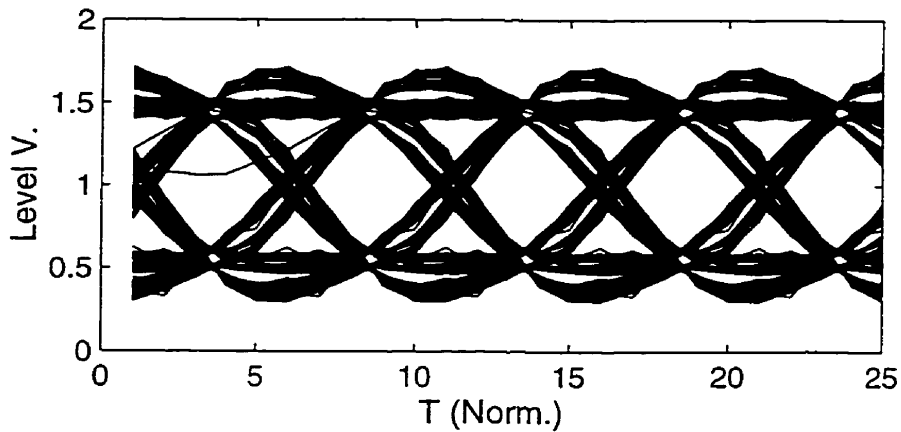


Figure 3.7. Eye pattern for 300 km COSSB signal - minimum phase compensation.

Figures 3.5 and 3.7 show a sequential improvement of the received signal with the respective compensation methods. The eye pattern captured using the MPC method is very close in appearance to the original data. The enhanced performance of the MPC method is indicated when the fiber length is increased to 800 Km as is shown in Figures 3.8 and 3.9.

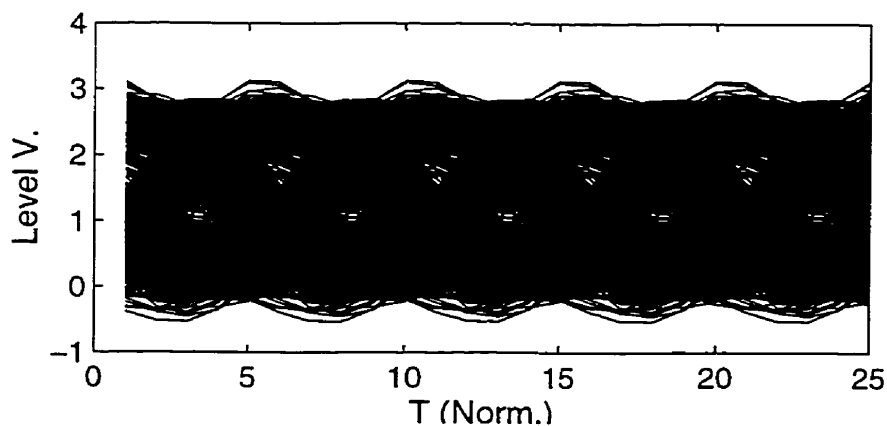


Figure 3.8. Eye pattern for 800 km dispersive fiber COSSB signal enhanced with AFHD.

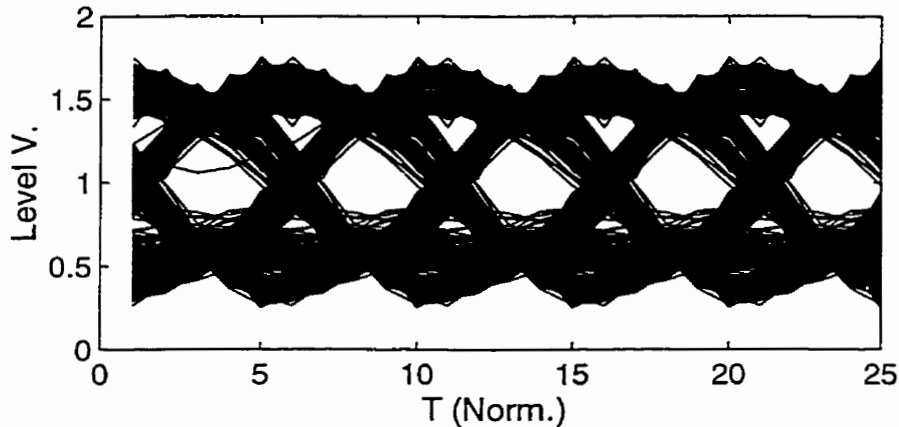


Figure 3.9. Eye pattern for 800 km dispersive fiber COSSB signal with minimum phase compensation.

In Figure 3.8 the information signal is unusable whereas in figure 3.9 the eye is open somewhat and the information is recoverable. In this simulation, the MPC method outperforms the AFHD method as a dispersion compensation method for signals with high modulation indices.

In order to explain the above compensation phenomenon it is necessary to consider the effect that chromatic dispersion has on the minimum phase characteristics of the signal as it propagates on the fiber. The simulations suggest that chromatic dispersion has a reduced effect for the fiber lengths tested on the minimum phase quality of the signal. This being the case the minimum phase relationship between the amplitude and phase of the electric field are maintained at the detector.

3.5. Theoretical Development

Rather than try to develop a comprehensive theory based on the transform characteristics of the optical fiber, it is possible to take a more general approach to the problem. We consider the trajectory characteristics of the COSSB signal and borrow some results from control theory[47]. The trajectory is a parametric

plot of the imaginary part of the signal versus the real part of the signal. For theoretical background we define a mapping of the complex variable 't' into a complex plane 'F' such that F is the response of the system Y to the stimulus 't'. In this case 't' is time and as such is real. It may however also be complex. The complex parametric plot of Y (ie Imaginary(Y) versus Real(Y)) is called the trajectory of Y. If we define the time domain minimum phase COSSB signal to be Y, it can be shown that if the trajectory of Y never encircles the origin of the 'F' plane then the number of poles and zeros in the upper half 't' plane are equal. This is a consequence of the Argument Principle in function theory which states:

"If C is a simple closed contour with positive orientation in the z plane, and f is a function that is analytic in and on C, except possibly for poles interior to C, the image Γ of C under the transformation $w = f(z)$ is a closed contour in the w plane. For a single transition over the curve C, The number of times that the contour Γ encloses the origin indicates the number of excess poles or zeros inside the contour C.[44] "

For the signal of interest in this study, it can be assumed that no poles ever exist in the upper half 't' plane and absolutely never exist on the real 't' axis (If any did exist then we wouldn't have a usable time domain signal nor would we be able to get the Fourier transform of Y) . We showed additionally in Chapter 2 that the minimum phase analytic signal may not have upper half 't' plane zeros. This plus the argument principle dictates that the trajectory of Y should not encircle the origin.

Figures 3.10 and 3.11 show the trajectories of the complex minimum phase modulating signal used for the previous simulations before and after transmission down 800 Km of dispersive fiber.

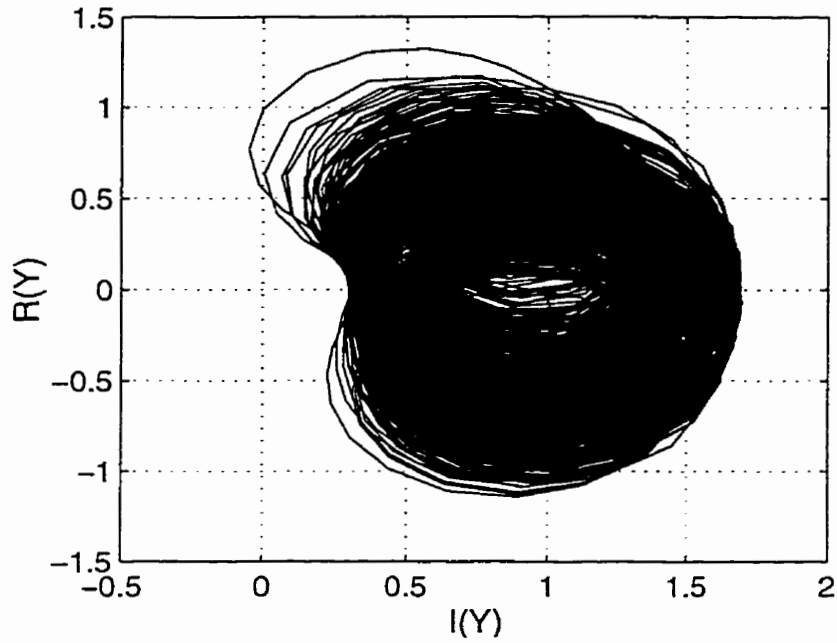


Figure 3.10. Trajectory of 10 GB/s complex minimum phase signal (parametric in 't').

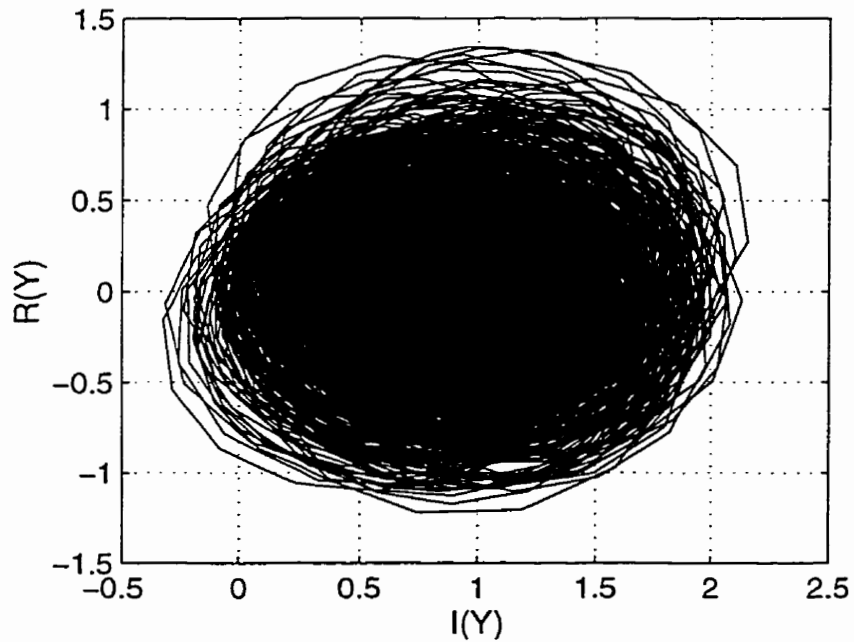


Figure 3.11. Trajectory of 10 GB/s complex minimum phase signal after transmission on 800 km dispersive fiber: $D = 18 \text{ ps}/(\text{nm}\cdot\text{km})$.

Clearly the trajectory never encircles the origin in Figure 3.10 and since there are no poles in the signal by construction, all of the zeros of the signal are in the lower half 't' plane and the minimum phase system state is confirmed. In figure 3.11, we see that the trajectory is distorted from the non-dispersed case and partially encircles the origin. This means that the signal is still 'mostly' minimum phase in the sense that only a minority of the total number of zeros in the system were shifted by the dispersion distortion so as to cause the trajectory to encircle the origin. This claim is additionally borne out by the fact that the signal is compensatable by minimum phase assumptions as shown in the above simulations. If we reduce the dispersion severity by reducing the fiber length to 600 Km as shown in Figure 3.12, the trajectory moves back to a point where there is significantly less overlap with the origin.

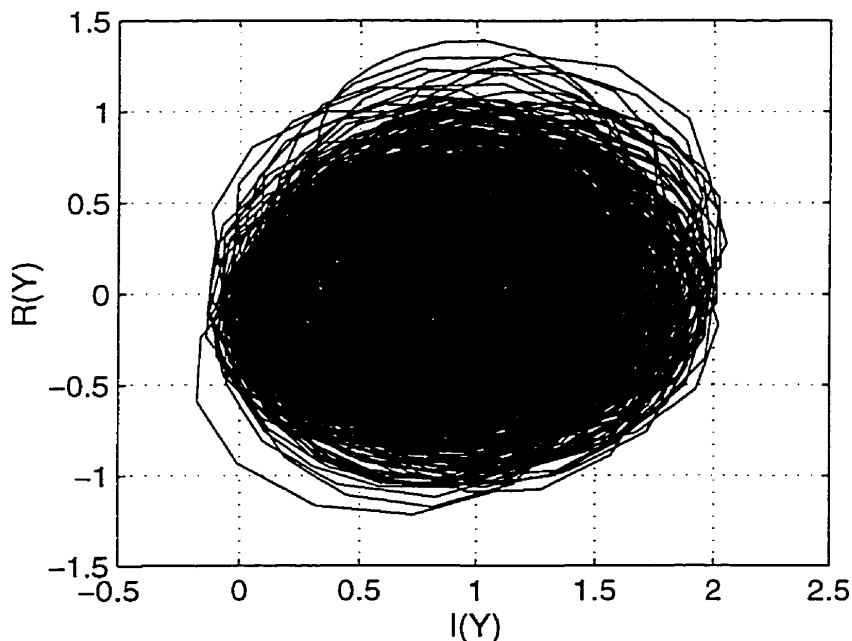


Figure 3.12. Trajectory of 10 GB/s complex minimum phase signal after transmission on 600 km dispersive fiber: $D = 18 \text{ ps}/(\text{nm}\cdot\text{km})$.

We could continue this process until the trajectory was completely removed from the origin. When this occurs, minimum phase dispersion compensation should be exact. This was illustrated in the above simulation for a 300 Km

dispersive fiber where the quality of the compensated signal was extremely close to that of the transmitted signal.

3.6. Forced Minimum Phase Condition

For the moment we consider another characteristic of minimum phase signals. In this case it is conceptually more comfortable to consider the minimum phase frequency domain signal. It can be shown that for a frequency domain minimum phase process, the corresponding time domain process recovered from the frequency domain process is minimally delayed in time. That is to say that for all time domain processes corresponding to the frequency domain processes that share the same spectral envelope but different phase characteristics, the time domain process corresponding to the minimum phase frequency domain process (which is unique in the set) will have the minimum delay of all of the time domain processes[48]. If we can show the inverse, ie if we can show that for a minimally delayed time domain sequence, the corresponding frequency domain process is minimum phase, we have a partial proof of the minimum phase compensation method.

To analyze this case, it is more convenient to use the Z transform since this reduces the problem to one of analyzing the amplitude of the zeros of a polynomial in a small circular region defined by the unit circle[48]. The condition for minimum phase in the Z transform is that all of the zeros of the transform polynomial $H(z)$ be inside the unit circle. The necessary condition for zeros inside the unit circle for real data sequences may be acquired through the Jury stability test[59]. It is possible to force a sufficient condition for a real or complex sequence by increasing the relative magnitude of the first point in the sequence relative to the following points. Let a causal sequence be given by

$$s(t) = \{h_i\}_{i=0}^N. \quad (3-9)$$

The Z transform of h is given by

$$H(z) = \sum_{i=-\infty}^{\infty} h_i z^{-i} \quad (3-10)$$

and if h is of finite length then

$$H(z) = \sum_{i=0}^N h_i z^{-i} \quad (3-11)$$

As in the Jury stability test, information about the roots of the polynomial in 3-11 may be gained from the polynomial coefficients. The condition required for sufficiency that all the zeros are inside the unit circle is that

$$|h_0| > \sum_{i=1}^N |h_i|, 1 > \sum_{i=1}^N \left| \frac{h_i}{h_0} \right|. \quad (3-12)$$

This can be proven by considering that, for the case of a root of (3-11):

$$\sum_{i=0}^N h_i z^{N-i} = 0. \quad (3-13)$$

For any system the Schwarz Inequality must hold[37]. Assuming $h_0 = 1$,

$$1 = \left| \sum_{i=1}^N h_i z^{-i} \right| \leq \sum_{i=1}^N |h_i| |z|^{-i}. \quad (3-14)$$

Now say we constrain the system such that

$$\sum_{i=1}^N |h_i| < 1. \quad (3-15)$$

Now consider that case of zero on or outside the unit circle, $|z| \geq 1$,

$$1 \geq |z|^{-1} \geq |z|^{-2} \geq \dots |z|^{-N}.$$

However if $\sum_{i=1}^N |h_i| < 1$ then (3-14) can't be true[58]. Therefore $\sum_{i=1}^N |h_i| < 1$ is a sufficient condition such that h_n produces a minimum phase sequence as its transform. Since the constraints impose conditions only on the amplitude of the signal, any phase function may be applied to the sequence and a minimum phase system always results. Relating this result to the delay characteristics of the signal we can say that adding a large component to the signal at the origin (making h_0 larger relative to the other components) has the effect of reducing the delay of the overall sequence. Thus by controlling the delay of the signal we can ensure that the z-transform of the signal is always minimum phase.

Relating this result to the optical signal of interest, we may set the sufficient condition for minimum phase in the time domain signal by setting the component at the origin in the frequency domain representation of the time domain signal (the DC coefficient) to a value whose absolute magnitude is greater than the sum of the absolute magnitudes of the all of the non DC components. This will ensure the signal will strictly be minimum phase in the time domain irrespective of the phase distortion imposed on the signal in the frequency domain by chromatic dispersion. Consequently the complete signal will always be recoverable from the detected envelope. The apparent problem encountered in the case where the phase portion of the signal is extracted from the envelope in the manner prescribed in Chapter 2 for COSSB signals, is that while we can force COSSB conditions on a sequence by ensuring that it is always positive and combining it with a phase signal that is extracted from the Hilbert(log) of the signal, this doesn't ensure that we meet the condition in (3-15). Consider the case of the COSSB signal with a large modulation index. A close-up of the resulting trajectory near the origin is shown in Figure 3.13. The non encirclement of the origin indicates that the system is minimum phase. However if we test the data according to (3-14) in the frequency domain we would find that the absolute value of the DC coefficient is much less than the sum of the absolute values of the non-DC coefficients.

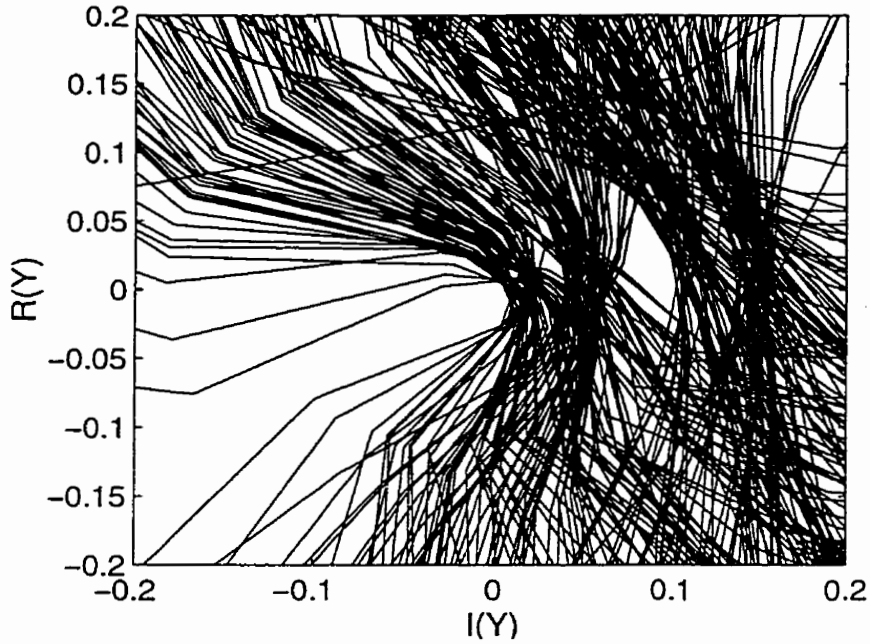


Figure 3.13. Trajectory of minimum phase signal with large modulation index

Since this violates the sufficiency condition in (3-15), the COSSB signal is conditionally minimum phase. To illustrate this we separate the signal into two factors: the real factor that we have been referring to as the envelope and the complex factor that is composed of the phase term. Say we take an arbitrary real signal $s(t)$ which is bipolar and add a DC level and a very small imaginary component to the signal so that the resulting signal trajectory never encircles the origin. In a way we have satisfied the argument principle since the 'trajectory' of this real signal never encircles the origin and therefore has no UHP zeros. When the COSSB phase factor is included, the trajectory associated with the information signal is simply rotated back and forth around the origin as dictated by the phase argument. The composite phase accrued never amounts to a total encirclement of the origin and the fact that the trajectory never crosses the origin due to the imposed DC offset means that the signal complies with the argument principle.

When the phase of the Fourier Transform of the signal is distorted by chromatic dispersion the relationship between the 'information' and the DC offset is disrupted. Coherent phase conditions may arise where the real factor of the COSSB signal actually becomes negative causing the trajectory to cross over or wrap around the origin causing some of the zeros to appear in the UHP. This destroys the fixed relationship between the amplitude and phase of the signal. This in turn degrades the dispersion compensation method. This process is gradual as the number of origin encirclements of the signal trajectory increases with increasing dispersion distortion. This explains why, it was observed in simulation, that improvement of the compensation method degrades for larger modulation indices as the dispersion increases whether due to fiber length or severity of the dispersion on the fiber. This indicates that there are degrees of advantage of compensation in the case of the AFHD and the MPC method. It appears that MPC works better than the AFHD method but both methods are eventually defeated by large modulation indices and extreme dispersion on the fiber.

This fact suggests that for the method to have use in a practical setting a metric must be established for determining what magnitude of modulation index is appropriate for a given fiber length. Determining this metric is straightforward but will be dependent on the type of modulation, filter methods, bit rate and other factors. For now we can conclude that for moderate modulation indices and fiber lengths, the method can outperform antidispersive equalization with self homodyne detection. Further, this will only be of interest in broadband communication since phase correction is not required in subcarrier transmission as will be shown in later chapters. It is then left for further study that this method be fully characterized from a theoretical standpoint to establish the mechanism of compensation and the exploitation for a given modulation scheme and fiber length.

3.7. Conclusions

It is conceded that much more could be said about this topic, however to advance beyond the present would require development well beyond the scope of this study. Concluding, it has been shown through simulation and some theory that dispersion compensation of COSSB signals based on exploitation of the minimum phase characteristics of the transmitted optical signal is possible. This has been shown in simulation for a simple case. This means that signals might be sent with higher modulation indices relative to the optical carrier component. Gaining a solid theoretical grip of this method would require specific graphical analysis of the method to determine the tradeoffs between signal complexity, modulation index and fiber dispersion compensation is possible. Nevertheless the exercise is merited by the potential signal quality improvements that may be achieved.

4. Subcarrier Optical Single Sideband: Transmission Characteristics

4.1. Introduction

In this chapter the focus is on the theoretical issues associated with the transmission of subcarrier signals on dispersive fiber. The discussion in Chapter 2 relating to dispersion effects on optical broadband signals will be reviewed and expanded upon to illustrate implications of chromatic dispersion on subcarrier systems. Since the synthesis of single sideband signals using the theory of COSSB signals was established in Chapter 2 for the general case of broadband optical modulation signals, no attempt will be made to verify the theory for subcarrier signals. Instead the theory will be modified to attain more realizable structures for subcarrier modulation. The functionality of the three modulator structures investigated in Chapter 2 will then be addressed from the subcarrier transmission perspective. The non-linear characteristics of optical modulators that may be exploited for achieving frequency translation, will be investigated within the context of increasing the implementation efficiency of optical links for radio service delivery. Simulation results for each modulator structure for linear and non-linear harmonic subcarrier modulation will also be presented.

4.2. Chromatic Dispersion and CW Subcarrier Signals

In Chapter 2, it was shown that, while the essential mechanism of fiber dispersion distortion on IMDD fiber links is similar for baseband and subcarrier processes, the resulting distortion is different. Frequency selective fading is observed in the detected signal spectrum for broadband modulating. Subcarrier signals display a complete periodic power fading of the detected signal as a function of fiber length. A common term used in radio science to describe this type of uniform destruction of the signal power across the entire signal spectrum is 'flat fading'. This term will be used in the present examination with the qualification that the underlying mechanism is different that of the radio channel

process. Shown again for convenience is the result of the derivation in Chapter 2 that captured the expression for the detector current from an IMDD link modulated, in DSB mode, with a sinusoidal modulating signal:

$$\begin{aligned}
 I_{DF1}(t) &\propto \left[\cos\left(2\pi f_c t + \frac{\pi L \lambda_0^2 D f_c^2}{c}\right) + \cos\left(2\pi f_c t - \frac{\pi L \lambda_0^2 D f_c^2}{c}\right) \right] \\
 &\propto \cos\left(\frac{\pi L \lambda_0^2 D f_c^2}{c}\right) \cos(2\pi f_c t)
 \end{aligned} \tag{4-1}$$

where L is the fiber length, λ_0 is the optical wavelength D is the dispersion parameter, c is the speed of light in a vacuum and f_c is the modulation frequency of the input sinusoid. Figure 1.6 is reprinted as Figure 4.1 for convenience and shows the simulated detected power, corrected for fiber attenuation, versus fiber length for an 18 GHz CW subcarrier modulated in DSB-AM fashion on a 1550 nm optical carrier with $D = 18$ ps/(nm•km).[21]

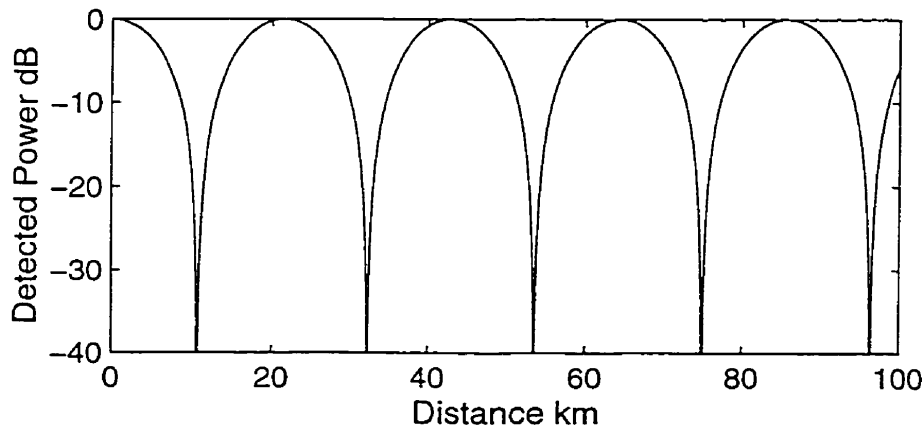


Figure 4.1. Simulated detected power as a function of dispersive fiber length, $f_c = 18$ GHz, $D = 18$ ps/(nm•km), $\lambda_0 = 1550$ nm.

At approximately 11 km (and afterward at multiples of approx. 22 km) the detected signal goes into a deep fade. Also noted is the fact that the detected power is a function of sinusoid frequency f_c , dispersion parameter D , and to a certain extent, optical wavelength (see Appendix B). If, for example the

subcarrier frequency was doubled, all other parameters held constant, the density of the nulls as a function of fiber length in Figure 4.1 would increase by a factor of 4 due to the square law relationship with frequency in equation (4-1).

It was additionally shown in Chapter 2 that if one of the optical spectrum sidebands was removed before detection by the use of single sideband modulation, the detector output current would be proportional to either the upper or lower sideband given by

$$I_{DF1}(t) \propto \cos\left(2\pi f_c t + \frac{\pi D \lambda_o^2 f_c^2 L}{c}\right) \text{ or } \cos\left(2\pi f_c t - \frac{\pi D \lambda_o^2 f_c^2 L}{c}\right) \quad (4-2)$$

for which the detected power at the fundamental frequency would be constant with fiber length, frequency, and all other parameters.

4.2.1. Non-Ideal OSSB

The compensating effect of subcarrier OSSB is a very robust process in the sense that it is not necessary to completely remove the upper or lower sideband in the optical electric field to achieve significant improvement of the detected power as a function of fiber length. If one of the optical sidebands (in this case the lower sideband) was reduced by a factor $\rho < 1$, rather than completely removed, the detector output current would be proportional to

$$I_{DF1}(t) \propto \left[\cos\left(2\pi f_c t + \frac{\pi L \lambda_o^2 D f^2}{c}\right) + \rho \cos\left(2\pi f_c t - \frac{\pi L \lambda_o^2 D f^2}{c}\right) \right]. \quad (4-3)$$

Using trigonometric identities and normalizing to the maximum value, the detected subcarrier power would be proportional to

$$W \propto \frac{1}{(1+\rho)^2} \left[1 + \rho^2 + 2\rho \cos\left(\frac{\pi 2L \lambda_o^2 D f^2}{c}\right) \right]. \quad (4-4)$$

For $\rho = 1$, the power would vary as in Figure 4.1. The benefit of partial OSSB is shown by example. Say that $\rho = 0.2$, the detected power as a function of fiber length for $D = 18$ ps/nm•km, $f = 18$ GHz, $\lambda_0 = 1550$ nm is shown in Figure 4.2 compared to the detected DSB power.

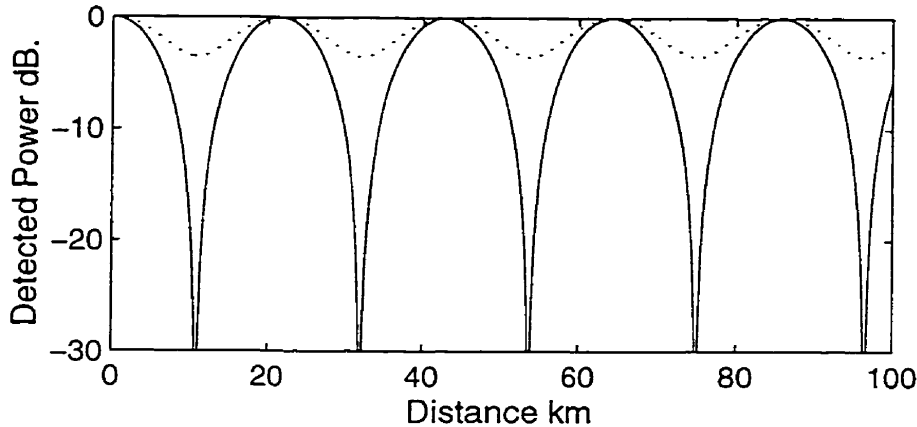


Figure 4.2. Normalized detected power as a function of fiber length for DSB ($\rho = 1$ - solid) And $\rho = 0.2$ (dotted).

Figure 4.2 shows that reduction in amplitude of one of the sidebands in a DSB optical E-field by a factor of 0.2 or 14 dB in optical power results in a fluctuation in detected power versus fiber length of only 4 dB. This indicates that sideband cancellation need not be perfect to achieve significant improvement in detected power characteristics. The practical implication of this fact is that non-ideal modulator behavior such as finite extinction ratio in the MZM or temperature drift will have negligible effect on the performance of the modulators in an subcarrier SSB application.

4.3. Finite Bandwidth Subcarrier Signals

4.3.1. Double Sideband Modulation

For DSB modulated subcarriers the issue of signal bandwidth is important from the perspective of modeling the detected power fading process as flat or frequency selective. Consider the modulated sinusoid

$$s(t) = r(t) \exp[j2\pi f_c t] \quad (4-5)$$

whose Fourier transform is non-zero valued for a section of spectrum spanning $(f_c - \Delta f/2)$ to $(f_c + \Delta f/2)$ where Δf is the signal bandwidth. When we modulate an optical carrier with this signal in DSB mode and then observe the fading characteristics we can define the departure point from CW fading for increasing signal bandwidth as the point at which the difference in fade characteristics at the upper and lower bandedges in the detected signal exceeds a specified value. Assuming perfect self-homodyne demodulation of the subcarrier signal from the optical carrier, the detected power characteristics for the individual Fourier components at the bandedges follow equation (4-1). The difference in normalized power as a function of fiber length for the bandedge components is given by

$$\Delta W_{dB} = \cos^2 \left(\frac{\pi L \lambda_o^2 D \left(f_c - \frac{\Delta f}{2} \right)^2}{c} \right) - \cos^2 \left(\frac{\pi L \lambda_o^2 D \left(f_c + \frac{\Delta f}{2} \right)^2}{c} \right) \quad (4-6)$$

where Δf is the signal bandwidth. When we calculate this value and normalize it to the maximum detected power, this measure may be referred to as 'flatness'. Equation (4-6) may be represented by a product of sinusoids as in

$$\Delta W_{dB} = \sin \left(\frac{2\pi L \lambda_o^2 D \left(f_c^2 + \frac{\Delta f^2}{4} \right)}{c} \right) \sin \left(\frac{2\pi L \lambda_o^2 D (\Delta f)}{c} \right). \quad (4-7)$$

For large subcarrier frequencies ($f_c > 10$ GHz) the second term in equation (4-7) varies much more slowly than the first term with fiber length and determines the local maximum deviation in bandedge power for a given fiber length. The spectral flatness parameter defined to quantify the power deviation at the detected signal bandedges as a function of fiber length may then be given by

$$\Phi(L) = 10 \log_{10} \left[1 - \left| \sin \left(\frac{2\pi L \lambda_0^2 D(\Delta f)}{c} \right) \right| \right]. \quad (4-8)$$

Setting maximums of $L = 100$ km and $\Phi = -1$ dB (which represents a standard flatness specification for filters), for $D = 18$ ps/nm•km and $\lambda_0 = 1550$ nm, the required bandwidth is 2.28 GHz. For subcarrier signal bandwidths exceeding this value the fading is termed frequency selective, whereas if the bandwidth is less than this value the fading behavior is termed flat. Recalling the discussion in Chapter 1 regarding the general bandwidth requirements for radio broadband delivery schemes, it was stated that total bandwidth allocations in Canada and the US are on the order of 0.5 - 1 GHz for multiservice delivery. Considering that any individual service within these allocations would necessarily be less than the total allocation, the above calculation would suggest that a flat fading assumption would accurately characterize all of the signals of interest in the present study.

4.3.2. Single Sideband Modulation

In Chapter 2 it was shown that the frequency selective fading effect brought about by dispersion on IMDD links was completely mitigated by OSSB modulation. It follows that the dispersion effect is similarly extinguished on subcarrier links. Since the fading (flat or frequency selective) is removed, the notion of spectral flatness defined in the previous section is no longer pertinent. In the OSSB case, and assuming that the optical carrier is well away from the dispersion minimum (see Appendix B), the fading problem is replaced by an excess phase shift across the signal band that follows a squared frequency behavior. This is due to the dispersion transfer function of the fiber given by equation (2-66) shown again for convenience

$$\Delta(f) = \exp \left(\frac{j\pi D \lambda_0^2 f^2 L}{c} \right) \quad (2-66)$$

where the parameters are defined as in equation (4-1). A development of this formula is given in Appendix B. In this case the nature of the phase distortion across band is used to determine the signal bandwidth. It is difficult to quantify this parameter due to the fact that some modulation schemes will be more vulnerable to this type of phase distortion. However for the signal bandwidths of interest in this document (0.5 - 1 GHz) it can be shown that if there is no significant change in the fading characteristics across the information band there is no significant change in the excess phase shift across the band[60]. For this reason the excess phase shift due to dispersion effects is assumed to be small and its effects on the detected signal are negligible.

Since the phase distortion is linear and as such appears as pure delay in the time domain detected signal, single sideband modulation serves as a stand-alone compensation for narrowband OSSB subcarrier signals. With the above assumption of linear phase distortion, once the narrowband OSSB subcarrier signal is detected it is theoretically fully compensated for dispersion effects and, unlike the broadband OSSB signals investigated in Chapter 2 and 3, no further dispersion compensation is required. It is noted, however that if the subcarrier information bandwidth exceeds the limit under which the dispersion may be modeled as linear phase distortion (ie. the argument of (2-66) is small), then the subcarrier information signal will be distorted in a similar manner as was shown for broadband signals in Chapters 2 and 3.

4.4. Subcarrier Hilbert Transforms

Hilbert Transforms for narrowband subcarrier processes are much easier to achieve than baseband processes. This is due to Bedrosian's Theorem [61] which states that the analytic signal associated with the non-analytic product of two signals may under certain conditions, be the product of one signal and the analytic signal associated with the other signal. Defining the operation performed on a non-analytic signal to produce its analytic signal to be $A[.]$, the theorem may be written as

$$A[s_1(t)s_2(t)] = s_1(t)A[s_2(t)]. \quad (4-9)$$

The required conditions under which (4-9) is true relate to the non-existence of negative frequencies in the spectrum of the analytic signal. If $s_2(t)$ is a sinusoid as in

$$W(t) = s_1(t) \cos(2\pi f_c t), \quad (4-10)$$

then

$$A[W(t)] = s_1(t) \{ \cos(2\pi f_c t) + j \sin(2\pi f_c t) \} = s_1(t) \exp\{j2\pi f_c t\}. \quad (4-11)$$

The Fourier transform of $s_1(t)$ is given by $S_1(f)$ so the Fourier transform of (4-11) is given by

$$S_{A[W]}(f) = S_1(f - f_c) \quad (4-12)$$

where $S_1(f)$ is the Fourier transform of $s_1(t)$. As long as $S_1(f)$ is bandlimited to $|f| < f_c$, (4-12) will have no negative frequency content which means that its inverse Fourier transform must be analytic. Following the proofs in Chapter 2 regarding the analytic signal, the real and imaginary parts of (4-11) must be Hilbert Transforms.

4.5. Linear Subcarrier OSSB Hybrid Modulators

The three modulator structures outlined in Chapter 2 will now be addressed from the perspective of linear OSSB subcarrier modulation.

4.5.1. Laser intensity Modulator with Cascaded External Phase Modulator

The ideal (chirpless) laser phase OSSB modulator will be dealt with first. From Chapter 2, the normalized output e-field complex envelope of the OSSB laser/phase device is given by

$$E(t) = \sqrt{1 + ms(t)} \exp \left[jm_p \frac{H_L[1 + ms(t)]}{2} \right] \quad (4-13)$$

where $s(t)$ is the information signal, m and m_p are the laser and phase modulation indices respectively. It was shown in Chapter 2 that effective COSSB behavior could be achieved for certain signals without the \ln operation in the phase term. Following this, the most obvious simplification in the laser/phase cascade modulator is to remove the log operation in the $H_L(\cdot)$ operator. This gives

$$E(t) = \sqrt{1+ms(t)} \exp[jm_p H[1+ms(t)]]. \quad (4-14)$$

Since a DC offset has no effect in the Hilbert transform, it may be removed giving

$$E(t) = \sqrt{1+ms(t)} \exp[jm_p H[s(t)]]. \quad (4-15)$$

The factors of m and $1/2$ have been incorporated into the phase modulation index m_p . If it is assumed that the subcarrier signal is narrowband, it may be approximated by a CW signal given by

$$s(t) = \cos(2\pi f_c t). \quad (4-16)$$

Thus (4-15) becomes

$$E(t) = \sqrt{1+m \cos(2\pi f_c t)} \exp\left[jm_p \frac{\sin(2\pi f_c t)}{2}\right]. \quad (4-17)$$

Figure 4.3 shows the simulated electric field spectrum from (4-17) with $m = 0.2$ and $m_p \sim 0.1$. The approximation for m_p is due to the Taylor approximation that may be applied in the envelope of (4-17) as will be shown.

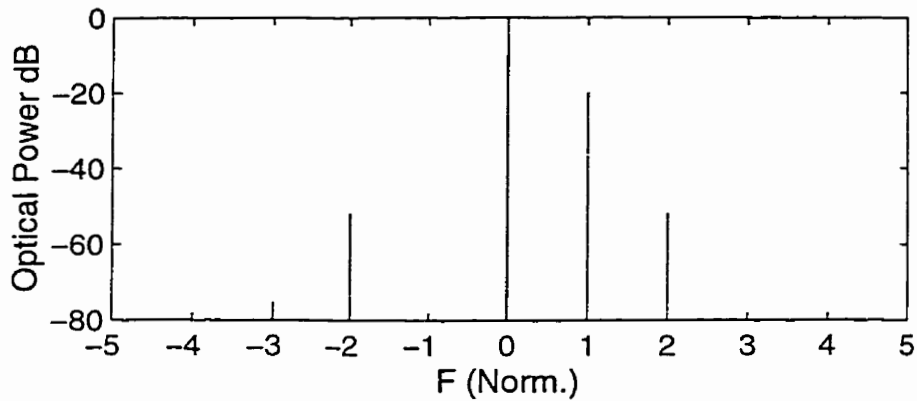


Figure 4.3. OSSB E-field spectrum for subcarrier modulated laser/phase modulator with simple sinusoid phase function with $m = 0.2$, $m_p \sim 0.1$.

There is complete signal cancellation at the lower fundamental term subcarrier. Some higher harmonic components are present but these are at relatively low amplitudes compared to the optical carrier term and the fundamental and would have insignificant effect in the detection process. A plot of the detected power versus fiber length for $D = 18 \text{ ps}/(\text{nm}\cdot\text{km})$, $f_c = 18 \text{ GHz}$, and $\lambda_0 = 1550 \text{ nm}$ is shown in Figure 4.4.

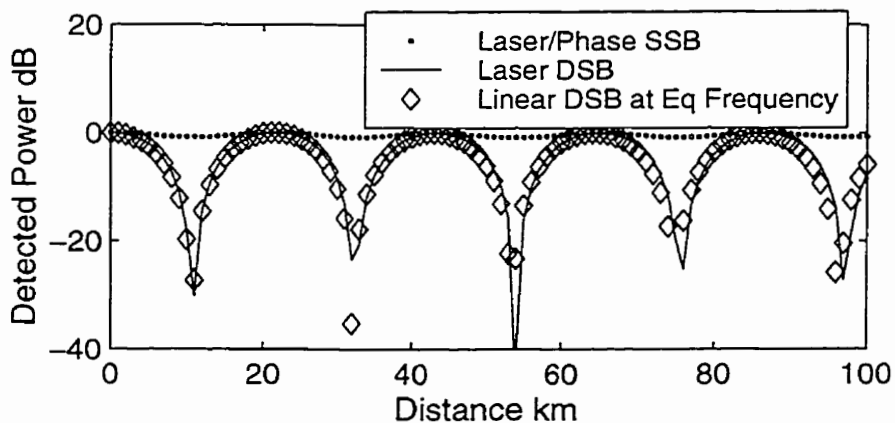


Figure 4.4. Detected power for dispersive fiber using ideal laser phase modulator with $m = 0.2$, $m_p \sim 0.1$, $D = 18 \text{ ps}/(\text{nm}\cdot\text{km})$, $f_c = 18 \text{ GHz}$, and $\lambda_0 = 1550 \text{ nm}$.

The laser double sideband plot is a simulation of a laser driven with a sinusoid with no phase modulator cascade and the linear DSB is a simulation of an ideal amplitude modulator with no cascaded phase modulator. These conditions cause the optical electric field to have equal upper and lower sidebands about the optical carrier. The nulling behavior with fiber length and associated OSSB compensation are apparent in the plot and it can be concluded that flat fading on laser diode modulator IMDD links is mitigated by OSSB modulation.

To analyze the above situation, the sinusoidal phase in (4-17) may be expanded using the identities[62]

$$\begin{aligned}\exp(ju \sin x) &= \sum_{n=-\infty}^{\infty} J_n(u) \exp(jnx) \\ \exp(ju \cos x) &= \sum_{n=-\infty}^{\infty} j^n J_n(u) \exp(jnx)\end{aligned}\tag{4-18}$$

where $J_n(\cdot)$ is the n th order Bessel Function of the first kind. Dealing with the laser E-field is somewhat more complicated due to the square root function. To simplify this task we first observe the laser characteristics for low modulation index ($m < 0.2$). Using the Taylor series approximation

$$\sqrt{1+x} \approx 1 + \frac{x}{2}; x \ll 1, \tag{4-19}$$

the laser/phase modulator expression is of the form

$$E(t) = \left[1 + \frac{m}{2} \cos(2\pi f_c t) \right] \exp[jm_p \sin(2\pi f_c t)] \tag{4-20},$$

where m is assumed to be small. Expanding the phase term we get

$$w(t) = \left[1 + \frac{m}{2} \cos(2\pi f_c t) \right] \sum_{n=-\infty}^{\infty} J_n(m_p) \exp(jn2\pi f_c t). \tag{4-21}.$$

A symbolic algebra program was used to isolate the components at the first harmonic of (4-21) to determine the interactions between the components that produce SSB in the modulator output. This was done using Mathematica[63], where the expansion of the phase term summation index was taken from -6 to 6 for a precision of 13 terms. We isolate the coefficients which multiply the upper and lower fundamental real terms about the optical carrier. The coefficient for the lower fundamental sideband was found to be

$$C_{-1} = \frac{m}{2} \left[\frac{J_{-2}(m_p)}{2} + \frac{J_0(m_p)}{2} \right] + J_{-1}(m_p). \quad (4-22)$$

For the real upper fundamental we have

$$C_1 = \frac{m}{2} \left[\frac{J_2(m_p)}{2} + \frac{J_0(m_p)}{2} \right] + J_1(m_p). \quad (4-23)$$

Table 4.1 shows the numerical values corresponding to the various harmonics

Harmonic	-2	-1	0	1	2
Lower $C_{-1} = 0$	$\frac{J_{-2}(m_p)}{2}$ = 0.0013	$J_{-1}(m_p)$ = -0.0502	$\frac{J_0(m_p)}{2}$ 0.9975		
Upper $C_1 = 0.1005$			$\frac{J_0(m_p)}{2}$	$J_1(m_p)$ = 0.0502	$\frac{J_2(m_p)}{2}$ 0.0013

$$m = 0.2, m_p = 0.1$$

Table 4.1. Harmonic components for laser/phase electric field.

Interestingly, we get interactions between higher order harmonics to achieve cancellation at the fundamental frequency. This is manifested by the order of the Bessel terms present in the coefficients. This means that the overall cancellation process required more bandwidth in the optical frequency domain than that required to contain the fundamental frequency. This doesn't represent a problem however since bandwidth in the optical substrate is abundant. This topic will be addressed further in Chapter 6.

The Laser/Phase hybrid simulation was rerun with $m = 0.8$ and $m_p = 0.443$. The optimal phase modulation index is now significant higher than the Taylor approximation in (4-19) would suggest due to the larger amplitude modulation index. At this modulation index more harmonics were observed as is apparent in a plot of the optical electric field spectrum shown in Figure 4.5.

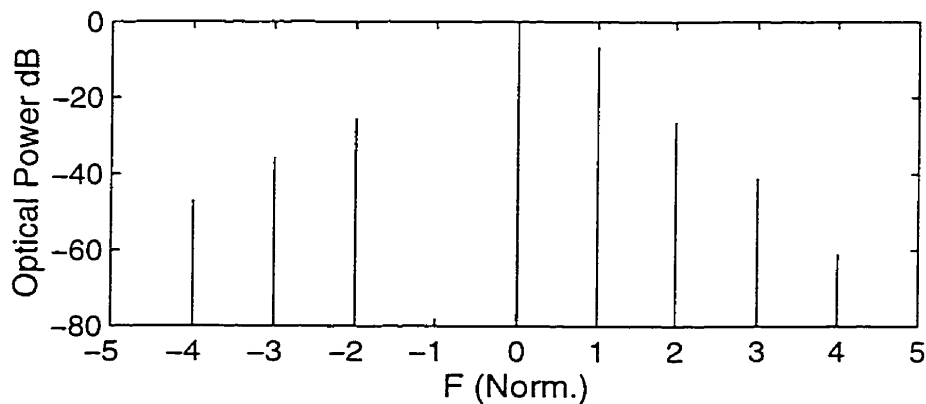


Figure 4.5. OSSB E-field spectrum for subcarrier modulated laser/phase modulator With $m = 0.8$, $m_p \sim 0.4$.

Nonetheless there is complete cancellation of the lower fundamental sideband. Figure 4.6 shows the detected power in the fundamental component versus fiber length.

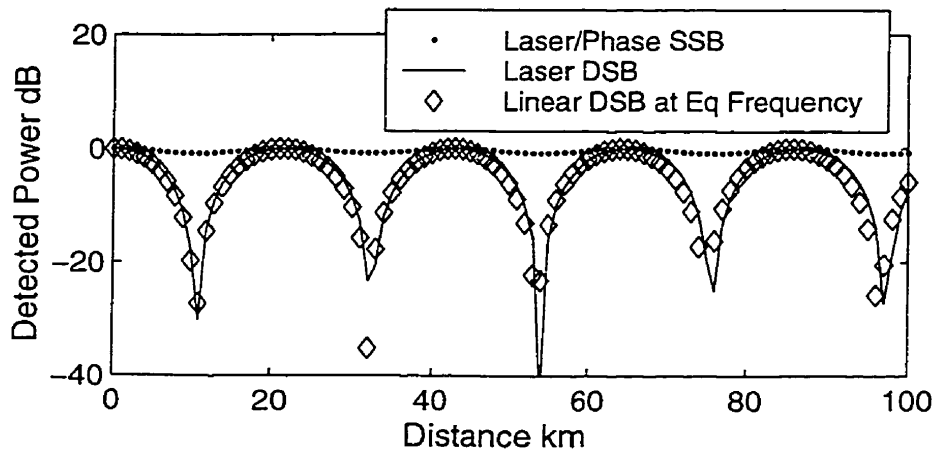


Figure 4.6. Detected power for dispersive fiber using ideal laser phase modulator with $m = 0.8$, $m_p \sim 0.4$, $D = 18 \text{ ps}/(\text{nm}\cdot\text{km})$, $f_c = 18 \text{ GHz}$, and $\lambda_0 = 1550 \text{ nm}$.

The results are only slightly different than that for the previous simulation with much lower modulation indices. An attempt was made to capture the E-field Fourier coefficients of the fundamental terms near the optical carrier; however the resulting expression was unusable in any tutorial sense due to its complexity.

The nulling behavior is similar to the low modulation index DSB and mitigation of the power fading is apparent with OSSB modulation. Thus it is shown in simulation that the nulling characteristic of a DSB laser diode subcarrier signal over dispersive fiber is mitigated by subcarrier COSSB modulation.

4.5.2. Laser FM Cascaded with MZM External Amplitude Modulator.

Since this device model was shown to be mathematically equivalent to the MZM/Phase modulator cascade, the following section on The MZM/Phase modulator cascaded device may be deemed applicable to the laser FM/ MZM cascaded device and discussion is deferred to the following section.

4.5.3. MZM Amplitude Modulator with Cascaded External Phase Modulator

The MZM/phase structure was defined in Chapter 2 and is shown again for convenience in Figure 4.7. It will be shown the MZM/Phase cascade device is a very useful structure for the present purpose due to its desirable characteristics which include good harmonic generation potential, amenity to mathematical analysis, bandwidth capability and numerous others that will be shown. Additionally it will be shown that the MZM/Phase device is mathematically equivalent to the Hartley MZM that was discussed in Chapter 2 and has been used successfully for subcarrier OSSB by other researchers as well [26].

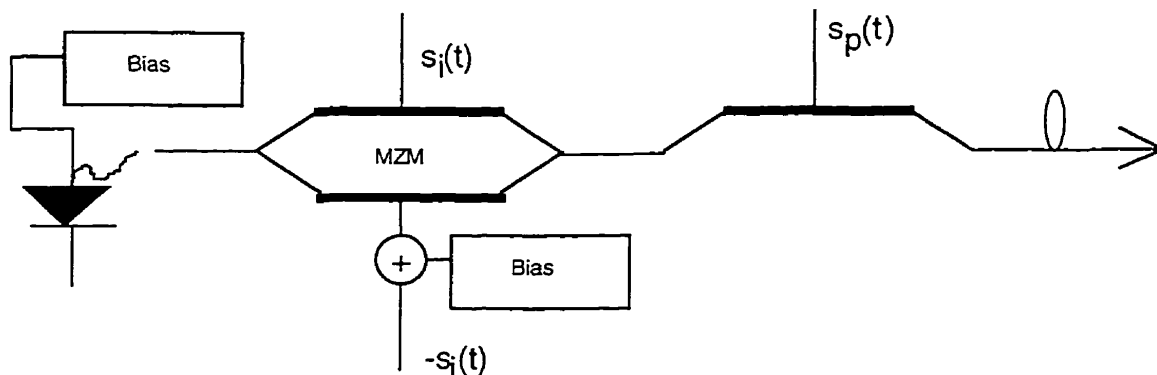


Figure 4.7. MZM/Phase COSSB modulator.

In the circuit model in Figure 4.7, the Mach-Zehnder modulator is driven with inverted signals to achieve 'chirpless' amplitude modulation. The phase modulator is driven with the Hilbert Transform of the MZM modulation signal. The complex optical transfer characteristic is given by

$$\begin{aligned}
 E_{\text{out}} &= \frac{E_{\text{in}}}{2} \left\{ \exp\left(j \frac{m\pi s_i(t)}{V_\pi}\right) + \exp\left[j\left(V_{\text{bias}} - \frac{m\pi s_i(t)}{V_\pi}\right)\right] \right\} \cdot \exp\left(j \frac{m_p \pi s_p(t)}{V_\pi}\right) \\
 &= \frac{E_{\text{in}}}{2} \left\{ \exp\left(j \frac{\pi m (s_p(t) + s_i(t))}{V_\pi}\right) + \exp\left[j\left(\frac{\pi m (s_p(t) - s_i(t))}{V_\pi} + V_{\text{bias}}\right)\right] \right\}. \quad (4-24)
 \end{aligned}$$

When $s_p(t) = \sin(2\pi f_c t)$; $s_i(t) = \cos(2\pi f_c t)$,

$$E_{\text{out}} = \frac{E_{\text{in}}}{2} \left\{ \exp\left(j \frac{\pi m \sqrt{2} \cos\left[2\pi f_c t - \frac{\pi}{4}\right]}{V_\pi}\right) + \exp\left[j\left(\frac{\pi m \sqrt{2} \sin\left[2\pi f_c t - \frac{\pi}{4}\right]}{V_\pi} + V_{\text{bias}}\right)\right] \right\}. \quad (4-25)$$

The time shift in the arguments of the cos and sin functions may be discarded. As well as the $\sqrt{2}$ factor may be incorporated into the modulation index and so the cascade MZM /phase modulator transfer characteristic may be given by

$$\begin{aligned}
 E_{\text{out}} &= \frac{E_{\text{in}}}{2} \left\{ \exp\left(j \frac{\pi m \cos(2\pi f_c t)}{V_\pi}\right) + \exp\left[j\left(\frac{\pi m \sin(2\pi f_c t)}{V_\pi} + V_{\text{bias}}\right)\right] \right\} \\
 &= \frac{E_{\text{in}}}{2} \left\{ \exp(j\pi m \cos(2\pi f_c t)) + \exp[j(\pi m \sin(2\pi f_c t) + V_{\text{bias}})] \right\}; \quad V_\pi = 1V
 \end{aligned} \quad (4-26)$$

which is equivalent to a single Mach Zehnder Modulator driven with Hilbert Transform CW signals. We refer to this modulator as a Hartley MZM due to its structural similarity to the Hartley Radio modulator from Chapter 2. It is noted that this equivalence is due only to the nature of the trigonometric identities. This equivalency does not hold for broadband optical structures. This indicates that the cascade structure, which is effective for broadband OSSB as shown in

Chapter 2, will reduce, for narrowband subcarrier modulation, to the single dual drive Mach-Zehnder modulator with Hilbert drive signals.

Noting the equivalency of the MZM/Phase device with the Hartley OSSB dual drive MZM and the fact that the subcarrier OSSB capability of the dual drive Mach Zehnder has been confirmed in the literature[26,64,65], the only simulation undertaken was a confirmation of the power compensating effects of MZM/Phase OSSB on dispersive fiber. Figure 4.8 shows the normalized detected power from the cascaded MZM/Phase OSSB device as a function of fiber length for an 18 GHz CW subcarrier signal on a dispersive fiber. The modulation index of the subcarrier drive signals relative to V_π was set at 0.2. The DSB characteristic from a single dual drive MZM with inverted sinusoidal drive signals is shown in addition to the ideal DSB amplitude modulator.

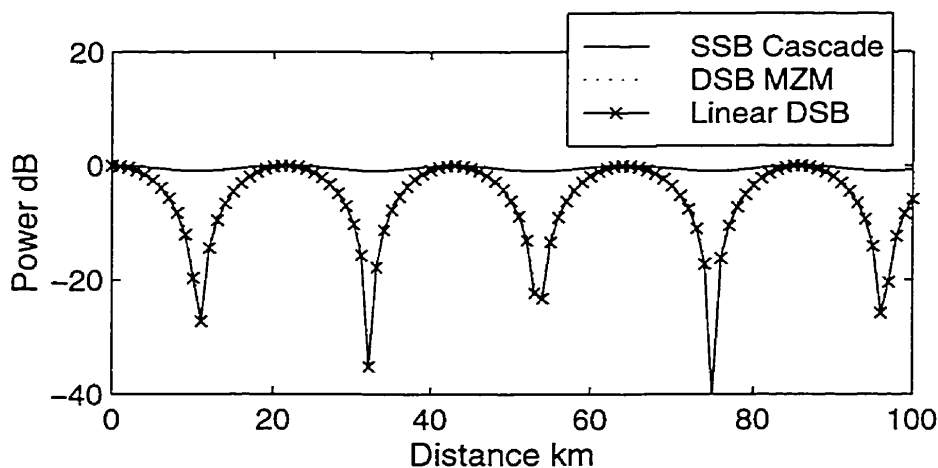


Figure 4.8. Detected power vs. fiber length for dispersive fiber using MZM/phase modulator for $m = 0.2$, $D = 18$ ps/(nm•km) and $\lambda_0 = 1550$ nm.

As with the laser/phase modulator and the linear ideal modulator, the COSSB MZM/Phase device has mitigating effects on the fiber length dependent power fading. The behavior of the DSB MZM detected power which is achieved by

driving the MZM with inverted sinusoids as function of fiber length device is very similar to that of the linear DSB from the ideal amplitude modulator.

4.6. Harmonic Generation With Optical SSB

The harmonic frequency translation potential of the hybrid optical links is now investigated. General harmonic frequency translation is carried out in two-port devices in which the transfer characteristic is inherently non-linear. A general expression for the output from such a device for a periodic input is given by

$$R(t) = \sum_{n=1}^{N-1} a_n \exp(jn2\pi f_c t) \quad (4-27)$$

where a_n is a coefficient determined by the nature of the non-linearity and f_c is the fundamental input frequency.

For a CW input, frequency translation is achieved by capturing one of the higher order output harmonics with a bandpass filter. The bandpass filter removes all but the harmonic component corresponding to the desired frequency at the network output, and so it could be said that the response of the network to the input CW subcarrier signal is one of pure frequency translation of the original signal. If, in the case of a modulated input, say a phase modulated sinusoid, the information characteristics can be preserved through the frequency translation process, a system benefit is accrued in certain situations.

There are obvious concerns relating to distortion of the input signal as is shown in the output expression for a harmonic frequency translation device for a phase modulated input given by $\exp\{j[2\pi f_c t + \phi(t)]\}$

$$R(t) = \sum_{n=1}^{N-1} a_n \exp\{jn[2\pi f_c t + \phi(t)]\}. \quad (4-28)$$

The phase information is multiplied in the same manner as the carrier term resulting in distortion. Additionally this type of signal upconversion usually precludes any sort of amplitude modulation of the input subcarrier. There are potential solutions to these issues and these will be addressed in Chapter 5.

As regards the optical devices under study, it has been shown[4-6,19] that IMDD optical links may serve as frequency translators as well as trunking elements in subcarrier optical communication systems. This is carried out by exploitation of the inherently non-linear characteristics of optical modulators and optical detectors. The method involves producing harmonics of the modulating signal about the optical carrier by driving the modulating device beyond some standard operating point such as the clip point in a laser diode, or simply using the inherently non-linear characteristics of the device as in the MZM device. The electric field then undergoes a further non-linear conversion in the square law detector where it is translated to baseband from the optical carrier frequency. The fundamental harmonic process is then the interaction of the non-linear modulator and the non-linear square law detector. The net effect of the process is that the optical link behaves as a two-port frequency translation device to which a bandpass filter may be connected to capture the required output harmonic. The link then serves the dual purpose of transporting the radio signal to the destination and translating the input radio signal to a higher carrier frequency at the detector output. This method is particularly attractive if the required output frequency is relatively high and the costs associated with local frequency translation, using microwave sources and mixers (with the associated maintenance costs), are reduced with harmonic translation. If OSSB modulation is simultaneously employed then a dispersion benefit, in a form similar to that of linear OSSB subcarrier modulation, is possible.

4.6.1. Laser/Phase Non-Linear Upconverter

The accessible non-linear mechanism in the laser that may be exploited to achieve harmonic modulation is the clipping phenomenon at the threshold point as shown in Figure 4.9.

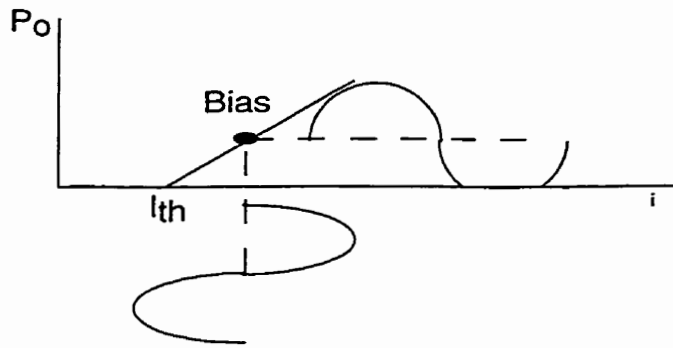


Figure 4.9. Laser transfer characteristic.

In the ideal laser device this clipping is achieved by setting the laser modulation index to a value greater than unity. This process may also be enhanced by biasing the laser close to the clipping point on the laser transfer characteristic in Figure 4.9. The positive portion of the output optical power waveform from the laser device is assumed to vary linearly with input current while the power output corresponding to input current below the threshold (which for the ideal laser model as defined in Chapter 2 is set to zero) is fixed at zero output. Thus there is a discontinuity in the ideal laser transfer characteristic at $1 + m s(t) = 0$. Simulation may be performed to aid in the analysis. Selecting $m = 1.5$, a laser diode modulated with a CW input will have harmonics in the E-Field output as shown in Figure 4.10, that will be maintained in the output of a square law detector as shown in Figure 4.11.

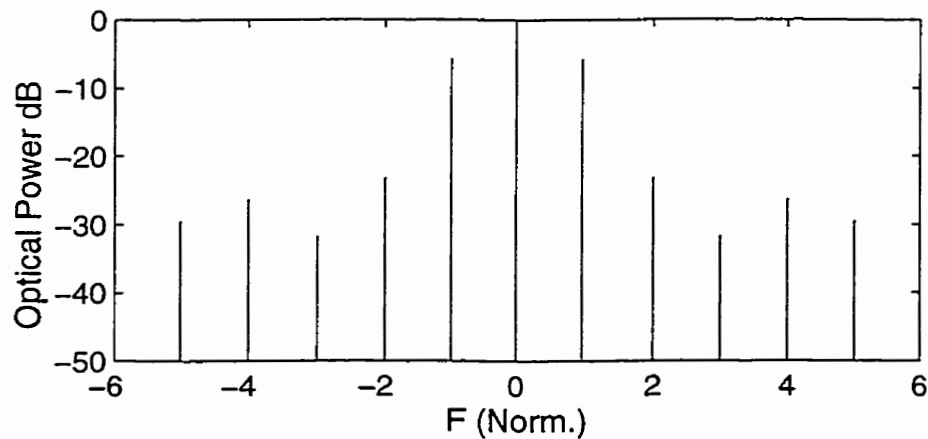


Figure 4.10. Clipped laser E-field spectrum, $m = 1.5$.

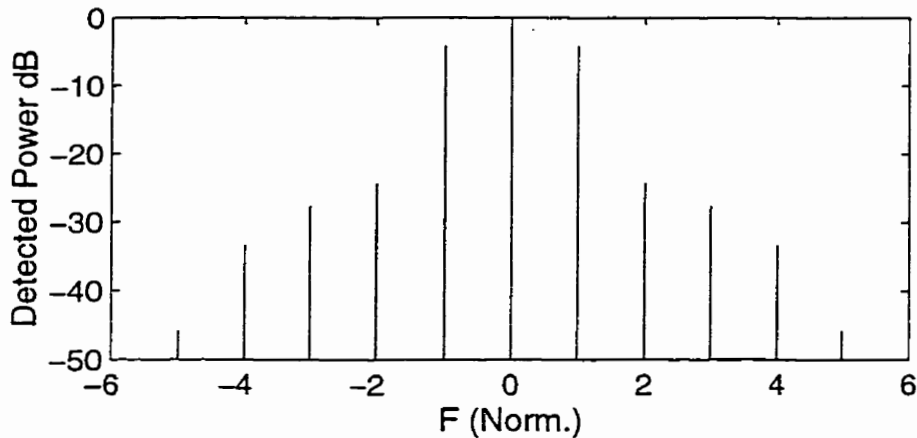


Figure 4.11. Clipped laser detector output spectrum $m = 1.5$.

While it is clear that while the laser will produce harmonics in this manner, Figure 4.11 shows that the process is rather inefficient in that the roll-off in harmonic power is quite severe with increasing frequency even for a significantly high modulation index. This indicates that the process would yield a subcarrier at the detector output that would require significant amplification to be of use in the radio channel. A more desirable situation would be to have more power distributed into the higher frequency components, and ideally concentrated at the desired harmonic in the detector output. This is not the case however, as increases in the modulation index do not produce a corresponding increase in relative harmonic power as is shown in Figure 4.12 over. Figure 4.12 shows the amplitude ratio of a set of harmonic outputs from a laser diode harmonic upconverter to the detected DC term (H_0). Since the DC term in the detector output represents the power in the optical signal this ratio is a convenient measure of the conversion efficiency of the non-linear process for any individual harmonic output component. Observing Figure 4.12, H_5 , for example represents the change in ratio of the 5th harmonic of the input sinusoid to the DC term as a function of modulation index. As expected, harmonic activity starts at $m = 1$, however as the modulation index increases, none of the

observed harmonic amplitudes exceed a factor of about -15 dB relative to the DC Output.

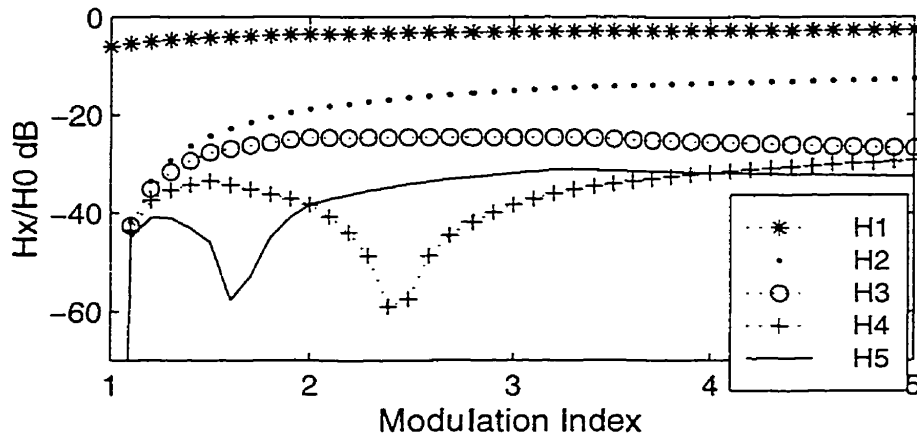


Figure 4.12. Ratio of detected harmonic amplitude to detected dc term versus modulation index from laser diode IMDD harmonic upconverter, H_x refers to harmonic order x .

As a harmonic generator, this performance is quite poor as compared to that of the other modulator structures in this study, as will be seen. This process may improve by adding an FM component to the laser characteristic to reflect the chirp non-ideality. However, preliminary analysis also indicated that attaining even marginal and predictable OSSB behavior in the optical E-field spectrum was quite difficult. Due to these issues and also to the fact that no experimentation will be performed on the laser device in this study, the investigation of the laser and laser/phase IMDD links as a harmonic generator will not be pursued any further.

4.6.2. Laser FM Cascaded with MZM External Amplitude Modulator.

Since, again, this device model is mathematically equivalent to the MZM/Phase modulator cascade, the following section on The MZM/Phase modulator cascaded device may be deemed applicable to the laser FM/MZM cascaded

device and discussion will be deferred to the following section. It should be noted that the laser clipping characteristic is not used to produce harmonics in the modulator output. Harmonics in the laser are produced by the chirp process which is modeled as a linear FM process which inherently generates harmonics. The harmonic process for the MZM is outlined in the following section.

4.6.3. Hartley MZM and MZM/Phase Modulator Cascade

Subcarrier frequency upconversion may be achieved in the Hartley MZM and MZM/Phase device through exploitation of the inherent nonlinearity in external optical waveguide phase modulators[2-6,13]. Using equation 4-26, setting $V\pi$ to unity and normalizing the fractional argument with a modulation index 'm' gives

$$E_{out} = \frac{E_{in}}{2} \left\{ \exp(jm\pi \cos(2\pi f_c t)) + \exp[j(m\pi \sin(2\pi f_c t) + \theta_{bias})] \right\}. \quad (4-29)$$

Applying a bias (θ_{bias}) so as to offset the modulating arms by $\pi/2$, the resulting expression is given by

$$\begin{aligned} E_o(t) &= E_i(t) \left\{ \exp(jm\pi \cos(2\pi f_c t)) + \exp\left(jm\pi \sin(2\pi f_c t) + \frac{\pi}{2}\right) \right\} \\ &= E_i(t) \left\{ \exp(jm\pi \cos(2\pi f_c t)) + \exp(jm\pi \sin(2\pi f_c t)) \exp\left(j\frac{\pi}{2}\right) \right\} \\ &= E_i(t) \left\{ \exp(jm\pi \cos(2\pi f_c t)) + j \exp(jm\pi \sin(2\pi f_c t)) \right\}. \end{aligned} \quad (4-30)$$

Using the identities:

$$\exp(jm \sin x) = \sum_{n=-\infty}^{\infty} J_n(m) \exp(jnx) \quad (4-31)$$

$$\exp(jm \cos x) = \sum_{n=-\infty}^{\infty} j^n J_n(m) \exp(jnx),$$

$$E_o(t) = E_i(t) \left[\sum_{n=-\infty}^{\infty} j^n J_n(m\pi) \exp(jnx) + j \sum_{n=-\infty}^{\infty} J_n(\pi m) \exp(jnx) \right] \quad (4-32)$$

whose spectrum, when m is sufficiently high in amplitude, displays an alternating cancellation of the odd harmonics starting with the lower first harmonic as shown in Figure 4.13 for $m = 0.7$.

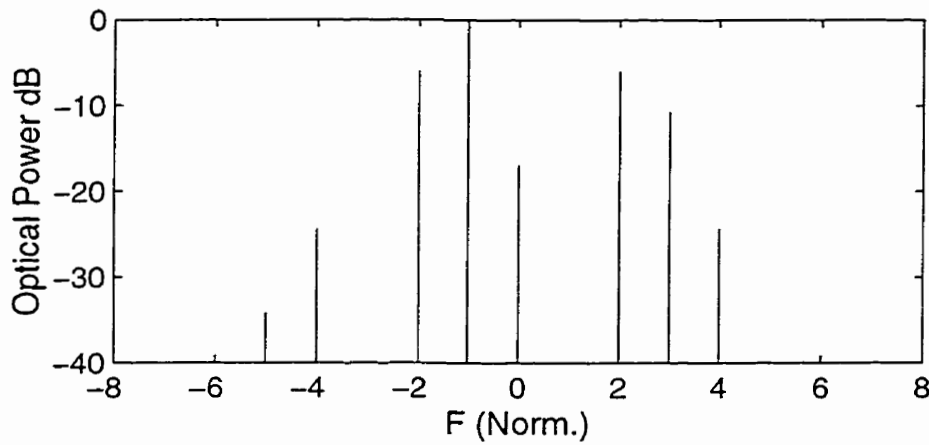


Figure 4.13. Electric field spectrum from Hartley MZM driven with sinusoids at $m = 0.7$.

The output current from a square law detector with the above input signal is given by

$$I_o \propto |E_o(t)|^2 = k \cos^2 \left[m\pi \frac{\sin(2\pi f_c t) - \cos(2\pi f_c t) - \frac{\pi}{2}}{2} \right]$$

$$\begin{aligned}
&= \frac{k}{2} + \sin[2m\pi \cos(2\pi f_c t)] \\
&= \frac{k}{2} + 2 \sum_{n=1}^{\infty} (-1)^{n+1} J_{2n-1}(2m\pi) \cos[(2n-1)f_c t]. \quad (4-33)
\end{aligned}$$

It is also noted that the detector output signal for a lone MZM driven with sign-inverted sinusoids is equivalent to the MZM/Phase since the phase term in the MZM/Phase disappears in square law detection leaving a squared amplitude differential drive MZM signal as the detector output. The detector harmonic output is shown in Figure 4.14, where it is observed that only odd harmonic components are present .

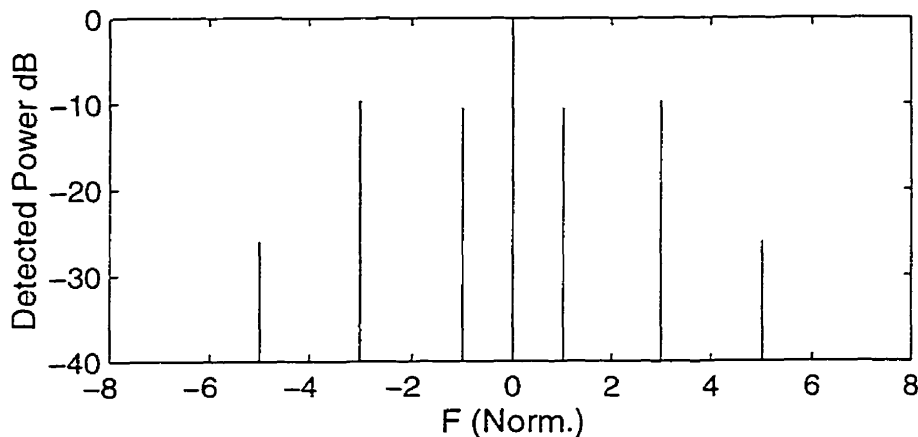


Figure 4.14. Detected photocurrent spectrum from Hartley MZM driven with sinusoids at $m = 0.7$.

It is immediately apparent from Figure 4.14 that the Hartley MZM non-linear process is quite efficient in producing harmonics in the detected signal. For a modulation index of 0.7, which is quite achievable on commercially available modulators with reasonable drive power, the harmonic power for the third and fifth order harmonics (H3 and H5) are quite significant relative to the DC output. Increasing the modulation index causes a change to the argument of the Bessel functions that represent the detector output in (4-33) which in turn causes the magnitude of the higher harmonics in the electric field to increase. Figure 4.15

shows the relative amplitude of the detected harmonics with respect to the detected DC term as a function of modulation index and it can be seen that the efficiency of the harmonic generation process of the MZM/Phase and MZM Hartley modulators is much better than the laser/phase device discussed earlier.

Additionally, unlike the laser device, the optical E-field spectrum has a characteristic behavior that is relatively easy to reconcile with the mathematical expression for the device. H2 and H4 are not present in the detector output and are omitted in the plot.

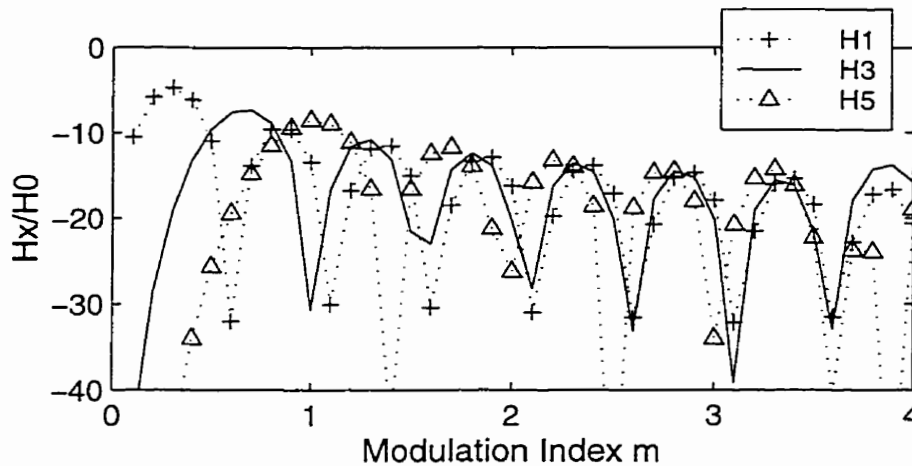


Figure 4.15. Ratio of detected harmonic amplitude to detected DC term versus modulation index from MZM/phase IMDD harmonic upconverter.

Figure 4.15 shows a more even distribution of power among the harmonic outputs with clear maxima associated with specific harmonics as a function of modulation index. Additionally the highest local maxima are situated at low modulation indices which reduces the demand on auxiliary signal drive equipment such as amplifiers.

4.7. Fiber Dispersion and Harmonic Subcarriers

4.7.1. Mathematical Model

The effects of fiber dispersion on the transmission of harmonically upconverted subcarriers is harder to analyze due to the considerably more complicated signal that is applied to the photodetector. However it has been shown that the coefficients of the harmonic components may be captured at the output of the detector [66,67]. We expand on the method of Walker et al[67]. The expression for the optical electric field with carrier is given by

$$e(t) = e_c(2\pi f_c t) \exp(2\pi f_0 t) \quad (4-34)$$

where e_c is a periodic function with fundamental frequency f_c representing the complex envelope of the optical signal. Since $e_c(t)$ is periodic, it may be represented as a Fourier Series given by

$$\begin{aligned} e(t) &= \sum_{n=-\infty}^{\infty} C_n \exp[j2\pi(f_0 + nf_c)t] \\ &= \exp(2\pi f_0 t) \sum_{n=-\infty}^{\infty} C_n \exp[j2\pi n f_c t]. \end{aligned} \quad (4-35)$$

Neglecting the optical carrier term leaves the Fourier series of the complex electric field

$$e_c(2\pi f_c t) = \sum_{n=-\infty}^{\infty} C_n \exp[j2\pi n f_c t], \quad (4-36)$$

where

$$C_n = \frac{1}{2\pi} \int_{-\pi}^{\pi} e_c(\theta) \exp(-jn\theta) d\theta \quad (4-37)$$

Recall the transfer function of the dispersive fiber complex electric field at the optical carrier is given by

$$H(f) = \exp\left(\frac{j\pi D\lambda_0^2 f^2 L}{c}\right) \quad (4-38)$$

where D is the dispersion parameter in ps/(nm•km), λ_0 is the optical wavelength in nm, f is the modulation frequency offset from the optical carrier, L is the fiber length and c is lightspeed in free space. (Appendix B). This expression is referred to as the fundamental dispersion term in the following development.

The Fourier Transform of (4-36) is given by

$$E_c(f) = \sum_{n=-\infty}^{\infty} C_n \delta[f - nf_c]. \quad (4-39)$$

Combining (4-38) and (4-39) gives

$$E_c(f) = \sum_{n=-\infty}^{\infty} C_n \exp\left(\frac{j\pi D\lambda_0^2 (nf_c)^2 L}{c}\right) \delta[f - nf_c]. \quad (4-40)$$

The inverse transform of (4-40) gives the time domain complex E-Field of the periodic function e_c on a dispersive fiber.

$$e_{cD}(t) = \sum_{n=-\infty}^{\infty} C_n \exp\left(\frac{j\pi D\lambda_0^2 (nf_c)^2 L}{c}\right) \exp[jn2\pi f_c t]. \quad (4-41)$$

Since $e(t)$ is periodic with period f_c , the photocurrent at the output of a square-law detector due to (4-41) is also periodic with period f_c and is given by

$$i(t) \propto |e_{cD}(t)|^2 = \left| \sum_{n=-\infty}^{\infty} C_n \exp\left(\frac{j\pi D\lambda_0^2 (nf_c)^2 L}{c}\right) \exp[j2\pi n f_c t] \right|^2. \quad (4-42)$$

Since (4-42) is periodic it may also be represented as a Fourier series which is generalized to

$$i(t) = \frac{1}{2\pi} \sum_{p=-\infty}^{\infty} I_p \exp(j2\pi p f_c t). \quad (4-43)$$

The coefficients of (4-43) are difficult to extract from (4-42). A simplification may be implemented by expanding the squared term in equation (4-42). Letting the fundamental dispersion term be represented by $\exp(j\phi)$ and $2\pi f_c t$ by θ , (4-42) becomes

$$\begin{aligned} i(t) &\propto |e_{CD}(t)|^2 = \left| \sum_{n=-\infty}^{\infty} C_n \exp\left(\frac{j\pi D \lambda_0^2 (n f_c)^2 L}{c}\right) \exp[j2\pi n f_c t] \right|^2 \\ &= \sum_{n=-\infty}^{\infty} C_n \exp(jn^2\phi) \exp[jn\theta] \sum_{m=-\infty}^{\infty} C_m^* \exp(-jm^2\phi) \exp[-jm\theta]. \end{aligned} \quad (4-44)$$

The Fourier coefficients are extracted via

$$I_p = \frac{1}{2\pi} \int_{-\pi}^{\pi} i(\theta) \exp(-jp\theta) d\theta \quad (4-45)$$

$$\begin{aligned} &= \frac{1}{2\pi} \int_{-\pi}^{\pi} \sum_{n=-\infty}^{\infty} C_n \exp(jn^2\phi) \exp[jn\theta] \sum_{m=-\infty}^{\infty} C_m^* \exp(-jm^2\phi) \exp[-jm\theta] \exp(-jp\theta) d\theta \\ & \quad (4-46) \end{aligned}$$

which will only yield a term when $p = n-m$. Setting $m = n-p$ gives

$$\begin{aligned} I_p &= \frac{1}{2\pi} \int_{-\pi}^{\pi} \exp(-jp\theta) d\theta \sum_{n=-\infty}^{\infty} C_n \exp(jn^2\phi) \exp[jn\theta] \cdot \\ & \quad \sum_{n-p=-\infty}^{\infty} C_{n-p}^* \exp(-j(n-p)^2\phi) \exp[-j(n-p)\theta] \end{aligned}$$

$$\begin{aligned}
 &= \frac{1}{2\pi} \int_{-\pi}^{\pi} \exp(-jp\theta) d\theta \sum_{n=-\infty}^{\infty} C_n \exp(jn\rho\phi) \exp[jn\theta] \cdot \\
 &\quad \sum_{n-p=-\infty}^{\infty} C_{n-p}^* \exp(jp(n-p)\phi) \exp[-j(n-p)\theta]. \quad (4-47)
 \end{aligned}$$

Considering that

$$\begin{aligned}
 e_c(2\pi f_c t + \rho) &= \sum_{n=-\infty}^{\infty} C_n \exp[jn(2\pi f_c t + \rho)] \\
 &= \sum_{n=-\infty}^{\infty} C_n \exp[j2\pi n f_c t] \exp[jn\rho], \quad (4-48)
 \end{aligned}$$

(4-46) may be given by

$$I_p = \frac{1}{2\pi} \int_{-\pi}^{\pi} e_c(\theta + p\phi) e_c^*(\theta - p\phi) \exp(-jp\theta) d\theta. \quad (4-49)$$

This gives a general expression that may be used to simplify the process of capturing various terms in the series expansion of periodic signals. As an example consider the ideal amplitude modulator with sinusoidal input given by

$$e_c(2\pi f_c t) = 1 + \cos(2\pi f_c t). \quad (4-50)$$

Letting the fundamental dispersion term be represented by $\exp(j\phi)$ and $2\pi f_c t$ by θ , the Fourier coefficient at the fundamental for (4-50) is given by (4-49) as

$$\begin{aligned}
 I_1 &= \frac{1}{2\pi} \int_{-\pi}^{\pi} [1 + \cos(\theta + \phi)][1 + \cos(\theta - \phi)] \exp(-j\theta) d\theta \\
 &= \frac{1}{2\pi} \left[\int_{-\pi}^{\pi} \exp(-j\theta) d\theta + \int_{-\pi}^{\pi} \cos(\theta) \cos(\phi) \exp(-j\theta) d\theta + \right. \\
 &\quad \left. \int_{-\pi}^{\pi} \cos(\theta + \phi) \cos(\theta - \phi) \exp(-j\theta) d\theta \right]
 \end{aligned}$$

$$\begin{aligned}
 &= 0 + \frac{1}{2} \cos(\phi) + 0 \\
 &\propto \cos\left(\frac{\pi D \lambda_0^2 f_c^2 L}{c}\right)
 \end{aligned} \tag{4-51}$$

which is in agreement with the development in Chapter 2.

It is instructive to consider the behavior of a pure optical phase modulator with sinusoidal input whose transfer characteristic is given by [67]

$$e_c(2\pi f_c t) = \exp[jm\pi \cos(2\pi f_c t)]. \tag{4-52}$$

The amplitude of any particular harmonic at the output of an IMDD dispersive fiber link is the Fourier coefficient at the detector output given by equation (4-49).

$$\begin{aligned}
 I_p &= \frac{1}{2\pi} \int_{-\pi}^{\pi} e_c(\theta + p\phi) e_c^*(\theta - p\phi) \exp(-jp\theta) d\theta \\
 &= \frac{1}{2\pi} \int_{-\pi}^{\pi} \exp\{jm\pi[-\cos(\theta - p\phi) + \cos(\theta + p\phi)]\} \exp(-jp\theta) d\theta \\
 &= \frac{1}{2\pi} \int_{-\pi}^{\pi} \exp\{jm\pi[\sin(p\phi) \sin(\theta)]\} \exp(-jp\theta) d\theta \\
 &= J_p \left[2m\pi \sin \left[\frac{\pi D \lambda_0^2 p f_c^2 L}{c} \right] \right].
 \end{aligned} \tag{4-53}$$

A comparative plot of the 5th harmonic captured using (4-53) and a computer simulation of a phase modulator based dispersive optical link is shown in Figure 4.16.

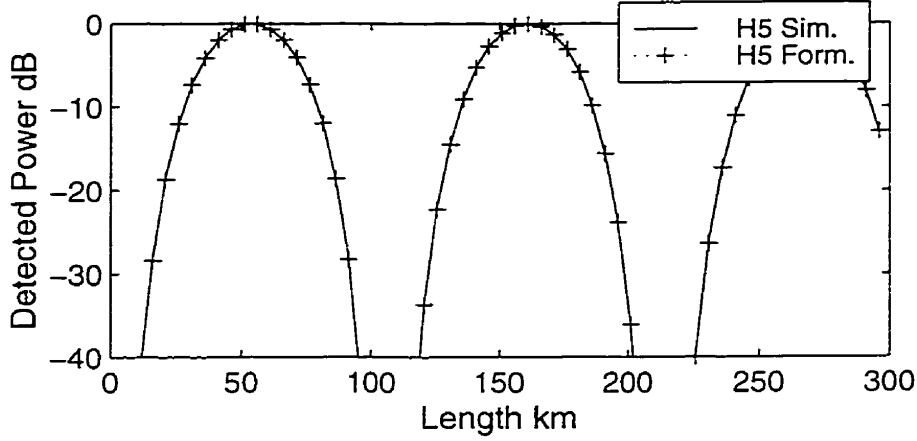


Figure 4.16. Power in H5 from nonlinear phase modulator as a function of fiber length, $f_c = 18/5$ GHz, $m = 0.7$ $D = 18$ ps/(nm•km) and $\lambda_0 = 1550$ nm.

The plot indicates that the fifth harmonic varies in amplitude with fiber length but still undergoes signal power loss at the zeros of (4-32) as a function of fiber length. It is clear that the simplified Fourier method is extremely powerful in capturing arbitrary Fourier coefficients from the detector output.

Next, the MZM modulator driven in DSB chirp free mode is considered. The modulation term is given by

$$E_{\text{out}} = \frac{E_{\text{in}}}{2} \left\{ \exp\left(j \frac{\pi m s(t)}{V_{\pi}}\right) + \exp\left[j \left(\frac{\pi m (-s(t))}{V_{\pi}} + V_{\text{bias}} \right) \right] \right\}. \quad (4-54)$$

Setting $s(t)$ to $\cos(\theta)$ and V_{bias} to $\pi/2$, the complex electric field is given by

$$e_c(\theta) = \exp[jm\pi \cos(\theta)] + \exp\left(j \frac{\pi}{2}\right) \exp[-jm\pi \cos(\theta)]. \quad (4-55)$$

Setting the dispersion term to ϕ , the p th term in the harmonic output at the photodetector is given by (4-49),

$$I_p = \frac{1}{2\pi} \int_{-\pi}^{\pi} \exp[jm\pi \cos(\theta + p\phi)] + \exp\left(j\frac{\pi}{2}\right) \exp[-jm\pi \cos(\theta + p\phi)] \cdot \exp[-jm\pi \cos(\theta - p\phi)] + \exp\left(-j\frac{\pi}{2}\right) \exp[jm\pi \cos(\theta - p\phi)] \exp(-jn\theta) d\theta. \quad (4-56)$$

Using Trigonometric identities and some manipulation gives

$$I_p = \frac{1}{2\pi} \int_{-\pi}^{\pi} \cos[2m\pi \sin p\phi \sin \theta] + \sin[2m\pi \cos p\phi \cos \theta] \exp(-jp\theta) d\theta \quad (4-57)$$

which indicates that the modulation depth for any particular harmonic becomes a function of the fiber dispersion.

Using the identities

$$\begin{aligned} \cos(u \sin x) &= J_0(u) + 2 \sum_{n=1}^{\infty} J_{2n}(u) \cos 2nx \\ \sin(u \cos x) &= 2 \sum_{n=1}^{\infty} (-1)^{n+1} J_{2n-1}(u) \cos(2n-1)x \end{aligned} \quad (4-58)$$

(4-58) becomes

$$I_p = \frac{1}{2\pi} \begin{cases} \int_{-\pi}^{\pi} J_0(2m\pi) + 2 \sum_{n=1}^{\infty} J_{2n}(2m\pi \sin(2n\phi)) \cos(2n\theta) \exp(-j2n\theta) d\theta; \\ p = 2n \text{ even} \\ \int_{-\pi}^{\pi} 2 \sum_{n=1}^{\infty} (-1)^{n+1} J_{2n-1}(2m\pi \cos(2n-1)\phi) \cos(2n-1)\theta \exp[-j(2n-1)\theta] d\theta; \\ p = 2n-1 \text{ odd} \end{cases} \quad (4-59)$$

where the integral has been separated into two sections to accommodate even and odd harmonics. As a check consider the case with no dispersion. It was shown in Figure 4.14 that there would be only a DC term and odd harmonics in the detector output. This is proven by the fact that, for the even harmonic portion of (4-59): $J_0(0) = 1$ and $J_n(0) = 0$; $n \neq 0$, which leaves the DC term in 4-59 and the second integral which only has odd harmonics.

Now consider the 5th harmonic given by

$$I_5 = J_5 \left(2m\pi \cos \left(\frac{\pi D \lambda_0^2 5f_c^2 L}{c} \right) \right). \quad (4-60)$$

A comparison for the exact formula in (4-59) versus a full simulation is shown in Figure 4.16 using $D = 18 \text{ ps}/(\text{nm} \cdot \text{km})$, $\lambda_0 = 1550 \text{ nm}$, $f_c = 18/5 \text{ GHz}$ and $m = 0.7$.

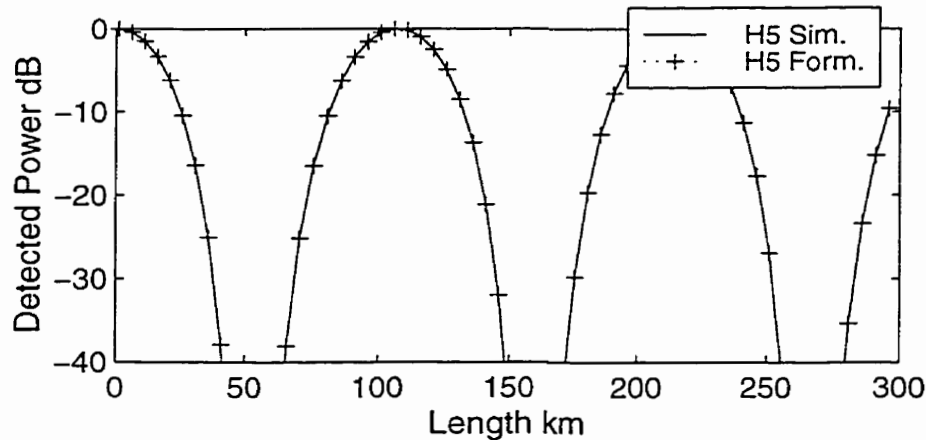


Figure 4.17. Power in H5 as a function of fiber length for a ‘chirpless’ MZM $D = 18 \text{ ps}/(\text{nm} \cdot \text{km})$, $\lambda_0 = 1550 \text{ nm}$, $f_c = 18/5 \text{ GHz}$ and $m = 0.7$.

It is apparent that there is a dispersion compensating effect in using harmonic DSB instead of linear DSB in the fact that the inevitable power null is delayed until further out on to the fiber than was observed for linear modulation. Recall

the linear modulation case in Figure 4.1 where the first null was observed at approximately 11 km with repetition at intervals of 22 km.

4.7.2. OSSB Harmonic Modulation

We conclude the theoretical investigation of transmission characteristics of non-linear optical devices with the harmonic OSSB modulator using the Hartley MZM modulator structure. In this case the normalized electric field is given by

$$e_c(2\pi f_c t) = \exp[jm\pi \cos(2\pi f_c t)] + \exp\left(j\frac{\pi}{2}\right) \exp[jm\pi \sin(2\pi f_c t)]. \quad (4-61)$$

Again using (4-49)

$$\begin{aligned} I_p &= \frac{1}{2\pi} \int_{-\pi}^{\pi} \exp[jm\pi \cos(\theta + p\phi)] + j \exp[jm\pi \sin(\theta + p\phi)] \cdot \\ &\quad \exp[-jm\pi \cos(\theta - p\phi)] - j \exp[-jm\pi \sin(\theta - p\phi)] \exp(-jp\theta) d\theta \\ &= \frac{1}{2\pi} \int_{-\pi}^{\pi} \exp[-j2m\pi \sin p\phi \sin \theta] + j \exp\left[-j2m\pi \sin\left(\theta + \frac{\pi}{4}\right) \sin\left(p\phi - \frac{\pi}{4}\right)\right] + \\ &\quad - j \exp\left[-j2m\pi \sin\left(\theta - \frac{\pi}{4}\right) \sin\left(p\phi + \frac{\pi}{4}\right)\right] + \exp[j2m\pi \sin \phi \cos \theta] \exp(-jp\theta) d\theta \end{aligned} \quad (4-62)$$

It was found that the resulting expression was more difficult to simplify and didn't indicate clearly the fading characteristics as was the case with the chirpless MZM in equation 4-59. However, the coefficient for H5 is given by

$$\begin{aligned} I_5 &= (j-1)J_5(2m\pi \sin 5\phi) + \\ &\quad j \exp\left(j\frac{-5\pi}{4}\right) \left\{ J_{-5}\left(2m\pi \sin\left(5\phi - \frac{\pi}{4}\right)\right) - J_{-5}\left(2m\pi \sin\left(5\phi + \frac{\pi}{4}\right)\right) \right\}. \end{aligned} \quad (4-63)$$

A comparison of numerical results the plots for a full simulation versus the formula in (4-63) is shown in Figure 4.18. The detected power is observed to be periodic over fiber length and has no deep power nulls as was observed in the double sideband cases. This clearly shows the compensating effect of OSSB modulation on detected power. For the MZM/Phase device it can be shown that the detected power vs fiber length for Hartley MZM and the MZM/phase are equivalent when the modulation index enhancement of the MZM/Phase device is taken into account. This subject will be addressed further in Chapter 5.

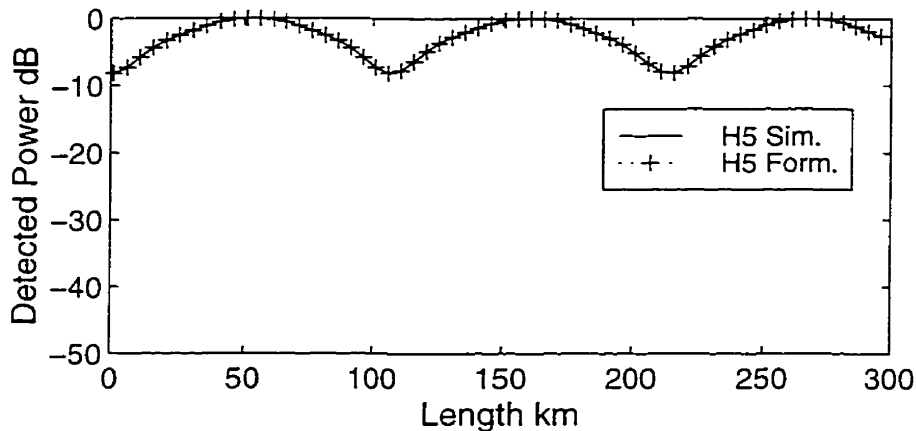


Figure 4.18. Power in H5 from Hartley OSSB harmonic upconverter as a function of fiber length $D = 18 \text{ ps}/(\text{nm}\cdot\text{km})$, $\lambda_0 = 1550 \text{ nm}$, $f_c = 18/5 \text{ GHz}$ and $m = 0.7$.

4.8. Conclusions

It has been shown in Chapter 4 that all of the modulator structures outlined in Chapter 2 show reasonable potential for linear subcarrier OSSB modulation. OSSB is shown in all cases to mitigate the effects of fiber dispersion on IMDD optical links. In the case of harmonic subcarrier modulation where some higher harmonic of the input signal is captured at the output of the optical link, the laser structure was found in preliminary simulation to be non ideal in this respect with poor power transfer characteristics to the higher harmonics. Further work needs to be done on the laser to determine if the laser chirp characteristic may be exploited in this case. The MZM/Phase modulator and equivalent MZM Hartley

modulator are shown to be efficient structures from the perspective of distributing the available detected power into the higher harmonics. Based on the MZM/Phase Hybrid structure, an algorithm has been developed that simplifies the task of analysis and conceptualization of the fiber dispersion mechanism from a frequency domain perspective. This algorithm drastically simplifies the computing time required to simulate the harmonic modulation process as well.

It is noted that many other structures and configurations of non-linear modulators are achievable with the various components outlined in the previous discussion. The configurations shown focus on what might be referred to as 'pure harmonic frequency translators' in which the harmonic upconversion process involves a solitary subcarrier signal applied to the optical modulator. The problem remains as to which type of subcarrier modulation will be suitable for this type of harmonic generation. This issue will be dealt with in Chapter 5.

5. Transmission of Modulated Harmonically Upconverted OSSB Subcarriers

5.1. Introduction

In this chapter, the focus is on transmission of harmonically upconverted modulated subcarriers over OSSB fiber links. Methods for predistorting subcarrier signals, to make them suitable for harmonic upconversion, are discussed, and it will be shown, in the case of phase modulated signals, that compression of the phase by a factor of n , where n is the desired frequency multiplier, prevents phase distortion due to argument multiplication in the upconversion process. Additionally, an amplitude predistortion method is introduced that can be used in conjunction with the phase predistortion technique to allow harmonic upconversion of QAM type signals with improved distortion behavior on specific harmonic devices. Both methods are shown, by simulation example, to work on IMDD optical links.

5.2. Linear Subcarrier Modulation

The topic of linear subcarrier modulation on optical links has been explored in some detail in the literature. The functionality of the MZM as a DSB and SSB device has been established and this topic won't be addressed in this study[64,65]. There is likewise little doubt that the MZM/phase modulator or 'hybrid' modulator will perform satisfactorily in linear schemes within the bandwidth limits outlined in Chapter 4 and the linear operation of the device. This is due to the equivalence of the Hartley MZM and the hybrid device. This was also established in the simulations of Chapter 2 for the broadband process. For these reasons the topic of linear modulation on optical links will be deferred to the experimental section in Chapter 6 where it will be shown, simply, that OSSB mitigates dispersion induced loss on linear subcarrier optical links.

5.3. General Harmonic Upconversion

In Chapter 4 it was stated that the general expression for the output from a non-linear network in response to a CW input is given by

$$R(t) = \sum_{n=1}^{N-1} a_n \exp(jn2\pi f_c t) \quad (5-1)$$

where a_n is a coefficient determined by the nature of the non-linearity, N is the number of harmonics in the output and f_c is the fundamental input frequency. It was further stated that when a non-linear network is used as a harmonic upconverter, distortion of the phase of the output signal results due to argument multiplication of the input signal. This is shown in the general expression for the output of a non-linear network in response to a phase modulated input given by $\cos(2\pi f_c t + \phi(t))$

$$R(t) = \sum_{n=1}^{N-1} a_n \exp\{jn[2\pi f_c t + \phi(t)]\}. \quad (5-2)$$

The phase information is multiplied in the same manner as the carrier term resulting in distortion. It is apparent that, from the perspective of any individual harmonic 'n' at the output of the non-linear network, if the phase modulation of the input signal term is divided by n before being injected into the non-linear network, the multiplying effect of the harmonic conversion would be neutralized and the distortion effect would be removed[68]. If, for example, a 5th harmonic subcarrier with QPSK modulation was required at the output from the harmonic generator, the required input signal would be a QPSK subcarrier at a 5th subharmonic of the output frequency and in which the absolute value of the phase modulation had been divided by 5.

This method is illustrated by example. Firstly we compose a QPSK constellation by generating a binary PRBS and then coding successive pairs of bits (dibits) in the sequence onto $\pi/4$ offset constellation points. The absolute

phase of the individual constellation points are then mapped to a new compressed constellation via division by the harmonic number (In this example H5). This compressed constellation is shown in Figure 5.1.

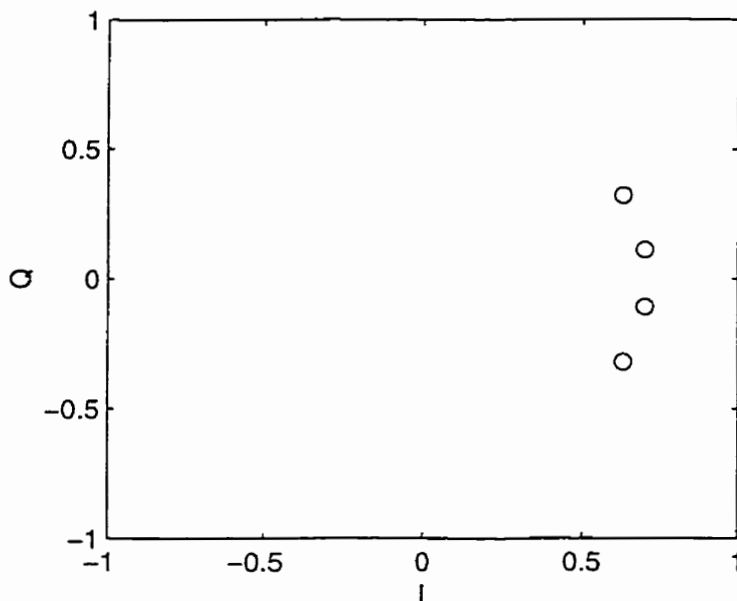


Figure 5.1. Compressed input constellation.

The compressed constellation is then modulated onto a real carrier as in

$$s(t) = \sin(2\pi f_c t + \phi(t)). \quad (5-3)$$

This carrier signal is then applied to a nonlinear 2 port network whose complex transfer characteristic in this example is pure phase modulation, given by

$$E_{out} = E_{in} \exp[jms(t)] \quad (5-4)$$

where $s(t)$ is the input signal and m is the modulation index. It is assumed that E_{in} is a CW carrier signal. Using the identity

$$\exp(jm \sin x) = \sum_{n=-\infty}^{\infty} J_n(m) \exp(jnx) \quad (5-5)$$

where $J_n(x)$ is the n th order Bessel Function and combining (5-3) and (5-5) gives

$$y(t) = \exp\{jm \sin[2\pi f_c t + \phi(t)]\} = \sum_{n=-\infty}^{\infty} J_n(m) \exp\{jn[2\pi f_c t + \phi(t)]\}. \quad (5-6)$$

The output 5th harmonic is captured with a bandpass filter and is given by

$$y_{H5}(t) = J_5(m) \exp\{jn[2\pi f_c t + \phi(t)]\}. \quad (5-7)$$

In the case of harmonic frequency translation this subcarrier signal would then be transmitted into the radio channel. This means that the signal has to be of sufficient quality with respect to distortion and degradation through the non-linear upconversion process to survive the journey through the radio channel. This issue will be addressed later in more detail. However for the simulation the subcarrier signal will be demodulated at this point to observe any degradation to the quality. In the case of the phase non-linearity, the subcarrier signal is demodulated using quadrature methods to capture the information.

The above algorithm was simulated in MATLAB using the circuit model shown in Figure 5.2.

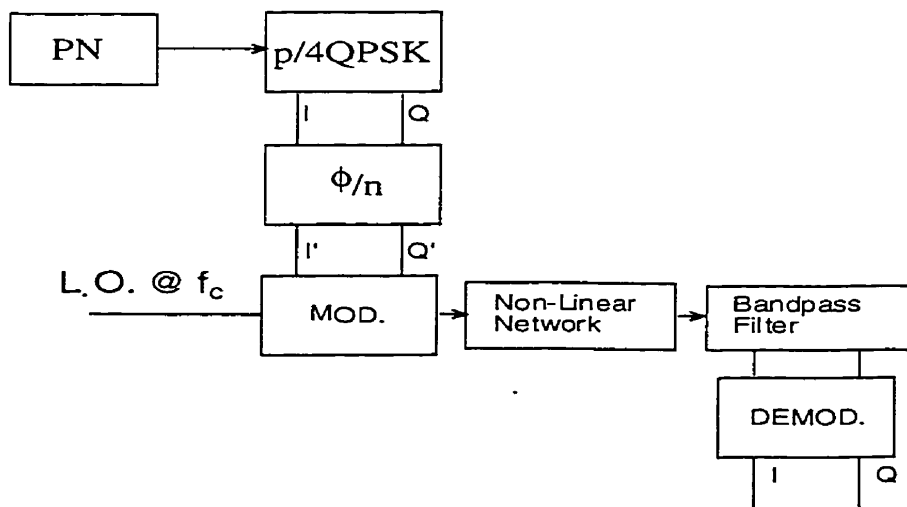


Figure 5.2. Circuit model for general non-linear upconverter and demodulator simulation.

Briefly, the PN sequence is coded into a QPSK constellation. The phase of the constellation is then compressed in the ϕ/n network and modulated onto the fundamental subcarrier. The bandwidth of the quadrature information signal is approximately 30% of the fundamental subcarrier frequency and the simulation was set up to mimic a 5th harmonic 18 GHz harmonic subcarrier. The modulated carrier with predistorted phase is then fed through the non-linear network phase modulator where harmonic replicas of the input signal are produced with phase multiplied by n for each harmonic. At the bandpass filter, the harmonic of interest is captured by using a 'brick-wall' bandpass filter with bandwidth set at the symbol rate. The signal is then demodulated using a quadrature device to capture the receive constellation.

A eye diagram of the received information waveform, recovered through interleaving of the real and imaginary components in the received signal, from the fifth harmonic is shown in Figure 5.3. The sequence is sampled at a rate of 5/bit. Clearly the eye is of good quality.

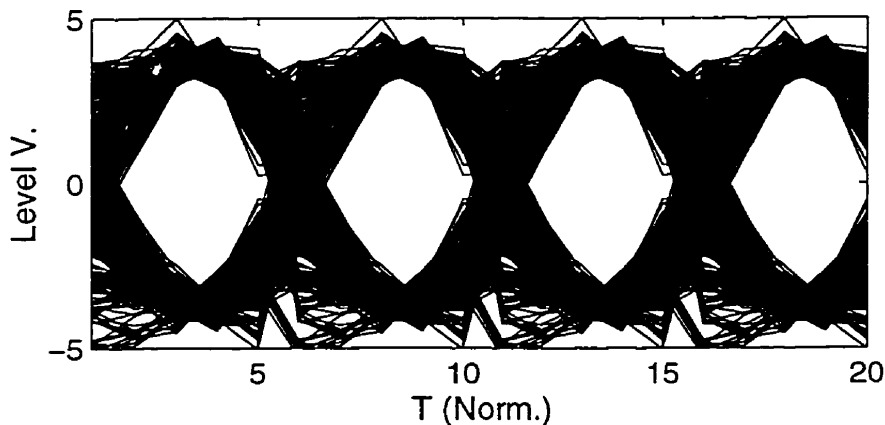


Figure 5.3. Eye diagram of recovered output from fifth harmonic for general non-linear upconverter.

In order to verify the accuracy of the information, the highly selective cross correlation properties of pseudo noise sequences[69] were exploited. Since the input information sequence was a maximal length PN sequence, the accuracy of the information can be confirmed by performing a discrete circular

mathematical cross-correlation of a single period of the sampled output data from the demodulated subcarrier signal with a single period of the sampled input data sequence. If a well-defined peak is observed with a peak signal to noise ratio on the order of that dictated by

$$\gamma = 20 \log_{10}(N) \quad (5-8)$$

where N is the characteristic length of the input PN sequence in chips, it can be concluded that the demodulated information is correct. If the sequence is garbled by phase distortion or any unknown mechanism, the resulting cross-correlation sequence would appear noise-like with no coherent peaks in the output. The PN sequence used in this experiment was of length 1023. This indicates a correlation peak of about 60 dB relative height. Figure 5.4 shows the correlation of the above data sequence with the original input sequence. The presence of the large correlation spike and the purity in the shape of the correlation function near the peak indicates that the recovered information stream is accurate.

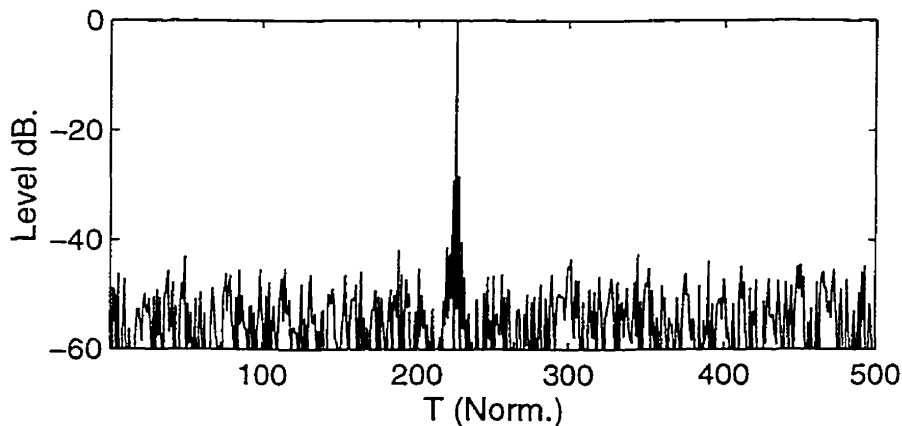


Figure 5.4. Cross-correlation function of recovered output with original information signal from fifth harmonic for general non-linear upconverter.

This simulation is not definitive in the sense that noise and other influences have not been addressed. Additionally the relative signal bandwidth is much

higher than would be implemented in a real system. However it is clear that the phase compression method preserves the phase information in its original state through the upconversion operation, verifying the theoretical claim. Figure 5.5 shows a short section of the recovered sequence sent without phase compression compared to the original bit stream.

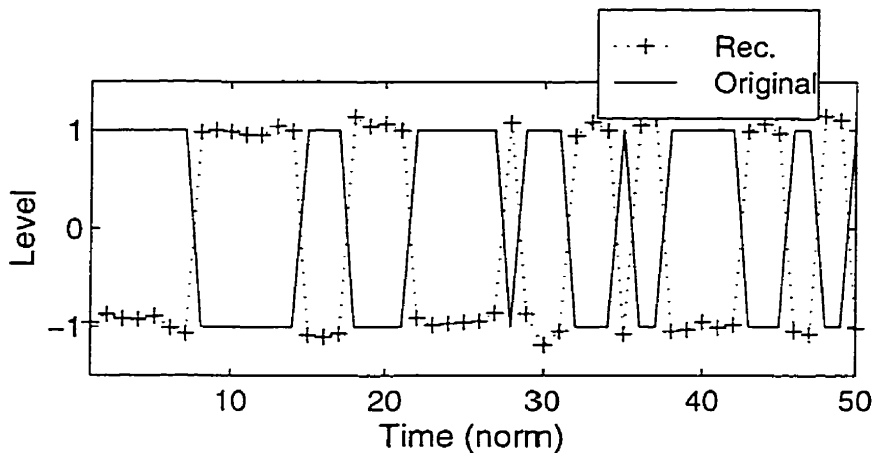


Figure 5.5. Recovered output from fifth harmonic without phase predistortion.

The recovered information sequence is inverted which is expected for this illustrative case. It was also confirmed that the eye diagram of the data in Figure 5.5 was of similar quality to the phase compressed case. The reader may ask: why predistort at all if inversion is the only observed distortion effect? The short answer is: this phenomenon only applies to specific cases where the phase states happen to map uniquely in the distorted spectrum. In this case only odd harmonics would yield a signal with unique phase states. Other types of signals with more complex phase functions, such as 16QAM, would be irreparably damaged by the phase multiplication process. This will be verified later. The present example verifies the theory for a relatively simple non-linear device.

5.3.1. Optical Harmonic Upconverter

It was shown in Chapter 4 that a suitable IMDD harmonic process may be generated in a MZM/Phase modulator based optical link to produce a harmonic

signal that is amenable to square-law envelope detection. In this investigation the MZM/Phase modulator cascade is used as an OSSB harmonic upconverter. The fundamental modulated carrier is synthesized in the same manner as for the phase modulator. The normalized optical complex envelope E-field expression for the MZM/Phase device is given by

$$E_{\text{out}}(t) = \left\{ \exp[jm\pi s(t)] + \exp[j(V_b - m\pi s(t))] \right\} \exp[jm_p \hat{s}(t)] \quad (5-9)$$

where m is the modulation index of the MZM and m_p is the modulation index of the phase modulator. If there is no dispersion on the fiber then upon square-law detection the phase term disappears and the normalized detector output is given by

$$\begin{aligned} I_b(t) &= k \cos^2 \left[m\pi \cos(2\pi f_c t + \phi(t)) - \frac{V_b}{2} \right] \\ &= \frac{k}{2} + \sin \left[2m\pi \cos(2\pi f_c t + \phi(t)) \right] \end{aligned} \quad (5-10)$$

where we have let $s(t)$ be a phase modulated subcarrier given by

$$s(t) = \cos(2\pi f_c t + \phi(t)). \quad (5-11)$$

Using the identity

$$\sin(u \cos x) = 2 \sum_{n=1}^{\infty} (-1)^{n+1} J_{2n-1}(u) \cos[(2n-1)x], \quad (5-12)$$

the output from the square law detector is given by

$$I_b(t) = k + 2k \sum_{n=1}^{\infty} (-1)^{n+1} J_{2n-1}(2m\pi) \cos[(2n-1)(2\pi f_c t + \phi(t))] \quad (5-13)$$

for which only odd harmonics are present. If, as in the previous simulation, the fifth harmonic was desired at the detector output, a bandpass filter would be applied to the detector output to capture this subcarrier component.

The MZM/Phase device was simulated in the same manner as the phase device above using the circuit model shown in Figure 5.6.

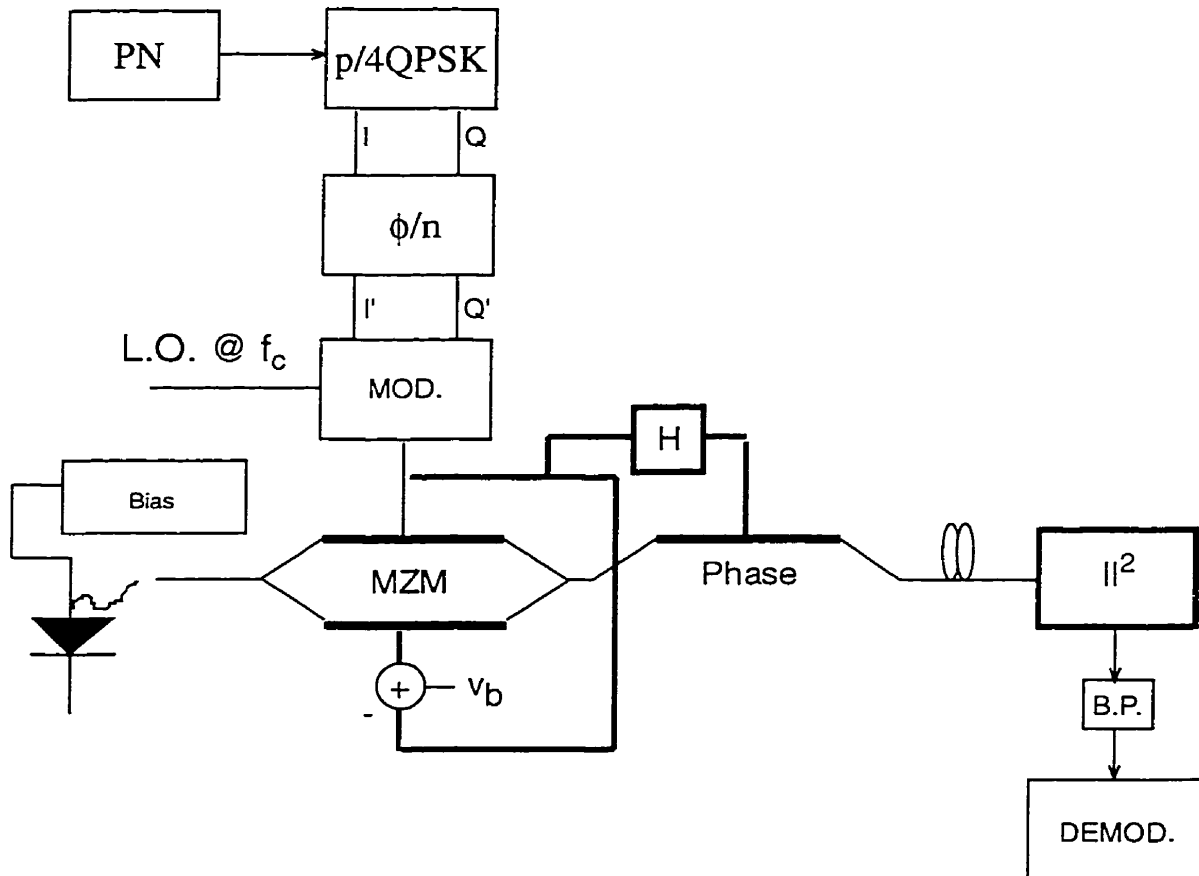


Figure 5.6. Circuit model for optical MZM/phase COSSB upconverter and demodulator simulation.

The compressed phase subcarrier is generated as in the previous simulation. The subcarrier is then applied to the MZM and phase modulator in OSSB fashion with a modulation index of 0.7 relative to the V_π . Harmonic replicas of the input signal are produced with phase multiplied by n for each harmonic. At the bandpass filter (BP) the fifth harmonic in the square-law detected signal is captured by using a 'brick-wall' bandpass filter with bandwidth set at the symbol

rate. The 5th resulting subcarrier signal was then demodulated using coherent methods to recover the information. The simulation was again set up to mimic the behavior of an narrowband 18 GHz subcarrier on an optical link with dispersion parameter of $D = 18 \text{ ps}/(\text{nm}\cdot\text{km})$, $\lambda_0 = 1550 \text{ nm}$ and $L = 0$, representing a dispersionless link. An eye diagram of the demodulated information signal is shown in Figure 5.7.

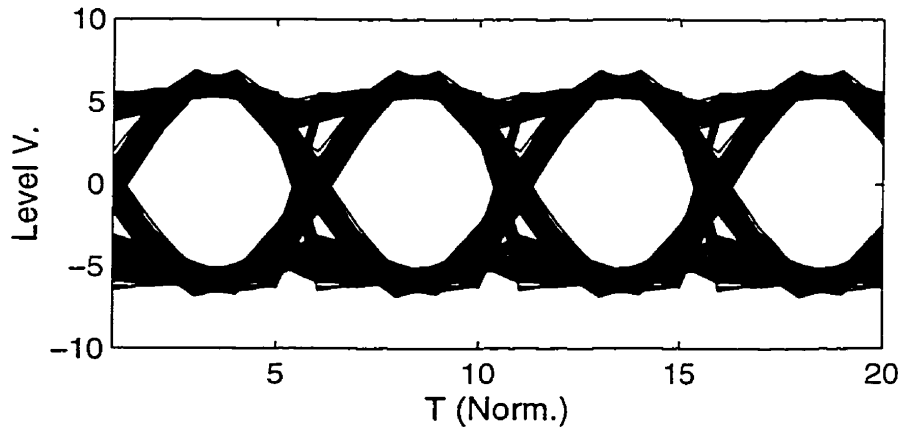


Figure 5.7. Eye diagram recovered output from fifth harmonic for MZM/phase OSSB modulator, $m_z = 0.7$, $m_p = 0.7$, $f_c = 18 \text{ GHz}$, $D = 18 \text{ ps}/(\text{nm}\cdot\text{km})$, $\lambda_0 = 1550 \text{ nm}$ and $L = 0$.

In this case the eye quality is better than that of the general non-linear network. The accuracy of the original data was again verified using the cross-correlation properties of the recovered information and the original sequence and the result is shown in Figure 5.8. It is apparent that the more complicated MZM/Phase device has had no additional distorting effect on the data than the simple phase device and the phase compression theory applies to the more complicated hybrid IMDD optical link.

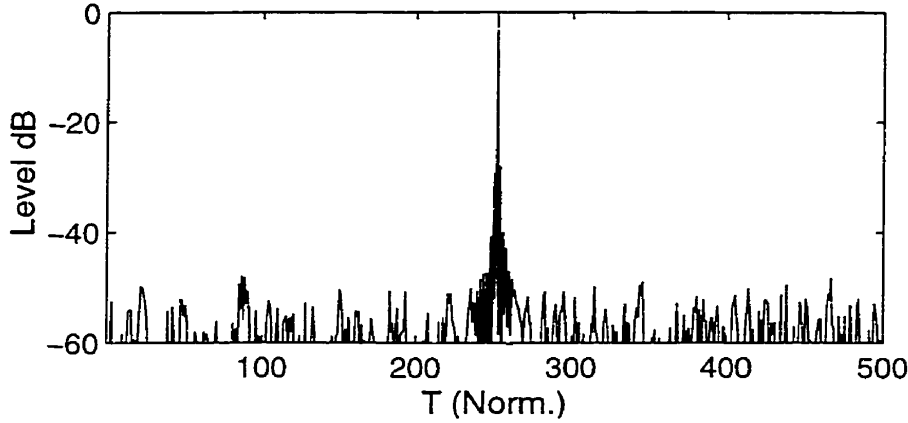


Figure 5.8. Cross-correlation function of recovered output with original information signal from fifth harmonic for optical mzm/phase non-linear upconverter.

5.4. Dispersion Performance

It was shown in Chapter 4 that chromatic dispersion had a similar effect on double sideband harmonic IMDD subcarrier optical links to that observed for linear subcarrier links that being an excess attenuation of the received RF power with link distance over that due to fiber loss. Theory and simulation showed that harmonic OSSB modulation had a mitigating effect on this dispersion induced fiber loss. The next step in the present examination is to observe the effects of fiber dispersion on the phase compression scheme to observe any degradation to the signal.

Using the results of Chapter 4, it can be shown that the Fourier coefficient of the n th harmonic from a detected output expression from a dispersive optical link with a Hartley OSSB (and equivalently the MZM/Phase Hybrid) modulator is given as

$$\begin{aligned}
 I_p = & J_{-p} \left(2m\pi \sin \left(p \frac{\pi D \lambda_0^2 f_c^2 L}{c} \right) \right) + j^p J_p \left(2m\pi \sin \left(p \frac{\pi D \lambda_0^2 f_c^2 L}{c} \right) \right) \\
 & j \exp \left(\frac{-p\pi}{4} \right) \left\{ J_{-p} \left(2m\pi \sin \left(p \frac{\pi D \lambda_0^2 f_c^2 L}{c} - \frac{\pi}{4} \right) \right) - J_{-p} \left(2m\pi \sin \left(p \frac{\pi D \lambda_0^2 f_c^2 L}{c} + \frac{\pi}{4} \right) \right) \right\}
 \end{aligned} \tag{5-14}$$

where n is the harmonic number, m is the modulation index, $J_n(x)$ is the n th order Bessel function of the first kind, D is the dispersion parameter, λ_0 is the optical wavelength and L is the fiber length. In the case of phase modulation the modulated signal may be represented accurately by the above expression. If amplitude modulation is present or the information sidebands of the harmonic components overlap, the integrity of the above expression is degraded.

We again simulate the effects of fiber dispersion of the received constellation of a fifth harmonic QPSK signal for $H5 = 18$ GHz $D = 18$ ps/nm•km, $\lambda_0 = 1550$ nm. The subcarrier information bandwidth is 30%. For a zero length link the received constellation from an MZM/Phase IMDD OSSB link is shown in Figure 5.9.

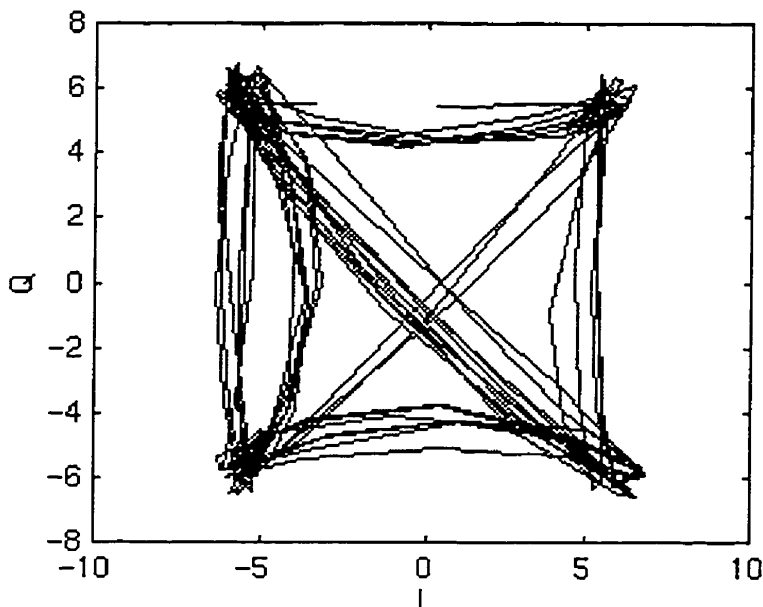


Figure 5.9. Recovered QPSK constellation from harmonically upconverted modulated subcarrier on zero length link (with phase recovery), $H5 = 18$ GHz, $D = 18$ ps/nm•km, $\lambda_0 = 1550$, $B = 30\%$.

The constellation in Figure 5.9 is of good quality with sharp corners and clean transitions from state to state. It was noted in the previous phase modulator simulation that a similar quality constellation was not observed until the

modulation index was set to about 1.5 relative to the V_{π} . This is likely due to the modulation index enhancement inherent in the MZM/Phase hybrid device.

Next we show a succession of constellations in Figure 5.10 with graduated fiber lengths. For 20 Km of dispersive fiber the constellation begins to rotate clockwise.

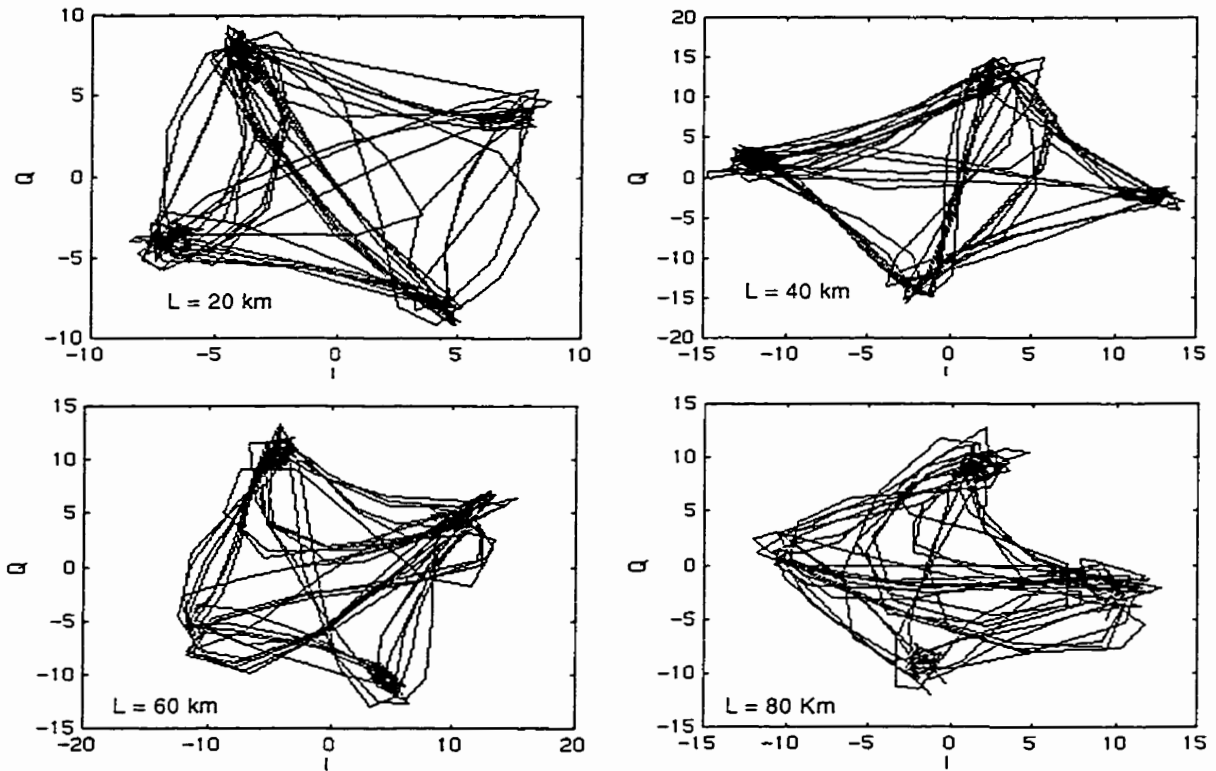


Figure 5.10. Recovered QPSK constellation from dispersive link harmonically upconverted modulated subcarrier, $H_5 = 18$ GHz, $D = 18$ ps/nm•km, $\lambda_0 = 1550$, $B = 30\%$.

For 40 Km the constellation is rotated further in a clockwise direction and although the four corners of the constellation are visible it is also apparent that the constellation is being distorted somewhat by the increase in dispersion distortion. This is due to the increase in group delay distortion brought about by lengthening the fiber. The data from a 40 Km optical link was recovered at the

demodulator and an eye diagram is shown in Figure 5.11. It is apparent that the eye quality is still good.

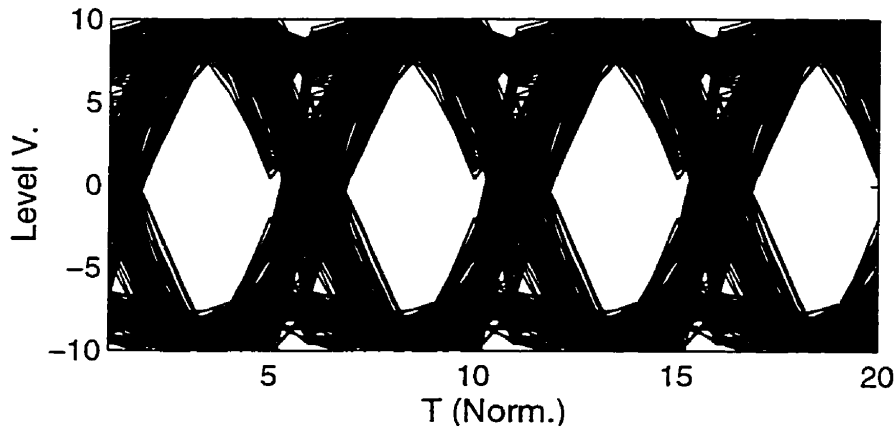


Figure 5.11. Eye diagram from recovered output from fifth harmonic for mzm/phase OSSB modulator, $m_z = 0.7$, $m_p = 0.7$, $f_c = 18$ GHz, $D = 18$ ps/(nm•km) $\lambda_0 = 1550$ nm and $L = 40$ km.

However the eye diagram from an 80 km optical link, shown in Figure 5.12 (over) indicates signs of degradation. It was also verified that there were bit errors in the demodulated information sequence for the 80 km link. This shows that subcarrier information signals will degrade over dispersive links if the fiber dispersion is severe.

The above simulations verify the theoretical claims for the phase predistortion algorithm on an OSSB Harmonic link. In the 30% bandwidth simulation the recovered data was observed to be correct to a length of 40 Km. Beyond this length, fiber dispersion began to degrade the recovered information sequence. The simulation was performed for a 30% bandwidth subcarrier to strain the circuit and allow visual observation of the effects of fiber dispersion. The intended applications would likely never require bandwidth of this order so it is reasonable to assume that the phase compression algorithm would be of practical use in a real system.

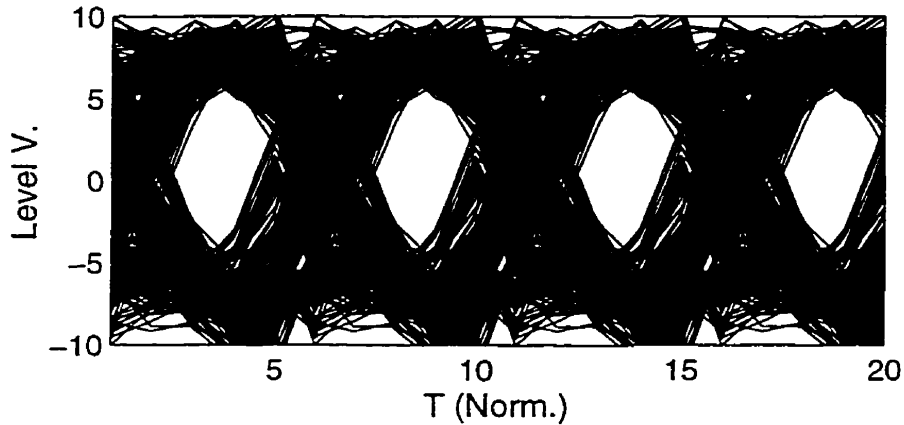


Figure 5.12. Eye diagram from recovered output from fifth harmonic for mzm/phase OSSB modulator, $m_z = 0.7$, $m_p = 0.7$, $f_c = 18$ GHz, $D = 18$ ps/(nm•km) $\lambda_0 = 1550$ nm and $L = 80$ Km.

It was confirmed, but is not shown, that the eye quality was improved at 80 Km for a 20% information bandwidth of the input subcarrier.

5.4.1. Amplitude/Phase Predistortion

A related pre-distortion method may be applied to Quadrature Amplitude QAM signals but in this case the amplitude distorting nature of the non-linear frequency translator must be well characterized. In the MZM and other devices that are based on phase modulation, this is possible since the harmonic coefficients follow Bessel functions. This suggests that amplitude predistortion according to a Bessel function may allow accurate demodulation of the upconverted signal. In the case of amplitude and phase modulation, the input signal, to the harmonic device is given by

$$s(t) = m(t) \cos(2\pi f_c t + \phi(t)). \quad (5-15)$$

In this case the amplitude process is modeled as a time varying modulation index. Using the phase non-linearity device from section 5.3. as a tutorial simulation exercise, the 5th harmonic output is given by

$$y_5(t) = -J_5[m(t)] \exp\{jn[2\pi f_c t + \phi(t)]\}. \quad (5-16)$$

To achieve the proper prescaling, the amplitude is scaled by the inverse of the Bessel function at the harmonic of interest. To acquire the fifth harmonic, the amplitude of the input signal must be prescaled by the inverse of the Fifth order Bessel term function for the range of the modulating signal. In this case it is necessary to isolate a linear or nearly linear section of the Bessel function that scales practically into the modulation scheme. This method will be illustrated by example with 16 QAM signal.

Firstly a 16 QAM signal is constructed by mapping dibits of a PRBS sequence into 2 orthogonal amplitude shift signals which are then combined in a complex fashion with one AM process on the real axis and the other AM process on the imaginary axis. The 16 QAM constellation is shown in Figure 5.13. The 16 QAM signal may then be modeled as a complex process of amplitude and phase as in

$$s(t) = m(t) \exp[j(2\pi f_c t + \phi(t))]. \quad (5-17)$$

To condition the signal for harmonic upconversion, the phase portion of the signal is compressed by a factor of 5 as in the QPSK case above.

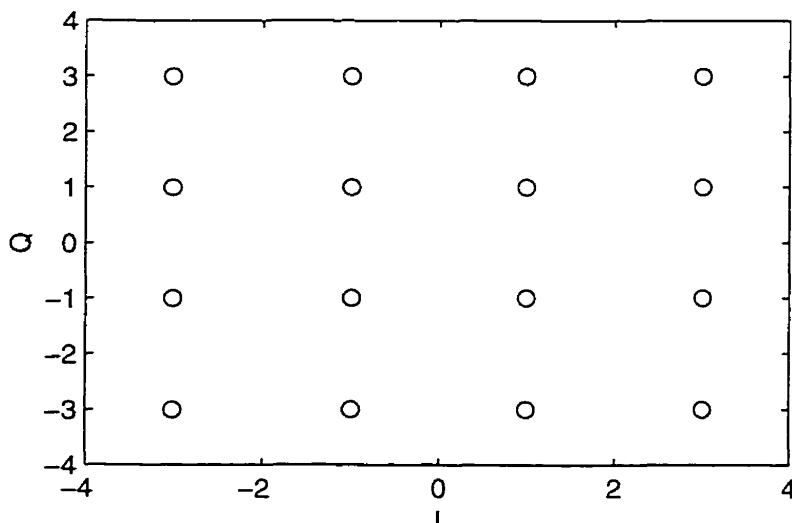


Figure 5.13. 16 QAM constellation.

To scale the amplitude the characteristics of the 5th order Bessel function, a section of which is shown in Figure 5.14, must be considered.

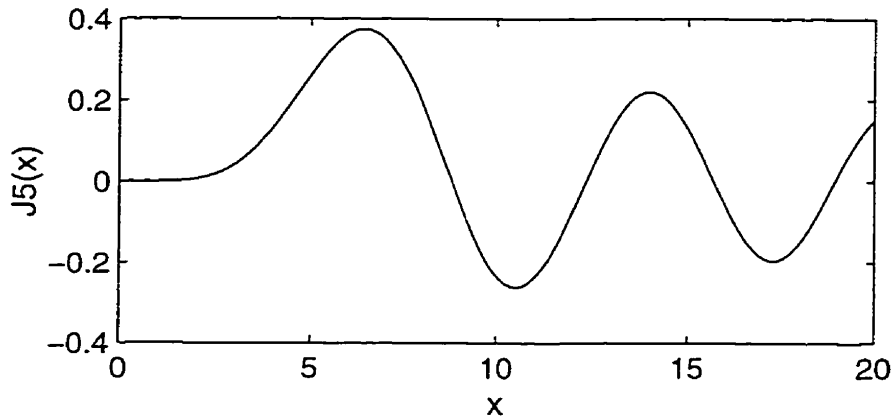


Figure 5.14. Fifth order Bessel function.

A suitable amplitude scaling involves mapping the amplitude of the QAM constellation into the piece-wise linear range of the fifth order Bessel function for argument 'x' between 3.7 to ~5.7. This range is selected due to its positive slope. If a larger linear range was desired and a negative mapping was acceptable, the negative linear range between 7 - 10 would be selected. The selected range is shown below in Figure 5.15.

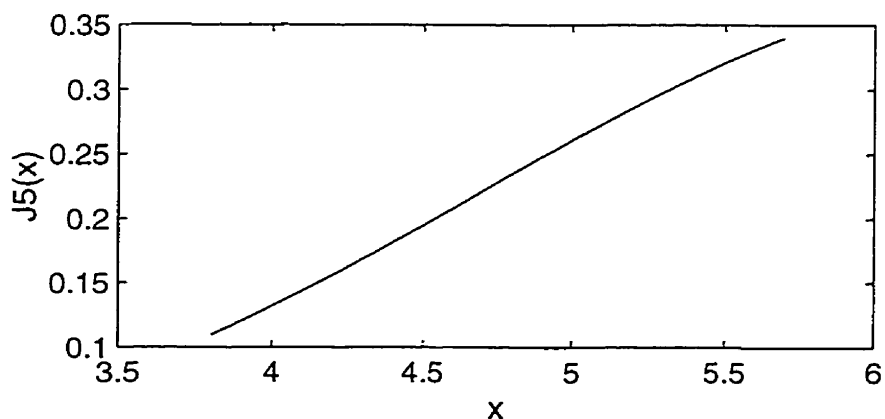


Figure 5.15. Fifth order Bessel function.

The amplitude $m(t)$ of the input signal would be scaled into the range 3.7 - 5.7 . A block diagram of the AM/PM Harmonic upconverter is shown in Figure 5.14.

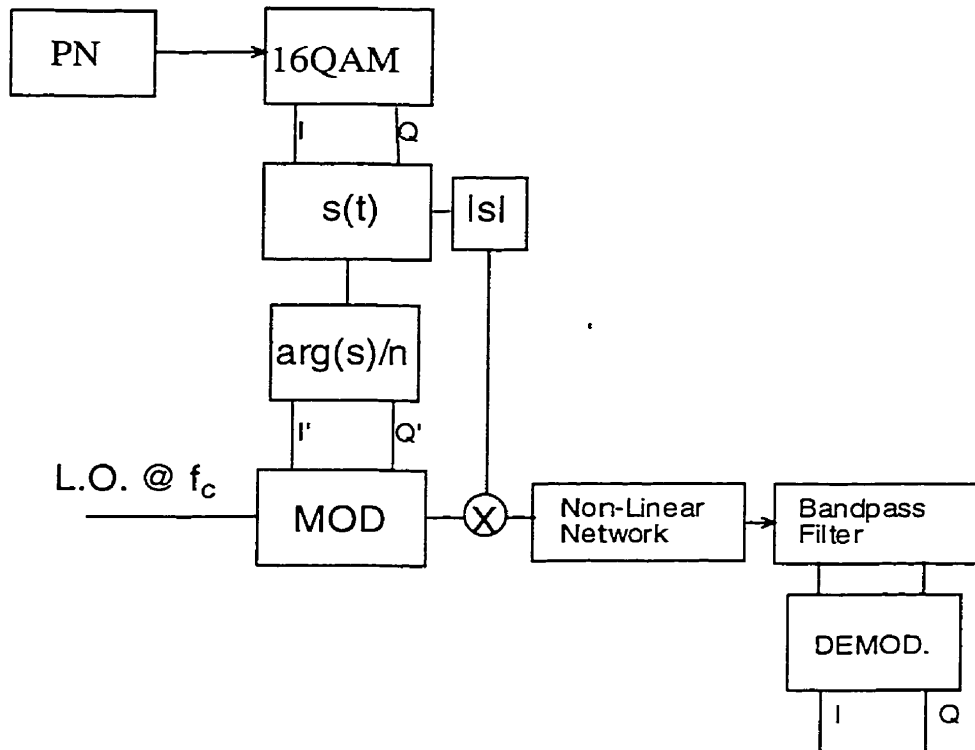


Figure 5.16. AM/PM harmonic upconverter block diagram.

In this simulation, three 511 'chip' PN sequences were concatenated and mapped into a complex 16QAM constellation. The amplitude and phase of the complex 16QAM constellation were then separated. The phase of the constellation was then compressed in the ϕ/n network and modulated onto the fundamental subcarrier. The amplitude of the 16QAM signal was extracted and mapped into the predistorted amplitude using the numerical map

$$R_m(t) = 3.7 + \{R(t) - \min[R(t)]\}0.7283 \quad (5-18)$$

where $R_m(t)$ is the predistorted amplitude, $R(t)$ is the 16QAM amplitude and \min is the minimum operator. The constants are determined from numerical methods to map the range of the 16QAM amplitude ($\sqrt{2} - 3\sqrt{2}$) in to the required predistorted range. The predistorted signal was then upconverted in the phase

modulator. The 5th harmonic was captured at the output of the phase non-linearity with a 'brick-wall' bandpass filter with cutoff at the symbol rate. The scaling of the Bessel function was such that no special re-mapping was required at the demodulator output. The demodulated signal was simply multiplied by a constant to attain the proper voltage levels with respect to the original signal.

A comparison of the quadrature or 'Q' process from the recovered upconverted subcarrier and the original information sequence modulated onto the radio subcarrier is shown in Figure 5.17. The plot shows only slight distortion of the recovered information sequence.

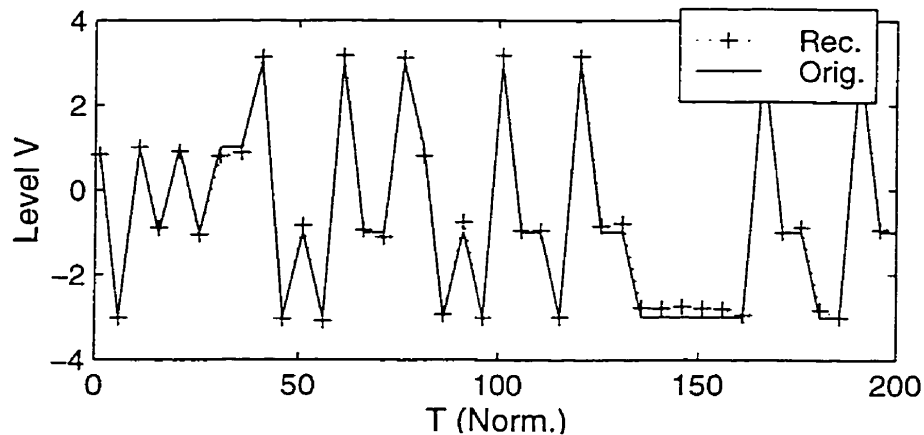


Figure 5.17. Comparison of 'Q' recovered data with original information signal from 16QAM signal predistorted for harmonic upconversion.

Similar accuracy was achieved for the inphase or 'I' process as shown in Figure 5.18. The above results were acquired by relatively rough visual methods and are still of sufficient quality to use in a real radio system. If the linear map were acquired by more exact numerical function minimization methods the fits depicted in figures 5.17 and 5.18 could be improved.

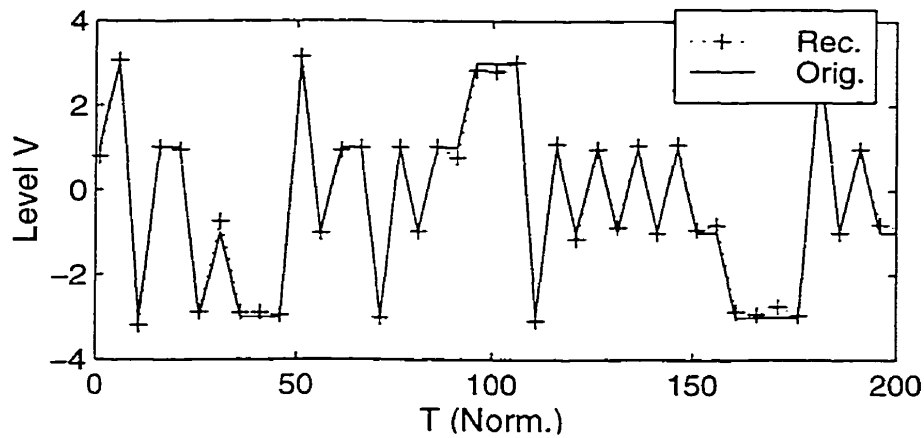


Figure 5.18. Comparison of '1' recovered data with original information signal from 16QAM signal predistorted for harmonic upconversion.

The amplitude and phase predistortion method was also applied to the MZM/Phase OSSB device. In this case the phase modulator non-linearity is replaced with a non-linear optical link. The block diagram is shown in Figure 5.19.

The output from the detector is given by equation (5-13) which, when modified for amplitude modulation gives

$$I_D(t) = k + 2k \sum_{n=1}^{\infty} (-1)^{n+1} J_{2n-1}[2m(t)\pi] \cos[(2n-1)(2\pi f_c t + \phi(t))] \quad (5-19)$$

where $m(t)$ is the modulation index relative to V_π for the MZM or the phase modulator.

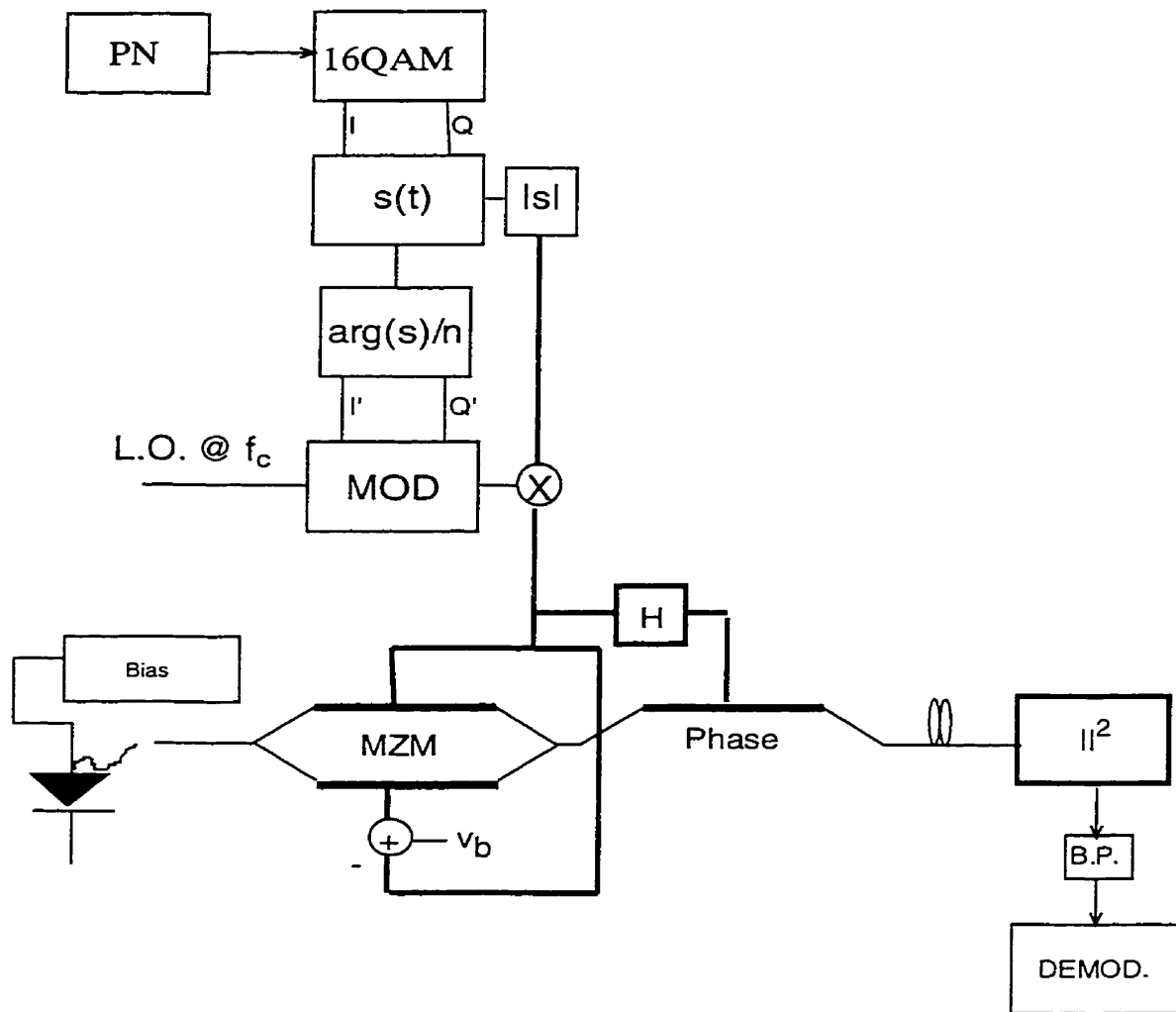


Figure 5.19. COSSB harmonic upconverter simulation block diagram, $f_c = 18$ GHz.

The MZM/Phase harmonic upconverter was simulated using the required scaling and the result for the Q process is shown in Figure 5.20. Again the agreement between original and predistorted information sequences is extremely close. Similar results were attained for the inphase process. As with the previous simulation no special numerical method beyond visual graphical methods was used, and it is again conjectured that the quality of the signal could be improved with more comprehensive function minimization routines. The actual range of modulation index used for the MZM and the Phase modulator was reduced by a divisor of $2\sqrt{2}$ from the scaling used in the Phase

modulator simulation (max. = $3.7 \cdot V_{\pi}$). This means that the required input amplitude signal to the MZM/Phase device is well within the range of conventional device extinction voltage ratings.

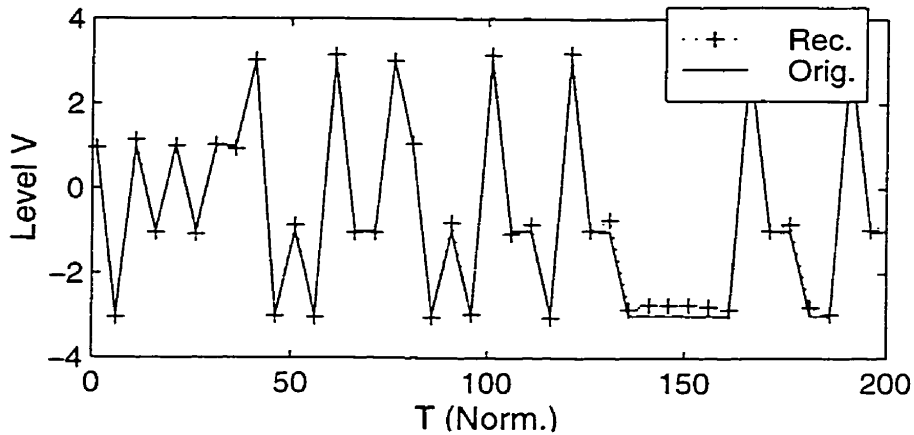


Figure 5.20. Comparison of 'Q' recovered data with original information signal from 16qam signal predistorted for harmonic upconversion.

Figure 5.21 shows the Q process from a 16QAM signal in which the phase precompression was not applied.

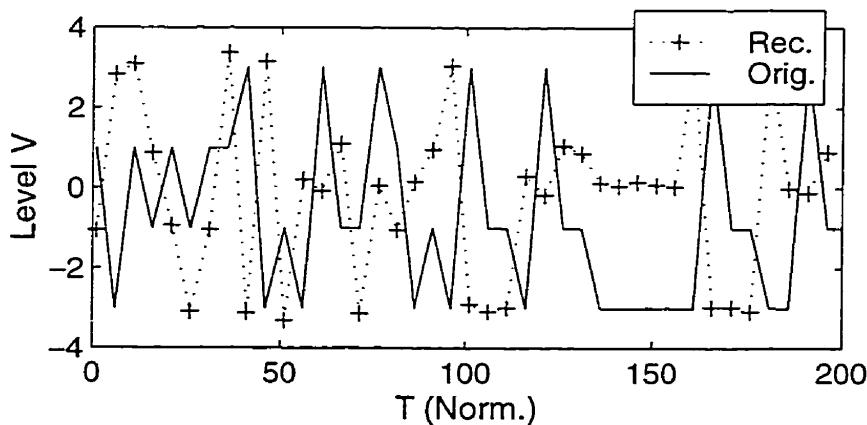


Figure 5.21. Comparison of 'Q' recovered data with original information signal from 16qam signal without phase pre-distortion.

The plot in Figure 5.21 verifies that the phase compression is crucial to this method. The constellation for the above process is shown in Figure 5.22.

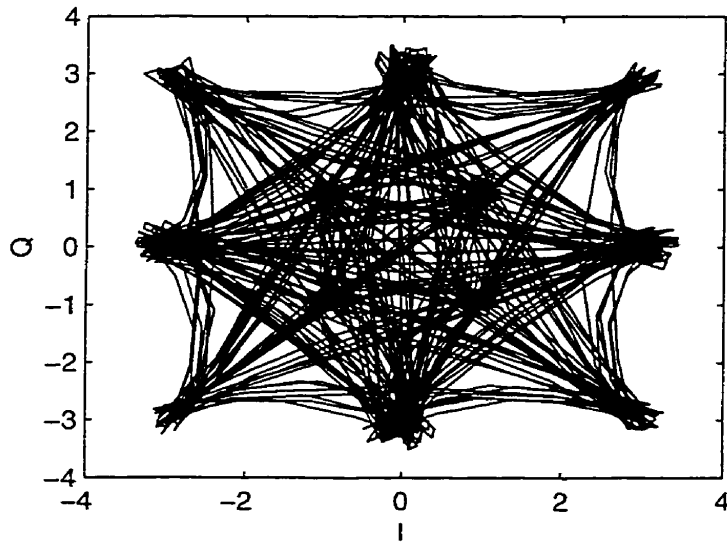


Figure 5.22. 16QAM signal without phase pre-distortion.

The plot shows that points in the original 16 point constellation have been collapsed and the resulting constellation is badly distorted. Figure 5.23 shows the harmonically upconverted 16QAM signal constellation without amplitude pre-distortion for a modulation index of 0.7 on the MZM and phase modulator.

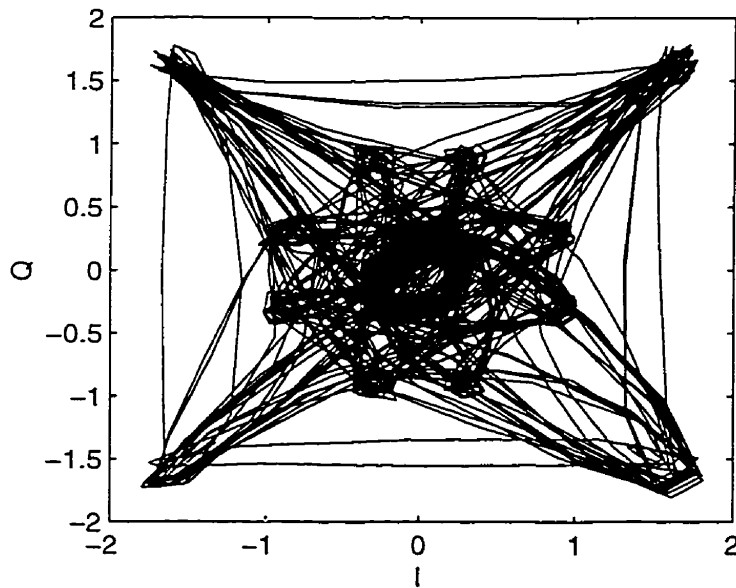


Figure 5.23. 16QAM signal without amplitude pre-distortion.

Again the constellation is badly distorted

5.4.2. Amplitude/Phase Predistortion and Fiber Dispersion

It was shown in Chapter 4 that the behavior of harmonic signal on dispersive links was somewhat more complicated than linear signals. This was due to the complex interactions of E-field harmonic components in the detector. In the Hartley MZM optical link the Fourier coefficient for the n th harmonic from a dispersive link is given by (5-14). It is apparent from this expression that changing the modulation index to a time varying quantity would possibly have the effect of inducing phase distortion on the desired harmonic. This was confirmed in the previous simulations of constant envelope signal where a rotation of the demodulated constellation was observed as a function of fiber length. If phase predistortion were implemented on an input subcarrier so as to produce a harmonic with a coefficient given by (5-14), The inherent undesired phase modulation that could arise as the result of varying the modulation index would affect the phase portion of the demodulated signal. To illustrate, Figure 5.24 shows a plot of the simulated phase and amplitude versus modulation index for an MZM/Phase OSSB link with a constant length of 60 km.

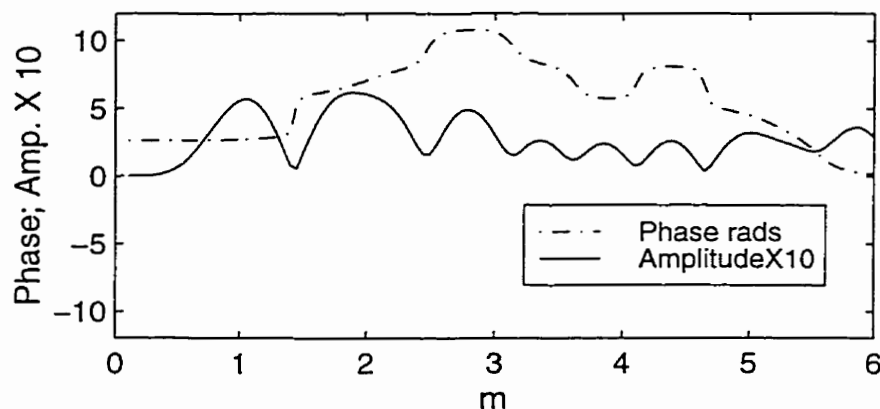


Figure 5.24. Phase and amplitude of 5th harmonic mzm/phase over 60 km dispersive fiber modulation index. $D = 18$ ps/(nm•km), $f_c = 18$ GHz.

The phase remains flat to about $m = 1$ and the amplitude characteristic has a usable section of piece-wise linear range from $m = 0.5$ to 1. This behavior is not

constant with fiber length, however, due to the general non-linear behavior of equation (5-14). This problem may be addressed by containing the range of the product of the modulation index and the fiber length to a range that ensures a piece-wise linear range will be attainable for modulation purposes. This is not obvious from equation (5-14) however this problem may be again addressed by using function minimization techniques. In any case, further investigation of the topic of phase and amplitude precompression for dispersive fiber links is left for further study and the discussion of predistortion techniques is concluded.

5.5. Conclusions

Theory and simulations have been presented that outline some of the pertinent issues regarding information subcarrier modulation on OSSB optical links. It has been shown that predistortion may be applied to phase modulated and QAM subcarrier signals for direct upconversion in non-linear optical modulators and other types of nonlinear harmonic upconverters in which the particular harmonic component is well characterized. The above simulations were non-optimal and they were only carried out to prove concept. The proper development scheme would be to search for more efficient methods of calculation of the signal amplitudes and phase compression relations. It is clear however that as a first effort at proving concept, the mentioned predistortion algorithms are worth further examination, especially in light of the potential system benefits. In Chapter 6, some of these issues will be addressed by experiment.

6. Proof-Of-Concept Experiments

6.1. Introduction

In this chapter the results of a series of experiments are presented that confirm some of the salient theory presented in the previous chapters. It will be shown that OSSB modulation serves as an effective mitigation for dispersion induced signal loss on linear and non-linear IMDD optical links. A series of experiments were also carried out to prove concept for the subcarrier phase modulation precompression scheme outlined in Chapter 5.

6.2. Studies

The following experiments were conducted:

1. An investigation of the transmission characteristics of CW subcarrier on dispersive fiber. This served as a verification that dispersion loss as a function of fiber length could be mitigated with OSSB modulation.
2. Verification that the information signal on Bi-phase phase-modulated BPSK subcarriers would survive the linear and non-linear optical modulation process.
3. Verification of the phase precompression method outlined in Chapter 5.

All of the later experiments in which modulated subcarriers were employed were done with a dual drive Mach-Zehnder modulator instead of a Mach-Zehnder - Phase modulator cascade. This was due to the unavailability of a suitable phase modulator for the harmonic modulation experiment within the time frame of the present study. Since the equivalence of the Hartley MZM and

the MZM/Phase modulator were established in Chapter 4, this represented a valid alternative.

6.2.1. Verification of Transmission Characteristics of CW OSSB Linear Subcarrier Modulation

In this experiment, three optical modulator structures were tested: a cascade of an external optical phase modulator and a dual drive Mach-Zehnder amplitude modulator (a 'hybrid' modulator) configured for OSSB, a solitary dual drive MZM configured for OSSB and a dual drive MZM configured for chirpless DSB modulation. A block diagram of the test bed configured for hybrid OSSB modulation is shown in Figure 6.1.

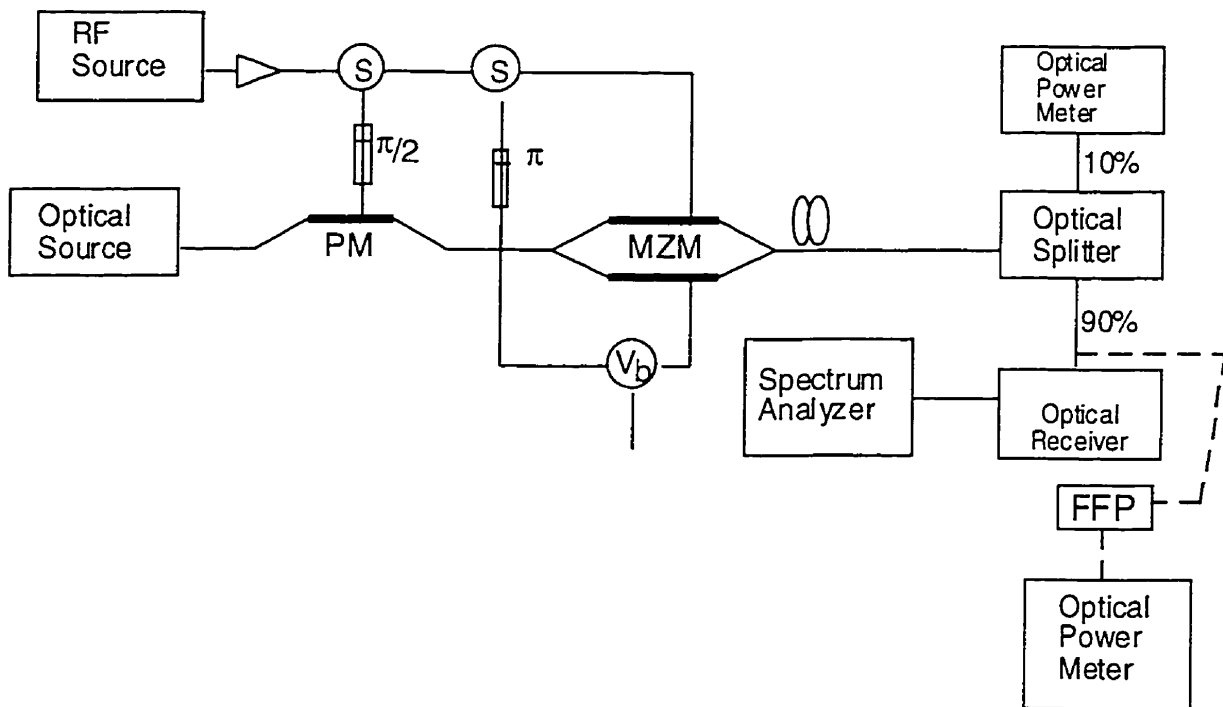


Figure 6.1. Experimental test bed for transmission experiments.

The optical source supplied a CW optical signal with linewidth 12 MHz to a UTP phase modulator which was in turn connected to the Lucent MZM. The phase modulator was placed first in the circuit due to the fact that it had polarization maintaining fiber on the input and output which ensured that the optical signal was injected into the MZM with proper polarization. The

MZM/phase modulator structure is commutative and so order is not important in the configuration. The signal from the MZM was then fed to an optical splitter with 10% and 90% outputs. The 90% output was fed to a New Focus 1011 optical photodiode receiver which was in turn connected to a spectrum analyzer to capture the demodulated subcarrier. To set up the optical spectrum the 90% output was also alternately connected to a Fiber Fabry Perot Device (FFP) which served as a tunable optical bandpass filter. The free spectral range (FSR) of the FFP was 40 GHz with a finesse of 400 giving it an optical bandwidth of 100 MHz. The 10% output was connected to an optical power meter to monitor the received optical power. To observe the transmission characteristics of the particular modulator structure, the optical and detected subcarrier power were simultaneously recorded as function of increasing dispersive fiber length. The experimental set-up in Figure 6.1 was used for the MZM/phase, Hartley MZM and the DSB MZM modulator classes. The input signals to the optical modulators were all CW type RF carriers. The output frequency of interest in both the linear and non-linear modulation experiments was approximately 17 GHz. This was achieved in the linear modulation experiment by simply injecting a 17 GHz CW signal with a small modulation index into the optical modulators. In the case of non-linear harmonic upconversion a subharmonic of approximately 3.5 GHz with a large modulation index was used and the fifth harmonic was captured at the optical link output.

6.2.1.1. Linear Modulation

In this test the RF drive signals were configured to be CW Hilbert Transforms, for the OSSB modulation and CW sign inverted signals for the double sideband (DSB) experiments. This was achieved by splitting the RF signal and phase shifting one of the splitter outputs with a line stretcher. The MZM was fed complementary CW signals for the DSB and MZM/Phase OSSB experiments. For the DSB test, the RF input to the phase modulator was grounded while for the hybrid OSSB test the phase modulator signal was acquired by phase shifting the MZM positive or reference signal by $\pi/2$ and feeding this signal to the phase modulator. For the Hartley MZM test the MZM was fed Hilbert CW

signals which were acquired by splitting the RF signal and shifting one of the splitter outputs by $\pi/2$. The three modulator structures are shown in Figure 6.2 - 6.4.

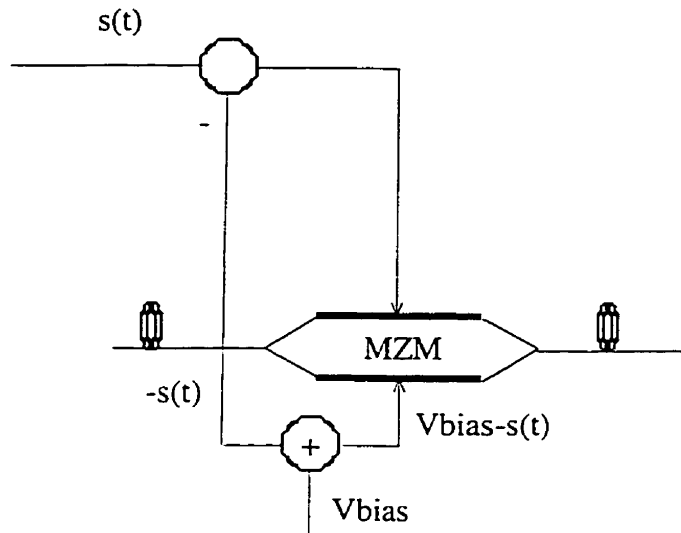


Figure 6.2. Chirpless DSB Mach-Zehnder modulator.

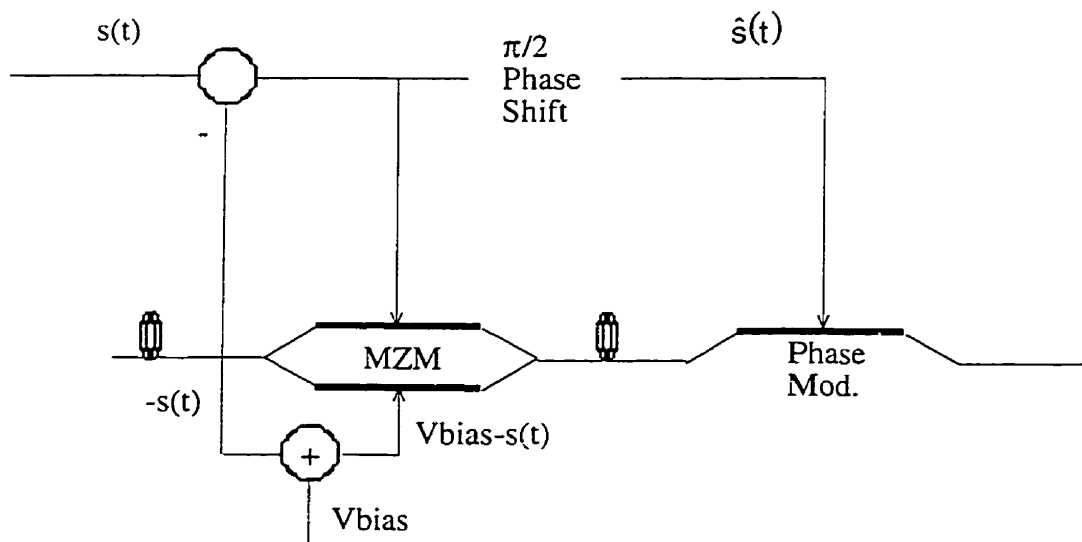


Figure 6.3. Cascaded MZM/Phase OSSB modulator.

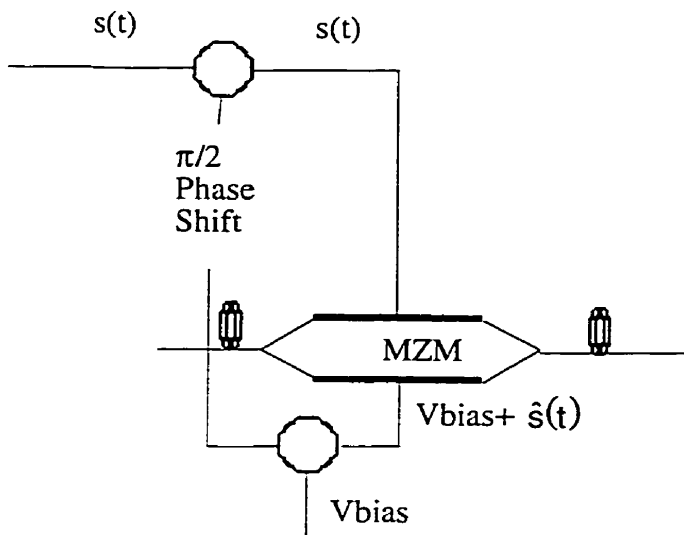


Figure 6.4. Hartley Mach-Zehnder modulator.

For the 17 GHz CW linear modulation, the phase shifts were easily carried out with a small coaxial line stretcher with maximum delay of 40 ps. This was due to the fact that a π or $\pi/2$ phase shift on the 17 GHz CW subcarrier signal was attainable with 28 or 14 ps of time delay in the line stretcher. Once the phase shifts were attained the CW signals were applied to the RF ports of the modulators at an amplitude that established a peak modulation index of 20% relative to the estimated RF extinction voltage of the device (~ 4 V). It was necessary to observe the power cancellation effects of the dispersion independent of the fiber loss and the variation in power readings due to the many connections that were required to increment the fiber length. To achieve this the measured optical power just before the detector was multiplied by 2 and subtracted from the measured RF power at the spectrum analyzer. Since the total optical power is unaffected by dispersion, this supplied an optical power reference at the detector. The bandpass filtered RF power at the spectrum analyzer would be affected by the aforementioned fiber attenuation and connection loss and also the detector specific power cancellation effects due to dispersion. Since the detector is a square law device, any optical loss in dB across the band is doubled in the detector output. Thus if the optical power in dB is multiplied by 2 and subtracted from the detected power the fiber and connections losses are normalized.

The method employed to capture the optical spectrum and verify the modulation conditions was to set up the optical modulator with the proper drive and bias and feed the DSB or OSSB optical signal to the FFP device. The FFP was then connected to a photodetector and driven with a swept DC voltage that was calibrated to cause the FFP to cover the required range of optical frequencies. This relatively early investigation involved the use of a digital oscilloscope to capture the output of the detector which was connected to the FFP output rather than an optical power meter. The spectral plots are shown in figures 6.3 - 6.5. The expected result was as outlined in Chapter 4.

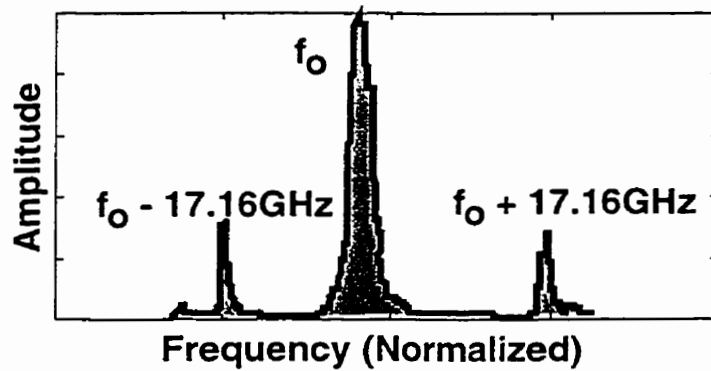


Figure 6.5. DSB experimental optical spectrum.

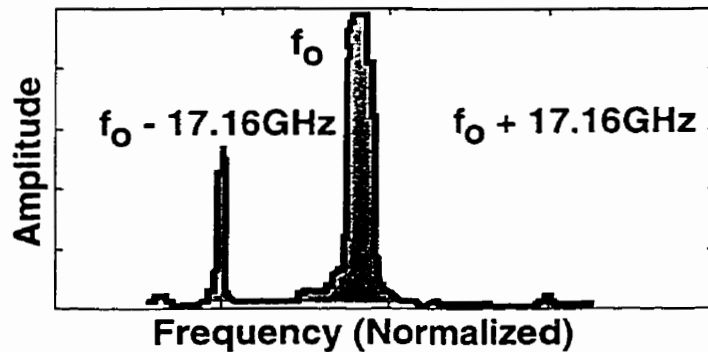


Figure 6.6. Experimental OSSB optical spectrum from cascade MZM/phase modulator.

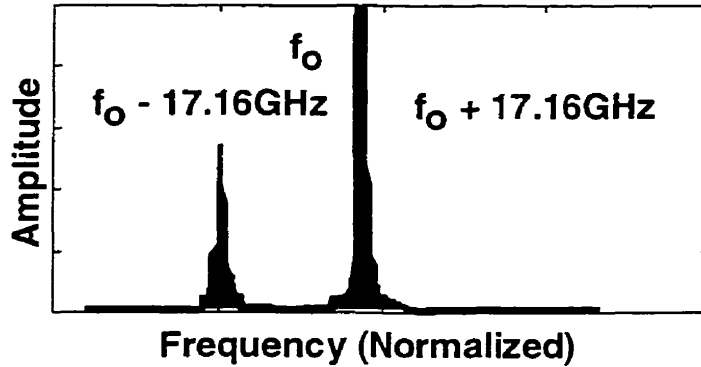


Figure 6.7. Experimental OSSB optical spectrum from Hartley configured MZM.

The appearance of the plots is rather crude since the method for capture was to simply copy the screen from the GPIB control program for the oscilloscope directly to a bitmap file. The sidebands are not equidistant from the optical carrier due to the nonlinear relationship between the FFP drive voltage and the tuned passband of the device. Additionally, the optical carrier component was cropped to enhance the vertical resolution of the sideband components and allows the relative quality of sideband cancellation to be observed. So while SSB modulation was achieved, no correspondence between the carrier and sidebands exists in the plots. The detected RF power as a function of fiber length is shown in Figure 6.8.

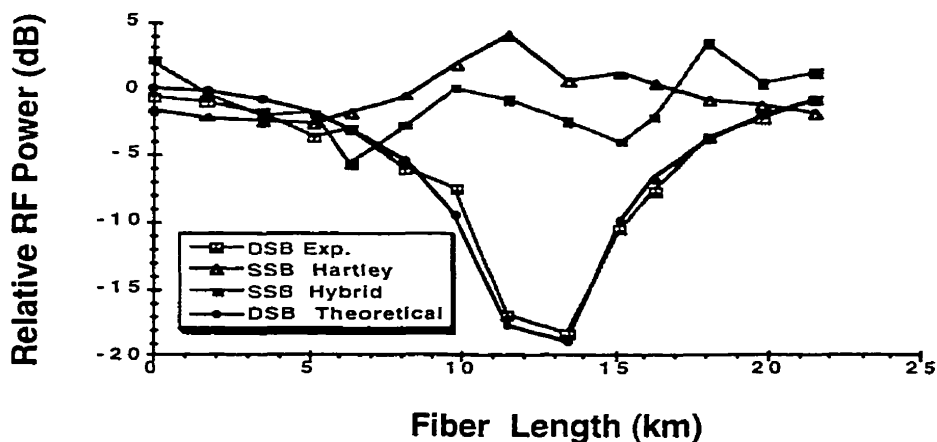


Figure 6.8. Detected power as a function of fiber length for DSB and OSSB modulation on dispersive Fiber, $D \sim 16.5 \text{ ps}/(\text{nm}\cdot\text{km})$, $f_c = 17.16 \text{ GHz}$, $\lambda_0 = 1550 \text{ nm}$, $m = 0.2$.

Observing the plots for the detected power for experimental and theoretical DSB, it is clear that the theory is sound as regards destruction of the detected power in dispersive fiber. The DSB plot shows the power null that is characteristic of this type of link. The experimental OSSB plots, while clearly indicating that SSB yields a power improvement, are far from perfect with approximately 6 dB of ripple about an average power level of about 0 dB. This was likely due to the method of observing the actual cancellation of sidebands in the optical spectrum. Modulator settings based on the coarse spectra in Figure 6.5 - 6.7 likely resulted in unresolved residual sideband being left to affect the measurement. The closeness of the DSB plot to theory would tend to confirm this conjecture since this case was easy to observe in the experimental method. Nevertheless the compensation potential with OSSB modulation is clear in the sense that the DSB detected power as a function of fiber length displays considerable signal destruction that is significantly improved with OSSB modulation.

A later experiment was performed on the DSB and Hartley configured MZM with the FFP output directly fed into an HP power meter. The optical spectrum is shown in Figure 6.9.

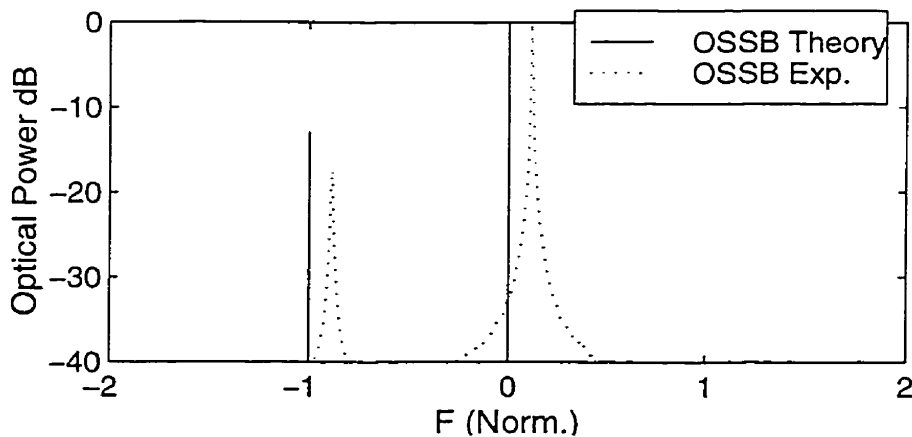


Figure 6.9. Theoretical and experimental linear OSSB electric field spectrum from Hartley MZM, $f_c = 17.35$ GHz, $m = 0.1$.

The peaks are offset slightly for ease of observation. In this case it is clear that the experimental optical output power in the lower sideband is reduced from theory. The bandwidth rating of the MZM used in the experiment was 8 GHz. However the slope of the magnitude of the specified frequency response is quite shallow with approximately 6 dB of loss observed at 16 GHz. Thus it was reasonable to use the device for the frequencies of interest. It is clear that while there is attenuation of the 17.35 GHz sideband, the performance of the device is better than expected from the specification sheet.

The corresponding detected power as a function of fiber length for the DSB and Hartley MZM OSSB modulation are shown in Figure 6.10. Clearly there is better performance when the modulator drive is set up properly. These results have been confirmed by other investigators also[26].

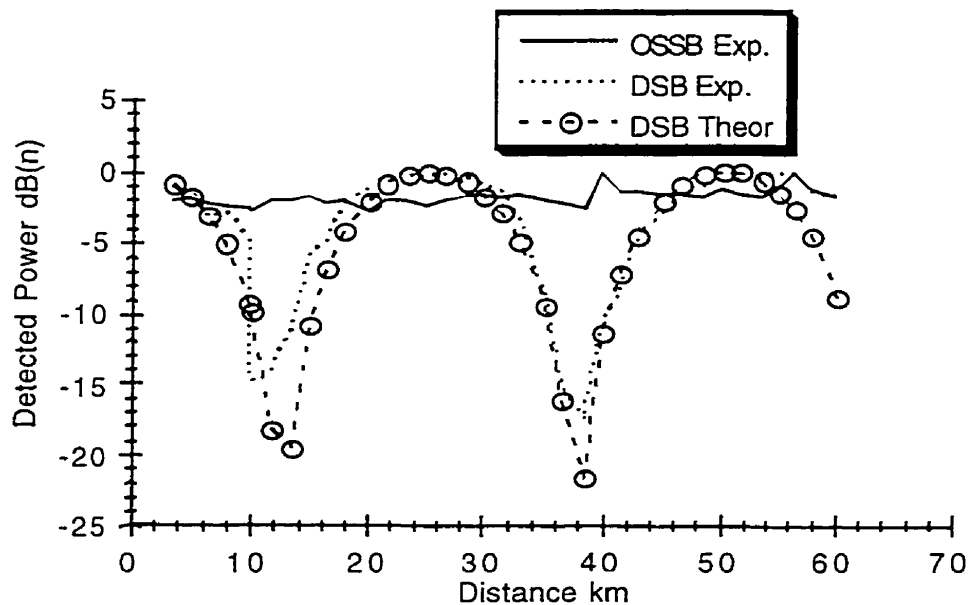


Figure 6.10. Detected power vs fiber length for OSSB and DSB over dispersive fiber, $m = 0.1$, $f_c = 17.16$ GHz, $\lambda_0 = 1550$ nm, $D \sim 16.5$ ps/(nm•km).

These preliminary experiments proved out two major theoretical points that were postulated in the previous chapters. Firstly that the periodic cancellation of the detected power from a subcarrier modulated optical signal is mitigated with OSSB modulation and secondly that the MZM/Phase modulator and the Hartley

MZM structure displayed equivalent behavior in transmission of linear CW subcarriers over dispersive fiber.

6.2.1.2. Harmonic Subcarrier Modulation

The second investigation focused on the transmission characteristics of harmonically upconverted subcarriers. It was shown in Chapter 4 that harmonic frequency translation was possible using the Hartley Mach-Zehnder modulator and the hybrid MZM/Phase modulator cascade. In this experiment the experimental test bed used for the linear modulation examination was again used to supply the drive signals to the optical modulators. The difference was that the drive voltages were now increased to approximately 0.7 relative to the rated $V\pi$ of the Mach-Zehnder and Phase modulator and the drive frequency was reduced to 17.35/5 or 3.47 GHz. The fifth harmonic at 17.35 GHz was captured at the link output.

Figure 6.11 shows the captured optical electric field spectrum of a double sideband signal from the Lucent MZM using the scanning FFP device and an optical power meter with large dynamic range. As with the plots in Figures 6.5-6.7, the misalignment of the harmonic peaks and the normalized frequencies on the abscissa on the plot is due to the nonlinear relationship between the FFP drive voltage and the actual location of the tuned passband of the device.

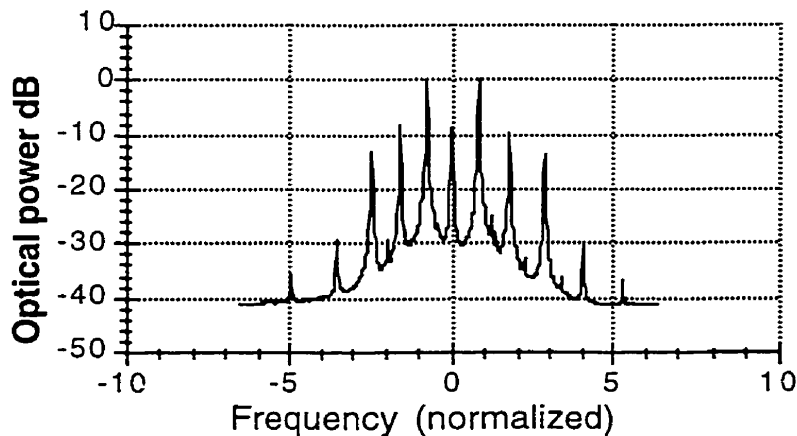


Figure 6.11. Experimental harmonic DSB optical spectrum for $m \sim 0.7$, $f_c = 3.47$ GHz, $\lambda_0 = 1550$ nm.

Comparing with a simulated plot from an ideal modulator shown in Figure 6.12, we see that the MZM device behavior for non-linear operation is reasonably close to theory. The accuracy of the experimental plot is affected by the resolution of the data acquisition method.

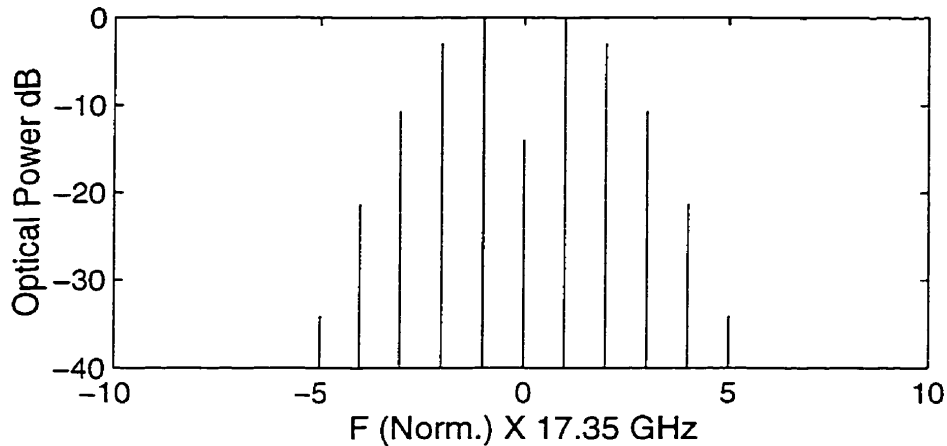


Figure 6.12. Simulated harmonic DSB optical spectrum, $m \sim 0.7$, $f_c = 3.47$ GHz, $\lambda_0 = 1550$ nm.

The experimental OSSB Harmonic spectrum from an OSSB Hartley configured dual drive Mach-Zehnder is shown in Figure 6.13.

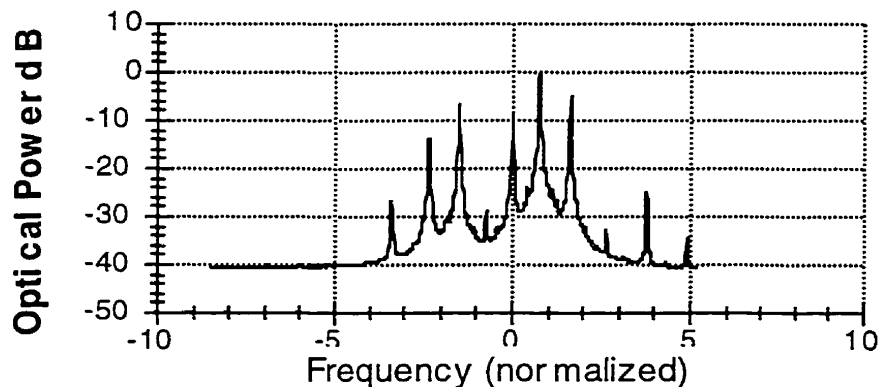


Figure 6.13. Experimental OSSB harmonic spectrum from OSSB Hartley MZM, $m \sim 0.7$, $f_c = 3.47$ GHz, $\lambda_0 = 1550$ nm.

Figure 6.14 shows the optical electric field from the OSSB cascaded MZM/PM modulator. In this case the cancellation is inverted to show that OSSB modulation may be applied to the upper or lower harmonic with symmetry.

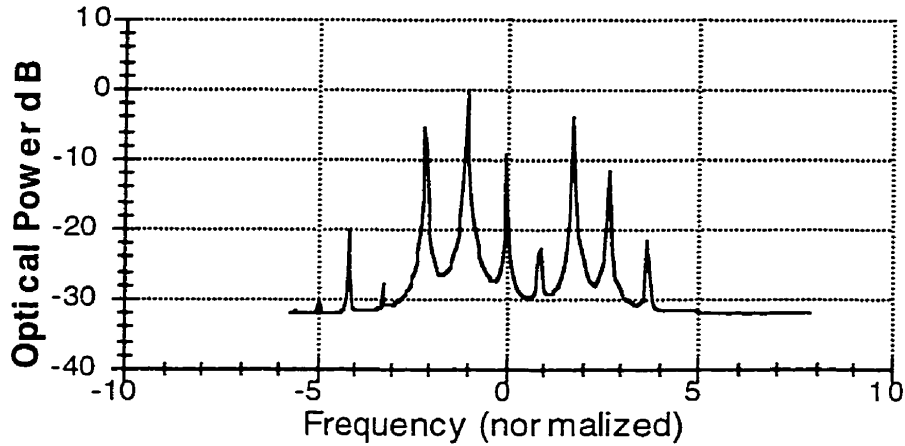


Figure 6.14. Experimental OSSB harmonic spectrum from OSSB MZM/phase hybrid modulator, $m = 0.7$, $f_c = 3.47$ GHz.

The theoretical OSSB spectrum for a MZM/Phase device with equivalent modulation index is shown in Figure 6.15.

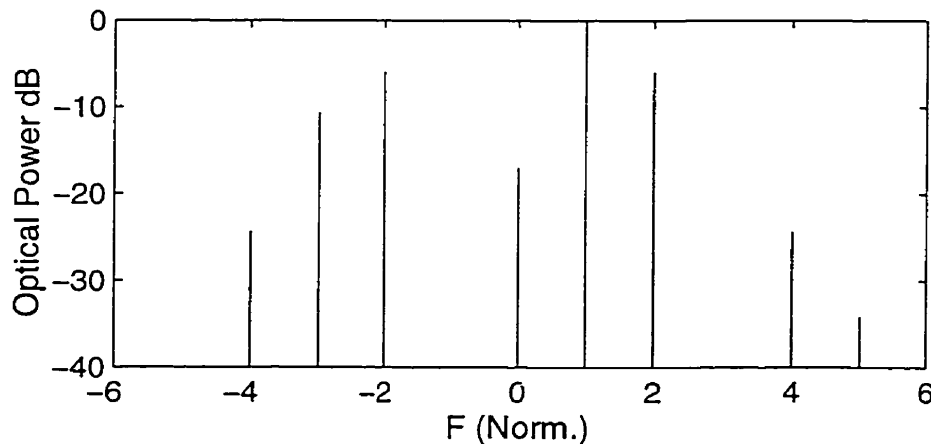


Figure 6.15. Simulated OSSB harmonic spectrum from OSSB MZM/Phase hybrid modulator $m \sim 0.7$, $f_c = 3.47$ GHz, $\lambda_0 = 1550$ nm.

Once again there is good agreement between theory and experiment for the non-linear OSSB spectrum. The enhanced drive condition of the hybrid device is apparent in the increase in sideband power over the Hartley MZM device. It is also apparent that the power in the sidebands that are above the 3 dB RF bandwidth of the MZM and the phase modulator (8 GHz) are not excessively attenuated over their theoretical counterparts in Figure 6.11. None of the theoretical spectral plots have been adjusted for device roll-off due to lowpass effects. This indicates that the MZM and the phase modulator are actually operating beyond their RF bandwidths. This is likely due to the fact that the non-linear process that produces the harmonics is actually contained in the optical substrate of the modulator which has a much higher bandwidth than that indicated by the device specification. As long as the signal that is applied to the optical modulators is within the RF bandwidth of the device, there is essentially no limit on the efficiency of the harmonic process and much higher harmonic frequencies are attainable at the modulator output than are indicated by the specified device bandwidth.

Figure 6.16 shows the experimental detected power as function of fiber length for the Hartley, MZM/Phase cascade and the MZM DSB modulator structures.

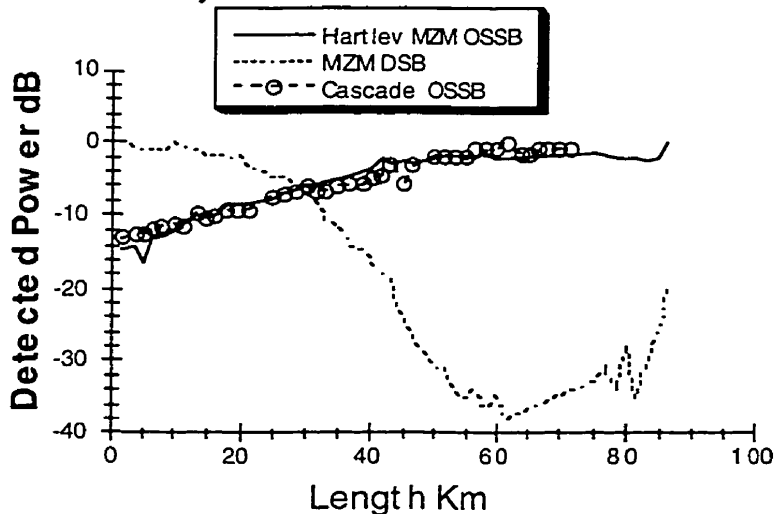


Figure 6.16. Experimental transmission characteristics of 5th harmonic modulation of CW subcarrier signals on dispersive fiber, $m \sim 0.7$, $f_c = 3.47$ GHz.

The plots in Figure 6.16 are normalized to their respective received optical power so as to remove fiber loss and also have been normalized to their respective maxima. Recall that the input and output frequencies were 3.47 and 17.35 GHz respectively. The transmission characteristics of the harmonic signal over increasing lengths of dispersive fiber is qualitatively similar to linearly modulated signals in the sense that there is degradation and subsequent improvement of the detected power as due to dispersion effects with DSB and OSSB modulation. Figure 6.17 shows a simulated plot for a similar case based on the theory from Chapter 4.

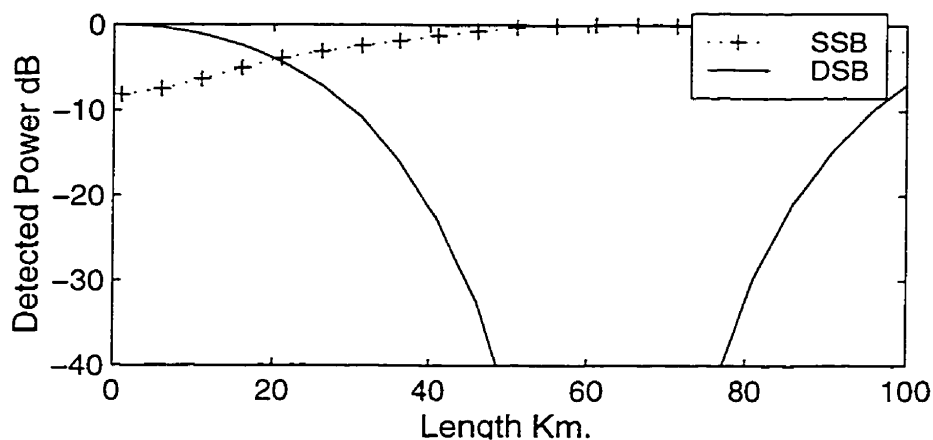


Figure 6.17. Power in H5 as a function of fiber length for a ‘chirpless’ MZM and an OSSB Hartley modulator, $m = 0.7$, $D = 16.5$ ps/(nm•km), $f_c = 3.47$ GHz.

It is clear that the experimental and theoretical plots are similar.

The detector output power conversion characteristics were investigated. However it was found during regular investigations that the New Focus 1011 wideband detector that was used in the experiment had been damaged. This had an effect on the RF spectral flatness at the output of the device. It was confirmed that the linearity in the output power characteristics of the device was valid at the frequency investigated. The spectrum was investigated later with a different device and, while this device had a good spectral response the output from the detector was quite non-ideal in terms of the expected harmonic

content. Due to these experimental issues plus the theoretical complexity of this issue, the experimental conversion properties were not addressed. It was clear that sufficient power was available to confirm the transmission characteristics and this was deemed sufficient from the perspective of proving concept for the transmission and modulation issues addressed in the previous chapters.

6.3. Modulated Subcarriers

In this third experiment the characteristics of modulated subcarriers were examined to address some of the modulation schemes that may be employed in linear and harmonic radio-on-fiber. Since the optical link and its effect on the signal is the focus of the study, little attention was given to the effects of the radio channel on the signal. This kind of information is readily available in the literature and the present examination is restricted to back-to-back measurements in which the transmitter and receiver modules were connected via cable over the RF path. Additionally all of the modulation experiments were carried out on a single dual drive Mach-Zehnder modulator rather than the cascade device consisting of the MZM and phase modulator. This configuration was chosen for a number of reasons. Firstly it was discovered shortly after the data was collected for the harmonic transmission experiments outlined above (Mid 1997) that the resistive termination for the phase modulator was likely rated well below the required drive voltage required for harmonic upconversion with the hybrid modulator. It was also rated well below the '27 dBm Maximum RF Power' stamped on the modulator body. There was no option to upgrade the device due to packaging constraints. Secondly, since the hybrid structure is equivalent to the Hartley Modulator as has been shown in theory and experiment, verification of the theory was valid on the dual drive MZM device. At this writing the author has acquired a prototype hybrid device with significantly more robust drive capabilities but final testing of the device will be relegated to future work.

6.3.1. Linear BPSK Modulation

In this experiment the **I.R.I.S.** development system (See appendix A) was used to create waveforms and perform modulation and demodulation of all RF waveforms. In the present case the IRIS system was used to produce radio subcarriers that were used in linear and harmonic modulation and to recover the RF signal that was emitted from the optical link

A block diagram of the test bed used for both the linear and nonlinear modulated subcarriers is shown in Figure 6.18.

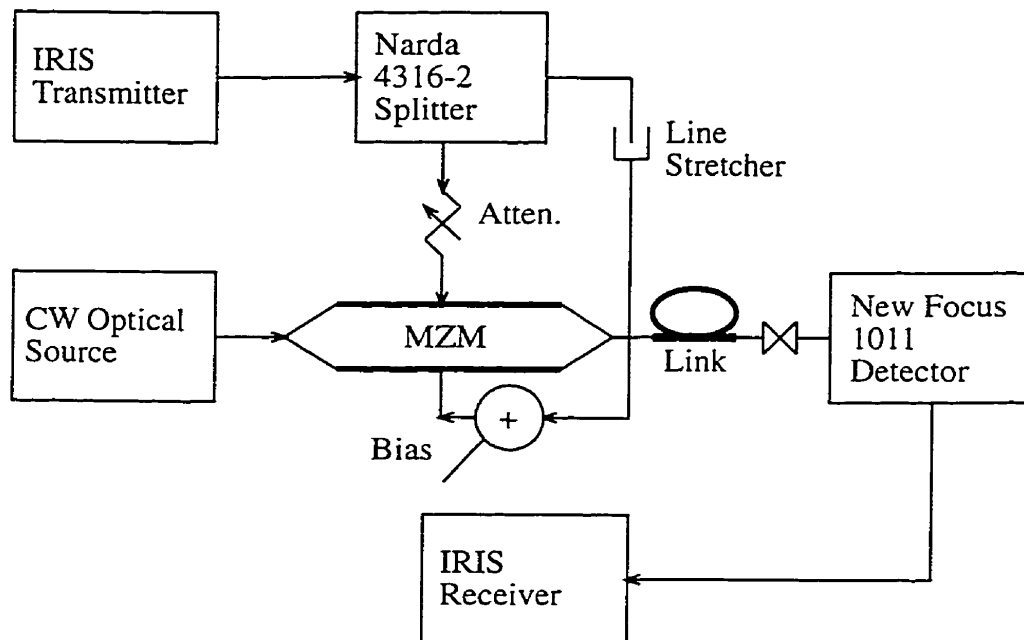


Figure 6.18. Linear modulation test bed.

The modulating signal was a 17.35 GHz subcarrier signal with varying bandwidths composed on the IRIS transmitter and then split in the Narda Splitter. One version of the radio subcarrier signal was run directly to the upper arm of the MZM while the other signal was run through a line stretcher to change the phase offset to π rads for the DSB modulator tests or $\pi/2$ rads for the OSSB tests. There were obvious concerns relating to the time alignment of the individual signals, so care was taken to ensure that the actual differences in

length of the overall path from signal source to modulator arm did not degrade the output signal. For comparison, an eye diagram of the test bed in back to back mode with the optical link components removed, is shown in Figure 6.19.

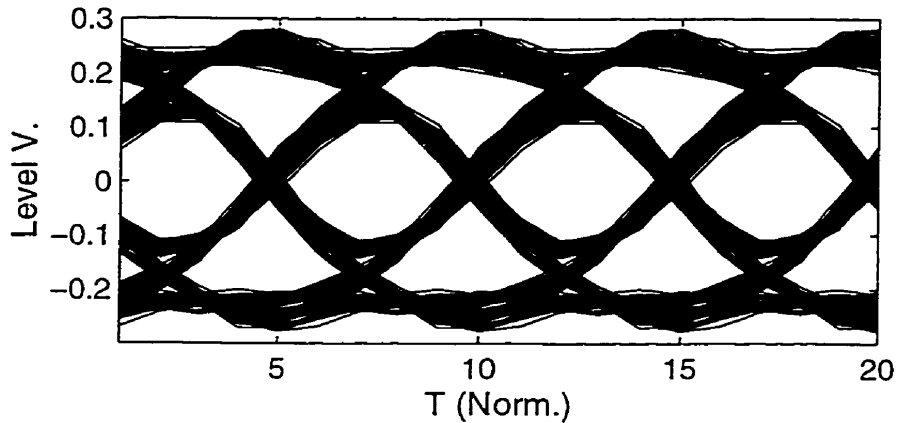


Figure 6.19. Eye diagram of test bed in back to back mode on 17.35 GHz radio carrier At B = 200 Mb/s.

Additionally it was found that an optical amplifier was required to enable capture of the digital signal at the detector for the longer fiber lengths. This was done to normalize the received power at the detector for each fiber length and allow the signal attenuation properties of the dispersive fiber to be observed exclusive of fiber loss.

The first experiment on the linear subcarrier modulation test was to confirm that the modulation was lost when the optical signal was detected at a fiber link distance that corresponded to a power null for the experimental conditions. It was concluded from transmission experiments that the first power null for linear operation at 17.35 GHz was at approximately 12 km. This would correspond to a fiber dispersion parameter of about 16.5 ps/nm•km. A received eye diagram of a 200 MB/s BPSK pseudonoise sequence on a zero length fiber was captured at the IRIS receiver. The result is shown in Figure 6.20.

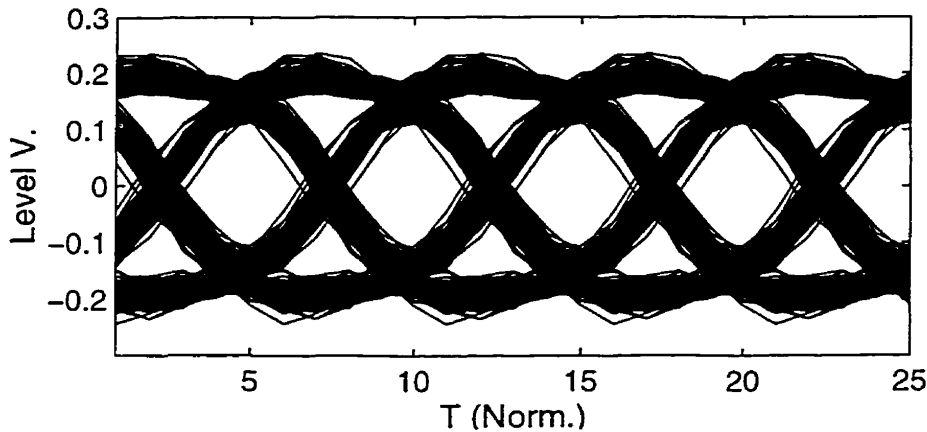


Figure 6.20. Eye diagram for 200 MB/s BPSK signal on DSB linear 17.35 GHz radio carrier and zero length fiber, $m = 0.1$.

The optical link degradation is apparent in the widening of the trace indicating more noise and sampling jitter. However the signal quality is good. To verify that the DSB signal was effectively extinguished at the null point, an additional eye diagram was captured at a fiber distance of approximately 10 Km. The resulting eye diagram is shown in Figure 6.21.

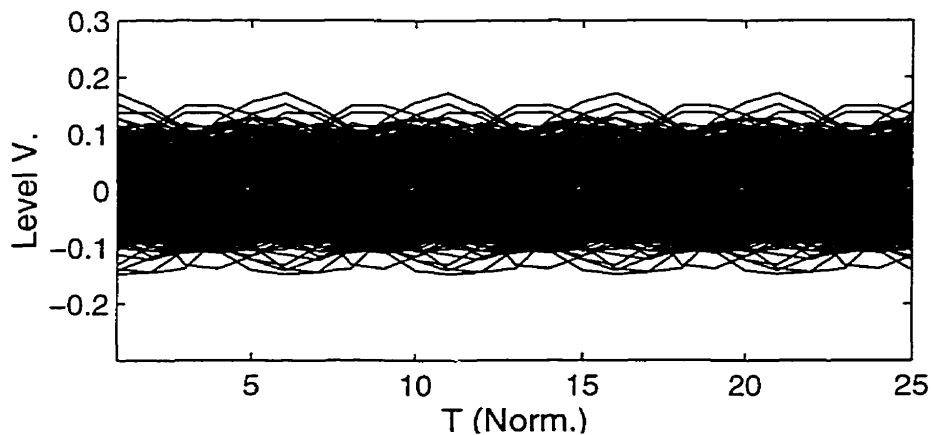


Figure 6.21. Eye diagram for 200 MB/s BPSK Signal on DSB linear 17.35 GHz radio carrier 10 km fiber (at null), $m = 0.1$.

Clearly the information has been destroyed. Another eye diagram was taken at approximately 20 Km and the signal returned as shown in Figure 6.22.

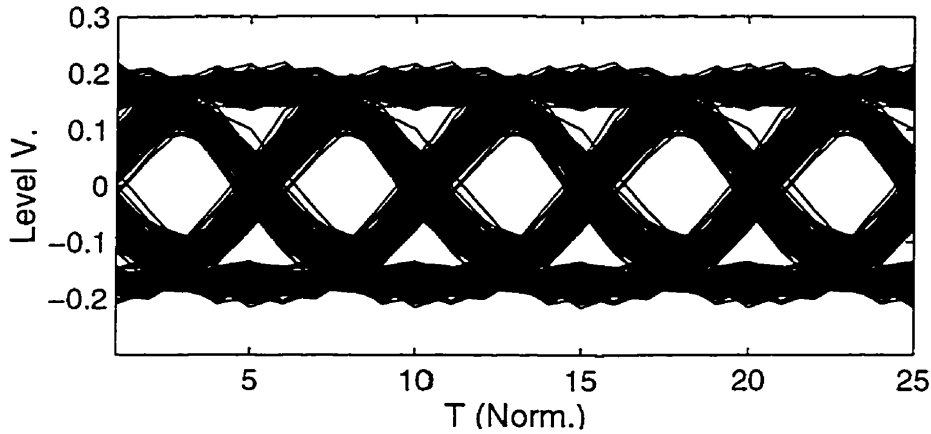


Figure 6.22. Eye diagram For 200 MB/s BPSK signal on DSB linear 17.35 GHz radio carrier at 20 Km fiber, $m = 0.1$

Finally to show that OSSB modulation mitigated the signal loss at 10 Km, the eye diagram is shown for OSSB at 10 Km in Figure 6.23.

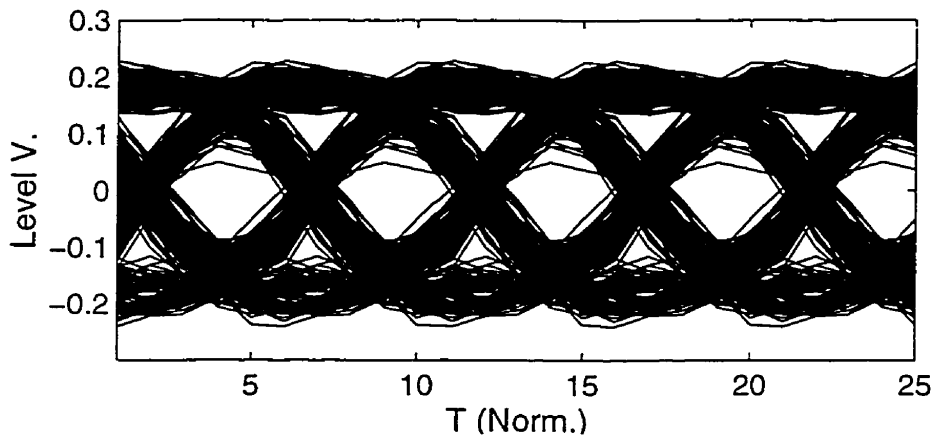


Figure 6.23. Eye diagram For 200 MB/s BPSK signal on OSSB linear 17.35 GHz radio carrier at 10 km fiber, $m = 0.1$.

The signal quality is slightly degraded from that for the DSB signal at 20 Km. Nonetheless the signal is much improved over the nulled DSB eye diagram in Figure 6.21. It was also noticed that the eye quality of the OSSB modulation was slightly degraded at zero length over the quality of the DSB eye. It is likely that a timing error between the optical modulator drives was introduced by the line stretching operation that was done to acquire the subcarrier Hilbert

Transform. This would distort the information signal. In any case it is clearly shown that OSSB modulation compensates for dispersive cancellation of the radio signal on moderate fiber lengths.

6.3.2. Linear QPSK Modulation

In the QPSK modulation experiment a QPSK constellation was composed by generating a binary PN sequence and then mapping individual dibits into a quadrature signal. This quadrature signal was modulated onto a 17.35 GHz radio carrier in the IRIS system and fed to the optical modulator. Figure 6.24 shows the constellation of the QPSK signal in back to back mode with the fiber subsystem removed.

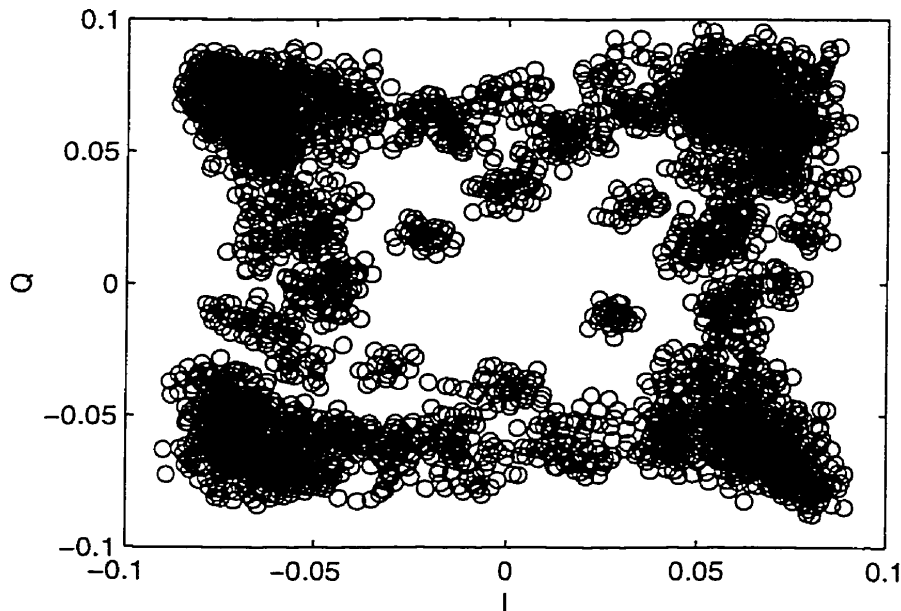


Figure 6.24. Constellation For 100 MS/s QPSK signal on back-to-back 17.35 GHz radio carrier.

Figure 6.25 shows the received constellation for a 100 MS/s QPSK signal on an OSSB optical link.

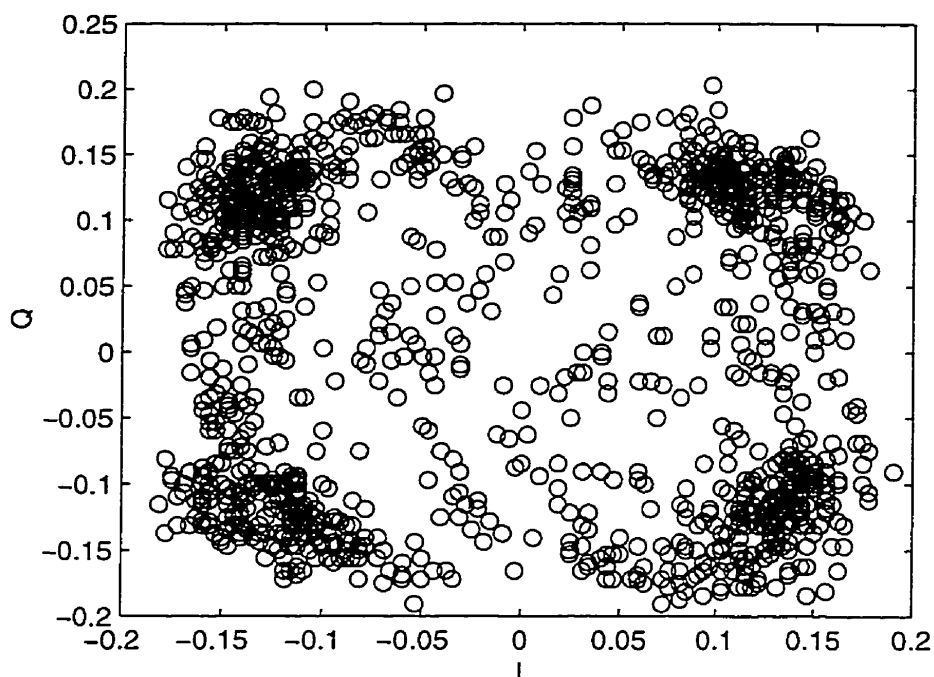


Figure 6.25. Constellation For 100 MS/s QPSK signal on OSSB linear 17.35 GHz radio carrier at 10 km fiber

The signal is detected at a fiber distance that would produce a complete loss of signal for Optical DSB modulation (10 km). The 4 constellation points are clearly visible with points outside the proper decision regions due only to transition samples. The constellation is more rounded in comparison to the back-to-back constellation in Figure 6.24. The corresponding eye diagram of the I process is shown in Figure 6.26.

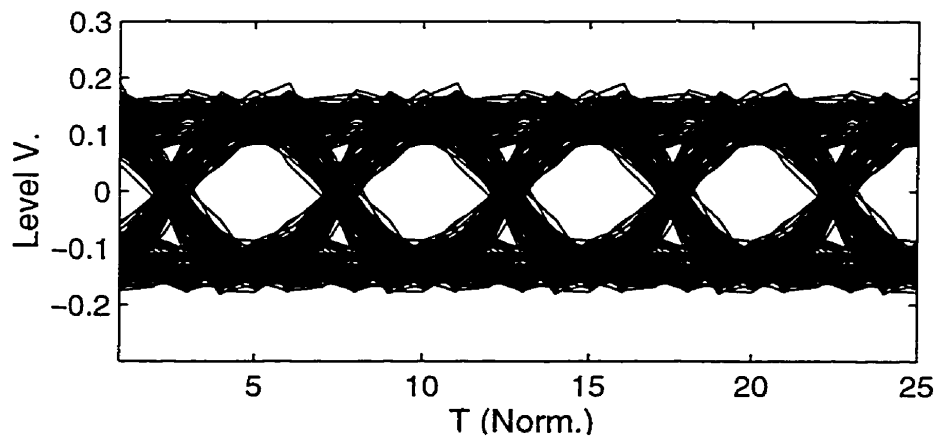


Figure 6.26. Eye diagram For 100 MS/s QPSK signal I process on OSSB linear 17.35 GHz radio carrier at 10 km fiber, $m = 0.1$.

The eye in this case is of good quality and although exhaustive BER testing was not done, it is apparent from the eye diagram that the above signal would yield high quality data transmission.

6.3.3. Linear Link Characteristics

The linear OSSB link showed good potential as a trunking element. The system was quite easy to set up and the manual method of phase shifting was adequate for the signal bandwidths used. This represents a significant hardware saving since phase shifting the RF subcarrier before modulation would require another mixer and bandpass filter. The MZM was found to drift from its operating point quite easily. However the robustness of the OSSB modulation scheme made the overall success of the data transmission scheme immune to drifting effects. In all, the theoretical claims regarding dispersion improvements for linear subcarrier links were confirmed in this experiment and no further results were sought.

6.4. Harmonic Modulated Subcarriers

The Harmonic Modulation test bed was identical to the linear test bed except that the drive stage of the IRIS transmitter was upgraded to handle the increased power required to drive the optical modulator at the desired modulation index. Additionally the input subcarrier frequency was reduced to 3.47 GHz so as to cause the optical link to produce a 17.35 GHz subcarrier at the selected 5th harmonic link output. The non-linear link output signal was treated identically to the linear link output. The maximum drive capability of the Lucent modulator used in the experiment was limited by the 1/2 Watt terminations on each modulator arm. This limited the peak drive voltage to about 7 Volts or approximately 200% of the measured V_{π} of the device at DC. It was noted however that the RF V_{π} increased to about 4.5 volts at a drive frequency of 3.47 GHz. This fact plus an observed inconsistency between the measured amplifier output and the harmonic behavior of the modulator, suggesting an impedance mismatch, indicated that the most prudent course

would be to limit the drive voltage to about 70% of V_{π} . This would also maintain consistency with the transmission experiments above. In any case the drive voltage was adequate to confirm the theoretical issues of interest. DSB and SSB data was collected for each experiment to illustrate the particular dispersion properties of the fiber in each case.

6.4.1. Biphase Modulation

In this test a binary PN sequence was modulated onto the 3.47 GHz subharmonic optical input RF carrier. This signal was amplified so as to deliver a modulation index of approximately $0.7 V_{\pi}$ to the MZM. The 5th harmonic of the input frequency was captured at the detector output and amplified by approximately 50 dB and demodulated in the IRIS receiver. Biphase modulation has a natural immunity to the inherent phase distortion in harmonic upconversion. This is due to the fact that for odd order harmonics a ' π ' phase shift simply becomes a $(2n+1)\pi$ phase shift and from the perspective of the demodulator the ' $2n$ ' part is invisible. This may be confirmed by simply demodulating the upconverted carrier and checking the resulting signal for accuracy. This was done and the resulting eye diagram is shown in Figure 6.27.

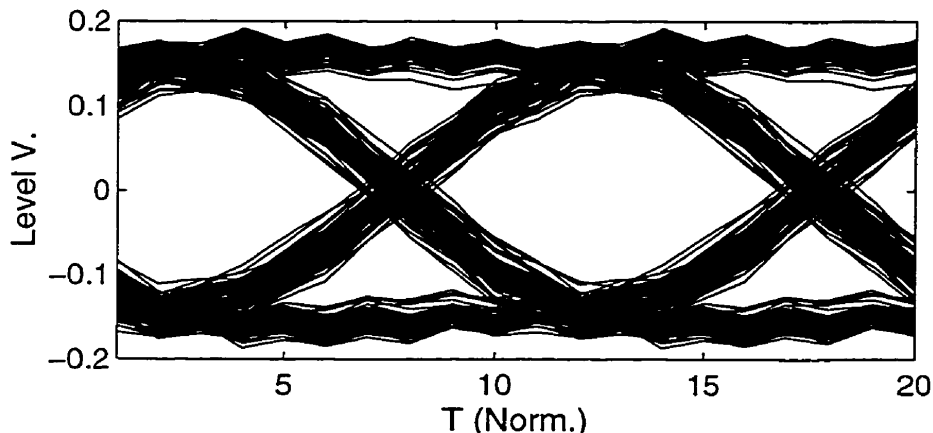


Figure 6.27. Eye diagram for H5 Hartley MZM upconverter with 100 MB/s BPSK modulation, $L = 60$ km.

It is immediately apparent that the eye quality is quite good. In order to verify the accuracy of the information, the method from Chapter 5 employing the cross correlation properties of pseudo noise sequences is used. Figure 6.28 shows the correlation function for the recovered data of Figure 6.27

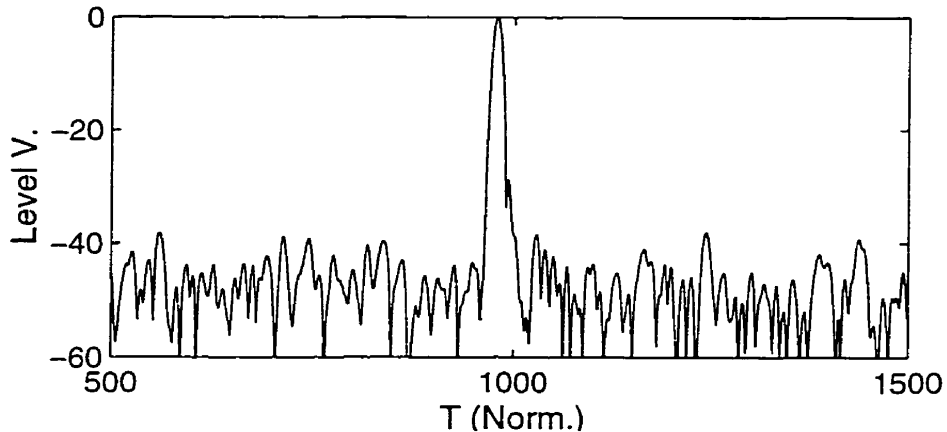


Figure 6.28. PN correlation function from BPSK data on H5 Hartley MZM harmonic upconverter.

The mean of the noise process in Figure 6.28 was calculated to be approximately -50 dB with a standard deviation of -53. This means that the information signal is accurate and practically noise free. This examination shows that the information stream for subcarrier BPSK modulation is unaffected by harmonic upconversion over non-linear optical links. It was additionally confirmed by experiment that the DSB signal was essentially destroyed by fiber dispersion at a link distance of 60 Km at which the detected signal is in a power null due to dispersion effects.

6.4.2. Quadrature Modulation

While it is encouraging that BPSK data streams can be successfully transmitted over nonlinear optical links, it is necessary to recognize that some type of phase modulation is required if the optical link succeeds as a practical fundamental element in radio systems. BPSK has limited application in real radio systems and will only work correctly for odd harmonics and for this reason the phase

compression algorithm in Chapter 5 was modified from [68] and adopted for the present purpose so as to provide a general method of pre-conditioning digital data for harmonic frequency translation. This section deals with the experimental verification for the phase compression algorithm developed in Chapter 5. Once again the IRIS transmitter was utilized to synthesize the modulating signal which was a 3.47 GHz subcarrier modulated with the phase compressed QPSK information signal.

The signal used in this examination was acquired by first generating a binary PN sequence and then mapping the sequence into a QPSK constellation. This type of modulation would require coherent demodulation at the receiver which was easily accomplished using the IRIS system receiver's flexible demodulation capability. Again the fifth harmonic was captured at the output of the optical link. Shown in Figure 6.29, is the QPSK phase constellation that has been compressed by a factor of 5.

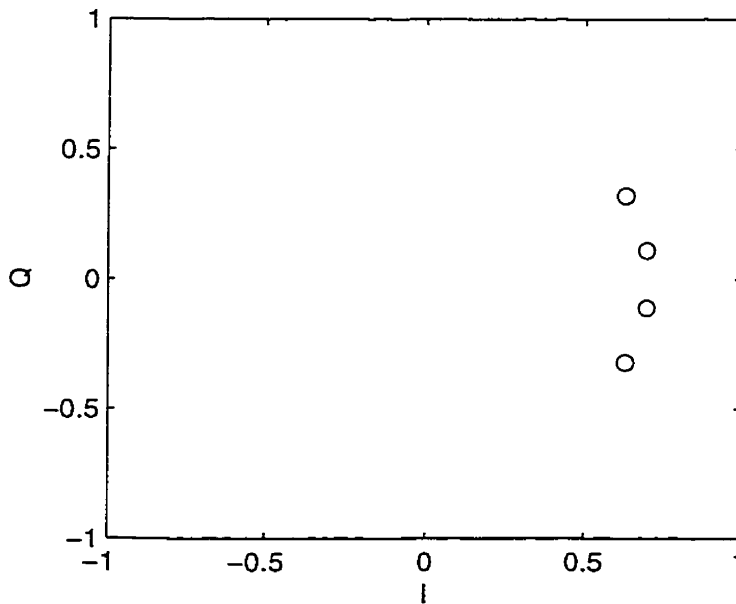


Figure 6.29. Compressed input constellation.

The test for accuracy of the information sequence was carried out in the same manner as with the BPSK experiment. In the QPSK case however the carrier reference had to be recovered and the data decoded from the received constellation. This was achieved by embedding sections of constant DC offset in the signal at specific phase angles. At the receiver the constellation was rotated until these sections of constant amplitude were at the correct phase angle. This was found to be a manageable problem and the data was recovered quite easily.

Shown in Figure 6.30 is the recovered constellation of a 5 MS/s QPSK signal after phase compression and subsequent 5th order harmonic conversion over a harmonic double sideband MZM optical link. For the constellation in Figure 6.30 the received baseband sampling rate was 10 per symbol so some samples were captured during state transitions causing the constellation to loose some detail.

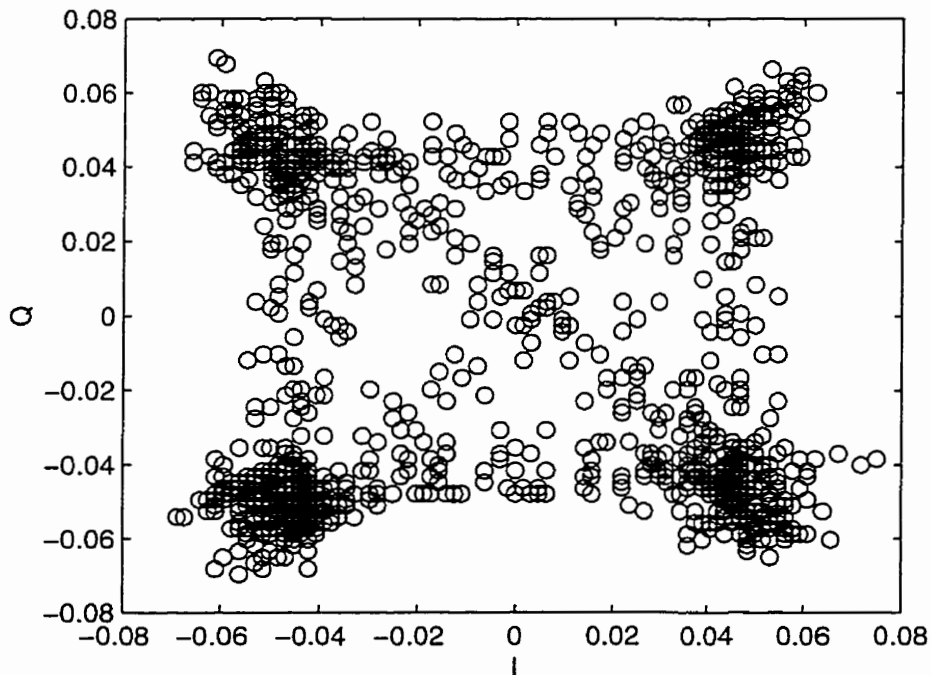


Figure 6.30. Recovered QPSK constellation From 5th order harmonic upconverter at data rate 5 MS/s, $m = 0.1$, $\lambda_0 = 1550$ nm, $D \sim 16.5$ ps/(nm•km)

An Eye Diagram of the recovered inphase (I) process is shown in Figure 6.31. which indicates a good SNR condition.

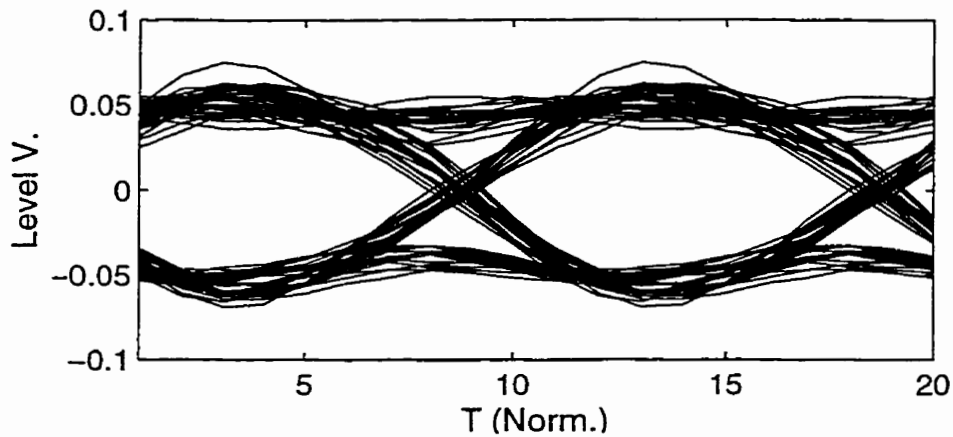


Figure 6.31. Eye diagram from recovered QPSK constellation from zero length fiber 5th order harmonic upconverter at data rate 5 MS/s.

The data was demodulated, interleaved and correlated with the original information sequence to verify the accuracy of the received sequence. The results are shown in Figure 6.32.

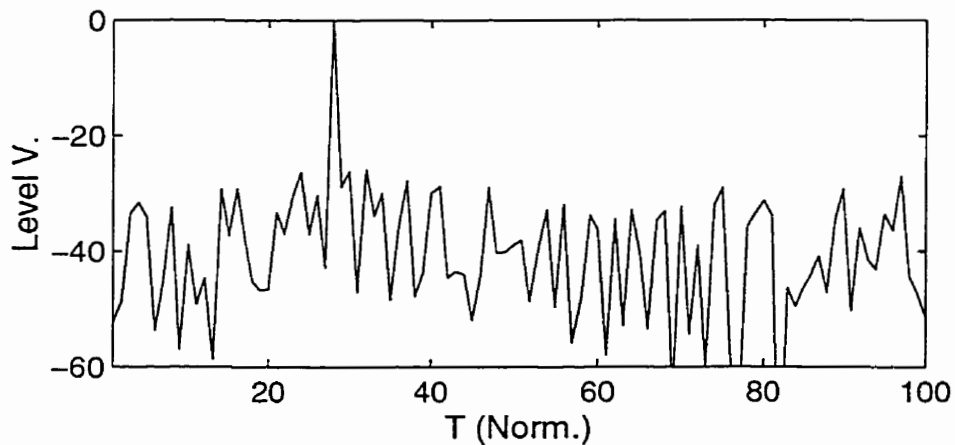


Figure 6.32. Correlation function for recovered data from QPSK phase compressed signal in Figure 6.29.

In this case a 255 bit PN sequence was used as an information signal. This length of sequence would cause a correlation spike of height 48 dB. The fact

that the correlation spike rises approximately 42 dB out of the noise indicates that more noise is apparent in this measurement than was observed for the previous BPSK test. This was likely due to the fact that a quadrature modulation scheme would be more vulnerable to phase noise than a BPSK system. The general rule for harmonic systems is that there is a 6 dB increase in phase noise for every octave of frequency translation. In the present case the 5th harmonic of the input frequency is selected for a frequency translation of 2.32 octaves causing an extra 14 dB of phase noise to be present in the link output. This noise process could easily account for the added 4 dB of noise observed in the quadrature measurement.

6.4.2.1. QPSK On Dispersive Fiber

In Chapter 4 we showed in simulation that dispersion had little or no effect on the integrity of compressed QPSK signals over dispersive fiber. To verify this experimentally. In this experiment, we examine a 100 MB/s (50 MSym/s) QPSK signal on a fiber length of 60 Km. The constellation is shown in Figure 6.33.

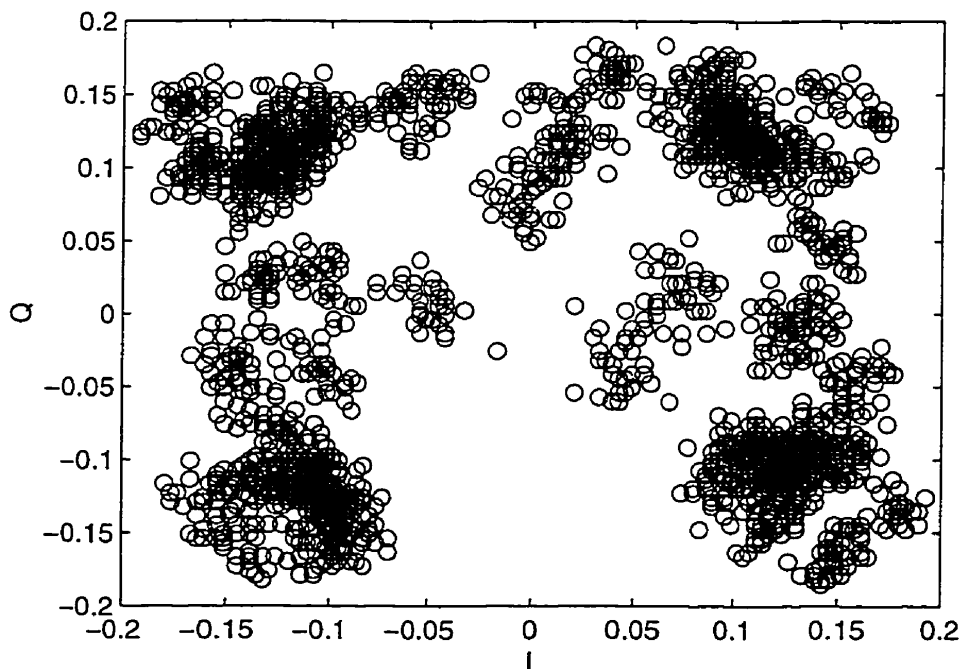


Figure 6.33. Constellation for QPSK phase compressed signal at 50 MS/s, $f = 17.35$ GHz, $L = 60$ Km.

The eye diagram of the recovered data is shown in Figure 6.34.

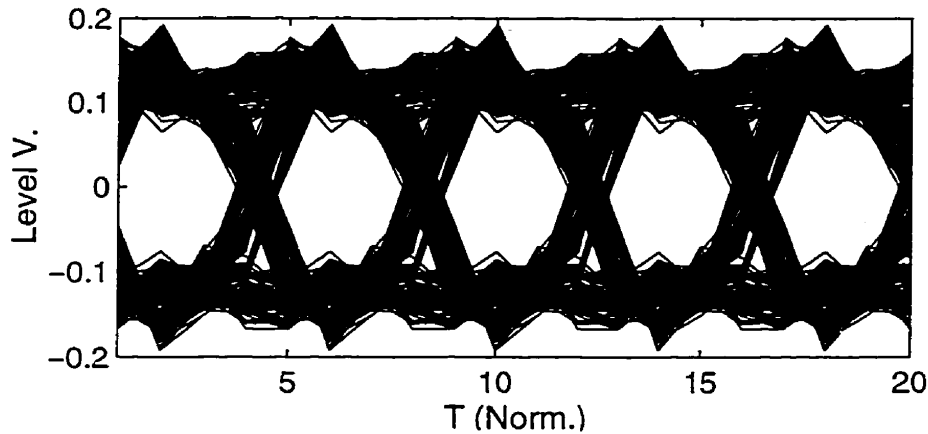


Figure 6.34. Eye diagram for I process for QPSK phase compressed signal at 50 MS/s, $f = 17.35$ GHz, $L = 60$ Km.

and the accuracy of the data was confirmed in the same manner as for the 5 MSym/s data above and shown in Figure 6.35.

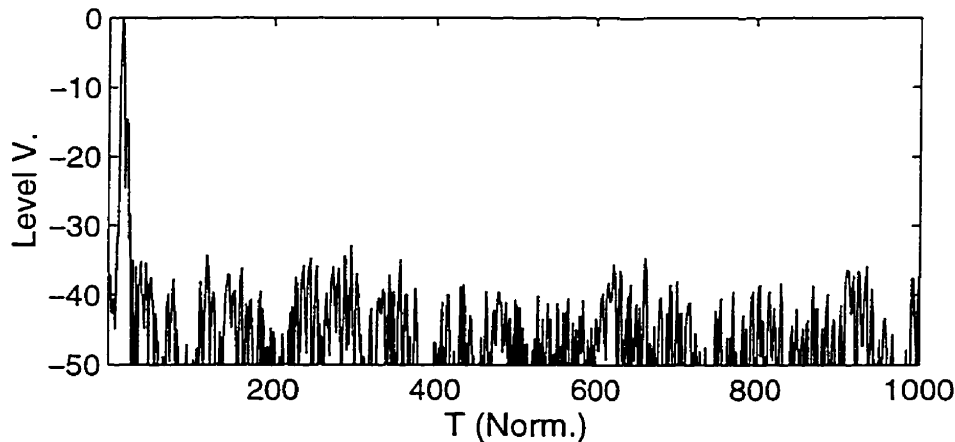


Figure 6.35. Correlation function for recovered data from $\pi/4$ 50 MS/s OSSB QPSK phase compressed signal over 60 km of dispersive fiber $f = 17.35$ GHz.

In this case a 1023 point PN sequence was used and it is quite clear that more noise is present in the tail of the correlation function in Figure 6.35. This is due

to the expanded bandwidth of the measurement system and possibly due to the added presence of the EDFA. Also there is an added noise component due to the length of dispersive fiber. The latter comes about due to the fact that there is a finite phase noise component in the laser output that, when transmitted through a dispersive fiber, converts to amplitude noise[70]. This process was partially confirmed in Chapter 4 when it was shown that a signal consisting of pure phase modulation could be converted to amplitude modulation through a dispersive fiber. In the case of laser phase noise, the process is transmitted through the detector and shows up in the demodulated signal.

In any case the signal in Figure 6.34 is of adequate quality to confirm the theoretical claims made with regard to the functionality of the phase compression scheme.

We conclude the experimental investigation with the Phase compressed QPSK data, transmitted over a 3 meter radio channel at 17.35 GHz. Shown in Figure 6.36 is the eye diagram of the Q process for a 5 MS/s QPSK signal on a zero length fiber.

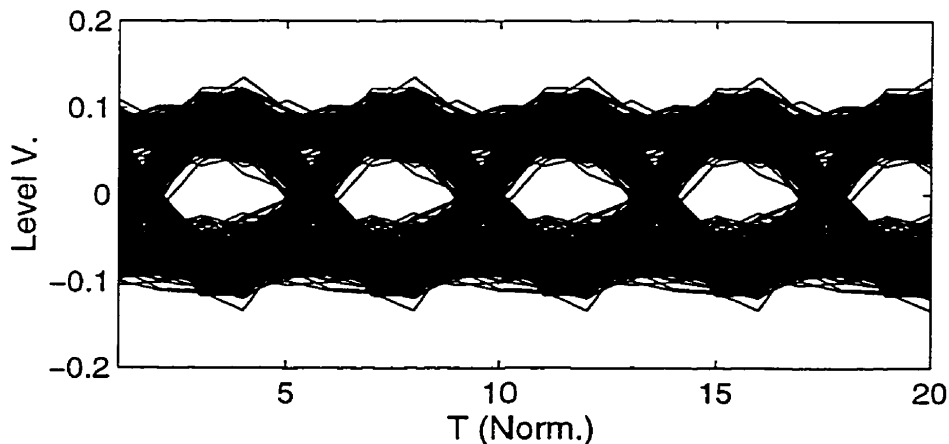


Figure 6.36. Eye diagram for the Q process from a harmonically upconverted 5 MS/s QPSK signal on a zero length fiber, $f = 17.35$ GHz, radio channel path length 3 m.

Figure 6.37 shows the same process for a 60Km OSSB fiber link with Optical Amplification.

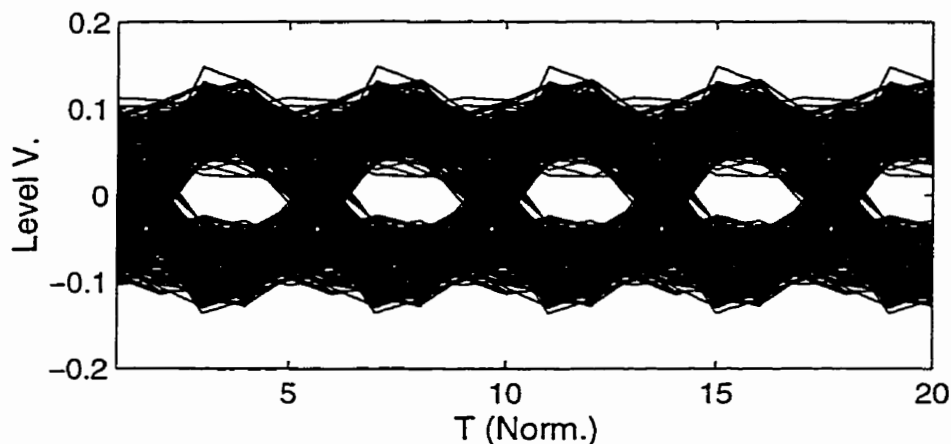


Figure 6.37. Eye diagram for the Q process from a harmonically upconverted 5 MS/s QPSK signal on a 60 km dispersive fiber, $f = 17.35$ GHz radio channel path length 3 m.

The plots are of similar quality indicating that the fiber dispersion has no effect on the signal at this relatively low symbol rate. The data accuracy was confirmed as in the previous simulations. Thus we have shown that the lower compressed QPSK radio signal will transmit correctly to yield good signals at the receive point.

6.5. Conclusions

Most of the theoretical claims made in the previous chapters with regard to subcarrier optical links have been taken to the proof of concept stage. OSSB modulation is shown to mitigate the effects of fiber dispersion on subcarrier IMDD links. The differences in behavior for harmonic and linear schemes has been verified in experiment with results that are very close in quality to the simulations in Chapters 4 and 5. BPSK subcarrier modulation was shown to be immune to phase distortion on harmonically upconverted subcarrier and QPSK modulation was shown to be a viable scheme for harmonic IMDD upconverters with proper phase precompression at the optical link input. More experimentation is required to determine the limits of the various methods and

the matching of modulation scheme to the type of optical link. It is safe to say that much tuning and optimization of the link is possible so that the results could be improved to the point that the non-linear optical link would appear transparent to the radio signal.

7. Conclusions

7.1. Thesis Review

The theory and experiment in this thesis serve as a foundation in establishing the case for fiber as a delivery tool for broadband radio services. Additionally the potential for OSSB modulation as a general scheme for dispersion compensation in broadband modulation is outlined with some development of new theory and suggestions for exploratory research. Some of the obvious hurdles for radio on fiber have been addressed and mitigations for such are presented with experimental results.

Chapter 1 established the case for fiber as a tool in the broadband delivery problem. The difficulties in redeployment of existing subscriber loop technology were presented along with the potential mitigations found in using a radio delivery scheme. This presentation was in the context of systems that are under development as the present experimental work progresses. It is likely that a Fiber-To-The-Curb infrastructure will eventually be deployed in any system, be it FTTH or fiber overlay. It was also pointed out that, as component prices fall, fiber/radio feasibility increases for traditional wireless services such as cellular.

Chapter 2 contained a presentation of the fundamental theory for Compatible Single Sideband Modulation on fiber. This was done within the context of the broadband fiber system since this represents the most general case for theoretical development. The original theory, developed in the 1950-60's, was resurrected and modified for use on fiber. It was shown that approximations to the exact theoretical expressions were usable and allowed some important simplifications that essentially determined whether or not the structure in question was implementable. In other cases the various structures that are available with fiber devices were outlined with modifications to the original theory to accommodate the particular behavior of the fiber devices. It was shown that the CSSB structure may be achieved in a cascaded laser/phase

modulator, and cascaded laser FM / MZM Amplitude modulator and the most practical structure from the experimental perspective: the cascaded MZM/phase modulator. The laser intensity modulator with its inherent 'chirp' or FM characteristic was shown to have potential as a single modulator structure device that would allow a crude type of OSSB modulation. Simulations were included and recommendations for research were included. As a footnote the laser chirp based OSSB device was confirmed in the lab by a research team consisting of the author and TR Labs interns Sean Hum and Brad Davis. Seven dB of sideband cancellation was observed.

Chapter 2 included an introduction of subcarrier processes in the context of the general dispersion problem. It was shown that the fiber dispersion loss mechanism is universal in the sense that it adversely affects broadband as well as subcarrier signals on fiber.

In Chapter 3, the focus was on a novel dispersion compensation method for broadband signals on fiber. This was included as an important consequence of the theoretical elements introduced in Chapter 2. The method was based on the fact that amplitude/phase relationships of the CSSB signals on fiber as defined in Chapter 2, are maintained over significant lengths of fiber even though the phase of the signal is badly distorted by fiber dispersion. Knowing the characteristics of the fiber dispersion allows the phase of the received signal to be recovered and compensated using post detection methods. While the Minimum Phase Dispersion Compensation method is not easily implementable, it is an important theoretical development that needs discussion within the context of this document.

Chapter 4 dealt with the theory and simulation of subcarrier processes on fiber. The linear OSSB subcarrier process was addressed within its dependence on the Bedrosian theorem which was an extension of the theory of minimum phase signals applied to products of Analytic functions. The nonlinear subcarrier process was addressed with the intent of developing practical methods for

dealing with non-linear systems on dispersive fiber. A powerful algorithm was developed that allowed direct observation of the interactions between spectral components of the optical electric field in square-law detector with the practical benefit of drastically reducing the computing time require to model these systems.

Chapter 5 outlined a novel method for predistorting a phase modulated subcarrier signal to make it immune to the distortions associated with harmonic upconversion. The reader might recall that when a signal is upconverted through some type of non-linearity the phase and amplitude the desired harmonic are both distorted by the nonlinear process. A method of phase predistortion that targeted the specific distortion characteristics as manifested on the desired harmonic was applied to the input subcarrier signal and was found to allow the accurate transmission of the radio signal after harmonic upconversion on the fiber link. This allowed a much simpler method of signal transmission over the fiber with arbitrary phase modulation. The phase precompression method was shown in simulation to be immune to fiber dispersion with the observed effect being a rotation of the constellation of the subcarrier signal with little or no distortion of the information signal. The method was then extended to include a QAM signal in which the phase and amplitude was predistorted. A crude simulation of a 16 QAM signal was presented with sufficient success as to spawn further research on the subject. This subject is likely sufficient to fuel a master's level study.

Chapter 6 contained the results of preliminary experiments to prove the salient theoretical points relating to subcarrier processes on fiber. The experimentation utilized the MZM/phase modulator from the CSSB group of modulators outlined in Chapter 2, and the lone (and equivalent for subcarrier processes) Hartley Configured MZM as described in Chapter 4. Starting with unmodulated radio carriers, the RF power compensation properties of OSSB versus double sideband modulation was investigated. Improvements to the detected RF power in both linear and nonlinear optical OSSB modulation was observed. The

cascade MZM/phase modulator was shown to exhibit similar behavior to the Hartley configured MZM thus establishing equivalence between the structures. This additionally established the fact that the hybrid OSSB method is a general solution to dispersion distortion allowing post detection compensation on broadband signals and complete mitigation of dispersion effects on subcarrier signals.

BPSK modulation on harmonically upconverted optical signals was shown to be immune to fiber dispersion on the odd harmonics and successful transmission over the fiber was confirmed. The phase compression method was proven experimentally over a short radio-fiber harmonic link to show the theoretical accuracy of the method. The predistortion method was then applied to a long (~60 km) fiber link to illustrate its immunity to fiber dispersion. Recall that 60 km was the length at which the double sideband harmonic modulator encountered complete power null. The method worked well under the experimental conditions for these 'first generation' tests. It is likely that improvements are available to make the method more efficient for use in real systems.

Which bring us to the topic of future research...

7.2. Further Research

Plans for future research are naturally split into two divergent streams: Broadband and subcarrier processes. For the broadband study, the MZM/phase modulator was tested in detail by Michael Seiben of TRILabs Edmonton/ University of Alberta in his PhD work[52]. It understates to say that he verified the operation of the device. Since the broadband thrust was not the prime focus of this thesis, it also suffices to state that the other structures outlined in Chapter 2, the laser/phase and laser FM/MZM device should be investigated to determine the usefulness of the method and, more fundamentally, whether the method even holds for structures like the laser intensity modulator with its inherent distortions due to chirp and line width difficulties. Future research for

broadband schemes should at least investigate the possibility of implementing the minimum phase dispersion compensator in a real system. Additionally, modulation schemes should be developed that carry the signal processing load away from the actual dispersion compensator at the detector.

Clearly the most important task in the subcarrier stream is the implementation of a field trial with a small group of users. There is no doubt that some variant of the MZM/phase structure with direct detection and harmonic upconversion could be the link of choice for broadband delivery. The testing should start with the downlink delivery and should be conducted with the accommodation of the uplink process in mind. This research is underway at TRILabs Calgary office in collaboration with TELUS Communications Inc.

Future work should include the optimization of the optical modulator for harmonic upconversion and the associated phase predistortion. It is clear that the present examination simply did little more than 'open the door' and that much improvement could be made to the phase compression method. Additionally the method was applied only to upconversion method with what we referred to as 'simple' nonlinearities. The laser/phase structure should be investigated to at least rule them out as serious contenders in the frequency translating class of optical modulators. Additionally, QAM and complex analog modulation should be addressed with the goal of developing a suitable predistortion scheme for non constant or smooth envelope characteristics. While most LMCS providers agree that DQPSK will be the ultimate modulation scheme for the digital portion of the signal, other standards are being assembled that call for such ornate schemes as 256QAM and Analog/Digital Orthogonal Frequency Domain Multiplexing (OFDM) which is, in principal, a digital modulation scheme but has the dynamic range requirements of an analog signal.

It should be noted that some harmonic upconversion schemes achieve the required frequency translation without the need for phase compression[4-6]

This is achieved by using the optical non-linear modulator as a mixer rather than as a pure frequency translation device. This is achieved in a manner similar to standard radio mixing where an unmodulated tone is added to the optical information subcarrier signal. By careful manipulation of the frequency and amplitude of the tone and modulated subcarrier a linear translation of the information subcarrier is achieved without phase distortion. This work was pioneered at TRILabs Edmonton. There is evidence in this study to indicate that QAM signals with suitably predistorted amplitude may be amenable to this type of frequency translation.

Finally deployment recommendations need to be developed for the uplink problem. It is more or less accepted that the uplink portion of the signal, which is the signal that returns from the user locations will never be extremely bandwidth intensive. This is due to the fact that uplink traffic from most users consists of sparse control commands that amount to little more than a trickle of information. This is, of course, excepted by the user with a requirement for broadband uplink due to home business usage or other requirements. In these extreme cases, upgrading of the cable based service will be required. In any case the deployment of the technologies included in this report are somewhat dependent on the willingness of suppliers to deploy the required Fiber-To-The-Curb infrastructure. Once this is done the implementation of a fiber radio based system becomes an evolutionary process. Additionally the integration of regular mobile communications should be investigated. The improvements available in this sector relate to the cosmetic problems associated with deployment of large base-station towers. If it is possible to integrate broadband traffic with mobility traffic on a radio fiber FTTC system, then the initial outlay for fiber to the curb becomes somewhat less of a burden on system developers, opening the door for leased services and other business arrangements that a large carrier might make to recover costs. This type of arrangement has a well established precedent in the telecommunication carrier / reseller relationship that has been in existence since the early 60's. The high cost of the FTTC infrastructure would validate this type of arrangement.

In closing, it can be said that the radio on fiber research stream holds much promise for achieving efficient signal transport. The behavior of COSSB signals on links with indeterminate phase distortion may hold potential as a fundamental theory for other applications on fiber as well as for radio links with complex multipath propagation characteristics. This topic will be investigated in by the author and it is hoped, by others.

References

- [1] Theodore S. Rappaport, *Wireless Communications Principles and Practice*, Prentice Hall PTR, USA, 1996.
- [2] A. J. Cooper, "Fiber/Radio For the Provision of Cordless/Mobile Telephony Services in The Access Network", *Electronics Letters*, vol. 26, no. 24, pp. 2054-2056, October 1990.
- [3] J.J. O'Reilly, P.M. Lane, R.Heidemann, R.Hofstetter, "Optical Generation of Very Narrow Linewidth Millimeter Wave Signals", *Electronics Letters*, vol. 28, no. 25, pp. 2309-2311, December, 1992.
- [4] Tom Young, "Free Carrier Generation", *TRLabs Internal Document*.
- [5] Tom Young, Jan Conradi, Wayne Tinga and Bob Davies. "Generation and Transmission of FM and $\pi/4$ DQPSK Signals at Microwave Frequencies Using Harmonic Generation and Optoelectronic Mixing in Mach Zehnder Modulators", *Tenth International Conference on Integrated Optics and Optical Fiber Communication - Technical Digest*, vol. 4, pp. 72-73, June 1995.
- [6] Tom Young, Jan Conradi and Wayne Tinga, "Generation and Transmission Of FM and $\pi/4$ DQPSK Signals at Microwave Frequencies Using Harmonic Generation and Opto electronic Mixing in Mach-Zehnder Modulators." *IEEE*

- Transactions on Microwave Theory and Techniques*, vol. 44, no. 2, pp. 446-453, March 1996.
- [7] Wake, D., Smith I.C., Walker N.G. Henning, I.D., Carver, R.D. "Video Transmission Over A 40 GHz Radio-Fibre Link", *Electronics Letters*, vol. 28, no. 21, pp. 2024-2025 Oct. 1992.
- [8] John M. Senior, *Optical Fiber Communications: Principals and Practice*, Second Edition, Prentice Hall, 1992.
- [9] *IEICE Transactions on Communications,-Special Issue on Fiber-optic Microcellular Radio Communication Systems and Their Technologies*, vol. E76-B, no. 9, September 1993.
- [10] T.E. Darcie and G. E. Bodeep, "Lightwave Subcarrier CATV Transmission Systems", *IEEE Transactions on Microwave Theory and Techniques*, vol. 38, pp. 524-533, 1990.
- [11] C. Baack, G. Elze, G. Grobkopf, F. Kraus, W. Krick L. Fuller, "Analogue optical transmission of 26 t.v. channels", *Electronics Letters*, vol. 17, no. 15, pp. 300-301, May, 1979.
- [12] Afshin S. Daryoush, Peter R. Herczfeld, Zygmund Turski, Pradeep K. Wahi, "Comparison of Indirect Optical Injection Locking Techniques of Multiple X-Band Oscillators", *IEEE Transactions on Microwave Theory and Techniques*, vol. MTT-34, no.12, pp. 1363-1369, December 1986.
- [13] J. J. O'Reilly, P. M. Lane, M. H. Capstick, H. M. Salgado, R. Heidemann, R. Hofstetter, H. Schmuck, "RACE 2005:

- Microwave Duplex Optical Antenna Link”, *IEE Proceedings-J*, vol. 140, no. 6, pp. 385-391, December 1993
- [14] Shibutani, Makoto, Kanai, Toshihito, Domom, Watani, Emura, Katsumi, Namiki, Junji, “Optical Fiber Feeder for Microcellular Mobile Communication Systems”, *IEEE Journal on Selected Areas in Communications*, vol. 11, no. 7, pp. 1118 -1126, September 1993.
- [15] Ogawa, Hiroyo, Polifko, David, “Fibre-Optic Millimeter-Wave Subcarrier Transmission Links for Personal Radio Communications Systems” , *IEEE MTT-S Digest*, pp. 555-558, 1992.
- [16] O'Reilly, J.J., Lane, P.M. “Fibre-supported optical generation and delivery of 60 GHz signals”, *Electronics Letters*, vol. 30, no. 16 , pp. 1329-1330, August 4, 1994.
- [17] Qing Z. Liu, R. Ian MacDonald, and Robert Davies, “A Simple and Cost effective Fibre Optic Microwave Link with Monolithic Integrated Optoelectronic Mixing Receiver”, *Proceedings of Wireless 94. The Sixth International Conference of Wireless Communications*, pp. 250-256, July 1994.
- [18] Jan Conradi, Bob Davies, Mike Sieben, David Dodds and Sheldon Walklin, "Optical Single Sideband (OSSB) Transmission for Dispersion Avoidance and Electrical Dispersion Compensation in Microwave Subcarrier and Baseband Digital Systems", *Optical Fiber Conference OFC-*

- 97 postdeadline paper, pp. PD29-1 - PD29-4, February 1997.
- [19] Bob Davies and Jan Conradi, "Hybrid Modulator Structures for Subcarrier and Harmonic Subcarrier Optical Single Sideband", *Photonics Technology Letters*, vol. 10, no. 4, pp. 600-602, April 1998.
- [20] Ali Motamedi, R. Vahldeick, "Generation of fourth harmonic microwave signals using Mach-Zehnder modulators", *Optical Fiber Conference OFC-97 Technical Digest*, pp. 354-355, February 1997.
- [21] H. Schmuck "Comparison of optical millimeter wave systems concepts with regard to chromatic dispersion" , *Electronics Letters*, vol. 31, no. 21, pp. 1848-1849, October 1996.
- [22] Jianmin Wang and Klaus Petermann, "Small Signal Analysis for Dispersiiove Optical Fiber Communication Systems", *Journal of Lightwave Technology*, vol. 10, no. 1, pp. 96-100, January 1992.
- [23] F. Devaux, Y Sorel, and J. F. Kerdiles, "Simple Measurement of Fiber Dispersion and of Chirp Parameter of Intensity Modulated Light Emitter", *Journal of Lightwave Technology*, vol. 11, no. 12, pp. 1937-1940, December, 1992.
- [24] Wedding, "Analysis of fiber transfer function and determination of receiver frequency response for dispersion

- supported transmission", *Electronics Letters*, vol. 30, no. 1, pp. 58-59, January, 1994.
- [25] John Park, Aly F. Elrefaie, Kam Y. Lau, "Fiber Chromatic Dispersion Effects on Multichannel Digital Millimeter-Wave Transmission", *IEEE Photonics Technology Letters*, vol. 8, no. 12, pp. 1716-1817, December 1996.
- [26] G.H. Smith, D. Novak, Z. Ahmed, "Technique for optical SSB generation to overcome dispersion penalties in fibre-radio systems", *Electronics Letters*, January 1997, vol. 33, no.1 pp. 74-75, January 1997.
- [27] Bob Davies and Jan Conradi, "Hybrid harmonic subcarrier optical single sideband with phase predistortion", *Electronics letters*, vol. 34, no. 17, pp. 1674-1675, August 1998.
- [28] G. H. Smith and D. Novak, "Broadband Millimeter-Wave (38 GHz) Fiber-Wireless Transmission System Using Electrical and Optical SSB Modulation to Overcome Dispersion Effects", *IEEE Photonics Technology Letters*, vol. 10, no. 1, pp. 141-143 January 1998.
- [29] Robert Olshansky, "Optical Modulator For Cancellation of Second-Order Intermodulation Products In Lightwave Systems", *US Patent* no. 5,239,401, August 1993.
- [30] Michael J. Wale, Robert G. Walker and Colin Edge, "Single-Sideband Modulator In GaAs Integrated Optics for Microwave Frequency Operation", *Integrated Photonics*

- Research, OSA, Technical Digest Series, 10, Post-Deadline Paper PD-8 (1992).*
- [31] Helge E. Engan, Byoung Kim, James N. Blake Herbert J. Shaw, "Fiber Optic Intermode Coupling Single Sideband Frequency Shifter" *US Patent*, no. 5,022,732, June, 1991.
- [32] Peter K. Cheo, Robert A. Rubino, Meyer Gilden, "Reentrant Traveling-Wave Single Sideband Optical Modulator" *US Patent*, no. 4,973,140, November 1990.
- [33] Peter Cheo, Gerald Meltz, "Single Sideband Waveguide Modulator", *US Patent*, no. 4,897,622, January, 1990.
- [34] Herbert Voelcker "Toward A Unified Theory Of Modulation - Part 1: Phase-Envelope Relationships", *Proceedings of the IEEE*, vol. 54, no. 3, pp. 340-353, March 1966.
- [35] Herbert Voelcker "Demodulation of single-sideband signals via envelope detection", *IEEE Transactions on Communication Technology*, vol. COM-14, pp. 22-30, February 1966.
- [36] Leonard R. Kahn, "Compatible Single Sideband", *Proceedings of the IRE*, pp. 1503-1527, October 1961
- [37] Simon Haykin, *An Introduction to Analog & Digital Communications*", John Wiley & Sons, New York, 1989.

- [38] P. P. Eckersley, "Asymmetric-sideband broadcasting", *Proceedings of the IRE*, vol. 16, pp. 1041 - 1092, September 1938.
- [39] N. Koomans, "Asymmetric-sideband broadcasting", *Proceedings of the IRE*, vol. 27, pp. 687 - 690, November 1939.
- [40] M. Izutsu, S. Shikama, T. Sueta, "Integrated optical SSB modulator/frequency shifter," *IEEE Journal of Quantum Electronics*, vol. QE-17, no. 11, pp. 2225-2227, Nov. 1981.
- [41] K. Yonenaga, N. Takachio, "A fiber chromatic dispersion compensation technique with an optical SSB transmission in optical homodyne detection systems," *IEEE Photonics Technology Letters*, vol. 5, no. 8, pp. 949-951, Aug. 1993.
- [42] John G. Proakis, *Digital Communications*, 3rd ed. New York, McGraw-Hill, 1995.
- [43] Leon W. Couch, *Digital & Analog Communication Systems*, 5th ed. Upper Saddle River, NJ, Prentice Hall, 1997.
- [44] Ruel V. Churchill, James Ward Brown, *Complex Variables and Applications*, McGraw-Hill Book Company, New York, 1984.
- [45] Alexander D. Poularikas: Editor-in-Chief, *The Transforms and Applications Handbook* CRC Press, USA, 1996.

- [46] Igor Filanovsky, Private Communication, University of Alberta, 1999.
- [47] Sundaram Seshu, Norman Balabanian, *Linear Network Analysis*, John Wiley & Sons, New York, 1959.
- [48] Alan V. Oppenheim, Ronald W. Schaffer, *Digital Signal Processing*, Prentice-Hall, New Jersey, 1975.
- [49] Gordon B. Lockhart, "A Spectral Theory for Hybrid Modulation", *IEEE Transactions on Communications*, vol. COM 21, no. 7, pp.790-800, July 1973.
- [50] William H. Press, Brian P. Flannery, Saul A Teukolsky, William T. Vetterling, *Numerical Recipes in C*, Cambridge UK, 1988
- [51] Villard O. G. Jr., "Composite amplitude and phase modulation", *Electronics* , vol.21, pp. 86-89, Nov. 1948.
- [52] Michael Seiben, "Single Sideband Modulation For Digital Fiber Optic Communication Systems", *PhD Thesis*. University of Alberta, May 1998.
- [53] Soichi Kobayashi, Yoshihisa Yamamoto, Minoru Ito and Tatsuya Kimura, "Direct Frequency Modulation In AlGaAs Semiconductor Lasers", *IEEE Journal of Quantum Electronics*, vol. QE-18, no. 4, pp. 582-595, April 1982.
- [54] S. Kobayashi, Y. Yamamoto, T. Kimura, "Modulation frequency characteristics of directly optical frequency

- modulated AlGaAs semiconductor laser", *Electronics Letters*, vol. 17, no. 10, pp. 350-351, May 1981.
- [55] J. M. Osterwalder and B. J. Rickett, "Frequency Modulation of GaAlAs Injection lasers at Microwave Frequency Rates", *IEEE Journal of Quantum Electronics* vol. QE-16, no. 3, pp. 250-252, March, 1980.
- [56] John Gowar, *Optical Communication Systems Second Edition*, Prentice Hall, 1993.
- [57] Hatim Zaghoul, Michel Fattouche, "Method and Apparatus for Demodulation of a Signal Transmitted Over a Fading Channel Using Phase Estimation", *U.S. Patent*, no. 5,369,670, February 1992.
- [58] Paul Binding, University of Calgary, Private Communication, Department of Mathematics and Statistics.
- [59] Lofti A. Zadeh and Charles Desoer, *Linear System Theory*, McGraw-Hill, 1963.
- [60] Jan Conradi, *NORTEL Fiber Optics Course*", September 1996.
- [61] Bedrosian E., "A product theorem for Hilbert transforms" *Proceedings of the IEEE*, pp. 868-869, May 1963
- [62] Edward C. Jordan, *Reference Data for Engineers: Seventh Edition*, Howard W. Sams & Company, 1985.

- [63] Stephen Wolfram, *Mathematica: A System for Doing Mathematics by Computer*, Addison-Wesley, California USA, 1988.
- [64] Graham H. Smith, Dalma Novak and Zaheer Ahmed, "Overcoming Chromatic-Dispersion Effects in Fiber-Wireless Systems Incorporating External Modulators", *IEEE Transactions on Microwave Theory And Techniques*, vol. 45, no, 8, pp. 1410-1415, August 1997.
- [65] Zaheer Ahmed, Dalma Novak, Rod B. Waterhouse, and Hai-Feng Liu, "37-GHZ Fiber-Wireless System For Distribution of Broadband Signals", *IEEE Transactions on Microwave Theory And Techniques*, vol. 45, no, 8, pp. 1431-1435, August 1997.
- [66] Basil W. Hakki, "Dispersion of Microwave-Modulated Optical Signals", *Journal of Lightwave Technology*, vol. 11, no. 3, pp. 474-480, March, 1993.
- [67] N. G. Walker, D. Wake and I. C. Smith, "Efficient millimetre-wave signal generation through FM-IM conversion in dispersive optical fibre links", *Electronics Letters*, vol. 28, no. 21, pp. 2027-2028, October, 1992.
- [68] D. M. Klymyshyn, S. Kumar, A. Mohammadi, "A 360 Degree Linear Microwave Phase Shifter with a FET Frequency/phase Multiplier," *Microwave Journal*, vol. 40, no. 7, pp. 130-137, July 1997.

- [69] Rodger E. Ziemer, Roger L. Pederson *Digital Communications and Spread Spectrum Systems*, Macmillan Publishing Company, New York, 1985.
- [70] K. Petermann, "FM-AM noise conversion in dispersive single mode fibre transmission lines", *Electronics Letters*, vol. 26, no. 25, pp. 2097-2098, December, 1990.
- [71] Davies Bob, "The IRIS Development System" , *TRLabs Internal Report*, 1991.
- [72] Donald C. Cox, "Delay Doppler Characteristics of Multipath Propagation at 910 MHz in a Suburban Mobile Radio Environment", *IEEE Transactions on Antennas and Propagation*, vol. AP-20, no. 5, pp. 625-635, September 1972.
- [73] Robert J. C. Bultitude, Samy A. Mahmoud, William A. Sullivan, "A Comparison of Indoor Radio Propagation Characteristics at 910 MHz and 1.75 GHz", *IEEE Journal on Selected Areas in Communications*, vol. 7, no. 1, pp. 20-30, January 1989.
- [74] R. Bultitude, P. Hou, R. Hahn, G. Hendratoro, D. Falconer and R. Berube, "Radio Propagation Data Pertinent to the Design Of Small Area Multipoint Communication Systems at 28 GHz", *ANTEM 98*. Canada, 1998.
- [75] P. A. Bello, B. D. Nelin, "The Effect of Frequency Selective Fading on the Binary Error Probabilities of Incoherent and Differentially coherent Matched Filter Receivers", *IEEE*

- Transactions on Communication Systems*, vol. CS-11, pp. 170-186, June 1963.
- [76] Homayoun Hashemi, "The Indoor Radio Propagation Channel", *Proceedings of the IEEE*, vol. 81, no. 7, pp. 943-968, July 1993.
- [77] N. Benvenuto, "Distortion Analysis on Measuring the Impulse Response of a System Using A Crosscorrelation Method", *AT&T Bell Laboratories Technical Journal*, vol. 63, no. 10, pp. 2171-2193, December 1984.
- [78] Max Born and Emil Wolf, *Principles of Optics*, 4rd Ed., Pergamon Press, Oxford, 1970.

Appendix A: The IRIS System

A.1. Introduction

The IRIS Development System[71] is a general purpose radio test set developed originally to acquire impulse response data from UHF radio channels in real time. IRIS, for **Impulse Response Identification System** was developed by the author as a support device for UHF/EHF radio research projects ongoing in TELUS Communications Inc. and TRILabs. The goal of the project was to allow flexibility in data collection that went beyond channel characterization. IRIS is a generic device that allows modulation and demodulation of custom bandpass waveforms. The system was designed so that the results of the channel probes, in which the waveform is some appropriate probing signal, could be used immediately to aid in the design of channel equalization schemes and modulation schemes that would mitigate the problems encountered in multipath radio channels.

To illustrate how the IRIS system aids in research, consider that the standard development cycle generally consists of 4 parts: The idea or inspiration, supporting theory development, simulation, and prototyping. The evolution from step 2 to step 3 is often an iterative process where theory is honed through repeated simulations to a point where the development of a prototype is deemed a reasonable risk. In the case of radio research, the simulation stage typically involves applying a mathematical model of the mitigation scheme to an additional model of the radio channel under examination. While the IRIS system was initially designed to serve as a channel sounder, with the singular task of characterizing radio channels, it was apparent soon after the system was assembled that the final system was capable of serving as a kind of channel 'emulator' that would practically remove the last 2 stages of the development cycle for modulation and equalization schemes. The new algorithm that the IRIS system allowed was that, after the theory stage, the remedy could be immediately tested on a real radio channel with the same convenience and simplicity that simulation stage in the

regular cycle involved. The benefit was that risk associated with the process of prototyping was removed; the investigator immediately had a good indication whether the idea was sound or if more theoretical work was required.

The versatility of the IRIS system has been extended to multiple studies that include radio-location using Time Domain Methods (TDR), Cellular Caller ID and location, and the focus of the present study, as a generic RF signal source.

A.2. System Description

A.2.1. Transmitter

The IRIS system is composed of a computer controlled bandpass signal transmitter and receiver. A block diagram of the transmitter is shown in figure A.1.

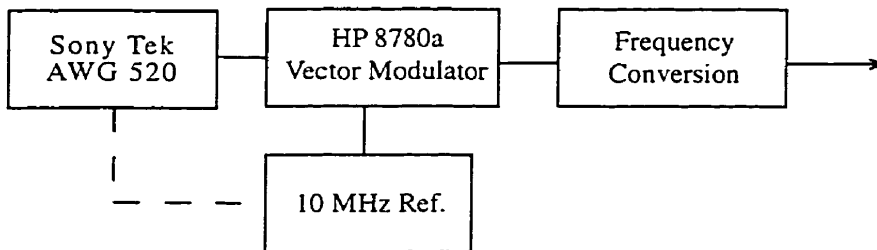


Figure A.1. IRIS Transmitter

Transmitter Main Components List.

- Sony/Tek AWG 520
- Hewlett Packard Model 8780a Vector Modulator (VMA)
- RF front end

The transmitter employs the principle of digital arbitrary waveform generation to give flexibility in the range of signal that may be generated and analyzed. This means that a waveform, in digital format, is stored in the device as a sequence of bytes or words in which each word represents the state of a digital to analog converter (D/A). The output waveform, which may be analog or digital in nature, is acquired by clocking the waveform sequence into the AWG's high speed output D/A. Waveforms are composed in a computer as a numerical sequence that is compatible with the AWG internal format and then transferred to the AWG via the standard IEEE 488.2 GPIB interface bus. The AWG has two types of memory, a RAM disk type for non-volatile storage of different waveforms in binary format and volatile high speed waveform memory for temporary storage and transfer of waveform data to the output D/A converters. The AWG output clock speed is variable up to 1 GS/s in dual output mode. Vertical resolution in the output waveform is 10 bits or 1024 levels. The analog bandwidth is limited to about 500 MHz, set by the finite rise time on the output D/A. Maximum waveform size is one million symbols per channel. The AWG has filters for bandlimiting to combat aliasing in the transmitted output.

Once the probing waveform is composed, RF modulation is accomplished in a Hewlett-Packard model 8780A Vector Modulator (VM). The VM is a high quality quadrature/FM modulator with variable output RF power from -110 to +10 dBm. The VM is also GPIB compatible and all RF parameters may be computer controlled. The 8780A has a 10 MHz reference output so that the data clock and carrier may be phase locked for synchronization. In addition to vector or quadrature AM modulation, FM modulation is available up to 12 MHz bandwidth. Carrier frequencies are in the ranges of 10 to 3000 MHz, directly achievable on the HP8780A, and auxiliary front end stages allow carrier frequencies at 3 - 5 GHz 16.5-18.5, 30, 40 and 60 GHz. The RF bandwidth of the VM is approximately 350 MHz which makes it useful for just about any channel research.

After modulation the signal is amplified and radiated in to the channel or test device via the antenna or other interface circuitry.

A.2.2. Receiver

The IRIS receiver Block Diagram is shown in Figure A.2.

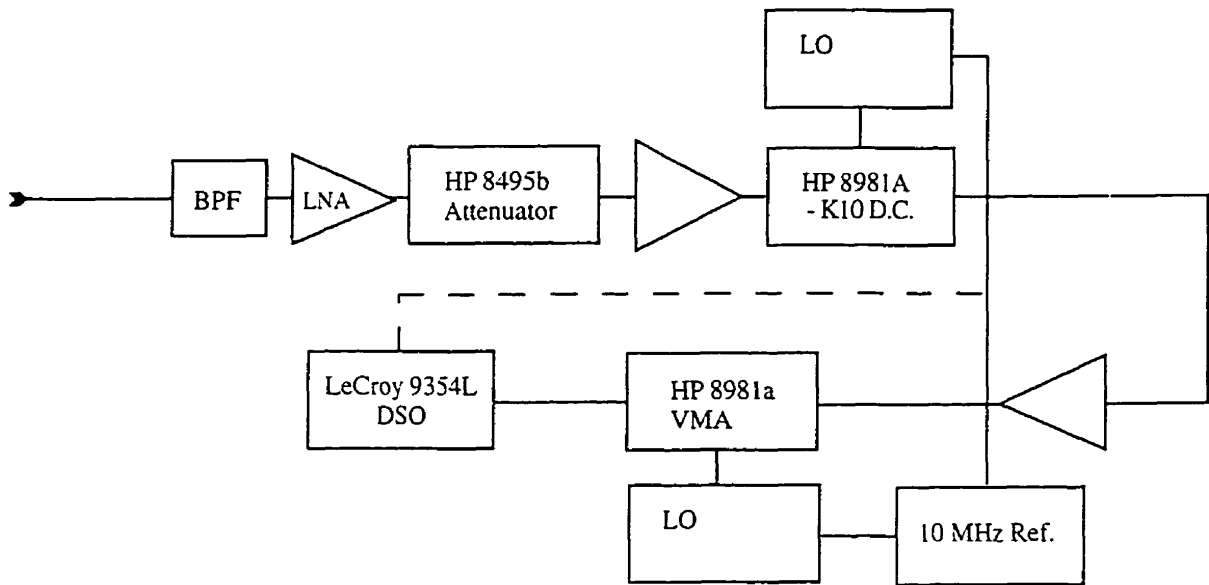


Figure A.2. IRIS Receiver

Receiver Main Components List

Low Noise Amplifier/Power amplifier

Adjustable Attenuator

HP 8981A-K10 Downconverter

Local Oscillators Sources.

HP 8981a Vector Modulation Analyzer

LeCroy 9384AL Digital Storage Oscilloscope

The received bandpass signal from the channel or test device is captured at the front-end bandpass filter to remove interference. The signal is then amplified and downconverted to a suitable intermediate frequency in the HP 8981 -K10 custom downconverter. The K10 has a continuous range of operation from 0.9-18 GHz. For the higher frequency ranges mentioned in the transmitter section, special downconverter are used in place of the K10. Additionally, The downconversion may be multistage depending on the required intermediate frequency (IF). After downconversion, the signal may be filtered and then demodulated to baseband through the HP8981A Vector Modulation Analyzer (VMA) or directly sampled at IF in the scope and digitally demodulated on the computer. If the IF at the demodulation stage is 200 MHz or less, the VMA is used. If it is higher than this due to signal bandwidth requirements, digital demodulation is carried out by sampling the IF frequency and then demodulating off-line. Naturally this type of demodulation is more storage intensive for a given information bandwidth than sampling at the baseband output from the VMA. The LeCroy 9384AL digital storage scope (DSO) has sampling capability up to 2 GS/s (1 GHz BW) on two input channels that each hold 4 million point data points. Each data point has 8 bits vertical resolution. The sampled data may be held in the memory of the scope until it is transferred to the computer via GPIB interface. The data may then be processed on a personal computer or transferred via network to a larger workstation. The RF bandwidth of the system is similar to that of the transmitter (~400 MHz). All components of the receiver are GPIB programmable allowing remote operation.

A.2.3. Design Philosophy

The decisions made in the development of the IRIS system related to the trade-offs between prototyping a stand-alone system versus using off-shelf

components. It was determined that, even though the current system has a hardware/software value in the range of seven figures, the flexibility and reliability afforded by quality shelf equipment was worth the extra expenditure. It was felt that components would accommodate any foreseeable test requirements within a reasonable bandwidth. Additionally the system could be upgraded (usually in higher carrier frequency and bandwidth) by replacing key subcomponents as opposed to the inevitable overhaul that would be required on a standalone device. Careful selection of equipment allowed more comprehensive testing of modulation schemes and channel equalization schemes in addition to channel characterization studies.

A.3. Applications

The IRIS system has been employed in 3 main areas of research and one instance of commercial development. Research areas are channel characterization, modulation testing and component studies.

A.3.1. Channel/Device Characterization

Information about the wideband characteristics of the multipath propagation channel assist in the development of specific remedies for channel degradations to the transmitted signal[72-76]. Information about reflection characteristics and fading characteristics are accessible if the channel is probed with a signal whose temporal characteristics are quick enough to allow observation of these transient conditions. Most of the channel testing involves probing the system under test with a wideband pseudonoise code.

A.3.2. Pseudo Noise Channel/Device Probes

Pseudo Noise characterization is a basic system identification method in which a finite bandwidth impulse response of a radio channel test device is acquired[76]. If the channel or system under investigation is assumed to be a linear filter having the impulse response $h(t)$ then the output response $y(t)$ to an arbitrary input $x(t)$ is given by

$$y(t) = \int_{-\infty}^{\infty} x(t-v)h(v)dv. \quad (\text{A-1})$$

Multiplying sides of (1) by $x^*(t+\tau)$ we get

$$y(t)x^*(t+\tau) = \int_{-\infty}^{\infty} x(t-v)x^*(t+\tau)h(v)dv \quad (\text{A-2})$$

The cross correlation function of y and x^* is given by

$$\int_{-\infty}^{\infty} y(t)x^*(t+\tau)dt = \int_{-\infty}^{\infty} \int_{-\infty}^{\infty} x(t-v)x^*(t+\tau)h(v)dvdt \quad (\text{A-3})$$

Letting $t = t - v$ in the right hand side of (A-3) gives

$$\int_{-\infty}^{\infty} y(t)x^*(t+\tau)dt = \int_{-\infty}^{\infty} R(\tau-v)h(v)dv \quad (\text{A-4})$$

and if $x(t)$ is a noise function whose autocorrelation function is impulsive then (A-4) is given by

$$\int_{-\infty}^{\infty} R(\tau-v)h(v)dv = \int_{-\infty}^{\infty} \delta(\tau-v)h(v)dv = h(\tau) \quad (\text{A-5})$$

Clearly, it is impractical to attempt to inject white noise into the channel. Instead, a Maximal Length Pseudo Random Binary Sequence (PRBS sequence) is used that has special self correlation properties that can be used to extract the required information about the channel[1]. As an example consider the 7 chip PN sequence

$$\text{A.3.2.1.} = [1 \ 1 \ 1 \ -1 \ -1 \ 1 \ -1] \quad (\text{A-6})$$

the circular autocorrelation of this sequence is

$$\{R_{pp}\} = [7 \ -1 \ -1 \ -1 \ -1 \ -1 \ -1]. \quad (A-7)$$

This autocorrelation function is characterized by a spike or triangle at 0 lag which repeats every 7 points. This type of correlation behavior is exhibited by all maximal length PN sequences. In a functional system the length of the PN sequence is much greater than 7 bits. Typically the length used for channel probes is length 255 or greater. When the code is made longer there is a corresponding proportional increase in the correlation peak height relative to the base value (which is always -1 for any length sequence), thus this method may be used in situations where the signal strength is well below the noise floor of the channel or test device. When the information sequence is convolved with a square pulse as in a real system, the result of the correlation operation is a triangle with a base width equal to 2 pulse widths which gives an indication of the temporal resolution of the systems. At 200 M chips per second this is 10 nS. It is also apparent from the above example in (A-6) and (A-7) that the correlation operation yields a processing gain of 7. There is a trade-off in that the entire 7 chip sequence is required to produce the peak in the autocorrelation sequence. This scaling tradeoff is of little consequence if the sequence transmission time is small relative to the time variation of the channel. For instance if a 511 chip PN code is used to characterize the channel at 200 MChip/s the code acquisition time is 2.555 μ S during which the channel is unlikely to change significantly. An additional concern is that the code repetition period be long enough to allow the transient behavior of the channel or test device to die out.

The other attribute of PN sequences that is crucial in this type of channel probe is orthogonality. With increasing sequence lengths the difference in processing gain between zero lag correlations vs misaligned sequences increases. This means that sequences may be superimposed upon each other and the individual sequences will be discernible as spikes in a plot of correlation vs lag. This property makes the PN sequence quite useful at resolving individual propagation paths in a multipath radio environment as long as the relative path delays exceed the chip period time.

Channel/device characterization has been undertaken on indoor and outdoor channels. Indoor measurements are generally straightforward. Outdoor measurements are acquired in a specially equipped vehicle that allows data to be captured in traffic situations. This measurement is restricted in bandwidth and output power to meet regulatory requirements. Most of the outdoor tests have focused on antenna placement experiments for cellular telephone. Bandwidths for outdoor measurements are in the range of 20 MHz centered at 915 MHz carrier frequency.

A.3.3. Modulation Testing

In this application the IRIS system is programmed to transmit a custom modulated signal into a test device. In the case of the phase compression algorithm in Chapter 5, the compressed phase signal was synthesized in the computer and downloaded to the AFG. The custom constellation was then upconverted to the required injection frequency and then transmitted through the OSSB fiber link.

At the receiver, the signal is bandpass filtered demodulated and sampled in the high speed oscilloscope. The data is transferred to the computer where it is processed.

A.3.4. Component Studies

In this configuration the system is used as component test bed to perform functions that are impossible on standard device testing equipment such as spectrum analyzers and network analyzers. This represents an important function since capital is conserved when the commercial radio prototype can be developed in house.

A.3.5. Instrumentation and Control

A number of upgrades to the system are planned to further automate the data collection process. Operator involvement in the measurement process could be

reduced to the point that the user simply calls a computer program to handle decisions, power levels and filtering requirements. Information could be transferred between transmitter and receiver on a separate fiber link or over the RF carrier in a wideband modulation scheme. In this way the measurement process is simplified, particularly for outdoor measurements.

A.3.6. Access

The IRIS system normally resides at TRILabs Calgary. A large software library exists and documentation is on hand to assist the new user. Students who use the IRIS system for their research typically spend one to two weeks in a tutorial effort with the author or other trained personnel. Usually, custom software is required to suit individual experimental requirements, and this is done by the student and becomes part of the students research effort. Data collected from the system is stored according to a site specific format called '.sff' or 'dot sff'. This is due to the names of the special files must be suffixed with '.sff' to be recognized by the computers. Information about the types of data is available on site.

Appendix B: Fiber Dispersion

B.1. Wave Packets and Group Velocity

To develop the dispersive fiber transfer function we first review the concept of wave packets and group velocity. These terms apply to the propagation characteristics of wave packets or wave groups[78]. Fourier theory states that, generally, any wave may be regarded as a superposition of monochromatic waves of different frequencies. A wave may be termed 'almost monochromatic' if the Fourier amplitudes of the components of the wave are non-zero within a very narrow frequency range given by

$$\bar{\omega} - \frac{1}{2} \Delta\omega \leq \omega \leq \bar{\omega} + \frac{1}{2} \Delta\omega; \quad \left(\frac{\Delta\omega}{\bar{\omega}} \ll 1 \right). \quad (\text{B-1})$$

This assumption is assumed to hold for the following development. Consider a wave group composed of 2 monochromatic waves of equal amplitude and slightly different frequencies.

$$V(z, t) = a \exp(j\omega t - \beta z) + a \exp[j(\omega + \delta\omega)t - (\beta + \delta\beta)z]. \quad (\text{B-2})$$

It can be shown that

$$V(z, t) = 2a \cos\left[\frac{1}{2}(t\delta\omega - z\delta\beta)\right] \exp[-j(\bar{\omega}t - \bar{\beta}z)] \quad (\text{B-3})$$

where

$$\bar{\omega} = \omega + \frac{1}{2} \delta\omega; \quad \bar{\beta} = \beta + \frac{1}{2} \delta\beta. \quad (\text{B-4})$$

This is a plane wave of frequency $\bar{\omega}$ and wavelength $2\pi/\bar{\beta}$ with a time varying amplitude. The maxima of the amplitude are at

$$\delta t = \left. \frac{4\pi}{\delta\omega} \right|_{z=0}; \quad \delta z = \left. \frac{4\pi}{\delta\beta} \right|_{t=0} \quad (\text{B-5})$$

and the maxima of the phase function are at

$$\delta t = \left. \frac{2\pi}{\bar{\omega}} \right|_{z=0}; \quad \delta z = \left. \frac{2\pi}{\bar{\beta}} \right|_{t=0}. \quad (\text{B-6})$$

Now, since $\delta\omega/\bar{\omega}$ and $\delta\beta/\bar{\beta}$ are small, we can say that the amplitude varies slowly with respect to the phase. Planes of constant amplitude propagate with velocity

$$v_g = \frac{\delta\omega}{\delta\beta} \quad (\text{B-7})$$

and planes of constant phase propagate with velocity

$$v_p = \frac{\bar{\omega}}{\bar{\beta}}. \quad (\text{B-8})$$

The term v_g is called the group velocity of the wave and v_p is the phase velocity. The frequency and propagation coefficient are related by

$$\beta(\omega) = n(\omega) \frac{\omega}{c} \quad (\text{B-9})$$

where $n(\omega)$ is a frequency dependent refractive index. In a non dispersive media n is constant and the phase and group velocity are equal. If the media is dispersive then the phase and group velocities will be different and β becomes a function of frequency $\beta(\omega)$.

Assuming that the fiber transfer function in a small range near the optical carrier affects only the phase of the wave, we can define the dispersive fiber transfer function as[60]

$$H(\omega, z) = \exp(-j\beta(\omega)z). \quad (\text{B-10})$$

Expanding β in a Taylor series around the carrier frequency ω gives

$$\beta(\omega) = \beta_c + \frac{d\beta}{d\omega}(\omega - \omega_o) + \frac{1}{2} \frac{d^2\beta}{d\omega^2}(\omega - \omega_o)^2 + \frac{1}{6} \frac{d^3\beta}{d\omega^3}(\omega - \omega_o)^3 + \dots \quad (\text{B-11})$$

so that the fiber transfer function is given by

$$H(\omega, z) = \exp \left[jz \left(\beta_c + \frac{d\beta}{d\omega}(\omega - \omega_o) + \frac{1}{2} \frac{d^2\beta}{d\omega^2}(\omega - \omega_o)^2 + \frac{1}{6} \frac{d^3\beta}{d\omega^3}(\omega - \omega_o)^3 + \dots \right) \right]. \quad (\text{B-12})$$

This gives the velocity profile for components of the signal traveling down the fiber relative to the optical carrier. Assuming that δ is small in equation (B-7), the group delay may be expressed as

$$\tau = \frac{1}{v_g} = \frac{d\beta(\omega)}{d\omega}. \quad (\text{B-13})$$

The quantity τ is usually described as a function of wavelength and is given in units of delay per unit length.

$$\tau = a + b\lambda^2 + c\lambda^{-2}. \quad (\text{B-14})$$

For silica fibers $a = -34.68$ ps/km; $b = 10.504$ ns/(km $\cdot\mu\text{m}^2$); $c = 29.988$ (ns $\cdot\mu\text{m}^2$)/km. τ is minimum near $\lambda = 1310$ nm.

The successive terms in (B-12) correspond to phase velocity, group velocity (from (B-13), and first and second order group velocity in dispersion effects. For the first order term

$$\frac{d^2\beta}{d\omega^2} = \frac{d}{d\omega} \left(\frac{1}{v_g} \right) = \frac{d\tau}{d\omega} = \frac{d\tau}{d\lambda} \frac{d\lambda}{d\omega} = \frac{d\tau}{d\lambda} \frac{1}{d\omega/d\lambda} = -\frac{\lambda^2}{2\pi c} \frac{d\tau}{d\lambda}. \quad (\text{B-15})$$

The second order term is acquired in a similar manner.

$$\frac{d^3\beta}{d\omega^3} = \frac{d^2\tau}{d\omega^2} = \left[\frac{d\tau}{d\lambda} \frac{d^2\lambda}{d\omega^2} + \left(\frac{d^2\tau}{d\lambda^2} \frac{d\lambda}{d\omega} \right) \frac{d\lambda}{d\omega} \right] = \frac{\lambda^2}{(2\pi c)^2} \left[2\lambda \frac{d\tau}{d\lambda} + \lambda^2 \frac{d^2\tau}{d\lambda^2} \right]. \quad (\text{B-16})$$

It is clear that there are common terms in the first and second order dispersion terms in $\frac{d\tau}{d\lambda}$, however when these are compared as in

$$\frac{\frac{1}{6} \left[\frac{2\lambda^3}{(2\pi c)^2} \right] \frac{d\tau}{d\lambda} (\omega - \omega_0)^3}{\frac{1}{2} \left[\frac{-\lambda^2}{(2\pi c)^2} \right] \frac{d\tau}{d\lambda} (\omega - \omega_0)^2} = \frac{\lambda(\omega - \omega_0)}{3\pi c} = \frac{(\omega - \omega_0)}{3\pi f_0} \quad (\text{B-7}),$$

where f_0 is the optical carrier frequency, following the primary assumption at the outset of this development, the second order term is necessarily small compared to the first order term and may be neglected. When the $\frac{d\tau}{d\lambda}$ becomes small as it is near the dispersion minimum the second order term in $\frac{d^2\tau}{d\lambda^2}$ may have an effect on the dispersion characteristics.

For wave lengths in the 1550 nm region second order terms are neglected and the fiber transfer function becomes

$$H(\omega, z) = \exp \left[-jz \left(\beta_c + \frac{d\beta}{d\omega} (\omega - \omega_0) - \frac{1}{2} \frac{\lambda^2}{2\pi c} \frac{d\tau}{d\lambda} (\omega - \omega_0)^2 \right) \right]. \quad (\text{B-18})$$

The flat phase component from the phase term β_c is neglected, and under the narrowband assumption the group velocity term, $\frac{d\beta}{d\omega}$, is assumed to be constant

thus imposing a linear phase shift which may also be neglected. Thus the transfer function of the fiber due to first order dispersion effects near 1550 nm is given by

$$H(\omega, z) = \exp \left[jz \frac{1}{2} \left(\frac{\lambda_0^2}{2\pi c} \right) D 4\pi^2 (f - f_0)^2 \right] = \exp \left[j \frac{\pi D L \lambda_0^2 f^2}{c} \right] \quad (\text{B-19})$$

where $D = \frac{d\tau}{d\lambda}$, and f is the frequency offset from the optical carrier. At $\lambda_0 = 1550$ nm D is approximately 16.45 ps/(nm•km)